Dependencies Between poly-Si Composition and Solar Cell Performance of poly-Si/SiO_x Passivating Contacts

Doctoral dissertation for obtaining the academic degree
Doktor der Naturwissenschaften (Dr.rer.nat.)

submitted by

Jonathan Steffens

at the

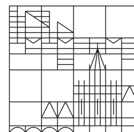

Universität Konstanz

Mathematisch-Naturwissenschaftliche Sektion
Fachbereich Physik

Konstanz, 2020

Konstanzer Online-Publikations-System (KOPS)
URL: http://nbn-resolving.de/urn:nbn:de:bsz:352-2-19tzla6vns71f7

Date of oral exam: 18.05.2020

1. Reviewer: Prof. Dr. Giso Hahn

2. Reviewer: Prof. Dr. Johannes Boneberg

Contents

Abstract v

List of Acronyms and Symbols vii

Introduction 1

Chapter 1. Passivating Contacts 3

1.1. Solar Cell Working Principle 3
1.2. Historical Development of Silicon-Based Solar Cell Concepts 5
1.2.1. Silicon Homojunction Solar Cells 5
1.2.2. Silicon Heterojunction Solar Cells 6
1.3. The poly-Si/SiO_x Passivating Contact 8
1.3.1. Interface Passivation 10
1.3.2. Charge Carrier Transport 10
1.3.3. Selectivity S_{10} as Figure of Merit for Passivating Contacts 12
1.3.4. State-of-the-Art 13

Chapter 2. Process Flow 15

2.1. Substrate Preparation 15
2.2. Interfacial Oxide Growth 17
2.3. a-Si Deposition 19
2.3.1. Plasma-Enhanced Chemical Vapor Deposition (PECVD) 19
2.3.2. Magnetron Sputtering Deposition (MSD) 22
2.3.3. a-Si Material Properties 25
2.4. Junction Formation 27
2.4.1. Solid Phase Crystallization (SPC) 27
2.4.2. Blistering 30
2.4.3. poly-Si Material Properties 32
2.5. Hydrogenation 34
2.5.1. SiN_x:H Deposition 35
2.5.2. Fast Firing (FF) 36

Chapter 3. Methods 39

3.1. Glow Discharge Optical Emission Spectroscopy (GD-OES) 39
3.1.1. Calibration Procedures 41
3.1.2. Hydrogen Calibration 43
3.1.3. Phosphorus Calibration 45

3.1.4. Correction for Atmospheric Contaminations 47
3.2. Fourier-Transform Infrared Spectroscopy (FT-IR) 49
3.2.1. Microstructure Factor R^* and Ratio Q^* 51
3.3. Raman Spectroscopy (RS) 52
3.3.1. Crystallinity χ_c 54
3.3.2. Crystallite Diameter d_c and Internal Stress σ 55
3.4. Spectroscopic Ellipsometry (SE) 56
3.4.1. Modeling 56
3.4.2. Optical Band Gap E_{gap} and E_{04} 58
3.4.3. Parasitic Absorption Current Density J_{PA} 59
3.5. Hall-Effect Measurement (HE) 60
3.5.1. Resistivity ρ_{HE} 61
3.5.2. Charge Carrier Concentration $n_{e/h}$ and Mobility $\mu_{e/h}$ 61
3.6. Photoconductance Decay Measurement (PCD) 62
3.6.1. Contact Recombination Current Density J_c 63
3.6.2. Implied Open Circuit Voltage iV_{oc} 64
3.6.3. Resistivity ρ_{PCD} 65

Chapter 4. As-Deposited Layers 67
4.1. Adjustment of PECVD Deposition Parameters 67
4.1.1. More Efficient SPC by nc-Si Deposition 67
4.1.2. Microstructure and Hydrogen Concentration in Relation to Blistering 69
4.1.3. Tuning of the Optical Band Gap for Reduced Parasitic Absorption 71
4.2. Variation of the Dopant Concentration 73
4.2.1. Influence of the Diborane Gas Flow Ratio on Interface Properties 73
4.2.2. Influence of the Diborane Gas Flow Ratio on Layer Properties 75
4.3. Incorporation of Light Elements 76
4.3.1. Larger Disorder to Avoid Blistering 76
4.3.2. Tuning of the Optical Properties for Reduced Optical Losses 78

Chapter 5. Crystallized poly-Si Layers 81
5.1. Strategies to Avoid Blistering 83
5.1.1. Adjustment of the PECVD Gas Flow Ratios 83
5.1.2. Adjustment of the PECVD Deposition Temperature 85
5.1.3. Section Summary 87
5.2. Variation of the Dopant Concentration 87
5.2.1. Composition 88
5.2.2. Microstructure 91
5.2.3. Optical Properties 92
5.2.4. Resistivity 94
5.2.5. Passivation Quality 97
5.2.6. Section Summary 101
5.3. Incorporation of Light Elements 101

5.3.1. Composition 101
5.3.2. Microstructure 103
5.3.3. Optical Properties 104
5.3.4. Resistivity 105
5.3.5. Passivation Quality 106
5.3.6. Section Summary 108
5.4. Adjustment of the SPC Parameters for Larger Crystallinity 109
5.4.1. Microstructure 109
5.4.2. Optical Properties 110
5.4.3. Resistivity 111
5.4.4. Passivation Quality 112
5.4.5. Section Summary 113

Chapter 6. Classification in Context of Solar Cell Performance 115
6.1. Dependencies Between Process Parameters and Solar Cell Performance 115
6.1.1. Dependencies Regarding the Dopant Concentration $\xi_{B/P}$ 116
6.1.2. Dependencies Regarding the Crystallinity χ_c 117
6.1.3. Dependencies Regarding the Optical Band Gap E_{04} 119
6.1.4. Dependencies Between J_c, ρ_{PCD} and J_{PA} 120
6.2. Applicability in a Solar Cell 122
6.2.1. Selectivity S_{10} and Ideal Solar Cell Efficiency η_{ideal} as Indicators for Solar Cell Performance 122
6.2.2. Applicability of Best Performing Layers 125
6.2.3. Influence of poly-Si Layer Thickness on Solar Cell Performance 126

Conclusions 129

List of Publications 131

Bibliography 133

Zusammenfassung 151

Appendix A. Appendix 155
A.1. List of tools 155
A.2. GD-OES Calibration Standards 157
A.3. a-SiC_x PECVD Deposition Parameters 158

Acknowledgements 159

Abstract

In this thesis, dependencies between incorporation of foreign elements in the poly-Si layer and solar cell performance of poly-Si/SiO_x passivating contacts are explored. For both dopant polarities a difference in total and electrically active dopant concentrations is observed. If applied on the front side of a solar cell, poly-Si/SiO_x contacts based on phosphorus doped poly-Si layers are rather limited by free carrier absorption and based on boron doped poly-Si layers are rather limited by detrimental strong dopant in-diffusion. Incorporation of the light elements oxygen, nitrogen and carbon widens the optical band gap and thus lowers parasitic absorption in the poly-Si layer at the expense of a higher resistivity. Both effects are mediated by a lower crystallinity compared to pure poly-Si layers without incorporated light elements. Therefore, the crystallinity was identified as key parameter for solar cell performance if applied on the front side of a solar cell. All investigated layer types yield an excellent passivation quality in terms of contact recombination current densities down to $J_c = 2.3$ fA/cm^2 and selectivities up to $S_{10} = 15.2$. The maximum achievable efficiency for an application of the investigated layers in an actual solar cell is estimated to $\eta_{ideal,max} = 24.2\%$ for a phosphorus doped poly-Si layer on the rear side and a boron doped poly-SiO_xN_y layer on the front side with thicknesses of 100 nm. This limit may be increased by $2\%_{abs}$ if the layer thicknesses are reduced to 30 nm.

List of Acronyms and Symbols

List of acronyms

Acronym	Description
ARC	Anti-reflection coating
a-Si	Amorphous silicon
a-Si:H	Hydrogenated amorphous silicon
a-SiC_x:H	Hydrogenated amorphous silicon carbide
a-SiO_x:H	Hydrogenated amorphous silicon oxide
a-SiO_xN_y:H	Hydrogenated amorphous silicon oxynitride
AlO_x:H	Hydrogenated aluminum oxide
B_2H_6	Diborane
BSF	Back surface field
BSG	Boron silicate glass
c-Si	Crystalline silicon
CVD	Chemical vapor deposition
Cz	Czochralski-grown silicon
DI-H_2O	De-ionized water
ECV	Electrochemical capacitance-voltage
FCA	Free carrier absorption
FF	Fast firing
FS	Fused silica
FT-IR	Fourier-transform infrared spectroscopy
FZ	Float-zone silicon
GD-OES	Glow discharge optical emission spectroscopy
HE	Hall-effect measurement
HF	Hydrofluoric acid
JMAK	Johnson-Mehl-Avrami-Komogorov
MSD	Magnetron sputtering deposition

Acronym	Description
nc-Si:H	Hydrogenated nanocrystalline silicon
NRA	Nuclear resonant reaction analysis
OM	Optical microscopy
PCD	Photoconductance decay measurement
PECVD	Plasma-enhanced chemical vapor deposition
PERC	Passivated emitter and rear cell
PMT	Photomultiplier tube
poly-Si	Polycrystalline silicon
poly-SiC_x	Polycrystalline silicon carbide
poly-SiO_x	Polycrystalline silicon oxide
poly-SiO_xN_y	Polycrystalline silicon oxynitride
PSG	Phosphorous silicate glass
PVD	Physical vapor deposition
QSS	Quasi-steady-state
RBS	Rutherford backscattering spectrometry
RS	Raman spectroscopy
SE	Spectroscopic ellipsometry
SEM	Scanning electron microscopy
SHJ	Silicon heterojunction
SiH_4	Silane
SiN_x:H	Hydrogenated silicon nitride
SiO_x	Silicon oxide
SPC	Solid phase crystallization
SRH	Shockley-Read-Hall
TCO	Transparent conductive oxide
TEM	Transmission electron microscopy

List of symbols

Symbol	Units	Description
α	(cm^{-1})	Absorption coefficient
α_{eff}	(cm^{-1})	Effective absorption coefficient
c_i	(at%)	Concentration of element *i*
χ_c	(%)	Crystallinity
d	(nm)	Layer thickness
d_c	(nm)	Crystallite size
E_{04}	(eV)	Optical band gap
E_{gap}	(eV)	Optical band gap
E_{ph}	(eV)	Photon energy
η	(%)	Solar cell efficiency
η_{ideal}	(%)	Solar cell efficiency according to the idealized one-diode model
I_i	-	GD-OES measured intensity of element *i*
I_x	(cm^{-1})	FT-IR measured absorption strength of bond *x*
iV_{oc}	(mV)	Implied open circuit voltage
J_0	(fA/cm^2)	Saturation current density
J_c	(fA/cm^2)	Contact recombination current density
J_{PA}	(mA/cm^2)	Parasitic absorption current density
J_{sc}	(mA/cm^2)	Short circuit current density
k	-	Extinction coefficient
λ	(nm)	Wavelength
$\mu_{e/h}$	(cm^2/Vs)	Charge carrier mobility of electrons / holes
n	-	Refractive index
$n_{e/h}$	(cm^{-3})	Charge carrier density of electrons / holes
n_i	(cm^{-3})	Atomic density of element *i*
n_{pin}	(cm^{-2})	Areal pinhole density
N_x	(cm^{-3})	Bond density of bond *x*
$P_{Si/B}$	(W)	Target power during MSD
q	- / (C)	GD-OES relative sputter rate or elemental charge
Q^*	-	Disorder ratio
Q_X	(sccm)	Gas flow of gas *X*
r_{pin}	(nm)	Pinhole radius
R^*	-	Microstructure factor
R_{sp}	(Ω)	Spreading resistance
R_X	(%)	Gas flow ratio with respect to Q_{SiH4}
ρ_c	(Ωcm^2)	Contact resistance
ρ_{HE}	(Ωcm)	HE determined resistivity
ρ_{PCD}	(Ωcm)	PCD determined resistivity
S_{10}	-	Selectivity
σ	(GPa)	Internal stress
T_{set}	(°C)	Deposition temperature
v_i	(at%)	GD-OES determined virtual concentration of element *i*
V_{oc}	(mV)	Open circuit voltage
V_{th}	(mV)	Thermal voltage
ω	(cm^{-1})	Wavenumber or Raman shift
ξ_i	(a.u.)	GD-OES and SE determined qualitative concentration of element *i*
z	(nm)	Position in layer parallel to the surface normal

Introduction

During the past year 2019, there has been an undeniable increase in awareness for intensified efforts towards a CO_2-free power generation in light of the climate change all over the world. In order to transform this increased awareness into actual change, not only political will and financial means but also new and improved technologies are necessary. One of these technologies is silicon-based photovoltaics which provides a durable and industrially established power generation. Its decentralized nature gives private individuals the opportunity to transform their increased awareness into actual change by directly participating in this environment-friendly power generation while being less dependent on unpredictable political decisions.

Since silicon-based photovoltaics is a worldwide accepted technology with a fast growing market, its improvement is expected to have a large impact. The average efficiency of today's commercial high-end modules is around 22% [1] while the world record laboratory module efficiency is 24.4% [2]. Closing this gap would hence increase the efficiency per module by roughly $10\%_{rel}$ with an increased laboratory efficiency not even being considered. To effectively benefit from this gain, it is important to sustain or even lower the $/kWh ratio, i.e. the enhanced power generation must not be compensated by larger production costs. This thesis contributes to these efforts towards a lower $/kWh ratio.

To be more specific, the present world record solar cell efficiency of 26.7% [2] was achieved with the silicon heterojunction (SHJ) concept whose production process is not compatible with existing production lines based on the aluminum back surface field (Al-BSF) or passivated emitter and rear cell (PERC) concept. Therefore, it could happen that the efficiency gain will be overcompensated by larger production costs. In contrast, passivating contacts based on polycrystalline silicon (poly-Si) on a thin interfacial silicon oxide layer (SiO_x) experience great interest as the laboratory cell efficiencies are close to the ones of the SHJ concept and an upgrade of existing PERC production lines with minor investments seems to be possible. A detailed description of these solar cell concepts with a focus on the passivating poly-Si/SiO_x contact is given in Chapter 1.

Besides its promising industrial feasibility, there are also drawbacks related to the poly-Si/SiO_x concept. In particular, the application of a standard poly-Si/SiO_x contact on the front side of a solar cell is limited by parasitic absorption within the poly-Si layer before the light reaches the silicon absorber. In this thesis, variations of the poly-Si layer composition in terms of dopant type and incorporation of foreign elements are investigated with regard to their influences on this parasitic absorption and efficiency potential.

To ensure comparability between different compositions, all layers are examined on structures prepared by a well-defined process as described in Chapter 2 and are evaluated by methods partly developed in the context of this thesis which are described in Chapter 3. In most cases the process

involves the deposition of initially amorphous silicon layers (a-Si) which are subsequently crystallized to poly-Si. Therefore, properties of these as-deposited layers and their influences on the crystallization process are presented in Chapter 4. The crystallized poly-Si layers with varying compositions were comprehensively studied in terms of microstructure, parasitic absorption, charge carrier transport as well as passivation quality and will be discussed in Chapter 5. Lastly, in Chapter 6 the applicability of these layers in a poly-Si/SiO_x based solar cell is evaluated with a particular focus on the application on the front side.

CHAPTER 1

Passivating Contacts

Nowadays, the most promising solar cell concepts are based on passivating contacts which are introduced in this chapter starting from the working principle of a semiconductor-based solar cell in Sec. 1.1. In order to understand today's great research interest in passivating contacts and the advantages of this concept, a historical outline of the development of previous silicon-based solar cell concepts is given in Sec. 1.2. The following Sec. 1.3 describes the details of a poly-Si/SiO_x passivating contact which constitutes the basis of this thesis. More specifically, the section discusses the involved passivation mechanisms, carrier transport through the contact, the definition of the selectivity as figure of merit for passivating contacts and ends with a brief outline of the state-of-the-art.

1.1. Solar Cell Working Principle

All semiconductor solar cell devices are based on the absorption of photons by the internal photoelectric effect during which electron-hole pairs are generated in an absorber material. These carriers have to be extracted from the solar cell via metal contacts before they recombine. To achieve this, semi-permeable membranes either for electrons or holes are placed on each side of the cell, which are also called selective contacts. The fundamental concept of such a membrane is a high conductivity for one charge carrier type (majority carrier) while the other type is effectively blocked by a low conductivity (minority carrier) [3]. The corresponding property is called selectivity and is fundamental for the working principle of a solar cell. Fig. 1.1 shows the band diagram of an ideal solar cell with an electron membrane and a hole membrane on opposing ends of the absorber. The band offset in the corresponding band edge blocks the minority carriers while the majority carriers easily pass the membrane for carrier extraction and power generation.

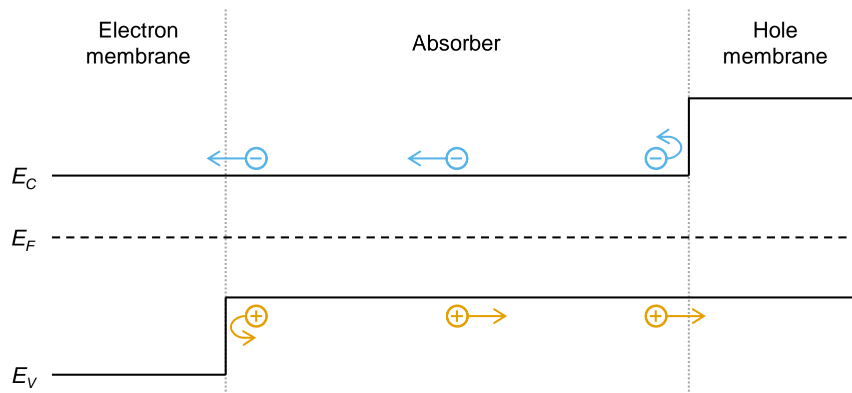

FIGURE 1.1. Band diagram of an ideal solar cell with the conduction band edge E_C, the valence band edge E_V and the Fermi energy E_F. The arrows of the electrons (–) and holes (+) illustrate the role of the membranes as being permeable for one charge carrier type while blocking the other one.

In a first approximation, the $J-V$ characteristics of a solar cell are described by the one-diode model [4]

$$J(V) = J_0 \left[\exp\left(\frac{V}{V_{th}}\right) - 1 \right] - J_{sc} \tag{1.1}$$

with the thermal voltage $V_{th} = kT/q$ at a given temperature T, the Boltzmann constant k, the elemental charge q and the short circuit current density J_{sc} for $V = 0$. The quantity J_0 is called saturation current density as the current saturates to this value under reverse bias voltage. In the context of photovoltaics, J_0 summarizes all recombination mechanisms into a recombination current density. For open circuit conditions $J(V) = 0$, eq. 1.1 can be rewritten as

$$V_{oc} = V_{th} \ln\left(\frac{J_{sc}}{J_0} + 1\right). \tag{1.2}$$

A third important quantity is the fill factor

$$FF = \frac{V_{mpp} J_{mpp}}{V_{oc} J_{sc}} \tag{1.3}$$

with V_{mpp} and J_{mpp} being the voltage and current density at the maximum power point. Combining eq. 1.1−1.3, the efficiency of a solar cell is defined as the ratio between the extractable electrical power at the maximum power point and the power of the incoming light P_{in}

$$\eta = \frac{V_{mpp} J_{mpp}}{P_{in}} = \frac{V_{oc} J_{sc} FF}{P_{in}}. \tag{1.4}$$

Limitations of this solar cell principle exist due to optical losses prior to conversion of incoming photons into electron-hole pairs, due to resistive losses during majority carrier transport from the absorber to the metal contacts and due to recombination of electron-hole pairs. Optical losses are mainly reflection, transmission or parasitic absorption in a surface layer which does not contribute to the generated photocurrent. This parasitic absorption within a surface layer can be quantified by a loss current density J_{PA} which contributes to the total optical loss current density J_{OL}. The resistive losses during majority carrier transport from the absorber through the membranes to the metal contacts are typically summarized by the contact resistance ρ_c in the context of passivating contacts.

Recombination takes place in the absorber material as well as at the surfaces, whereas the term *surface* refers in this context to the surface of the absorber which is typically passivated by an additional layer and is as such strictly speaking rather an interface. The recombination is divided into radiative recombination, Auger recombination and recombination via impurities or defects, also called Shockley-Read-Hall (SRH) recombination [5, 6]. As nowadays the silicon base material has a high purity, SRH recombination via defects at the surface is the dominating loss mechanism. The recombination near this surface can be quantified by the minority carrier recombination current density [7]

$$J_{rec} = J_c \left[\exp\left(\frac{V}{V_{th}}\right) - 1 \right]. \tag{1.5}$$

As the prefactor J_c is experimentally accessible and contributes to the saturation current density J_0 in eq. 1.1, it can be used as a quantification for the recombination near the surface [8]. In the following, J_c is referred to as the contact recombination current density since it mainly describes the recombination current density into the selective contact [7].

From eq. 1.2 it is evident that J_0 and thus J_c have to be minimized to achieve a high open circuit voltage V_{oc}, which in turn is necessary for high solar cell efficiencies (eq. 1.4). Such a reduction of the recombination current is achieved by surface passivation, typically divided into chemical and field-effect passivation. While the former aims at the saturation of interface defect states, the latter increases the density of one charge carrier type and decreases the density of the other type by a band offset in the surface region. This consequently reduces the recombination rate due to missing recombination partners.

The different solar cell concepts discussed in the following sections will be analyzed in terms of how far they minimize the optical loss current densities J_{OL} or J_{PA}, the contact recombination current density J_c and/or the contact resistance ρ_c.

1.2. Historical Development of Silicon-Based Solar Cell Concepts

In the following sections, the historical development of silicon-based solar cell concepts is outlined in order to emphasize the advantages of passivating contacts. After introducing the classical silicon homojunction cell concepts, in which selectivity is achieved solely by doping, the silicon heterojunction concept is described which achieves selectivity by a combination of materials with different band gaps.

1.2.1. Silicon Homojunction Solar Cells

Al-BSF Concept

The first industrially relevant solar cell concept was the Al-BSF concept for p-type crystalline silicon (c-Si) base material as absorber which is schematically depicted in Fig. 1.2 a). Charge carrier selectivity at the front side is achieved by a pn-junction in form of a phosphorus diffused emitter as electron membrane. An emitter is a highly doped n^+-region compared to the significantly lower p-type base doping which induces the desired differences in conductivities of both charge carrier types by a band offset[1] ΔE as shown in the band diagram in Fig. 1.2 c). The hole membrane at the rear side is an aluminum doped p^+/p high-low junction formed during full area aluminum metallization. A high-low junction on the rear side is also called back surface field, giving the Al-BSF concept its name. Surface passivation at the front side is provided by a hydrogenated silicon nitride (SiN_x:H) layer which saturates defect states and induces a field-effect via fixed charges, both reducing J_c. Additionally, the SiN_x:H layer acts as an anti-reflection coating (ARC) for a reduction of J_{OL}. The carrier extraction from the Al-BSF solar cell is achieved at the front side by contacting the emitter through the SiN_x:H with local screen printed metal fingers whilst at the rear side the full area aluminum provides the metal contact.

PERC Concept

The limitation of the Al-BSF concept is a large contact recombination current density J_c from the full area semiconductor-metal interface at the rear side and undesired absorption of infrared light in the p^+ doped region increasing J_{OL} [9]. In order to overcome this limitation, the PERC concept was developed [10] in which the rear side is contacted only locally, similar to the front side. In this way

[1]The term *band offset* is typically used in the context of discontinuous band structures in heterojunctions, but is also adopted for homojunctions within this thesis as the resulting effect on charge carrier selectivity is the same.

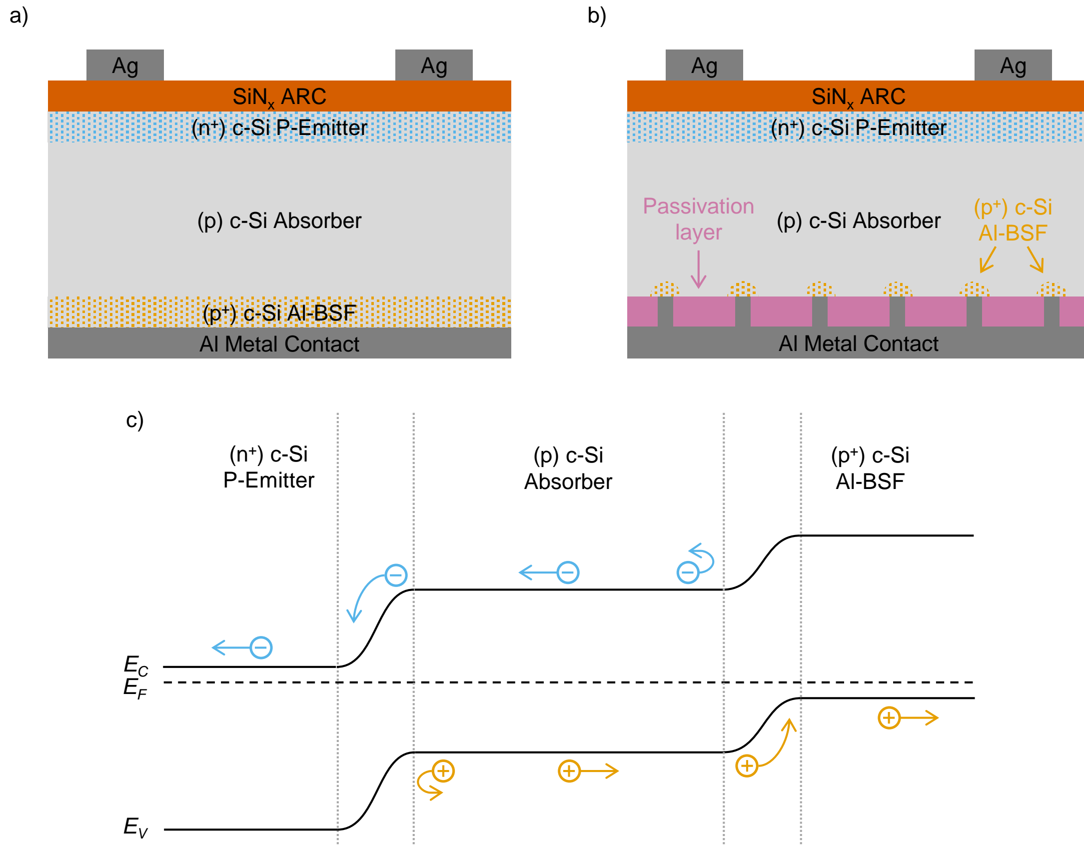

FIGURE 1.2. Sketches of an a) Al-BSF and b) PERC solar cell with phosphorus diffused (n^+) c-Si emitter and Al in-diffused (p^+) c-Si regions. c) Corresponding band diagram for both homojunctions at (p^+) c-Si regions, whereas the regions between the local metals contacts in the PERC solar cell are not considered.

the surface area fraction contacted by semiconductor-metal interfaces is reduced from $f_c = 1$ for the Al-BSF concept to lower values $f_c < 1$ which consequently decreases the total recombination current J_c. The band diagram under the local contact is essentially the same as for the Al-BSF concept (Fig. 1.2 c).

Fig. 1.2 b) schematically presents a p-type PERC solar cell. Charge carrier selectivity at the front side is achieved with a phosphorus diffused n^+-emitter as electron membrane. A SiN_x:H layer on top provides surface passivation and acts additionally as ARC, similar to the Al-BSF concept. The rear side is passivated over the full area by a dielectric passivation layer or layer stack with local contact openings forming local Al-BSFs as hole membranes.

1.2.2. Silicon Heterojunction Solar Cells

Even if the PERC concept significantly reduced the total semiconductor-metal interface area, the recombination at these interfaces and in the emitter still limits the solar cell efficiency [9]. The idea of an additional dielectric layer passivating the whole surface and thereby separating the c-Si base and the metallized material is called passivating contact. In this concept, ρ_c increases due to the additional dielectric passivation layer but is compensated by a significantly reduced contact recombination current density J_c since the base material is not directly in contact with a metal [11]. Thereby, full area contacts are formed ($f_c = 1$) without the large contact recombination current

density J_c from the full-area contact in the Al-BSF concept. This leads to a simple one-dimensional current flow pattern which eventually eliminates lateral resistive losses [12].

The first solar cell concept utilizing the concept of passivating contacts was the SHJ concept which is sketched in its present form in Fig. 1.3 a) [13]. The c-Si base is passivated on both sides with a few nanometer thin intrinsic hydrogenated amorphous silicon (a-Si:H) layer, providing both chemical passivation by hydrogen-induced interface defect saturation and field-effect passivation by the larger band gap of a-Si:H compared to c-Si. This larger band gap is the reason for the heterojunction character even though both materials are mainly silicon. Charge carrier selectivity is achieved with a highly doped (p^+) a-Si:H layer as hole membrane on one side and a (n^+) a-Si:H layer as electron membrane on the other side of the cell. Similar to the classical pn- or high-low junction, the minority charge carrier densities in these a-Si:H stacks are reduced leading to the desired differences in conductivities and thus selectivity.

The lateral conductivity of these a-Si:H stacks is too low for a sufficient lateral charge carrier transport to the local metal grid and parasitic absorption within these stacks increases J_{PA}. Therefore, transparent conductive oxides (TCO) addressing both issues are placed on top of these a-Si:H stacks. Furthermore, they act as ARC to reduce J_{OL} and are eventually metallized. The corresponding metal

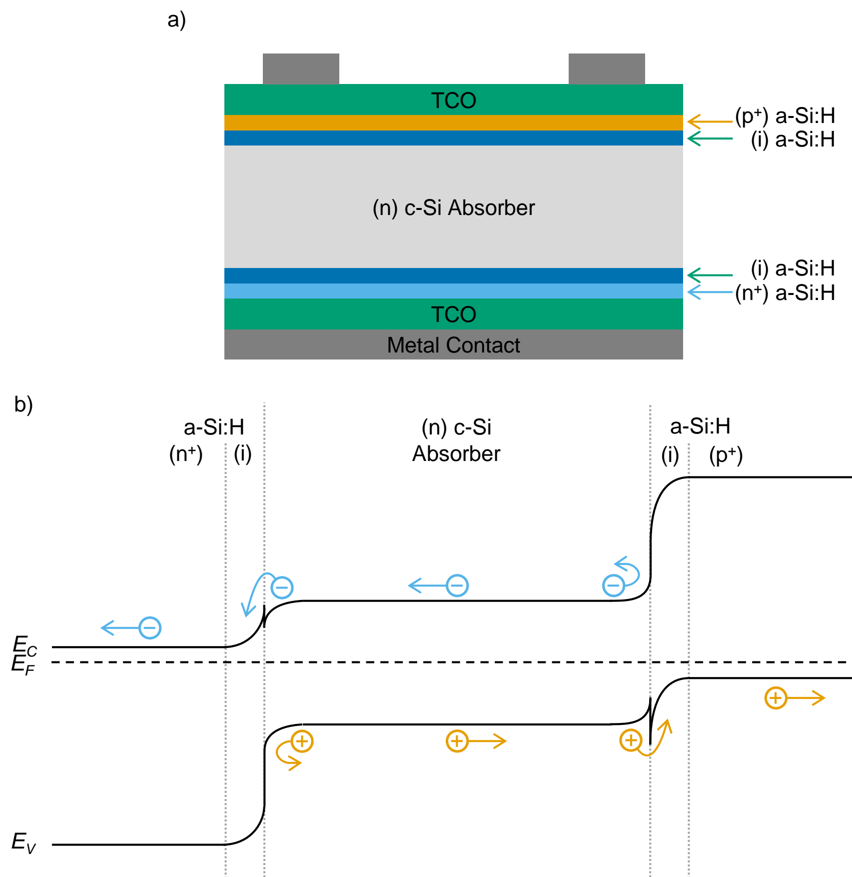

FIGURE 1.3. a) Sketch of a SHJ solar cell with a-Si:H stacks on both sides. b) Corresponding band diagram with band discontinuities in the band edge of the majority carriers induced by the (i) a-Si:H layer.

contacts cannot be fabricated with established processes from the previously discussed homojunction cell concepts as these processes require a high temperature treatment (∼ 800°C) for contact formation. In SHJ solar cells a high temperature treatment would force the hydrogen to effuse from the (i) a-Si:H layer and change the layer structure which would consequently remove the chemical passivation ability. Therefore, the whole fabrication process must not significantly exceed the typical deposition temperature of the a-Si:H layer stack of around 200°C. This requires challenging low-temperature metallization schemes and the abandonment of the beneficial impurity gettering effect, restricting SHJ solar cells to high-purity absorber material [14].

The band diagram of a SHJ solar cell is different to the one of both previously discussed homojunction cell concepts as can be seen in Fig. 1.3 b). Due to the larger band gap of a-Si:H compared to the c-Si base, on the one hand the band offset is significantly increased leading to a higher selectivity and thus more effective blocking of minority carriers. On the other hand, this larger band gap induces discontinuities in the band edge of the majority carriers, forming undesired potential barriers which increase ρ_c.

1.3. The poly-Si/SiO_x Passivating Contact

The poly-Si/SiO_x structure is known from its implementation in bipolar junction transistors since the 1970s [15] but receives growing attention in the field of photovoltaics only recently [11]. When applied in solar cells, it is quite similar to the SHJ concept and therefore also referred to as passivating contact. There are at least two acronyms for this concept, namely Polycrystalline Silicon on Oxide (POLO) [16] introduced by ISFH in Hameln, Germany, and Tunneling Oxide Passivating Contact (TOPCon) [17] introduced by Fraunhofer ISE in Freiburg, Germany. Both acronyms essentially refer to the same concept but mostly differ regarding the thickness of the SiO_x layer. To avoid this rather confusing terminology, the term poly-Si/SiO_x contact is used throughout this thesis.

In Fig. 1.4 a) the basic structure of a poly-Si/SiO_x contact is illustrated. Compared to the SHJ concept, the layer for chemical passivation separating the c-Si base from the metallized material is replaced by a thin interfacial silicon oxide layer with a thickness < 3 nm. Due to its large band gap it is a tunnel barrier for charge carriers and also a diffusion barrier for dopants [19, 20]. The inherent disadvantage in the SHJ concept, namely the discontinuities in the band structure of the majority carriers, is avoided by the poly-Si/SiO_x concept since the band gap of poly-Si is similar to the one of c-Si (Fig. 1.4 b). Charge carrier selectivity is achieved by degenerately doping of the poly-Si layers on top of the interfacial oxide, whereby (n^+) doping forms the electron and (p^+) doping forms the hole membrane. A second source of selectivity are the asymmetric tunnel barrier heights for tunneling of electrons (∼ 3.1 eV) and holes (∼ 4.8 eV) [18] through a sufficiently thin interfacial oxide, if tunneling is the dominant transport mechanism (Sec. 1.3.2). Similar to the SHJ contacts, poly-Si/SiO_x contacts significantly reduce the contact recombination current density J_c by an excellent interface passivation while accepting a higher contact resistance ρ_c due to the interfacial oxide acting as a tunnel barrier.

In contrast to the doped a-Si:H layer in the SHJ concept, the highly doped poly-Si layer is expected to feature a sufficient lateral conductivity for a direct metallization without an additional TCO layer.

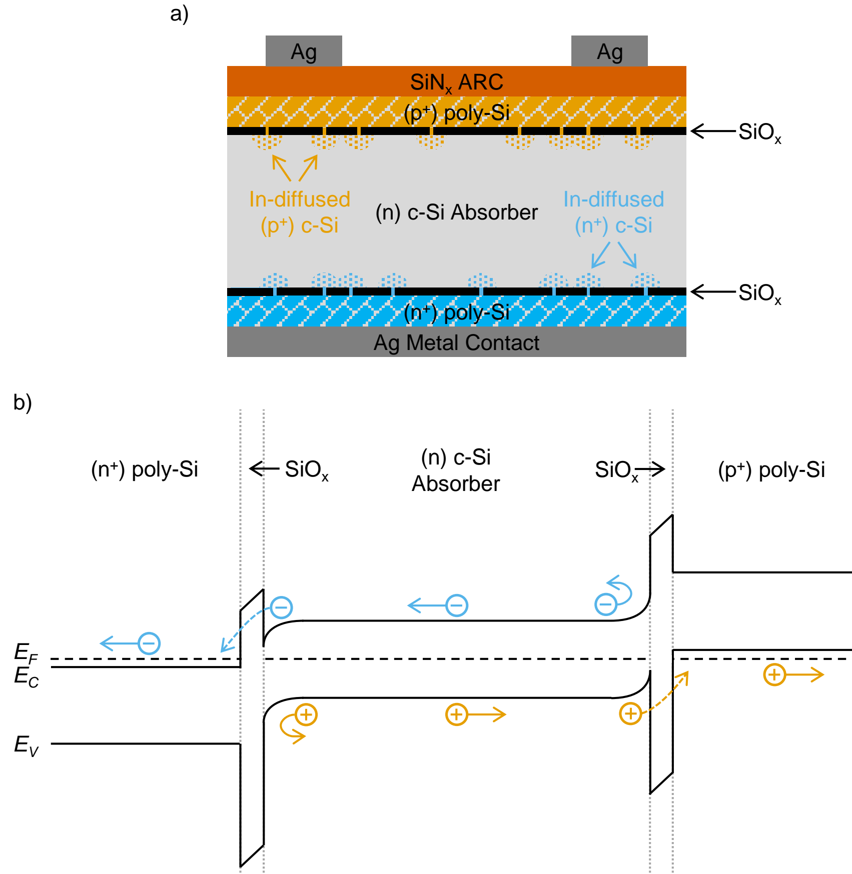

FIGURE 1.4. a) Sketch of a solar cell with poly-Si/SiO$_x$ contacts on both sides. Interruptions of the black lines (interfacial oxides) indicate pinholes with in-diffused (p^+/n^+) c-Si regions below. b) Corresponding band diagram with asymmetrical high potential barriers in both band edges induced by the interfacial oxide and degenerately doped poly-Si layers based on [18]. Dashed arrows indicate tunneling transport, whereas pinhole conduction is not considered in this band diagram.

The disadvantage of replacing the TCO by heavily doped poly-Si is a significantly increased parasitic absorption J_{PA} inside the poly-Si layer for comparable layer thicknesses and conductivities, in particular if applied on the front side of a solar cell. Considering the large dopant concentrations in the poly-Si layer, free carrier absorption (FCA) also takes place. This parasitic absorption could be easily controlled by the poly-Si layer thickness [21]. Unfortunately, a lower poly-Si layer thickness increases the danger of harming the interfacial oxide passivation during metallization utilizing established high temperature metal contact formation processes, as, contrary to the SHJ concept, poly-Si/SiO$_x$ contacts are temperature stable due to the crystallization of previously deposited a-Si into poly-Si during junction formation at $\sim 900°C$ (Sec. 2.4). In this sense, the upgrade of an existing production line for PERC solar cells towards an integration of poly-Si/SiO$_x$ contacts is more likely than towards an integration of the SHJ concept as the latter partly relies on process steps not compatible with the PERC concept, i.e. low temperature metallization [14, 22].

In the following sections, the poly-Si/SiO$_x$ contact is described in more detail. After first pointing out the involved passivation mechanisms for the reduction of the contact recombination current density J_c (Sec. 1.3.1), the not yet fully understood transport mechanisms through the interfacial oxide are discussed in the context of resistive losses, summarized by the contact resistance ρ_c (Sec. 1.3.2).

The combination of J_c and ρ_c eventually leads to the definition of the selectivity, a quantity which directly reflects the potential of high efficiencies achieved by passivating contacts (Sec. 1.3.3). In the last part of this section, a brief overview is given on the state-of-the-art and on current topics of intensive research regarding poly-Si/SiO_x contacts (Sec. 1.3.4).

1.3.1. Interface Passivation

The chemical passivation in a poly-Si/SiO_x contact is achieved by an interfacial oxide, which is a well-studied and established passivation material for silicon [23]. However, the interfacial oxide in a poly-Si/SiO_x contact with a thickness of < 3 nm saturates the interface defects only to some extent. Further saturation is achieved by supplying hydrogen to the interface after the junction formation, which is typically referred to as hydrogenation (Sec. 2.5).

Regarding the field-effect passivation, there are several ways to induce a band offset in semiconductors. For heterojunctions (i.e. SHJ) the difference in the band gap energy is sufficient, whereas for homojunctions (i.e. Al-BSF, PERC) the band offset is achieved by doping. As the energy band gap of poly-Si is similar to the one of the c-Si base, poly-Si/SiO_x contacts achieve the band offsets by heavy doping of the poly-Si layer. Fig. 1.4 b) shows the band diagram of a (n^+) poly-Si/SiO_x contact. The band offset follows from the condition that in equilibrium the Fermi energy E_F has to be constant over the whole structure. Based on this condition, an offset evolves between regions of different dopant concentrations since doping shifts E_F closer to the band edge. A corresponding band diagram is sketched in Fig. 1.4 b) for a moderately doped (n) c-Si base and a highly doped (n^+) poly-Si layer. Additionally, the shift of E_F avoids a barrier in the majority charge carrier band at the semiconductor-metal interface.

During junction formation at $\sim 900°C$ dopants diffuse from the poly-Si through the interfacial oxide into the c-Si base and form a shallow emitter [20, 24]. Even though this in-diffusion supports the passivation by further reducing the minority carrier density at the interface, excessive doping of the a-Si before or during crystallization causes the recombination to increase again by a detrimental strong in-diffusion into the c-Si base. Interestingly, Auger recombination was found to play a minor role in this context [18, 24]. Rather an increased recombination at the SiO_x/c-Si interface due to dopant penetration of the interfacial oxide was proposed as an explanation. This has at least been reported for boron doping [25]. However, Auger recombination in the poly-Si itself accompanied by FCA is expected to degrade the total solar cell performance [26]. Altogether, these effects lead to the existence of an optimal dopant concentration which has to be adjusted carefully [19, 21].

Poly-Si is a defect-rich material providing many recombination centers (Sec. 2.4.3). However, due to the excellent interface passivation and hence low minority carrier density in the contact, this large defect density is not a limiting factor as the recombination partners are few.

1.3.2. Charge Carrier Transport

Besides a good passivation quality, resistive losses during transport through the electron and hole selective contacts should be minimized, described by a low ρ_c. As mentioned above, passivating contacts significantly reduce the contact recombination current density J_c while accepting an increased ρ_c. For poly-Si/SiO_x contacts, this increase is mainly attributed to the transport through the

interfacial oxide, which will be discussed in the following. A description of the conduction within the poly-Si layer is given later in Sec. 2.4.3.

The involved conduction mechanisms through the interfacial oxide have been continuously discussed since the first application of poly-Si/SiO$_x$ contacts in bipolar transistors in the 1970s [27, 28]. In the context of photovoltaics, two models are typically mentioned, namely tunneling through the oxide [29] and transport via pinholes which are local microscopic breakups of the oxide [30]. As far as tunneling is concerned, the actual transport mechanism is expected to strongly depend on the oxide thickness. Likewise, the pinhole density can also be thought of as a function of the oxide thickness and additionally of the junction formation process. In particular, the dopant in-diffusion if based on pinholes forming a shallow emitter is necessary for pinhole conduction and as such for a functioning poly-Si/SiO$_x$. Based on these dependencies on the actual process parameters and the experimentally not observed asymmetry between electron and hole selective contacts due to different tunnel barrier heights as indicated in Fig. 1.4 b), it is evident that in the general case rather a combination of both transport mechanisms is an appropriate description. Indeed, a more elaborate model combining both mechanisms leads to improved agreement with experimental data [18]. Nevertheless, for a specific realization of a poly-Si/SiO$_x$ contact, either tunneling or transport via pinholes might be the dominant mechanism, mostly determined by the thickness of the interfacial oxide.

For rather thick interfacial oxides ($>$ 2 nm) the tunnel probability is strongly reduced and hence the charge carrier transport is dominated by pinhole conduction. In [30] the authors described the conduction by a homogeneously and highly doped hemisphere region below the pinhole on the substrate side formed by dopant in-diffusion from the poly-Si layer through the pinhole. This situation is sketched in Fig. 1.5 exemplarily for a (n^+) poly-Si/SiO$_x$/(n) c-Si structure with the in-diffused and highly doped (n^+) c-Si hemisphere region below the pinhole in the interfacial oxide. The corresponding contact resistance is then determined by the actual dopant concentration in this region. In this thesis, such concentrations in the substrate were not measured and therefore this approach was adjusted so that the contact resistance ρ_c is directly determined by the resistivity in the poly-Si layer ρ_{poly} as follows. Considering the same hemisphere and the occurrence of current crowding, the

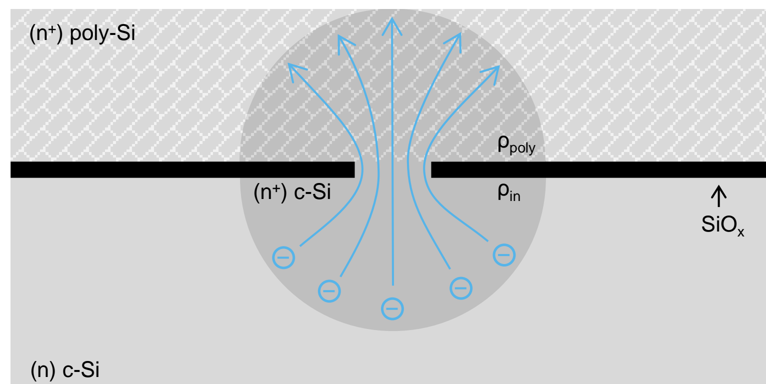

FIGURE 1.5. Sketch of a pinhole in a (n^+) poly-Si/SiO$_x$/(n) c-Si structure with the in-diffused highly doped (n^+) c-Si hemisphere below the pinhole with resistivity ρ_{in} and the hemisphere above the pinhole with resistivity ρ_{poly}. The current crowding is illustrated by the flow paths (arrows) of the electrons (–).

corresponding resistance can be described by the general expression for the spreading resistance [31]

$$R_{sp} = \frac{\rho_{in}}{2\pi\, r_{pin}} \tag{1.6}$$

with the resistivity of the highly doped hemisphere in the c-Si substrate ρ_{in} and the radius of a pinhole r_{pin}. In contrast to [30], the second hemisphere on the poly-Si side of the pinhole is assumed to also contribute to the contact resistance and is equally dominated by the spreading resistance according to eq. 1.6 as function of the experimentally determined resistivity of the poly-Si layer $R_{sp}(\rho_{poly})$. Assuming the resistivity is similar in both hemispheres ($\rho_{in} \approx \rho_{poly}$), the contact resistance is then obtained by twice the spreading resistance divided by the areal pinhole density n_{pin} via

$$\rho_c = \frac{2\, R_{sp}}{n_{pin}} = \frac{\rho_{poly}}{\pi\, r_{pin}\, n_{pin}} \tag{1.7}$$

and as such a function of the experimentally determined resistivity of the poly-Si layer.

Admittedly, $\rho_{in} \approx \rho_{poly}$ is a strong assumption in face of typical dopant concentrations in the poly-Si layer of $\sim 10^{20}$ cm^{-3} compared to typical in-diffused dopant concentrations in the c-Si substrate of $\sim 10^{18}$ cm^{-3}, as is assumed for model input in [18]. Nonetheless, as will be described in detail later in Sec. 2.4.3, a significant difference in resistivity between poly-Si and c-Si for equal dopant concentrations up to one order of magnitude may occur within this concentration range. This gap is expected to be even larger for intentionally increased resistivities, in particular by incorporation of foreign elements as was done in the context of this thesis. A further justification for the mentioned assumption arises from the comparable hemisphere dimensions of $\sim$ 100 nm for both the poly-Si layer thickness and the depth of the in-diffused dopants [30]. Even though this assumption is not perfectly justified and absolute values of the contact resistance according to eq. 1.7 should be interpreted carefully, it offers an approach for qualitative comparisons based on the rather easily accessible resistivity of the poly-Si layer.

1.3.3. Selectivity S_{10} as Figure of Merit for Passivating Contacts

As mentioned in Sec. 1.1, charge carrier selectivity is the fundamental principle of a solar cell and should be quantified as such. This is done by the ratio between the minority ρ_m and majority ρ_M carrier resistances of the contact [7]

$$S = \frac{\rho_m}{\rho_M}. \tag{1.8}$$

The minority carrier resistance is approximated by the inverse slope of the current-voltage curve at zero voltage $\rho_m = V_{th}/J_c$, with the thermal voltage $V_{th} = kT/q$ at $T = 298.15$ K, while the majority carrier resistance is given by the contact resistance $\rho_M = \rho_c$. Based on this, eq. 1.8 leads to large numbers with a variation over orders or magnitude. Therefore, the decadic logarithm is used, eventually leading to the definition of the minority carrier selectivity

$$S_{10} = \log\left(\frac{V_{th}}{J_c\, \rho_c}\right) \tag{1.9}$$

as figure of merit for passivating contacts.

According to [7], this selectivity is linked to a maximally achievable efficiency η_{max} in the case of a limitation by extrinsic recombination via the monotonic formula

$$\eta_{max} = (2.4733 \cdot S_{10} - 4.432)\ \% \tag{1.10}$$

and in the case of a limitation by intrinsic recombination in a perfect silicon absorber via

$$\eta_{max} = \left[(2.452 \cdot S_{10} - 4.240)^{-19.52} + 29.21^{-19.52}\right]^{-\frac{1}{19.52}}\ \%. \tag{1.11}$$

It are these monotonic relations in eq. 1.10 and 1.11 between η_{max} and S_{10} which qualify the selectivity as appropriate figure of merit for passivating contacts.

The historical improvement of solar cell concepts as described in Sec. 1.2 is reflected in an increase of the selectivity as depicted in Table 1.1 [32]. In order to understand the superiority of the poly-Si/SiO$_x$ contacts, it is useful to express the selectivity in terms of the majority and minority carrier concentrations $n_{M/m}$ and mobilities $\mu_{M/m}$ assuming no recombination at the poly-Si/SiO$_x$ interface, infinite recombination velocity at the c-Si/poly-Si interface in the presence of pinholes in the interfacial oxide and no recombination in the c-Si base

$$S_{10} = \log\left(\frac{\mu_M\, n_M}{\mu_m\, n_m}\right). \tag{1.12}$$

The authors in [7] derived from the experimentally determined value of $S_{10} = 15.6$ for an (n$^+$) poly-Si/SiO$_x$ contact on an n-type c-Si base a majority carrier concentration of $n_M = 7 \cdot 10^{17}$ cm^{-3} and a minority carrier concentration of $n_m = 2.7 \cdot 10^2$ cm^{-3}. It is this difference in carrier concentrations of 15 orders of magnitude which causes the high selectivities for poly-Si/SiO$_x$ contacts. Interestingly, if eq. 1.12 is expressed in terms of the majority and minority carrier conductivities $\sigma_{M/m}$ via

$$S_{10} = \log\left(\frac{\sigma_M}{\sigma_m}\right) \tag{1.13}$$

it directly supports the picture in [3] that solely differences in conductivities between electrons and holes are responsible for the selectivity. Indeed, the authors in [3] proofed by simulations that these different conductivities can be equally achieved solely by large differences in charge carrier mobilities in the same material and thus in absence of any electric field. However, this scenario is not of practical relevance as such large mobility differences cannot be achieved within the same material.

1.3.4. State-of-the-Art

During the past few years, functioning poly-Si/SiO$_x$ contacts with a potential for application in high efficiency solar cells have been demonstrated for a variety of a-Si deposition and interfacial oxide

TABLE 1.1. Selectivities S_{10} according to eq. 1.9 for the solar cell concepts described in Sec 1.2 and 1.3. Data taken from [32].

	Electron selective contact $S_{10,e}$	Hole selective contact $S_{10,h}$
Homojunction	12.0	13.0
SHJ	14.1	13.5
poly-Si/SiO$_x$	16.4	14.3

growing techniques [33–40]. Within this development, the present world record cell efficiency with a p-type c-Si substrate of 26.1% was achieved by an interdigitated back contacted (IBC) solar cell with poly-Si/SiO_x contacts for both polarities on the rear side [37]. However, the processes leading to such high efficiencies are complicated and expensive and as such difficult to realize in industrial mass production. Therefore, a lot of research is currently invested into the development of industrially relevant processes. Such efforts include finding an a-Si deposition technique with high throughput and low maintenance, preferably with the possibility of in-situ doping to avoid an additional ex-situ doping process step like ion implantation or $POCl_3$- / BBr_3-diffusion. In-situ doped a-Si layers are in turn the requirement for a recently developed process flow which omits the crystallization step during junction formation. Therein, the fast firing (FF) step for metal contact formation was shown to be sufficient for the poly-Si/SiO_x junction formation [39].

Another topic currently investigated in light of industrial mass production is the screen-printed metallization without harming the interfacial oxide which requires a sufficiently thick poly-Si layer [38, 41]. Increasing attention is also paid to processes where the interfacial oxide is grown in the same device as the subsequent a-Si deposition will take place without breaking the vacuum [33]. A proof of principle in a pilot production line was recently reported [38].

Most of the successfully developed poly-Si/SiO_x contacts are based on phosphorus doped (n^+) poly-Si, while boron doping for (p^+) poly-Si seems to be more challenging. This is true in particular for plasma-enhanced chemical vapor depositions (PECVD) with in-situ boron doping which suffers from blistering during junction formation for wide deposition parameter ranges [34, 42, 43]. Additionally, the diffusion barrier character of the interfacial oxide is less pronounced for boron compared to phosphorus which causes a stronger detrimental boron in-diffusion into the c-Si base [20]. This asymmetry between the polarities and the potential for parasitic light absorption in the poly-Si layer are the main reasons for the typical application of an (n^+) poly-Si/SiO_x contact on the rear side of the solar cell in combination with a p-type PERC or SHJ front side. As only a small efficiency gain is expected for a combination with a PERC front side for both polarities [22], efforts are also put into the development of a suitable application of poly-Si/SiO_x contacts on the front side of a solar cell. The expected parasitic absorption is typically reduced by insertion of light elements in the poly-Si layer, i.e. oxygen or carbon [44, 45]. Besides the thereby reduced parasitic absorption, the resulting wider band gap also induces a larger band offset enhancing the field-effect passivation. The amount of light elements has to be adjusted carefully as the crystallinity decreases and in turn the resistivity increases with higher concentrations. Another approach is to reduce parasitic absorption by a standard PERC front side with locally aligned poly-Si/SiO_x structures below the metal grid, which was recently explored via numerical simulations [46].

The most recent progress has been the demonstration of an industrial production line for solar cells consisting of an (n^+) poly-Si/SiO_x rear and PERC front side, both metallized by screen-printing with solar cell efficiencies of up to 24.58% [47].

CHAPTER 2

Process Flow

In order to ensure comparability between poly-Si layers with different compositions, a well-defined process flow for poly-Si/SiO_x contact fabrication has been developed and applied throughout this thesis for all samples. In this chapter, this standard process flow is described accompanied by exemplifications of material properties and process step optimizations as performed in the experimental phase of this thesis. The process flow is summarized in Fig. 2.1 and the structure of this chapter follows the categories on the right hand side of this figure. After substrate preparation of three different substrate types (Sec. 2.1), the interfacial oxide was grown on both sides of the silicon substrates (Sec. 2.2). The subsequently deposited intrinsic or in-situ doped a-Si layers (Sec. 2.3) were crystallized to poly-Si during the junction formation by solid phase crystallization (SPC) either in inert N_2 atmosphere or by $POCl_3$-diffusion (Sec. 2.4). Hydrogenation to enhance the chemical passivation of the layers on silicon substrates was achieved by deposition of a SiN_x:H layer and a subsequent FF step (Sec. 2.5). It should be emphasized that only planar substrates were used and no metallization was performed throughout this thesis.

2.1. Substrate Preparation

Three types of substrates were used in this thesis. On the one hand, silicon monocrystals grown by the float-zone (FZ) [48] or the Czochralski process (Cz) [49] served as substrates for symmetrical test samples. Silicon FZ contains far less impurities than Cz grown silicon and is thus used to demonstrate high efficiency cell potentials. This higher purity implies higher process costs and therefore Cz material is chosen for industrial monocrystal-based solar cell production. On the other hand, fused silica (FS) substrates were used for specific characterization methods of the poly-Si layer since it

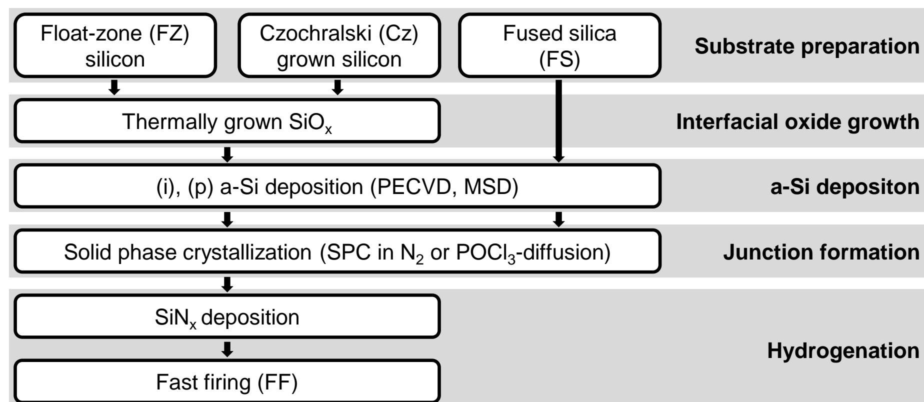

FIGURE 2.1. Standard process flow for fabrication of poly-Si/SiO_x contacts as applied throughout this thesis. On FS substrates neither an interfacial oxide was grown nor the hydrogenation was performed. The structure of this chapter follows the categories on the right hand side.

provides a higher contrast between layer and substrate in terms of crystal structure and conductivity compared to the silicon monocrystal substrates. Hence, neither the interfacial oxide was grown on FS substrates nor hydrogenation was performed. All three substrate types were commercially acquired and prepared as follows.

Float-zone silicon

The initial FZ substrates were delivered as 250 µm thick six inch circular wafers with a chemically polished surface and p-type boron or n-type phosphorus doping with a resistivity of 200 Ωcm. These wafers were manually cleaved into $\sim$ 5 x 5 cm^2 squares along crystal axes and labeled with a sample identifier with a diamond cleaver. To save material, the original circular wafer shape lead to curved edges on some samples. However, the exact dimension is not of interest for the applied characterization methods and hence the resulting uncertainty is neglected.

In a subsequent step, a silicon oxide deliberately grown by the manufacturer as surface protection was removed in a 2.5% hydrofluoric acid (HF) solution immediately before growing the interfacial oxide (Sec. 2.2). In some cases the breaking into 5 x 5 cm^2 squares was performed after the interfacial oxide was grown. This might influence the detailed characteristics of the final samples as the inner sample edges featured no interfacial oxide. However, a systematic deviation was not observed in the data.

Czochralski grown silicon

The Cz substrates were delivered with an unpolished and impurity-rich surface induced by wafer sawing. The base resistivity was $1-10$ Ωcm for both p-type boron and n-type phosphorus doped substrates. The dimensions of the wafers were initially 156 x 156 mm^2 semi-square with a thickness of $\sim$ 190 µm. These wafers were cut into exact 5 x 5 cm^2 and labeled with a sample identifier by a laser, inducing further surface damage. Both the saw and laser damage were removed in a KOH based solution by etching $\sim$ 10 µm on each side, during which a few micrometer high structure of square terraces with lateral dimensions of up to $\sim$ 100 µm evolved on the surface. For a subsequent polishing, the wafers were placed in a solution of acetic acid (CH_3COOH), nitric acid (HNO_3) and HF. In a last cleaning step, a surface oxide was grown in a piranha solution of hydrogen peroxide (H_2O_2) and sulfuric acid (H_2SO_4) to bind impurities, which were eventually removed by etching the oxide in 2.5% HF solution. As it was the case for the FZ substrates, the final HF etch step was performed immediately before growing the interfacial oxide (Sec. 2.2). At this stage, the thickness of the samples was reduced by the etching steps to roughly $160-170$ µm. The exact thickness as well as the base doping was determined for each experiment individually.

Fused silica

Two types of FS substrates were used in this thesis. The first type was delivered with a polished and cleaned surface in six inch dimension and 500 µm thickness, which were cut into 2 x 2 cm^2 pieces by an automatic dicing saw. A sample identifier was manually written on one side of the resulting samples with a diamond cleaver, marking this side as the rear side. Since the sawing was expected to deposit impurities on the surface, the wafers were pre-cleaned in an ultra-sonic

isopropanol solution bath before cleaning in a piranha solution followed by a 2.5% HF solution etch, similar to the cleaning of the Cz substrates.

The second type of FS substrates was delivered with a polished and cleaned surface in 2 x 2 cm^2 square dimension and $\sim$ 250 µm thickness. After a sample identifier was written manually on one side of the substrate with a diamond cleaver, marking this side as the rear side, no additional substrate preparation step was performed.

2.2. Interfacial Oxide Growth

As mentioned in Sec. 1.3.4, there are several techniques to deliberately grow an interfacial oxide with a thickness < 3 nm. These are commonly divided into thermally or wet chemically grown oxides. In both cases, the oxide grows by reaction with the present silicon atoms of the substrate. Interfacial oxides deposited with additional silicon atoms, in particular by PECVD deposition, are a third option. Throughout this thesis, a thermally grown interfacial oxide was used for the symmetrical test samples and hence only the growth mechanism of the thermal oxide is described in the following.

Thermal oxidation of a silicon substrate can be performed with H_2O as oxidant (wet oxidation) or in pure O_2 atmosphere (dry oxidation). In both cases, the oxygen atoms diffuse through the already existing oxide layer reacting with the silicon atoms in the underlying pure silicon substrate. The initial stage of the process is characterized by an increased growth rate, which can be described by the model in [50]. Therein, the oxide thickness d_{ox} as function of the process duration t at temperature T is given by

$$d_{ox}(t,T) = \left[\left(\frac{A}{2} \right)^2 + B\,t + \sum_{i=1}^{2} K_i\, \tau_i \left(1 - e^{-\frac{t}{\tau_i}} \right) + \left(d_n^2 + A\, d_n \right) \right]^{\frac{1}{2}} - \frac{A}{2} \tag{2.1}$$

with A and B being temperature dependent experimentally determined constants [51] and d_n the thickness of an initially existent native oxide layer. The four functions $K_i(T)$ and $\tau_i(T)$ are Arrhenius-like expressions and the corresponding prefactors and activation energies are listed in [50]. For thin oxides as applied in poly-Si/SiO_x contacts, the bond configuration is expected to differ from the dioxide stoichiometry ($x < 2$) due to the presence of bulk-like and diatomic-like silicon monoxides [52].

The interfacial oxide in this thesis was grown only on the silicon substrates and was the same for all experiments, ensuring an isolated study of the poly-Si layer properties. It was grown immediately after the terminating HF etch of the substrate cleaning in the same clean room environment by dry oxidation in a quartz tube furnace[2]. The process parameters were derived from [53]. After loading at 675°C, the samples were heated to the process temperature of 725°C with a heat rate of 4 K/min in a mixed N_2/O_2 10:1 atmosphere to achieve an increased layer homogeneity [53, 54]. Pure O_2 atmosphere was sustained at the process temperature for a duration of 10 min before the samples were cooled down to the loading temperature in inert N_2 atmosphere at a cooling rate of 4 K/min. Spectroscopic ellipsometry (SE) measurements (Sec. 3.4) revealed an average oxide thickness of

[2]Technical details can be found in the Appendix A.1.

2.5 nm on FZ substrates. This thickness guarantees a stable chemical passivation which is beneficial for an isolated investigation of the poly-Si layer influences on the poly-Si/SiO_x contact.

A calculation via eq. 2.1 for the given process parameter yields $d_{ox} = 2.5$ nm if an initial native oxide thickness of $d_n = 1.7$ nm is assumed. This value is reasonable since after the final HF etch the samples were rinsed in de-ionized water (DI-H_2O) possibly leading to a re-growth of a thin oxide which might even be boosted during loading the tube furnace in ambient atmosphere at elevated temperatures. However, this estimation is very rough as all constants in eq. 2.1 are expected to be temperature and furnace dependent, and strictly speaking, the model is only valid for the temperature range of 800 – 1000°C.

Storage Duration

As the quartz tube furnace was not constantly available over the time period when the experiments for this thesis were executed, a stock of silicon substrates was processed up to the growth of the interfacial oxide. Following experiments used these precursors for subsequent poly-Si/SiO_x contact processing. A longer storage time between the growth of the interfacial oxide and the subsequent a-Si:H deposition was found to decrease the passivation quality on the time scale of one day [55]. Based on these findings and to ensure comparability between all investigations, the influence of the storage duration on the passivation quality was analyzed on the time scale of one year. FZ precursors with a storage duration in a clean room environment ranging from three to twelve months and samples featuring a freshly oxidized interfacial oxide were simultaneously processed with magnetron sputter deposited (MSD) ex-situ doped (n)[3] poly-Si layers (Sec. 2.3.2). The results concerning the passivation quality in terms of contact recombination current density J_c (Sec. 3.6.1) after hydrogenation (Sec. 2.5) are depicted in Fig. 2.2. No systematic degradation with longer storage durations is observable. The deviation of the samples after three months of storage shows slightly increased J_c values whose origin is not clear due to the low statistics. Yet, there seems to be no systematical effect as the sample after nine month of storage shows the lowest J_c value. As repetitions of this

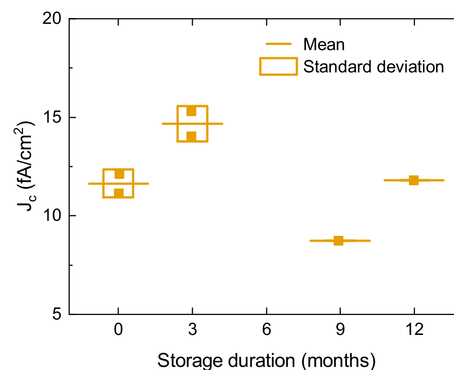

FIGURE 2.2. Photoconductance decay (PCD) determined contact recombination current density J_c of MSD deposited (n) poly-Si layers as function of the interfacial oxide storage duration in a clean room environment before the a-Si deposition.

[3]From this point on the superscripted plus sign indicating high dopant concentrations (n^+/p^+) is left out throughout this thesis since no demarcation has to be made with regards to lower concentrations as typical for silicon homojunctions.

investigation were practically not feasible due to the long storage durations, stability of the passivation quality in terms of no systematic reduction with storage duration of the interfacial oxide was assumed to hold for all substrate and process step combinations throughout this thesis.

2.3. a-Si Deposition

The SHJ concept relies on highly reproducible a-Si:H chemical vapor depositions (CVD) using the precursor gas silane (SiH_4), ensuring a significant amount of hydrogen necessary for chemical passivation. As the SHJ concept evolved earlier than the poly-Si/SiO_x concept, many scientific groups are already equipped with CVD devices. This is one reason why the majority of a-Si:H depositions for poly-Si/SiO_x contacts is done by CVD processes. From a technological viewpoint, hydrogen-free physical vapor deposition (PVD) techniques are equally suited as nearly the whole hydrogen content is effused from the CVD deposited a-Si:H layers during junction formation (Sec. 2.4) anyway.

In this thesis, amorphous silicon was deposited by the one-sided deposition techniques PECVD for hydrogenated a-Si:H, as described in Sec. 2.3.1, and MSD for hydrogen-free a-Si, as described in Sec. 2.3.2. It should be noted that the corresponding deposition tools were not located in a clean room environment so that impurity adsorption on the interfacial oxide during sample transport in ambient atmosphere could be an issue. Doping of the layers was achieved in-situ for p-type and ex-situ for n-type by $POCl_3$-diffusion (Sec. 2.4.1). For the symmetrical test samples on the silicon substrates the layer was deposited on both sides subsequently while on the FS substrates it was only deposited on the front side. Relevant properties of the as-deposited layers are pointed out in Sec. 2.3.3.

2.3.1. Plasma-Enhanced Chemical Vapor Deposition (PECVD)

In general, CVD processes rely on the dissociation of molecules in a gas chamber which then grow a layer by bonding via chemical reactions with surface atoms. Dissociation of the molecules during PECVD is achieved by an external voltage igniting a plasma. In parallel-plate devices the substrate lies on a heat supplied table which is also one electrode on ground potential. With a distance of a few millimeters the second electrode is supplied with a RF voltage as sketched in Fig. 2.3. This

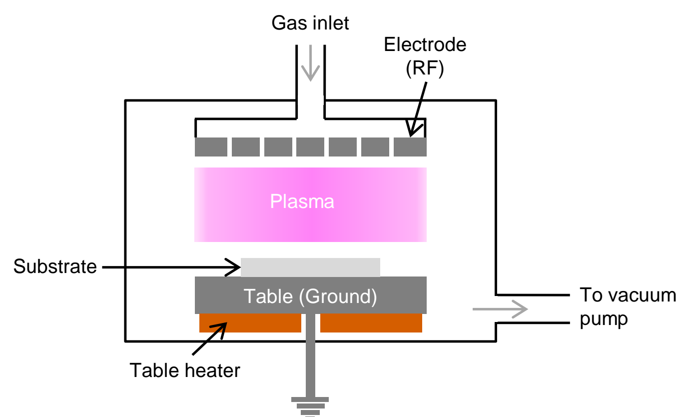

FIGURE 2.3. Simplified sketch of the PECVD setup used for a-Si:H deposition.

arrangement is located in a vacuum chamber with the precursor gases directed through small holes in the upper electrode to the region between the electrodes. Therefore, the ignited plasma is in direct contact with the substrate surface.

In order to deposit a-Si:H, SiH_4 is sufficient as precursor gas. According to [56], $\sim 85\%$ of the dissociated molecules in the plasma are SiH_3 from the following reactions

$$SiH_4 \rightarrow SiH_3 + H \tag{2.2}$$

$$SiH_4 + H \rightarrow SiH_3 + H_2 \tag{2.3}$$

whereas the released hydrogen atoms of reaction 2.2 further increase the SiH_3 radical content by reaction 2.3. Due to this high concentration, more than 90% of the radicals deposited on the samples surface are SiH_3. The main mechanisms occurring on the surface during the growth process as depicted in Fig. 2.4 are [57]:

I) Removal of surface H by incoming radicals:
$(\equiv Si - H) + H \rightarrow (\equiv Si-) + H$
$(\equiv Si - H) + SiH_3 \rightarrow (\equiv Si-) + SiH_4$

II) Bonding of SiH_3 to a surface Si dangling bond from (I):
$(\equiv Si-) + SiH_3 \rightarrow (\equiv Si - SiH_3)$

III) Building of a Si-Si bond from two Si-H bonds under release of molecular H_2:
$(\equiv Si - H) + (\equiv Si - H) \rightarrow (\equiv Si - Si \equiv) + H_2$

The microstructure and composition of the resulting layer can be controlled by adding different gases to the SiH_4 plasma whose approximate concentration in the plasma is described by the gas flow ratio of the additional gas flow Q_X with regard to the silane flow Q_{SiH4}

$$R_X = \frac{Q_X}{(Q_X + Q_{SiH4})}. \tag{2.4}$$

Addition of argon leads to PVD-like columnar growth due to shadowing and due to a low surface mobility of adsorbed radicals [57]. Excess addition of H_2 ($R_{H2} > 0.9$) causes a mixed-phase of small crystallites in the nanometer range embedded in an amorphous matrix, typically referred to as nano- or microcrystalline silicon (nc-/μc-Si). The mechanism behind this phase transition is that hydrogen atoms are able to diffuse below the plasma exposed surface into the already existing layer where they

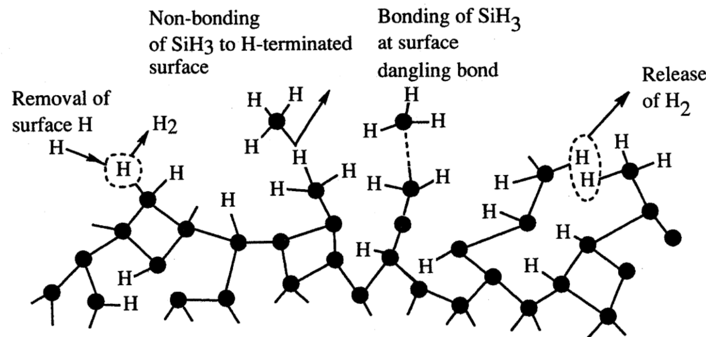

FIGURE 2.4. Main mechanisms occurring on the surface of the layer during PECVD growth. Figure taken from [57].

may reconstruct the amorphous network. Weak Si-Si bonds with a bond strength below the chemical potential of hydrogen in the plasma may be replaced by strong Si-Si bonds above this potential [57]. The rather sharp transition from the amorphous to the nanocrystalline regime with increasing R_{H2} is then explained by the chemical potential becoming larger than the weak Si-Si bond strength. Such a nanocrystalline structure might be beneficial for the poly-Si formation in the subsequent SPC step (Sec. 2.4.1).

It should be noted that an increase of R_{H2} does not significantly increase the hydrogen concentration in the resulting layer. Rather the substrate temperature during deposition is the dominating parameter as hydrogen effusion competes with hydrogen incorporation during layer growth, causing a lower hydrogen concentration for higher temperatures. Throughout this thesis, the term deposition temperature is used and refers to the substrate table heater set temperature T_{set} as the actual substrate temperature is hardly accessible and was not measured.

In this thesis, a parallel-plate plasma device[4] was used with separate deposition chambers for intrinsic and doped layers, respectively. All of the used deposition parameters are given in footnotes. A full parameter set consists of the plasma power P, the chamber pressure p, the deposition temperature T_{set}, the gas flow ratios R_X and the duration t. The thickness inhomogeneity on one sample due to an inhomogeneous electric field at different positions in the deposition chamber was determined to $\sim 7\%$ and is used as relative uncertainty for the layer thickness throughout this thesis, if not stated otherwise.

In addition to SiH_4 and H_2 gases, in-situ doping was achieved by diborane (B_2H_6) diluted to 3% in H_2. Incorporation of light elements was realized through carbon dioxide (CO_2) for hydrogenated amorphous silicon oxide (a-SiO_x:H), nitrous oxide (N_2O) for hydrogenated amorphous silicon oxynitride (a-SiO_xN_y:H) and methane (CH_4) for hydrogenated amorphous silicon carbide (SiC_x:H) layers. For all these additional elements in the amorphous silicon matrix a linear relation was found between the gas flow ratio R_X and the concentration determined by glow discharge optical emission spectroscopy (GD-OES, Sec. 3.1) as will be shown later in Sec. 5.2.1 and 5.3.1. Hence, a variation of R_X can be translated linearly into a corresponding elements concentration throughout this thesis.

Plasma Pre-Cleaning

As mentioned above, after growing the interfacial oxide and before the deposition of the a-Si:H layer the samples were temporarily exposed to ambient atmosphere. It is reasonable to assume that impurities such as H_2O molecules adsorb on the surface of the interfacial oxide. Therefore, a low power plasma pre-cleaning process within the PECVD chamber was developed, using either a pure H_2 or pure N_2O plasma at 20 or 50 W for 10 s immediately before a-Si:H deposition[5] without breaking the vacuum. Under these plasma conditions no etching of the interfacial oxide was observed. Fig. 2.5 shows the passivation quality in terms of implied open circuit voltage iV_{oc} (Sec. 3.6.2) after hydrogenation (Sec. 2.5) as function of the pre-cleaning plasma power P. For the H_2 plasma at 20 W, a significant increase is visible while for the N_2O plasma power the passivation quality degrades. This degradation could be explained by additional nitrogen incorporation in the interfacial oxide which was found to effectively block the detrimental boron in-diffusion but at the same time degrade the

[4]Technical details can be found in the Appendix A.1.

[5]PECVD deposition parameters: $P = 20$ W, $p = 400$ mTorr, $T_{set} = 400°$C, $R_{B2H6} = 1.2\%$, $R_{H2} = 99\%$, $t = 1200$ s.

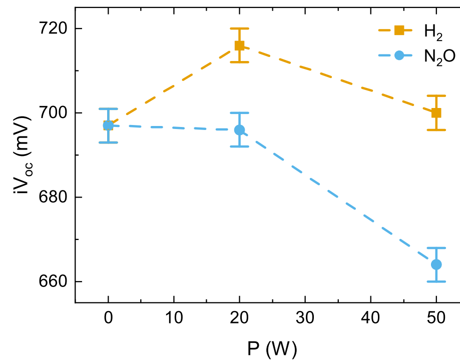

FIGURE 2.5. PCD determined implied open circuit voltage iV_{oc} of PECVD deposited (p) poly-Si layers as function of the pre-cleaning plasma power P before PECVD deposition for both H_2 and N_2O plasmas.

chemical passivation quality [20]. Based on these results, the H_2 plasma pre-cleaning at 20 W was applied immediately before all depositions, if not stated otherwise.

2.3.2. Magnetron Sputtering Deposition (MSD)

In contrast to PECVD, deposition by sputtering is classified as PVD and occurs when a target material is bombarded with particles and the energy as well as the momentum transfer to a target atom is large enough to overcome its binding energy. For the sake of layer deposition, a plasma is ignited in a vacuum chamber with the target material being the cathode, accelerating plasma ions towards the target. The sputtered atoms are then deposited on a substrate leading to the desired layer growth. In an advanced setup, magnets are placed behind the target, giving MSD its name. These magnets are placed in a way that the electrons are trapped on a circular path in a plane parallel to the targets surface instead of being directed towards the anode, leading to a locally increased plasma density [58]. The electrons may then escape only by collisions with an argon atom or ion. These collisions in turn significantly increase the total number of argon ions which are eventually accelerated towards the target. This in turn enables much lower plasma pressures and consequently higher deposition rates compared to the case without magnets. The influence of the magnetic field on the plasma ions is negligible due to the higher mass so that they are accelerated towards the target basically following the electric field. A corresponding setup is shown in Fig. 2.6.

In this thesis, a confocal magnetron sputter tool[6] with multiple sputter sources and a rotating sample stage was used. All of the used deposition parameters are given in footnotes. A full parameter set consists of the power applied to a target $P_{Si/B}$, the chamber pressure p, the argon flow rate Q_{Ar}, the deposition temperature T_{set}, the target-sample distance d_{target} and the duration t. It should be noted that, similar to the PECVD deposition, T_{set} refers to the substrate table heater temperature as the actual substrate temperature is hardly accessible and was not measured. For the intrinsic hydrogen-free a-Si layers, a pure silicon target was used with a purity of 99.9999% (6N). Depositions early in the experiment phase were performed with a target purity of 99.999% (5N) but no systematical difference between both targets was identified. In-situ doping was achieved by co-sputtering of

[6]Technical details can be found in the Appendix A.1.

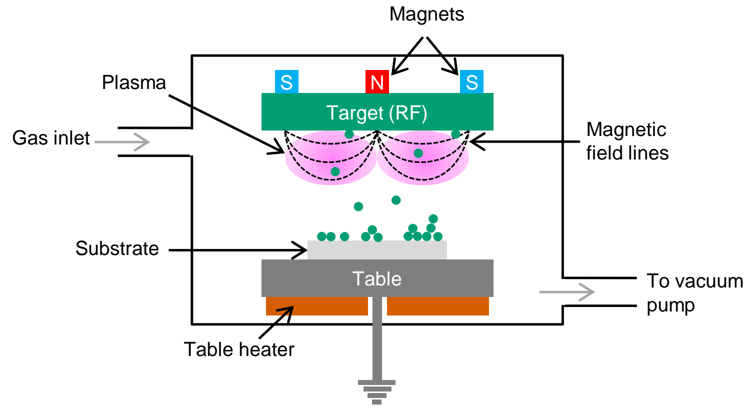

FIGURE 2.6. Simplified sketch of the MSD setup used for hydrogen-free a-Si deposition.

an additional pure boron target with a purity of 99.9% (3N) and iron being the prevalent impurity with roughly 100 ppm. Iron as an impurity in a silicon monocrystal induces energy states within the energy band gap of silicon and hence this impurity concentration has to be considered in the discussion of MSD deposited in-situ doped (p) a-Si layers. For a constant power applied to the Si 6N target during co-sputtering, a roughly linear relation between the power applied to the boron sputter target P_B and the GD-OES and SE determined boron concentration expressed as ξ_B (Sec. 3.1.4) can be observed in Fig. 2.7. This proves a linear incorporation of boron in the amorphous network. The thickness inhomogeneity on one sample due to a radially inhomogeneous pressure distribution was determined to $\sim 9\%$ and is used as relative uncertainty for the layer thickness throughout this thesis, if not stated otherwise.

Sputter Damage Reduction

During TCO sputter deposition for SHJ contact fabrication a sputter damage occurs which degrades the passivation quality at the c-Si/a-Si:H interface due to plasma irradiation and particle bombardment. This particle bombardment consists mostly of electrons, ions and argon atoms which were

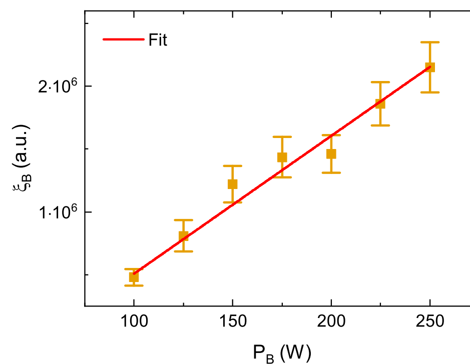

FIGURE 2.7. GD-OES and SE determined boron concentration expressed as ξ_B (Sec. 3.1.4) of MSD deposited (p) a-Si layers as function of the power applied to the boron sputter target P_B. The solid red line is a weighted linear fit.

neutralized and reflected at the target [59]. Besides a subsequent thermal treatment in order to partially reverse this damage, a careful adjustment of the plasma parameters may reduce the initially induced damage [59, 60]. Due to the similarities between the SHJ and the poly-Si/SiO_x concepts, a similar sputter damage to the interfacial oxide might be expected. Indeed, such a sputter damage was observed in the context of this thesis and already published in [61] and is described later in Sec. 5.2.5.

Starting from a benchmark parameter set, the following parameter adjustments were tested:

I) The deposition temperature was increased from room temperature to $T_{set} = 450°C$ providing additional thermal energy for reorganization processes during layer growth which might partially reverse the sputter damage in-situ.

II) The power applied to the silicon target was reduced from $P_{Si} = 300$ W to $P_{Si} = 100$ W in order to reduce the intensity of plasma irradiation.

III) The target-sample distance was increased from $d_{target} = 12$ cm to $d_{target} = 17$ cm to reduce the energies of the particles during bombardment by thermalization.

IV) The pressure was increased from $p = 2$ mTorr to $p = 10$ mTorr to reduce the energies of the particles during bombardment by thermalization similar to III).

Fig. 2.8 presents the passivation quality in terms of implied open circuit voltage iV_{oc} (Sec. 3.6.2) for these MSD deposition parameter adjustments for ex-situ doped (n) poly-Si layers on FZ substrate after junction formation (Sec. 2.4) but before hydrogenation (Sec. 2.5). It is clearly evident that the parameter adjustments significantly increased the passivation quality compared to the benchmark process and even reached the initial interfacial oxide passivation quality of a blank reference sample. Admittedly, this comparison should be treated carefully since for the sputtered samples after junction formation a $POCl_3$-diffusion induced field-effect and in-diffusion of dopants significantly influences iV_{oc}. As mentioned before, there is a risk for a detrimental strong dopant in-diffusion through the interfacial oxide during junction formation which might even be enhanced by a sputter damaged interfacial oxide. This could be a reason for the significantly lower iV_{oc} values yielded with the benchmark parameter set.

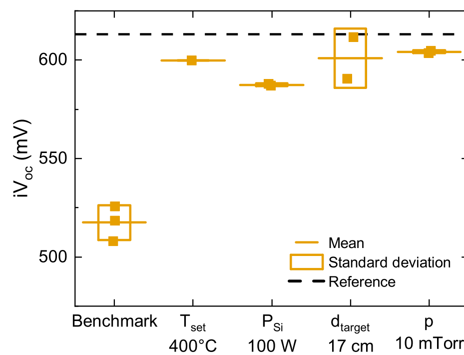

FIGURE 2.8. PCD determined implied open circuit voltage iV_{oc} of MSD deposited (n) poly-Si layers deposited with the parameter adjustments I)–IV). The horizontal dashed line corresponds to the passivation quality of a blank reference sample with only the interfacial oxide.

The parameter sets with reduced power II) and increased pressure IV) lead to strongly reduced deposition rates by a factor of up to eight and therefore to impractical long process durations and were thus abandoned. As the higher deposition temperature I) and the larger target-sample distance III) showed no significant influence on the deposition rate, these adjustments were combined and applied as standard parameter set[7] with an as-deposited layer thickness of ~ 75 nm for all MSD deposition throughout this thesis. This holds in particular if no explicit deposition parameters are given in footnotes similar to the PECVD depositions.

2.3.3. a-Si Material Properties

This section depicts the a-Si material properties relevant for this thesis following [57]. An amorphous semiconductor is described as a continuous random network and distinguished from a crystalline semiconductor due to the absence of a long-range order whereas a similar short-range order exists. The short range order is characterized by the specific number of bonds of each atom to its immediate neighbors, referred to as coordination number Z, which is determined by the 8-N rule

$$Z = \begin{cases} 8-N & \text{if } N \geq 4 \\ N & \text{if } N < 4 \end{cases} \tag{2.5}$$

with the number of valence electrons N. A defect is then defined by an atom with less or more bonds than its coordination number, mostly appearing as dangling bonds. Hydrogen is able to saturate such dangling bonds which is why hydrogen-free amorphous silicon (a-Si) has typically more defects than hydrogenated amorphous silicon (a-Si:H). Furthermore, hydrogen plays a crucial role for the microstructure of the amorphous network not only during the growth process as described above in Sec. 2.3.1, but also during post-deposition effusion which triggers reorganization of the silicon network and decreases its disorder.

Without the periodicity of a crystalline material the amorphous network can easily incorporate atoms with different coordination numbers. It should be underlined that the coordination number for both boron and phosphorus is $Z = 3$ in an amorphous matrix while in a single-crystal the valence number N as the relevant quantity for substitutional doping is different.

From these basic concepts of amorphous semiconductors the band diagram for a-Si follows as shown in Fig. 2.9. Compared to the crystalline band diagram, the sharp energy gap is replaced by the slightly lower mobility gap, defined by the conduction and valence mobility edges E_C and E_V, respectively. These edges separate the extended states on the band side of the mobility edge from the localized states on the gap side of the mobility edge, which also include band tail states. The states near the Fermi energy at the center of the mobility gap arise from defects, in particular from dangling bonds. Neglecting hopping conduction within these defect states at the Fermi energy E_F via tunneling, conduction occurs either within the extended states, following the relation for the conductivity

$$\sigma_{ext} = \sigma_{oe} \cdot e^{\left(-\frac{E_C - E_F}{kT}\right)}, \tag{2.6}$$

[7]MSD deposition standard parameter set: $P_{Si} = 300$ W, $p = 2$ mTorr, $Q_{Ar} = 80$ sccm, $T_{set} = 450$°C, $d_{target} = 17$ cm, $t = 2500$ s.

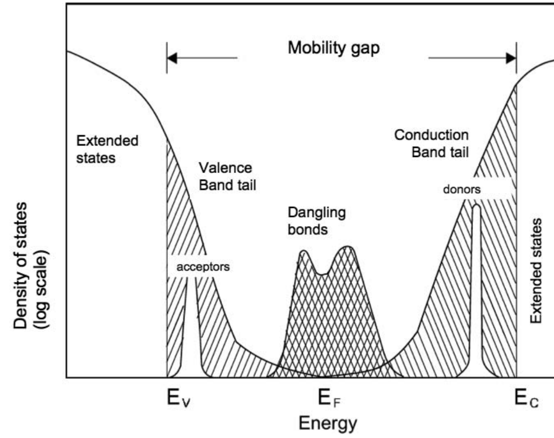

FIGURE 2.9. Density of states as function of the band energy for a-Si. Mobility gap defined by E_V and E_C separate extended states from band tail states. States evolving from dangling bonds located within mobility edge around the Fermi energy E_F. Doping induces states within the corresponding band tails. Figure taken from [62].

or within the band tail states, following a similar relation

$$\sigma_{tail} = \sigma_{ot} \cdot e^{\left(-\frac{E_{CT}-E_F}{kT}\right)} \tag{2.7}$$

with the average conductivities above and below the mobility edge $\sigma_{oe/ot}$, respectively, and the average energy of the band tail conduction path E_{CT}. The dominating conduction mechanism depends on the specific situation, in particular on the temperature T, as $\sigma_{oe} > \sigma_{ot}$ but $(E_C - E_F) > (E_{CT} - E_F)$.

Strictly following the picture of a continuous random network, substitutional doping as known from a crystalline semiconductor seems to be impossible. In fact, doping predominantly induces deep defects within the band gap in form of dangling bonds which increases the disorder of the amorphous network. Even extra charges from ionized dopants with a coordination number of $Z = 4$ are compensated by these deep defects. However, due to a small difference between dopant density N_D and compensating dangling bond density N_{DB}, a small excess band tail density of states $N_{BT} = N_D - N_{DB}$ evolves, as indicated in Fig. 2.9. This eventually increases the conductivity as the prefactor for the band tail conduction in eq. 2.7 is a function of this excess band tail density of states $\sigma_{ot} = \sigma_{ot}(N_{BT})$.

While the electrical properties can be controlled by doping, the optical properties may be controlled by incorporation of light elements, in particular oxygen, nitrogen or carbon. Depending on the specific deposition conditions, a-Si:H has a band gap in the rough range of $1.4 - 1.8$ eV while the band gaps of stoichiometric a-SiO_2 (8.9 eV) [63] and a-Si_3N_4 (5.2 eV) [64] are significantly larger. Therefore, a continuous increase of the band gap is expected with increasing concentrations of oxygen and nitrogen [44, 65]. A similar band gap widening with increasing concentration was also observed for carbon incorporation [66, 67]. Therefore, by controlling the concentration of these light elements in the a-Si:H layer it is possible to tune the optical band gap of the material.

As the stoichiometric counterparts are insulators, one could expect higher resistivities with increasing concentrations of light elements, which is indeed true for large concentrations. Interestingly, for lower concentrations, oxygen and nitrogen form donor-like states decreasing the resistivity [68]. However, for carbon incorporation a continuous increase in resistivity was observed [67].

2.4. Junction Formation

The term *junction formation* summarizes the crystallization of the initially amorphous layer and the necessary dopant diffusion from the poly-Si through the interfacial oxide into the c-Si (Sec. 1.3). In principle, these two mechanisms could be separated but in order to reduce the total number of process steps they are usually combined in one high temperature step. Hence, the corresponding parameters should be near the optimum for both the crystallization and dopant in-diffusion, a condition which is sometimes difficult to match. Parameters optimized for a high field-effect passivation by a shallow in-diffusion decrease J_c but if the crystallinity of the poly-Si layer is not large enough, ρ_c might be too large for a high selectivity. Likewise, parameters optimized for a fully crystallized poly-Si layer (large ρ_c) might lead to a detrimental strong in-diffusion degrading the passivation quality (large J_c).

In this thesis, the junction formation was performed by SPC in a quartz tube furnace either in inert N_2 atmosphere for initially in-situ doped (p) a-Si layers or by an ex-situ doping $POCl_3$-diffusion for initially intrinsic (i) a-Si leading to (n) poly-Si.

2.4.1. Solid Phase Crystallization (SPC)

For the temperature range typically used in silicon-based photovoltaics, two mechanisms of SPC have to be considered, namely the solid phase epitaxy and the random nucleation growth. The former relies on a crystalline substrate, which is not necessarily given in the presence of an interfacial oxide. Indeed, the authors in [69] found epitaxial growth only in areas close to local disruptions of ~ 1.5 nm thick interfacial oxides which only covered $\sim 5\%$ of the total interface area. From this observation it seems reasonable to neglect the solid phase epitaxy for the much thicker 2.5 nm interfacial oxide used throughout this thesis.

The random nucleation growth is typically described by the Johnson–Mehl–Avrami–Kolmogorov (JMAK) model for isothermal phase transformations with the following kinetics [70]. First, nucleation centers form at random positions which are described by a typically uniform probability distribution and a nucleation rate. These nucleation centers then grow as grains with a specific growth velocity uniformly in all directions until they reach another grain or the boundaries of the layer. This leads to a material with randomly oriented grains separated by amorphous-like grain boundaries and implies that high nucleation rates lead to low final grain sizes since the grains limit their growth by reaching each other earlier in the process and vice versa. As the nucleation rate increases with temperature, the final grain size should decrease with temperature. In contrast, increasing grain sizes with temperature were found in [71], directly reflecting the difficulty of a unified model describing all variations of poly-Si structures.

For theoretical final grain sizes larger than the layer thickness, these grains reach after full crystallization from the interface through the whole layer up to the surface wherefore a two dimensional formulation of the model has to be applied. The authors in [72] found that for PECVD deposited a-Si layers the two dimensional regime holds for layer thicknesses $\lesssim 170$ nm. As all layers studied in this thesis were thinner than 100 nm except for the SiC_x layers, it is reasonable to assume the two dimensional regime with grain dimensions in the range of the layer thickness after full crystallization. This assumption is further supported by the observed grain sizes in [71] for similar SPC temperatures and durations, as applied in this thesis.

Additional elements incorporated in the initial amorphous matrix influence on the one hand the nucleation rate and as such the grain size, and on the other hand the time necessary for maximum crystallization of the material at a given temperature. According to [73], boron and phosphorus doping both decrease the nucleation rate and hence increase the final grain size while the grain size enlargement was observed to be stronger for phosphorus doping [21, 71]. In contrast, incorporation of oxygen increases the nucleation rate and hence decreases the final grain size. Regarding the crystal growth velocity, oxygen and phosphorus incorporation decrease, whilst boron incorporation significantly increases this velocity and thus reduces the time necessary for a full crystallization of the material [73, 74]. Due to lack of specific literature, it is assumed that nitrogen and carbon incorporation have a similar effect on the SPC as oxygen incorporation has.

Ex-situ doping during SPC was achieved by a $POCl_3$-diffusion with a similar temperature profile as the SPC in inert atmosphere. Simultaneously to the SPC, P_2O_5 forms from a reaction of $POCl_3$ and O_2, which in turn reacts with the silicon surface atoms and results in the growth of a phosphorus silicate glass (PSG). Additionally, diffusion of phosphorus atoms from this PSG layer into the a-Si layer occurs [75]. The combination and simultaneity of these three processes leads to complicated interdependencies. In particular, phosphorus diffusion through a material during transition from the amorphous to the crystalline phase takes place while the inhomogeneous phosphorus profile in direction parallel to the surface normal in turn influences this phase transition as a function of the distance to the surface. However, homogeneous phosphorus depth profiles and well-behaving crystallinity measurements were observed after SPC, which suggest that the processes influenced by these interdependencies are mostly terminated for the investigated layers. The ex-situ doping by $POCl_3$-diffusion further features the well-known impurity gettering effect during conventional phosphorus emitter formation, which was also found in the context of poly-Si/SiO_x contact formation [76].

In this thesis, the SPC was performed in the same quartz tube furnace that was used for the growth of the interfacial oxide (Sec. 2.2) for the previously in-situ doped (p) a-Si:H layers from PECVD deposition. The samples were loaded at 800°C and heated to 920°C with a rate of 4 K/min in pure N_2 atmosphere. After 30 min, the samples were cooled down to the loading temperature with a cooling rate of 4 K/min. This process was applied to all PECVD deposited in-situ doped (p) a-Si:H layers, if not stated otherwise.

For ex-situ doping of MSD deposited (i) a-Si layers by $POCl_3$-diffusion, a second tube was used to prevent cross-contamination. In Fig. 2.10 a), the profile of the set values for the standard process is sketched. Except for the larger heat and cooling rate of 6 K/min, the temperature profile is the same as for the PECVD deposited in-situ doped (p) a-Si:H layers. The duration of the PSG growth phase and the following drive-in phase under high O_2 gas flow were both 15 min at 920°C. It was observed that the phosphorus concentration in the final (n) poly-Si layer is a function of the initial (i) a-Si layer thickness d_{a-Si} for constant $POCl_3$-diffusion parameters, as is evident from the GD-OES measured phosphorus profiles of MSD deposited[8] (n) poly-Si layers in Fig. 2.10 b). Therefore, the $POCl_3$-diffusion parameters as well as the MSD deposited (i) a-Si layer thickness were kept constant throughout this thesis to ensure comparability. After each $POCl_3$-diffusion the resulting PSG was removed with a 10% HF etch process. As the preceding PSG growth consumed the silicon

[8]MSD deposition parameters: $P_{Si} = 300$ W, $p = 2$ mTorr, $Q_{Ar} = 80$ sccm, $T_{set} = 20$°C, $d_{target} = 12$ cm, $t = 2400$ s.

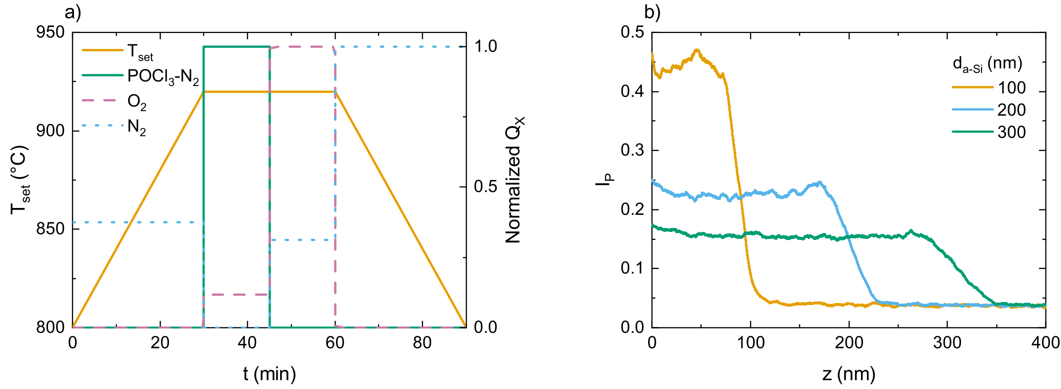

FIGURE 2.10. a) Profile of the standard $POCl_3$-diffusion process that was applied throughout this thesis with the set temperature T_{set} (left axis) and the gas flows Q_X normalized to each maximum flow for either $POCl_3$-N_2, O_2 or N_2 gas (right axis). b) GD-OES determined raw data phosphorus depth profiles along the direction parallel to the surface normal $I_P(z)$ with $z = 0$ nm being the surface of the MSD deposited (n) poly-Si layers after $POCl_3$-diffusion for different initial (i) a-Si layer thicknesses d_{a-Si}.

from the poly-Si layer, the resulting layer thickness after the HF etch was reduced compared to the as-deposited a-Si layer thickness by roughly 10 nm [61].

However, due to concerns regarding a contamination of the quartz tube from the iron content in the MSD in-situ doped (p) a-Si layers, they were processed in the same tube as used for ex-situ doping since inserted impurities are likely to be removed by a frequently applied pyrogenic cleaning process. This process was also applied before SPC of these boron doped layers in order to remove residual phosphorus atoms from the tube walls.

Wet Chemical Pre-Cleaning

At the high temperatures during junction formation adsorbed impurities are likely to diffuse through the a-Si layer and induce defects at the interfaces. Therefore, a cleaning step immediately before SPC seems reasonable. Several wet chemical pre-cleaning solutions were tested without leaving the clean room environment. In Fig. 2.11 the resulting passivation quality in terms of implied open circuit voltage iV_{oc} (Sec. 3.6.2) is presented for PECVD deposited[9] (p) polycrystalline silicon oxynitride (poly-SiO_xN_y) layers on Cz substrates after hydrogenation but with different wet-chemical pre-cleaning solutions immediately before SPC. Each tested solution was followed by a short etch process in 2.5% HF, except for the mixture of HCl/HF. The mean values of iV_{oc} gain > 10 mV compared to the references without pre-cleaning for all H_2O_2 based solutions while the solution of H_2O_2 and HCl led to the highest passivation quality. These higher iV_{oc} values for the H_2O_2 based solutions are a hint that the surface is predominantly contaminated with organic impurities since these are commonly removed by H_2O_2 while HCl alone mostly removes metallic contaminations.

It should be noted that, due to the outlier at $iV_{oc} = 651$ mV, the mean value of the reference samples is shifted towards lower values. However, removing this outlier from the analysis would still result

[9]PECVD deposition parameters: $P = 50$ W, $p = 600$ mTorr, $T_{set} = 300$°C, $R_{B2H6} = 0.6\%$, $R_{N2O} = 20\%$, $R_{H2} = 0\%$, $t = 75$ s.

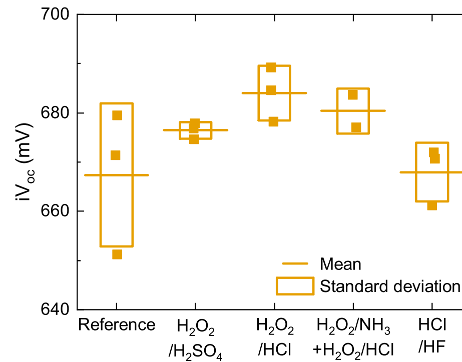

FIGURE 2.11. PCD determined implied open circuit voltage iV_{oc} of PECVD deposited (p) poly-SiO_xN_y layers for several wet-chemical pre-cleaning solutions immediately before SPC.

in a significant gain for the H_2O_2/HCl cleaning solution. Following these results, a H_2O_2/HCl pre-cleaning immediately before SPC without leaving the clean room environment was applied throughout this thesis, if not stated otherwise.

2.4.2. Blistering

Thermally induced blistering in silicon-based materials is a known phenomenon which has already been observed for hydrogenated aluminum oxide (AlO_x:H) [77], AlO_x:H/SiN_x:H stacks [78], a-Si:H [79] and c-Si [80, 81]. In the context of poly-Si/SiO_x contacts, blistering has mostly been observed during SPC of PECVD in-situ doped (p) a-Si:H layers [34, 42, 43, 82] and to a lesser extent during SPC of (n) a-Si:H layers [43, 83]. In both cases the passivation quality was reported to degrade and to promote detrimental strong dopant in-diffusion [84]. All studies linked blistering to the presence of hydrogen and observed a higher blister intensity with increasing layer thickness which corresponds to a larger number of total hydrogen atoms within the layer. Also in the context of this thesis blistering was observed only on PECVD deposited a-Si:H layers but not on the hydrogen-free MSD deposited a-Si layers.

A detailed microscopic mechanism is not yet identified but several suggestions have been given. As hydrogen is a necessary condition for blistering, it is sometimes assumed that hydrogen accumulates in microvoids [81] or in bubbles at the interface of two materials with different segregation coefficients for hydrogen [42]. The resulting internal pressure enlarges these cavities leading to dome-shaped elevations which might even explode in the extreme case along with local layer delamination. A different explanation assumes local uplifts of the whole layer from the underlying interfacial oxide due to interface strain whereas hydrogen accumulates in the resulting volume below increasing the internal pressure as first discussed in [85]. Eventually also dome-shaped surface elevations evolve as also observed in [82] and during hydrogen effusion measurements in [79] where the blistering was correlated to sharp peaks in the effusion spectra. The authors in [85] reported that blistering did occur on c-Si but not on molybdenum substrates. A similar substrate dependence was also observed in [83] where blistering occurred only if the layer was deposited on an interfacial oxide but not if directly deposited on the c-Si substrate. Also in this thesis blistering mostly occurred on silicon substrates with interfacial oxides and was hardly observed on the FS substrates.

Blister Structures

In Fig. 2.12 optical microscopy (OM) as well as scanning electron microscopy (SEM)[10] images of blistered surfaces of two representative PECVD deposited[11] (p) poly-Si layers on FZ substrate after SPC are shown. The above mentioned dome-shaped surface elevations are clearly discernible and marked by the solid arrow in Fig. 2.12 a). In the OM image these structures are identified by the existence of Newton rings as a consequence of optical interference at a slightly curved structure on a reflective flat substrate, which is naturally not observable in the SEM image. These elevations might also collapse, marked by the dashed arrow in Fig. 2.12 a) and appear as dark spots in the OM image without Newton rings. Apart from that, small bubbles (circles) or swales (squares) appear as either bright or dark spot in the OM image.

If blistering is stronger, barbell-shaped swales appear, as indicated by the dashed arrow in Fig. 2.12 b). From the SEM image they are clearly identifiable as areas where the whole layer or at least a part of it is delaminated. The corresponding delaminated layer piece may even be found close to these areas, as marked by the solid arrow. In the OM image these delaminated layer pieces appear as black spots while the bright spots with Newton rings correspond to intact dome-shaped elevations similar to the one in Fig. 2.12 a). Interestingly, all intact dome-shaped elevations are isolated while all delaminated areas have a barbell shape, leading to the conclusion that layer delamination predominantly occurs when two of these initially isolated dome-shaped structures reach each other during growth.

The size of most of these structures is in the range of micrometers which is only compatible with the explanation via uplifts of the whole poly-Si layer. Therefore, this mechanism is assumed to be the predominant one for the layers discussed within this thesis. Once these structures were identified, only the more easily accessible OM images were recorded and are presented throughout this thesis.

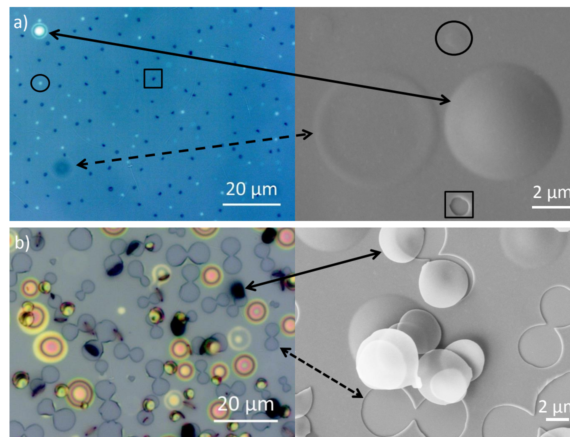

FIGURE 2.12. OM (left) and SEM (right) images of blistered surfaces after SPC of PECVD deposited (p) poly-Si layers. The images in one row a) or b) were taken on the same sample without tracking the position. Similar structures are marked by arrows, circles and squares.

[10]SEM images recorded by Johannes Rinder.

[11]PECVD deposition parameter: $P = 20$ W, $p = 400$ mTorr, $R_{H2} = 99\%$, $R_{B2H6} = 1.2\%$, $T_{set} = 150/200°C$, $t = 1800$ s.

2.4.3. poly-Si Material Properties

First of all, the term polycrystalline silicon (poly-Si) is not well-defined and has to be classified as opposed to nanocrystalline silicon (nc-Si), microcrystalline silicon (μc-Si) and multicrystalline silicon (mc-Si). The latter commonly refers to the low-cost raw absorber material with grain dimensions up to the centimeter scale. nc-Si and μc-Si are typically used in the context of small crystallites embedded in an amorphous matrix during thin layer deposition while the different naming suggests to be connected to the dimensions of these crystallites. Following this classification, poly-Si would be a material where the grain growth terminated so that the grains are in contact with each other without a surrounding amorphous matrix but separated by amorphous-like grain boundaries. However, such clear distinctions are not made in the literature. In this thesis, a clear definition is given by the distinction between the as-deposited material being either fully amorphous (a-Si) or consisting of small crystallites embedded in an amorphous matrix (nc-Si) and the material after SPC, which is constantly referred to as poly-Si regardless of the actual crystallinity and grain size.

The increasing interest in poly-Si due to its successful implementation in bipolar transistors in the 1970s was accompanied by the development of conduction models for poly-Si. According to [86], two main mechanisms were suggested, namely the carrier-trapping model [87] and the dopant segregation model [88]. Both models agree about the basic structure of poly-Si, namely that individual monocrystal-like grains are separated by amorphous-like defect rich grain boundaries. These grain boundaries form potential barriers and hence are responsible for the increased resistivity compared to a silicon monocrystal (Fig. 2.13 a). A sketch of the conduction band diagram corresponding to this structure is shown in Fig. 2.14 a).

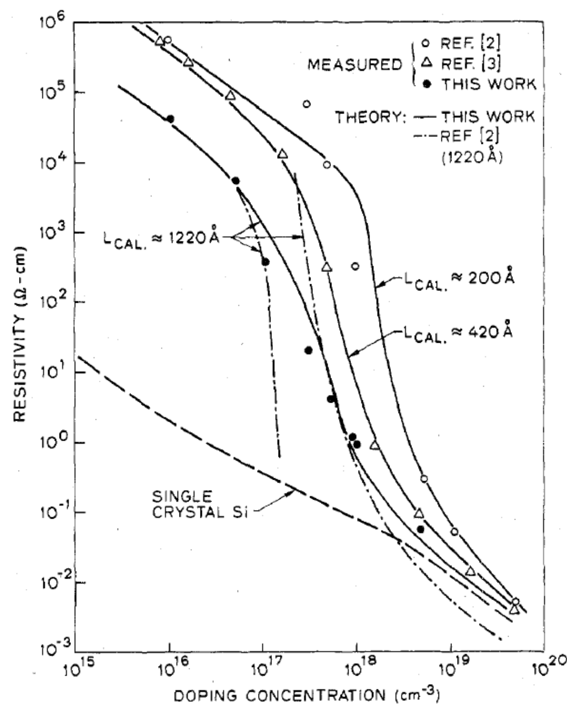

FIGURE 2.13. Resistivity as function of the doping concentration for poly-Si with several grain sizes $L_{CAL.}$ and a c-Si reference (dashed line). Figure taken from [89].

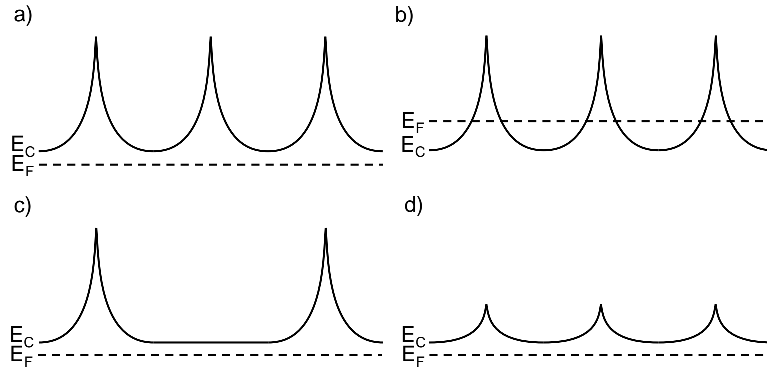

FIGURE 2.14. Changes in the conduction band E_C of (n^+) poly-Si with the peaks corresponding to potential barriers arising from grain boundaries. a) Reference case, b) heavy doping shifts the Fermi energy E_F to larger values, c) larger grains increase the distance between two potential barriers and d) defect saturation decreases the potential barrier height. Figure representation based on [90].

The carrier-trapping model assumes a homogeneous distribution of dopant atoms while a significant fraction of the additional free charge carriers is trapped at the grain boundaries, leading to inefficient doping in the range of $< 10^{18}$ cm^{-3} (Fig. 2.13 a). The rapid resistivity drop for dopant concentrations $> 10^{18}$ cm^{-3} is then attributed to a saturation of the charge carrier trapping and a resulting drop of the potential barrier height with regards to the Fermi energy with further increased doping (Fig. 2.14 b). In contrast, the dopant segregation model assumes an accumulation of the dopant atoms themselves at the grain boundaries where they become electrically inactive, leading to inefficient doping similar to the carrier-trapping model. The rapid resistivity drop for dopant concentrations $> 10^{18}$ cm^{-3} is then explained by a saturation of dopant atoms at the grain boundaries. As it is also the case for the transport mechanism through the interfacial oxide (Sec. 1.3.2), a combination of both models led to improved agreement with experimental data [86].

In the context of poly-Si/SiO_x contacts, the lateral transport through the poly-Si is of importance as mentioned earlier in Sec. 1.3. It is worth noting that the just described conduction models basically apply for all three dimensions. Nevertheless, a higher resistivity in lateral direction compared to the vertical direction could be introduced by grains which are large compared to the layer thickness and thus reach from the interface through the whole layer up to the surface. For such a structure, the charge carrier face less grain boundaries for transport in the vertical direction compared to transport in the lateral direction. Since the resistivity within one grain is assumed to be isotropic, this is rather a result of the related desired travel distances for the charge carriers of nanometer in the vertical and millimeter in the lateral direction.

As mentioned in the previous section, the final grain size of the poly-Si increases with dopant concentration for both phosphorus and boron doping. Larger grains in turn imply a lower density of grain boundaries which reduces the resistivity additionally to the extra charges (Fig. 2.14 c) [89]. If the crystallization process is not yet completed, the grains have not reached the final grain size and are separated and surrounded by an amorphous matrix. The larger the distance is between two grains, the higher is the resistivity. Hence, the resistivity is expected to decrease with higher crystallinities [90]. Such incomplete crystallization processes occur for low temperatures and short annealing durations during SPC.

For fixed SPC parameters, a lower crystallinity was observed for incorporation of the light elements oxygen, nitrogen or carbon [44, 45, 91]. Additionally, oxygen and nitrogen both form donor-like states decreasing the resistivity [92], similar to the amorphous case (Sec. 2.3.3). An alternative explanation for the reduced resistivity due to oxygen and nitrogen incorporation might be a decrease of the potential barrier height by saturating defects at the grain boundaries as sketched in Fig. 2.14 d). These mechanisms compete with the higher resistivity caused by a reduced crystallinity and so for each specific layer composition the resistivity dependencies have to be determined individually. However, carbon incorporation hinders crystallization but does not have a decreasing effect on the resistivity so that the resistivity simply increases for higher carbon concentrations [93].

Incorporation of the light elements in poly-Si is further expected to widen the optical band gap similarly to the amorphous case (Sec. 2.3.3). This in turn should decrease parasitic absorption, but might be overcompensated by a higher absorption coefficient due to a lower crystallinity [45]. Through additional heavy doping of these layers the Fermi energy E_F shifts to the corresponding band edge as exemplarily sketched in Fig. 2.15 a) for a polycrystalline silicon oxide (poly-SiO_x) layer. The Fermi energy alignment eventually leads in combination with the higher band gap to a larger band offset $\Delta E_{poly-SiOx} > \Delta E_{poly-Si}$ and thus a larger selectivity compared to the pure poly-Si. Less or inefficient doping causes a larger distance between the Fermi energy and the band edge, which eventually decreases the gain from the larger band offset even though the absolute value of the poly-SiO_x band gap does not change (Fig. 2.15 b).

2.5. Hydrogenation

Hydrogen originally incorporated in the as-deposited a-Si:H layers by PECVD deposition effuses from the layer during SPC and consequently from the passivating SiO_x/c-Si interface, leaving unsaturated interface defects behind. In contrast to the low temperature process for SHJ contacts where hydrogen from the a-Si:H layer is constantly located at the interface over the whole fabrication process, hydrogen has to be re-introduced for poly-Si/SiO_x contacts. Such interface defect saturation can be achieved by remote hydrogen plasma treatment or by forming gas anneal. A third possibility

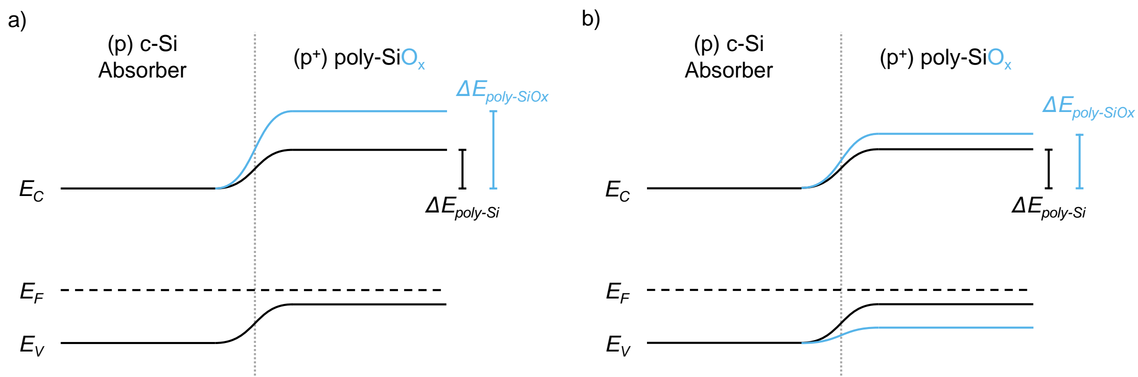

FIGURE 2.15. Band diagram sketch of a (p^+) poly-Si/SiO_x (black) and a (p^+) poly-SiO_x/SiO_x contact (blue) representative for incorporation of light elements with band offsets $\Delta E_{poly-Si}$ and $\Delta E_{poly-SiOx}$, respectively. a) Sufficient doping shifts Fermi energy E_F in the (p^+) poly-SiO_x close to the valence band edge resulting in a large band offset gain with respect to the (p^+) poly-Si layer. b) Insufficient doping decreases this gain. Potential barriers induced by the interfacial oxide not shown for the sake of simplicity.

is the deposition of a hydrogen-rich layer, typically SiN_x:H or AlO_x:H, which is subsequently annealed to activate hydrogen diffusion from this layer to the interface and was reported to be the most efficient process [43, 94]. The reason for this was found to be a larger hydrogen concentration at the SiO_x/c-Si interface compared to a hydrogen plasma treatment or forming gas anneal [95].

In this thesis, a SiN_x:H layer was deposited after junction formation as a hydrogen source and subsequently annealed during FF to activate the diffusion of hydrogen to the interface. This is the natural choice when applying a poly-Si/SiO_x contact on the front side of a solar cell since the SiN_x:H would be necessary as ARC and the FF for metal contact formation anyway. Both steps are described in the following sections.

2.5.1. SiN_x:H Deposition

All SiN_x:H layers were deposited with the PECVD technique using mixtures of SiH_4, N_2O, NH_3 and N_2. The full parameter sets of the in-house deposited layers are depicted in Table 2.1. To prove the observation of [43] that the hydrogenation efficiency does not depend on the choice of the hydrogen-rich layer type, three different layers were compared. On the one hand, a pure SiN_x:H layer (A) or a SiN_x:H/SiO_xN_y:H stack (B) was deposited in the same direct plasma PECVD tool that was used for the a-Si depositions (Sec. 2.3.1) but in a different deposition chamber which was never in contact with doping gases. On the other hand, a different SiN_x:H layer (C) was externally deposited in an industrially established microwave-based in-line PECVD tool[12].

In Fig. 2.16 the passivation quality after hydrogenation with the different hydrogen-rich layers is shown in terms of implied open circuit voltage iV_{oc} for MSD deposited (n) poly-Si layers on Cz substrates. Besides the scattering of the values, no significant differences can be observed in the mean values for all three layer types, at least not within this absolute range around $\sim$ 700 mV. However, if the outlier for the SiN_x:H/SiO_xN_y:H stack (B) is disregarded, the mean value would be a few mV larger. This could be explained by either a higher total hydrogen content of the stack or

TABLE 2.1. PECVD deposition parameter sets for the in-house deposited hydrogen-rich layer types, namely plasma power P, chamber pressure p, deposition temperature T_{set}, gas flows Q_X, duration t and resulting layer thickness d.

	(A)	(B)	
	SiN_x:H	SiN_x:H	SiN_xO_y:H
P (W)	90	100	20
p (mTorr)	800	650	1000
T_{set} (°C)	40	400	400
Q_{SiH4} (sccm)	11	11	6.5
Q_{NH3} (sccm)	13	13	0
Q_{N2} (sccm)	996	996	161.5
Q_{N2O} (sccm)	0	0	712
t (s)	110	103	81
d (nm)	75	68	88

[12]Technical details can be found in the Appendix A.1.

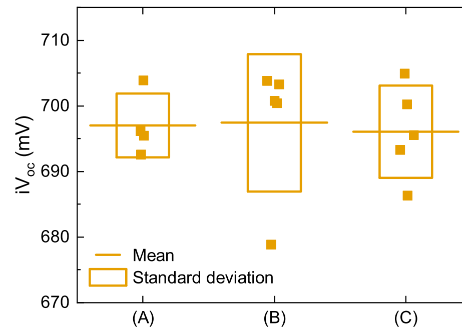

FIGURE 2.16. PCD determined implied open circuit voltage iV_{oc} of MSD deposited (n) poly-Si layers after hydrogenation with the different hydrogen-rich layers (A), (B) and (C) (Table 2.1).

by the SiO_xN_y:H acting as a capping layer which prevents the hydrogen from the SiN_x:H to effuse to the ambient and rather diffuse to the SiO_x/c-Si interface.

As both PECVD tools were not constantly available during the time period when the experiments were performed, a third quartz tube based PECVD tool was used for SiN_x:H deposition as an alternative. Even in the absence of a direct comparison, no obvious differences in passivation quality were observed. Therefore, for each experiment the deposition tool was chosen based on its availability.

2.5.2. Fast Firing (FF)

As the final process step, the hydrogen diffusion from the SiN_x:H layer to the SiO_x/c-Si interface was activated by an infrared heated firing belt furnace[13]. The FZ substrates used in this thesis were thicker than the Cz substrates and this difference in thermal masses was compensated by two different set temperature profiles, as indicated in Fig. 2.17. As the focus of this thesis is the variation of the poly-Si layer composition, these profiles have not been optimized for a maximum interface defect saturation and were kept constant for all experiments. However, the above discussed similar

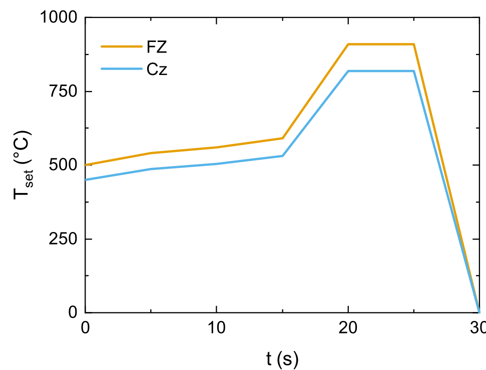

FIGURE 2.17. FF profiles of the set temperature $T_{set}(t)$ as applied throughout this thesis for a) FZ and b) Cz substrates.

[13]Technical details can be found in the Appendix A.1.

passivation quality after hydrogenation under variation of the hydrogen-rich layer is a hint for a terminated interface defect saturation near the optimum and hence for suitable temperature profiles.

CHAPTER 3

Methods

In this chapter, all characterization methods as well as data analysis procedures are described. Glow discharge optical emission spectroscopy (GD-OES) for the determination of elemental depth profiles is introduced in Sec. 3.1. Therein also the development of suitable calibration procedures and of enhanced measurement protocols is discussed, as they were already published in [61, 96, 97]. Since these activities constituted a major part of the experimental phase of this thesis, the GD-OES technique is described in more detail compared to the other methods. Information about the layer structure is received in form of bond densities I_x and structural disorder from Fourier-transform infrared spectroscopy (FT-IR) (Sec. 3.2). The crystallinity χ_c as well as the crystallite diameter d_c and internal stress σ are derived from Raman spectroscopy (RS) (Sec. 3.3). The optical constants n and k, optical band gap E_{gap} and layer thickness d are derived from spectroscopic ellipsometry (SE) measurements with special attention to the quantification of the parasitic absorption as the current density loss J_{PA} (Sec. 3.4). Electrical characterization was done by Hall-effect (HE) measurements in terms of resistivity ρ_{HE}, charge carrier concentration $n_{e/h}$ and mobility $\mu_{e/h}$ (Sec. 3.5) while the passivation quality was determined by photoconductance decay (PCD) measurements in terms of contact recombination current density J_c and implied open circuit voltage iV_{oc} (Sec. 3.6).

3.1. Glow Discharge Optical Emission Spectroscopy (GD-OES)

In order to analyze the layer composition it is useful to know the actual elemental concentration profiles of the dopant $c_{B/P}$ and of the incorporated light elements $c_{O/N/C}$ as well as the hydrogen concentration c_H. In this context GD-OES is particularly useful as it measures all desired elements simultaneously. After an outline of possible calibration procedures (Sec. 3.1.1), the development of calibrations for hydrogen (Sec. 3.1.2) and phosphorus (Sec. 3.1.3) are presented as they were published before in [97] and [61], respectively. Lastly, a correction for atmospheric contaminations is presented (Sec. 3.1.4) as developed in the context of this thesis and as was already published in [96]. The description regarding the measurement technique mainly follows [98] where also more details regarding GD-OES can be found.

The sample being the cathode is located in front of a hollow cylindrical copper anode and after evacuation of the region between both a power is applied igniting a plasma. Consequently, plasma ions are accelerated towards the sample surface where surface atoms are sputtered. These sputtered atoms are excited in the plasma and emit characteristic light during relaxation, which is then spectrally separated by an optical spectrometer in a Paschen-Runge arrangement. Photomultiplier tube (PMT) detectors are placed at positions on a Rowland-circle corresponding to characteristic wavelengths of the elements of interest, measuring the light intensity I_i of the element i as dimensionless relative intensity. As the measured light intensities are related to the initial elemental composition

in the sample and as the sputter process reaches deeper in the sample over time, GD-OES is suited for qualitative time-intensity $I_i(t)$ profiles or compositional depth-concentration $c_i(z)$ profiles, if appropriate calibrations are performed. Such calibrations are in some cases difficult to achieve, especially for the elements oxygen, nitrogen, carbon and hydrogen. For these only a few calibration standards with predominantly low certified concentrations are commercially available and hence laboratory standards have to be fabricated. Additionally, the measured intensities for oxygen, carbon and hydrogen suffer from atmospheric contaminations such as residual O_2, CO_2 and H_2O in the measurement chamber or adsorbed H_2O on the sample surface. These contaminations cause an exponentially decaying signal during the first measurement seconds.

In this thesis, a GD-OES tool[14] with an anode diameter of 2.5 mm and RF power supply was used enabling the measurement of non-conductive samples, in particular of high ohmic silicon and of FS substrates. In Table 3.1 the choice of emission lines for the analysis is depicted. An argon plasma was sustained under a constant voltage supply and the pressure was regulated to a set value so that the plasma current develops depending on the sample properties. Additionally, the power was supplied in a pulse mode for less thermal load in the sample which prevents diffusion and enables a lower sputter rate and thus a higher depth resolution. The depth resolution also strongly depends on the crater bottom shape which can be tuned by the plasma parameters. For the measurements in this thesis the plasma parameters were optimized[15] to a rather flat crater bottom on polished pure silicon substrate with an upper limit for the depth uncertainty of $\sim 5\%$ and an effective sputter rate (eq. 3.8) of $S_{eff} \approx 8$ nm/s. It is assumed that a similar flat crater shape evolves in all measured matrices. Without advanced measurement protocols concentrations down to 100 ppm were measured while the exact resolution depends on the nature of the chosen emission line and specific PMT model. For a silicon matrix this value converts into a resolution limit in terms of atomic concentration of $\sim 10^{18}$ cm^{-3}, which is above the typical silicon base dopant concentration. Therefore, GD-OES is suited rather for analysis of passivation or diffusion source layers with higher dopant concentrations.

TABLE 3.1. All GD-OES measured emission lines of the respective elements and related specifics which are to be considered in the data evaluation and interpretation.

Element	Emission line (nm)	Specifics
Si	288.158	-
B	208.959	-
P	178.287	Argon emission line nearby induces plasma parameters dependent zero intensity
O	130.217	Weak emission line Suffers from atmospheric contamination
N	149.262	Nitrogen impurity in argon gas induces plasma parameters dependent zero intensity
C	156.143	Suffers from atmospheric contamination
H	121.567	Suffers from atmospheric contamination

[14]Technical details can be found in the Appendix A.1.
[15]Optimized plasma parameters: $V = 700$ V, $p = 6$ mBar, pulse frequency $f = 2111$ Hz, duty cycle $D = 10\%$.

3.1.1. Calibration Procedures

As the sample itself is the cathode, the actual sputter rate depends not only on the plasma parameters but also on the electrical properties of the sample. Therefore, calibration in GD-OES needs to be discussed in detail. Starting from a standard calibration two further procedures are described, namely the multi-matrix calibration and the adjusted multi-matrix-calibration. Before a calibration can be applied, a simple linear drift correction has to be performed to correct the present intensities to the intensities measured at the time of calibration.

Standard Calibration

The intensity I_i of measured characteristic light emitted by the element i can be written as

$$I_i = k_i A_i R_i S_i + d_i \tag{3.1}$$

with the instrumental detection efficiency k_i, a correction factor for self-absorption A_i and the emission yield R_i defined as the number of photons emitted per sputtered atom. The element specific sputter rate $S_i = \Delta m_i / \Delta t$ is defined as the sputtered mass Δm_i per time interval Δt and d_i is a constant background term from the detector dark current, instrument noise, scattered light and light from other elements. Assuming a linear relationship between the total sputter rate S and the element specific sputter rate $S_i = c_i S$ with c_i being the concentration of the element i, eq. 3.1 can be rewritten in terms of the concentration

$$c_i = \frac{1}{k_i A_i R_i S} I_i - \frac{d_i}{k_i A_i R_i S} = a_i I_i + b_i. \tag{3.2}$$

Eq. 3.2 has the form of a linear calibration function and hence the intensity signal can be transferred into an actual concentration by determining the calibration constants a_i and b_i with individual calibration curves for each element i.

Multi-Matrix Calibration

As the calibration constants in eq. 3.2 are functions of the total sputter rate $a_i(S)$ and $b_i(S)$, this approach does only apply for measurements with similar sputter rates, i.e. samples with the same matrix. Certified calibration samples are available in a variety of matrices with different sputter rates. Therefore, a more elaborated approach is usually applied by the introduction of the relative sputter rate q in relation to a reference sputter rate S_{ref}. Starting from the definition of the sputter rate of the sample of interest

$$S = \frac{\Delta m}{\Delta t} \tag{3.3}$$

as sputtered mass Δm per time interval Δt, the relative sputter rate q is defined with regards to a reference sputter rate S_{ref}

$$q = \frac{S}{S_{ref}} = \frac{\rho \, \Delta z}{\rho_{ref} \, \Delta z_{ref}} \cdot \frac{\Delta t_{ref}}{\Delta t} \tag{3.4}$$

with the mass density ρ and the sputtered depth Δz. The relative sputter rate q is independent of the plasma parameters as well as of the specific device and thereby enables comparability between scientific groups and over time. Pure iron is commonly used as the reference material to ensure this comparability.

Multiplying eq. 3.2 by the relative sputter rate leads to a calibration function for virtual concentrations

$$v_i = q\,c_i = \frac{1}{k_i A_i R_i S_{ref}} I_i - \frac{d_i}{k_i A_i R_i S_{ref}} = a_{i,v} I_i + b_{i,v} \tag{3.5}$$

where the calibration constants are now functions of the reference sputter rate, $a_{i,v}(S_{ref})$ and $b_{i,v}(S_{ref})$, which is constant for given plasma parameters and hence equal for all calibration samples. In this way the sputter rate dependency is transferred from the calibration itself, $a_i(S)$ and $b_i(S)$, to the outcome of the calibration in form of the virtual concentrations $v_i(S)$. It is important to note that for each calibration sample the relative sputter rate q has to be known in order to determine the virtual concentrations and thus the calibration constants.

As the virtual concentrations v_i of an unknown sample determined by eq. 3.5 are most likely larger than one, the real concentrations $c_{i,real}$ of an unknown sample are obtained by normalization of these virtual concentrations for all elements incorporated in this sample

$$c_{i,real} = \frac{v_i}{\sum_j v_j} = \frac{c_i\,q}{\sum_j c_j\,q} \tag{3.6}$$

with q being the relative sputter rate of the unknown sample. As is evident from eq. 3.6, the sputter rate of the unknown sample simply cancels out and therefore needs not be determined. It should be emphasized that the virtual concentrations obtained by the calibration in eq. 3.5 are single values from which the relative sputter rate of the unknown sample q cannot be extracted. Only the concentrations c_i are obtained by the normalization in eq. 3.6.

Adjusted Multi-Matrix Calibration

The just described multi-matrix calibration procedure offers the main advantage that q of the unknown sample needs not be determined at the expense of a calibration function for each element included in the unknown sample. For a large number of constituents such multiple calibrations are impractical. An adjusted approach determines the concentration of the element i by simply dividing the virtual concentration obtained from eq. 3.5 by the relative sputter rate of the unknown sample via

$$c_i = \frac{v_i}{q}. \tag{3.7}$$

Hereby only the calibration for the element i has to be performed at the expense that the relative sputter rate of the unknown sample has to be determined.

Depth Calibration

In principle, the sputtered depth could be calculated for each data point from the concentrations obtained by the multi-matrix calibration and the plasma parameters [98]. However, a more convenient way is the definition of an effective sputter rate

$$S_{eff} = \frac{\Delta z}{\Delta t} \tag{3.8}$$

which should not be confused with the previously introduced sputter rates defined by the sputtered mass Δm per time Δt in eq. 3.3. To convert the sputter time into depth for regions with a constant sputter rate, it simply has to be multiplied by the effective sputter rate. Δz can be determined for homogeneous bulk samples by measuring the crater depth, e.g. using contact or confocal laser

profilometry [99], or for layers on a substrate by determining the layer thickness using SE (Sec. 3.4). The corresponding time interval Δt is the total sputter time or the duration until the sputter process reaches the interface between the layer and the substrate, respectively. This duration can usually be determined from the depth profile of an element with significantly different concentrations between the layer and the substrate.

Uncertainty Determination

The uncertainties of the calibration constants were taken from the weighted fit procedure during calibration with the statistical uncertainties of the measured intensities I_i as weights. In case of the multi-matrix and adjusted multi-matrix calibration the uncertainty of the relative sputter rate was determined by a Gaussian uncertainty propagation of eq. 3.4. Therein, the uncertainty of Δt was taken from the measured depth profiles and the uncertainty of Δz from either the average over the crater profile, measured by contact profilometry in case of commercial standards, or by the fit uncertainty of the SE determined layer thickness in case of laboratory standards. The uncertainty of the mass density ρ was either taken from the resolution of the scales and the manual volume measurement for the commercial standards or roughly estimated by 0.1 g/cm^3 for the laboratory standards, if not stated otherwise.

3.1.2. Hydrogen Calibration

Calibration standards containing hydrogen are available with low concentrations only which are not suited for the high concentrations in SiH_4-based CVD deposited layers that are investigated in this thesis. Thus, laboratory standards had to be fabricated, advantageously also based on CVD deposition. Such a calibration was demonstrated using laboratory a-Si:H standards by the authors in [100]. As the standards used therein are not publicly available, a similar calibration was performed for the device used in this thesis. This calibration is presented in this section and was published before in [97].

During PECVD deposition of a-Si:H the hydrogen content can be tuned by the deposition temperature (Sec. 2.3.1), which was varied in the range of $T_{set} = 100 - 400°C$ for fabrication of the calibration samples[16]. The depth profiles in terms of intensities I_H measured by GD-OES and hydrogen concentrations c_H determined by nuclear resonant reaction analysis (NRA)[17] for all samples are plotted in Fig. 3.1. Details on the NRA measurement technique can be found in [101]. The interface between the layer and the substrate is clearly visible in the sharp drop of the hydrogen intensity.

In the GD-OES profiles in Fig. 3.1 a) the above mentioned exponential decay of atmospheric contaminations is visible for $t < 10$ s. The values for the calibration were obtained by averaging over the GD-OES data for $t > 10$ s and over the whole constant layer signal for NRA. For the multi-matrix calibration according to eq. 3.5 the relative sputter rate q of all calibration samples had to be determined (eq. 3.4). Δz was chosen to be the layer thickness determined by SEM on a focused ion beam

[16]PECVD deposition parameters: $P = 10$ W, $p = 1000$ mTorr, $T_{set} = 100 - 400°C$, $R_{H2} = 50\%$, $R_{Ar} = 95\%$, $t = 1500$ s.
[17]NRA measurements were performed by Hans-Werner Becker at RUBION, Ruhr University of Bochum.

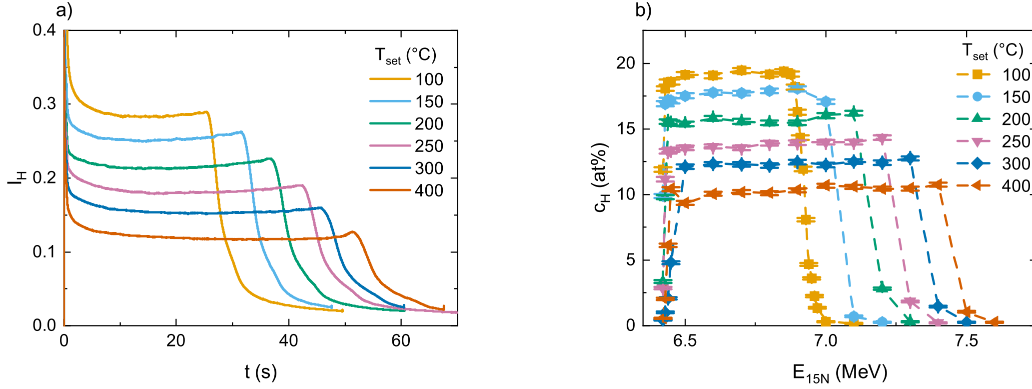

FIGURE 3.1. Hydrogen depth profiles of the laboratory a-Si:H standards. a) GD-OES measured raw intensity I_H as function of the time t and b) NRA measured hydrogen concentration c_H as function of the energy of the incident ^{15}N nitrogen ions E_{15N}. Dashed lines are a guide for the eye.

(FIB) cross section and Δt the corresponding GD-OES sputter duration up to the sharp interface in Fig. 3.1 a). The mass density was approximated by

$$\rho_{a-Si:H} = (m_{Si} + c_H m_H)\, n_{a-Si} \tag{3.9}$$

with $n_{a-Si} = 4.9 \cdot 10^{22}$ cm^{-3} being an estimation of the density of amorphous silicon according to [102] and the NRA determined hydrogen concentrations c_H. A pure iron reference sample[18] was used for determination of the relative sputter rates according to eq. 3.4. The silicon concentration was obtained by $c_{Si} = 1 - c_H$ with the NRA measured hydrogen concentrations assuming no additional elements in the a-Si:H layers within the GD-OES resolution. Two commercially available calibration standards with very low certified hydrogen concentration IARM 178D / 271A[19] were included in the calibration as well as a pure silicon FZ sample. All obtained values necessary for the calibration according to eq. 3.5 are depicted in Table 3.2 and the corresponding calibration curves for hydrogen and silicon are plotted in Fig. 3.2.

The calibration constants in Fig. 3.2 constitute a multi-matrix calibration valid for each material containing solely hydrogen and silicon without knowing its sputter rate. However, based on the data in Table 3.2 and Fig. 3.2 b) it is evident that for all a-Si:H samples similar silicon intensities I_{Si} were measured by GD-OES, even if the corresponding concentration c_{Si} as well as the measured intensity for hydrogen I_H vary by a factor of two. The reason for this might be that hydrogen predominantly binds to silicon dangling bonds in a-Si:H (Sec. 2.3.1 / 2.3.3), leaving the structure of the silicon network unaffected on the scale relevant for GD-OES. This could eventually lead to a constant silicon sputter rate S_{Si} which in turn would explain the measured constant intensities I_{Si} via eq. 3.1. Indeed, just a slight increase in the total sputter rate S with increasing c_H was observed which could be attributed to the additional hydrogen sputter rate S_H [97]. Altogether, these constant silicon intensities cause an underestimation (overestimation) of c_{Si} for lower (higher) hydrogen content. The crucial point is that the normalization of the virtual concentrations in eq. 3.6 transfers this uncertainty from c_{Si} to c_H which is consequently overestimated (underestimated). Such an overestimation was indeed observed in a verification of the calibration with NRA data for a-Si:H samples taken from [103], as

[18] See footnote 19.
[19] Details regarding the used calibration standards can be found in the Appendix A.2.

TABLE 3.2. All values of the calibration samples for the hydrogen calibration: GD-OES measured raw intensities I_i, concentrations c_i either determined by NRA measurements or taken from the certificate of the commercial standards and relative sputter rates q according to eq. 3.4.

T_{set} / Sample name	I_H (GD-OES)	I_{Si} (GD-OES)	c_H (at%) (NRA / certificate)	c_{Si} (at%) (NRA / certificate)	q
100°C	0.278 ± 0.007	1.480 ± 0.025	19.22 ± 0.08	80.78 ± 0.08	0.209 ± 0.027
150°C	0.251 ± 0.006	1.480 ± 0.026	17.67 ± 0.08	82.33 ± 0.08	0.199 ± 0.025
200°C	0.214 ± 0.006	1.478 ± 0.037	15.61 ± 0.07	84.39 ± 0.07	0.187 ± 0.024
250°C	0.180 ± 0.005	1.479 ± 0.020	13.77 ± 0.07	86.23 ± 0.07	0.190 ± 0.024
300°C	0.153 ± 0.005	1.480 ± 0.020	12.27 ± 0.07	87.73 ± 0.07	0.190 ± 0.024
400°C	0.117 ± 0.004	1.479 ± 0.040	10.10 ± 0.06	89.90 ± 0.06	0.178 ± 0.022
IARM 178D	0.015 ± 0.002	0.003 ± 0.001	0.074 ± 0.009	0.087 ± 0.003	0.326 ± 0.006
IARM 271A	0.010 ± 0.002	0.002 ± 0.001	0.596 ± 0.183	0.035 ± 0.003	0.316 ± 0.010
Bare FZ	0.007 ± 0.001	1.449 ± 0.058	0	99.99 ± 0.01	0.160 ± 0.002

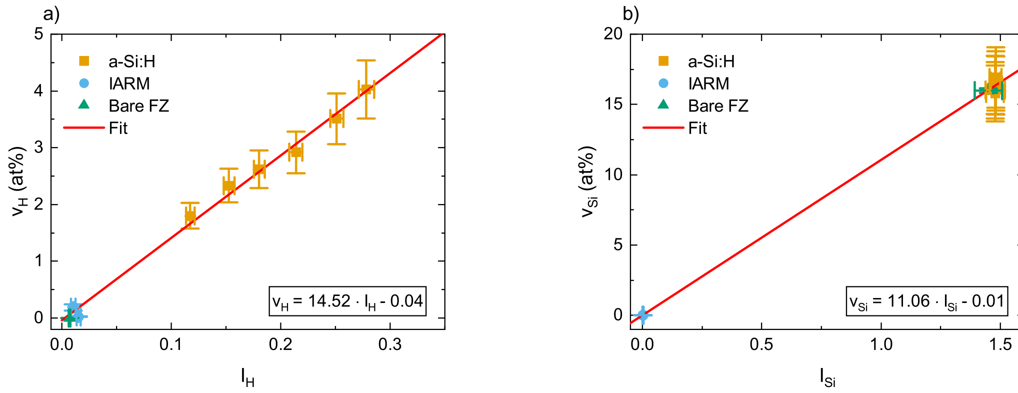

FIGURE 3.2. GD-OES calibration curves from raw intensities I_i to virtual concentrations v_i according to eq. 3.5 for a) hydrogen and b) silicon. Data are distinguished by the laboratory standards (a-Si:H), the commercial calibration standards (IARM) and a bare FZ substrate. Solid red lines are linear fits with corresponding parameters in the boxes.

shown in Fig. 3.3. Apart from the artificially high surface concentration from atmospheric contaminations, the overestimation is evident especially for the lower hydrogen concentrations.

3.1.3. Phosphorus Calibration

Besides the light elements, also a calibration of the dopant atoms is desired. For boron there are generally lots of calibration standards commercially available but they do not cover the whole concentration range relevant for this thesis. A successful calibration with laboratory standards consisting of boron silicate glass (BSG) with different concentrations was published in [104, 105].

In case of phosphorus one calibration standard with a comparably large concentration of ~ 10 at% was commercially available and therefore a calibration could be performed without the need for a fabrication of laboratory standards. A multi-matrix calibration for a measurement of a standard (n) poly-Si/SiO_x contact would also include a calibration for oxygen which was found to be exceptionally challenging and matrix-dependent [106]. Therefore, an adjusted multi-matrix calibration

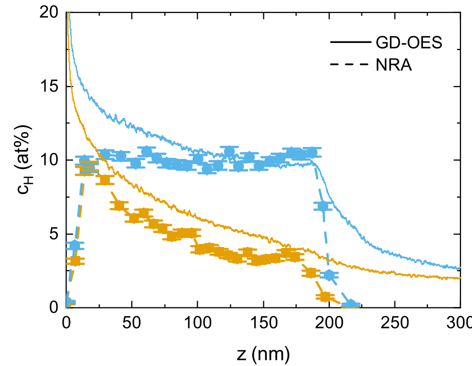

FIGURE 3.3. Verification of the GD-OES hydrogen calibration by measurement of two a-Si:H depth profiles $c_H(z)$ with a) GD-OES and b) NRA. a-Si:H layers and NRA measurements taken from [103]. Dashed lines are a guide for the eye.

was performed for the purpose of this thesis which was successfully applied and published in [61]. However, the fabrication of suitable laboratory standards and the determination of their concentrations was demonstrated in the context of silicon-based photovoltaics for boron as well as phosphorus by the authors in [107].

For the calibration two calibration standards were utilized[20] and additionally two zero points were included in form of one bare FZ substrate and one sample with a (n) poly-Si layer on top whilst the zero signal was taken from the measurement of the substrate below the layer. As stated in Table 3.1, the phosphorus PMT is located at a position that might be interfered by an argon emission line. Therefore, the zero intensity for phosphorus might depend on the intensity of this argon emission line which in turn depends on the plasma conditions and thus on the electrical properties of the sample. The heavily doped (n) poly-Si layer forms the contact between the sample and the cathode power supply. Therefore, an increased plasma current was observed due to the higher conductivity in this (n) poly-Si layer compared to the bare FZ substrate with a resistivity of 200 Ωcm. This in turn intensified the argon emission line and thus the zero phosphorus intensity in the underlying substrate. Using the (n) poly-Si layer as an additional zero point for the calibration corrects for this artifact to a certain extent.

For high concentrations self-absorption is expected to reduce the measured intensity [98]. Since the correction factor for self-absorption A_i in eq. 3.1 is hardly accessible in practice, a quadratic calibration curve is commonly applied to correct for the reduced measured intensities [98]. Such a quadratic fit was also performed for the present phosphorus calibration as can be seen in Fig. 3.4. Admittedly, using a quadratic calibration function instead of a linear one reduces the degree of freedom from two to one and hence this choice seems somehow arbitrary. However, it is justified based on the meaningful comparison of the resulting phosphorus concentration to electrochemical capacitance-voltage (ECV) profiling measurement as discussed in Sec. 5.2.1 and published in [61]. The calibration constants in Fig. 3.4 can be used to obtain virtual phosphorus concentrations which are then converted into real concentrations according to eq. 3.7, if the relative sputter rate of the measured sample is known.

[20] Details regarding the used calibration standards can be found in the Appendix A.2.

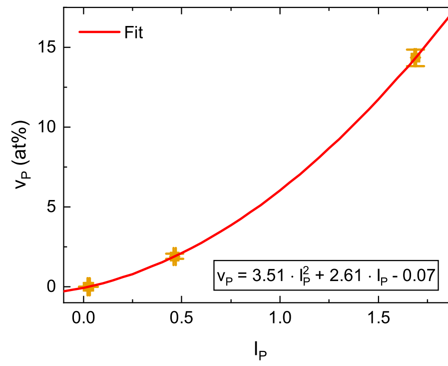

FIGURE 3.4. Phosphorus calibration curve from GD-OES determined raw intensities I_P to virtual concentrations v_P according to eq. 3.5. Solid red line is a quadratic fit with corresponding parameters in the box.

3.1.4. Correction for Atmospheric Contaminations

As stated above, during the first seconds of each GD-OES measurement the signal of oxygen, carbon and hydrogen is artificially increased by atmospheric contaminations with a typically exponential decay. As almost all measurements in this thesis aimed at the concentration of one of these elements in a region near the surface, the corresponding raw signal has to be corrected. Even worse, for a thin surface layer with a thickness of < 10 nm, as used for a-Si:H passivation in SHJ solar cells, such a correction is not feasible without further action. The method described in the following to correct for the atmospheric contaminations signal and to allow measurements of thin surface layers containing oxygen, carbon or hydrogen was published before in [96][21].

Fig. 3.5 a) shows the recorded hydrogen profile of a PECVD deposited[22] a-Si:H layer with a thickness of ~ 10 nm on a polished silicon FZ substrate. The signal from the layer is superimposed by the exponential decay from the atmospheric contamination and thus not identifiable. To separate both signals, a hydrogen-free ~ 500 nm thick copper buffer layer was MSD deposited on top of the a-Si:H layer. The corresponding hydrogen profile is shown in Fig. 3.5 b), where the signal from the a-Si:H layer appears as a clear peak overlying the atmospheric exponential decay. This separation allows for a two term exponential fit of the signal from the atmospheric contaminations, eventually leading to the isolated signal originating solely from the a-Si:H layer as shown in Fig. 3.5 c). Interestingly, this correction for the atmospheric signal is also applicable to GD-OES measurements of poly-Si/SiO_x contacts. In this case, the poly-Si acts as the buffer layer and the signal of interest is the oxygen signal originating from the interfacial oxide as shown in Fig. 3.5 d). Throughout this thesis the correction for atmospheric contaminations in the oxygen signal $I_O(t)$ was applied for all GD-OES measurements if not stated otherwise.

Following the just described method the questions arises whether a combination with the hydrogen calibration described in Sec. 3.1.2 is possible. As stated above in the introduction of Sec. 3.1, the

[21] For reasons of consistency within this thesis, the values of ξ_H (eq. 3.10) in [96] were corrected with regards to the layer thicknesses from nm to cm by a factor of 10^7.

[22] PECVD deposition parameters: $P = 10$ W, $p = 1000$ mTorr, $T_{set} = 100$°C, $R_{H2} = 50\%$, $R_{Ar} = 95\%$, $t = 30$ s and a previous ignition step with $P = 20$ W for $t = 5$ s.

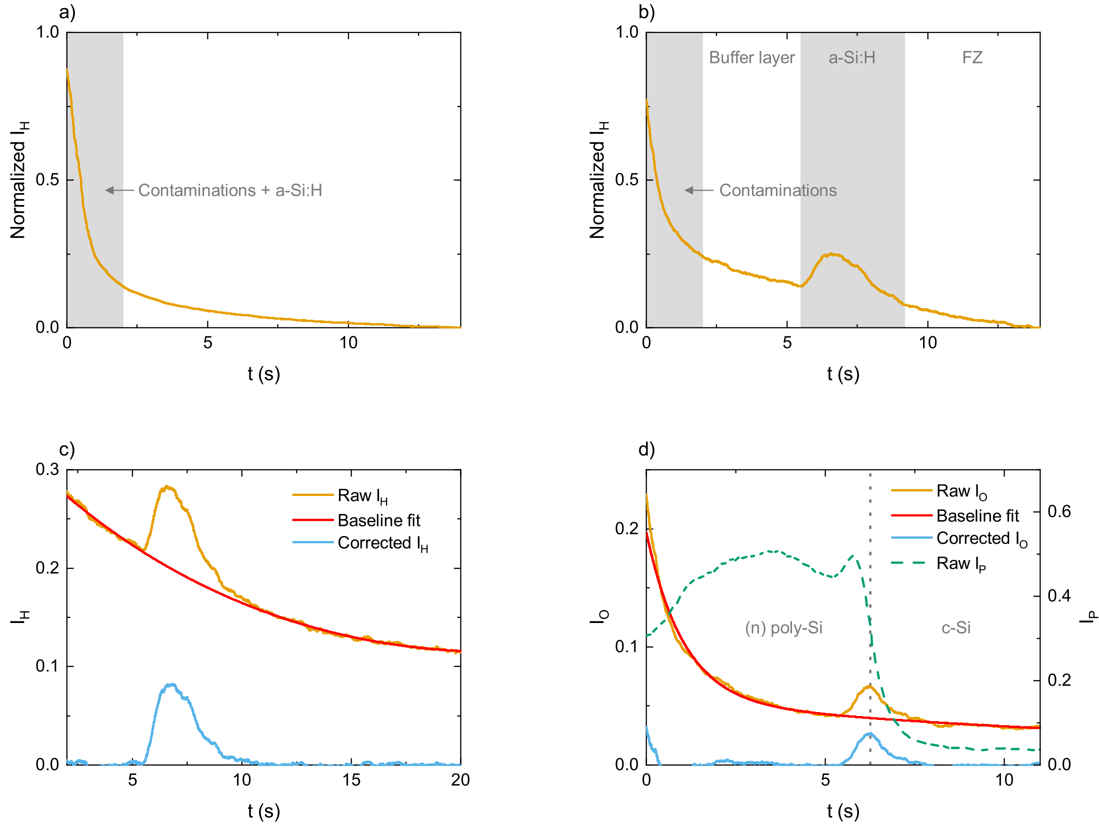

FIGURE 3.5. GD-OES measured hydrogen raw depth profile $I_H(t)$ of a 10 nm thin a-Si:H layer normalized to the maximum value a) without and b) with ~ 500 nm copper buffer layer. Areas affected by the atmospheric contaminations signal marked by an arrow. c) Raw $I_H(t)$ from b), two term exponential fit and subtracted profile $I_{H,corr}(t)$. d) Demonstration of the correction for atmospheric contaminations of the oxygen raw depth profile $I_O(t)$ (left axis) of a poly-Si/SiO$_x$ contact analogous to c). Additionally, phosphorus raw depth profile $I_P(t)$ (right axis) for illustration. Vertical dotted line marks the position of the interfacial oxide.

effective sputter rate in pure crystalline silicon was found to be $S_{eff} \approx 8$ nm/s. Assuming that this sputter rate also holds for the a-Si:H layer, the peak width in Fig. 3.5 c) suggests an a-Si:H layer thickness of $d_{a-Si} \approx 30$ nm. As the depth uncertainty in GD-OES increases linearly with the sputtered depth [98], the peak is strongly broadened and reduced in height by a loss in depth resolution during the sputter process of the 500 nm thick buffer layer. Therefore, a simple application of the hydrogen calibration would significantly underestimate the hydrogen concentration and cause misleading interpretations regarding the thickness of the layer.

Instead, the integral under the peak can be seen as a quantity linked to the total number of sputtered hydrogen atoms and hence can be calibrated to a hydrogen concentration. To achieve this, further a-Si:H layers with layer thicknesses of $d_{a-Si} \approx 10$ nm were deposited on polished silicon FZ substrates with identical deposition conditions as for the hydrogen calibration described in Sec. 3.1.2 under variation of the deposition temperature in the range of $T_{set} = 100 - 250°\mathrm{C}$ to make use of the NRA measurements presented therein. Differences in the resulting layer thicknesses d were corrected by dividing the integral under the corrected peak $I_{i,corr}$ by the layer thicknesses in centimeter, leading

to the definition of

$$\xi_i = \frac{\int I_{i,corr}(t)\,\mathrm{d}t}{d}. \tag{3.10}$$

As such, ξ_i qualitatively describes an elemental sheet concentration and all depth information is abandoned. Eq. 3.10 is valid for all elements i without restrictions. Fig. 3.6 presents a standard calibration of ξ_H with the NRA data presented in Sec. 3.1.2. A clear linear dependency is visible with a minimum detectable hydrogen concentration of 10 at% for $\xi_H = 0$. However, samples deposited at substrate temperatures > 250°C did not show a clear peak in the hydrogen profile so that the NRA determined hydrogen concentration for the a-Si:H layer deposited at 300°C of $c_H \approx 12.3$ at% seems to be the more suitable detection limit of this method.

Uncertainty Determination

The difference between the actual integral in eq. 3.10 and an integral with larger boundaries was chosen to represent the depth uncertainty of the corresponding GD-OES depth profile. The uncertainty of ξ_X was then determined by Gaussian uncertainty propagation of eq. 3.10 with this integral difference and the uncertainty of the SE determined layer thickness (Sec. 3.4.1).

3.2. Fourier-Transform Infrared Spectroscopy (FT-IR)

Infrared spectroscopy can be applied to observe bond vibrations at specific wavelengths as inverted peaks in the transmittance spectrum. In this way it is not only possible to identify specific bond configurations but also to approximate the concentration of an element and to gain information about the microstructure of the material. In contrast to a dispersive spectrometer measuring the transmittance for each wavelength individually, the Fourier-transform method uses a Michelson-interferometer to produce and modulate interferograms for the transmittance measurement instead of monochromatic light which allows for significantly reduced measurement durations. The transmitted interferograms are eventually Fourier-transformed into a standard transmittance spectrum. More details about FT-IR spectroscopy can be found in [108].

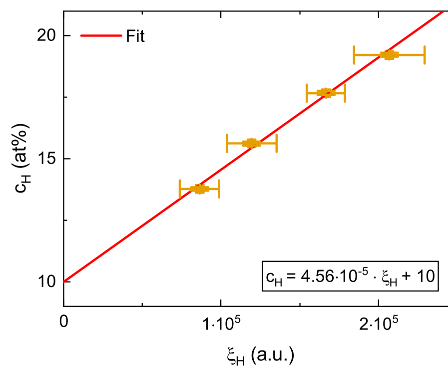

FIGURE 3.6. Hydrogen calibration curve from GD-OES determined ξ_H according to eq. 3.10. Solid red line is a linear fit weighted by the uncertainties in ξ_H with resulting parameters in the box.

In this thesis, a FT-IR spectrometer[23] was used only for the silicon substrate samples with a spectral range of $\omega = 400 - 4000$ cm^{-1} averaged over 50 measurements. The raw transmittance spectrum $T(\omega)$ was converted into an absorbance spectrum via

$$A(\omega) = -\ln[T(\omega)]. \tag{3.11}$$

After a baseline subtraction, a measurement of a bare substrate was subtracted in order to receive the absorbance of the investigated layer only. As this absorbance depends on the layer thickness d, the effective absorption coefficient was calculated via

$$\alpha_{eff}(\omega) = \frac{A(\omega)}{d \cdot \log_{10}(e)}. \tag{3.12}$$

Absorption via bond vibrations results in peaks in the absorption coefficient spectrum $\alpha_{eff}(\omega)$. In Table 3.3 all bond vibrations considered in this thesis are listed. A direct way to analyze these peaks is the definition of the absorption strength

$$I_x = \int_{\omega_1}^{\omega_2} \frac{\alpha_{eff}(\omega)}{\omega} \mathrm{d}\omega \tag{3.13}$$

with $\omega_{1/2}$ being suited integration boundaries and x corresponding to a literature position value for the absorption peak of interest. These peaks were fitted with Gauss functions and integrated over the total range of the measured spectrum. As the absorption peak height and hence the absorption strength increases for higher bond densities N_x, it can be used to approximate this bond density in presence of a suitable experimentally determined proportionality constant A_x via

$$N_x = A_x I_x. \tag{3.14}$$

TABLE 3.3. FT-IR absorption peak literature position value, contributing bonds and their vibration mode as well as a corresponding reference to literature for all peaks analyzed in this thesis.

Literature peak position (cm^{-1})	Bonds	Vibration mode	Reference
		Hydrogen	
640	Si-H / $Si-H_2$	Wag / Roll	[109]
840	$Si-H_2$ pairs / $(Si-H_2)_n$ chains	Bend	[110]
880	Isolated $Si-H_2$	Bend	[110]
2000	Si-H	Stretch	[111]
2080	$Si-H_2$	Stretch	[111]
		Oxygen	
780	(Si-H) / (Si-O-Si)	Bond coupling	[112]
980	Si-O-Si	Asymmetrical stretch	[112]
1107	O_i	Interstitial oxygen	[113]
		Nitrogen	
850	Si-N	Asymmetrical stretch	[114]

[23]Technical details can be found in the Appendix A.1.

This bond density can be in turn converted into atomic concentrations by division of the atomic density of the surrounding material whereas in this thesis the atomic density of crystalline silicon $n_{Si} = 5 \cdot 10^{22}$ cm^{-3} was used. It is important to sum the bond densities of all present bond configurations, in particular the stretch vibrations of both silicon monohydride (Si-H) and dihydride (Si-H_2) bonds (Table 3.3) for a determination of the hydrogen concentration in a-Si:H with proportionality constants of $A_{2000} \approx A_{2080} = 9.1 \cdot 10^{19}$ cm^{-2} [110].

Uncertainty Determination

The uncertainties of the absorption strength I_x was estimated by applying eq. 3.13 to the Gauss functions which arise if each fit parameter is enlarged by its uncertainty resulting from the fit procedure. The absolute difference to the original I_x was taken as the uncertainty.

3.2.1. Microstructure Factor R^* and Ratio Q^*

As stated above, the absorption coefficient spectrum contains not only information about the individual bond configurations but also about the surrounding material. In the case of a-Si:H, a frequently discussed quantity is the microstructure factor [115]

$$R^* = \frac{I_{2080}}{I_{2000} + I_{2080}} \tag{3.15}$$

with the absorption strengths of the stretch vibrations of silicon-hydrogen bonds (Table 3.3). The absorption peak at 2000 cm^{-1} is typically attributed to Si-H bonds while the peak at 2080 cm^{-1} is attributed to Si-H_2 bonds [111]. This clear attribution is in fact constantly discussed in the literature [109, 110, 116, 117] but is sufficient for a basic interpretation of the microstructure factor as follows. The presence of a large dihydride Si-H_2 bond density reflects a less ordered structure of the amorphous network compared to a high monohydride Si-H bond density since in the former case more silicon atoms are only twofold bonded to neighboring silicon atoms instead of threefold in the latter case. Eq. 3.14 links R^* to these bond densities. Therefore, larger R^* values correspond to a rather disordered, and lower R^* values to a rather ordered material. For illustrative purposes, effective absorption coefficient spectra showing the superposition of both peaks for different R^* values are depicted in Fig. 3.7 a) for PECVD deposited[24] a-Si:H layers on FZ substrate and were previously published in [118]. The shift from a more pronounced absorption peak at 2080 cm^{-1} to a more pronounced peak at 2000 cm^{-1} with decreasing R^* is clearly visible.

A second quantity containing information regarding the structure of the a-Si:H network is the ratio Q^* defined as

$$Q^* = \frac{I_{840}}{I_{880}} \tag{3.16}$$

with the absorption strengths of the bend vibrations of silicon-hydrogen bonds (Table 3.3). Following the interpretation in [116], inner surfaces of microvoids within the amorphous network are assumed to be decorated by Si-H_2 bonds close enough to form Si-H_2 pairs or $(\text{Si-H}_2)_n$ chains, both contributing to the absorption at 840 cm^{-1}. Contrary, the absorption at 880 cm^{-1} is attributed to isolated Si-H_2 bonds, qualifying a large Q^* value as indicator for the presence of microvoids in the amorphous network and thus a less ordered material, similar to the interpretation of the microstructure factor

[24] PECVD deposition parameters: $P = 10$ W, $p = 1000$ mTorr, $T_{set} = 100 - 400$°C, $R_{H2} = 50\%$, $R_{Ar} = 95\%$, $t = 1500$ s and a previous ignition step with $P = 20$ W for $t = 10$ s.

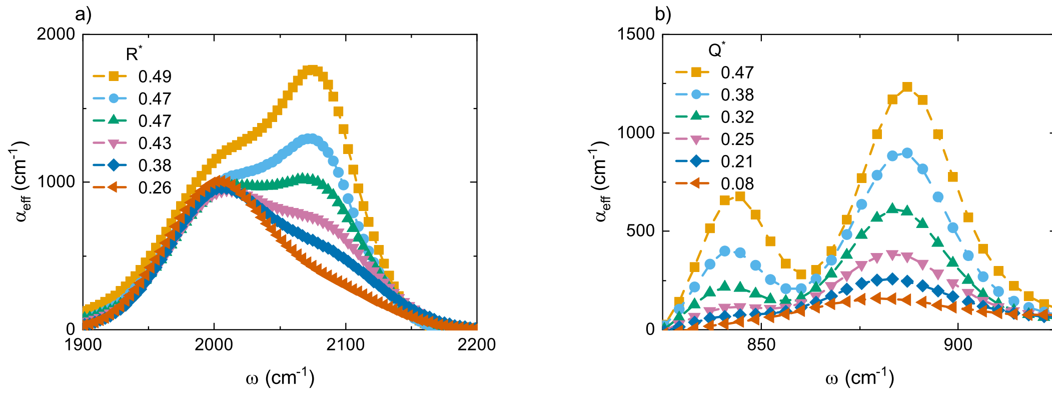

FIGURE 3.7. Representative FT-IR determined effective absorption coefficient spectra $\alpha_{eff}(\omega)$ according to eq. 3.12 resulting in a) different microstructure factors R^* and b) different ratios Q^* as indicated in the legends. Dashed lines are a guide for the eye.

R^*. Effective absorption coefficient spectra for several Q^* values are presented in Fig. 3.7 b) as illustration. The overall decreasing height of both absorption peaks with lower Q^* values is a result of a decreasing overall hydrogen concentration.

Additionally, the ratio Q^* is expected to depend on the overall hydrogen concentration as for low concentrations the distance between two Si-H_2 bonds might be too large to contribute to the absorption at 840 cm^{-1} even within the microvoids. Therefore, a large Q^* value verifies the presence of microvoids while a low Q^* value cannot exclude the presence of microvoids. However, the microstructure factor is not expected to depend on the hydrogen concentration as also isolated Si-H_2 bonds contribute to the absorption at 2080 cm^{-1}. In the following, R^* and Q^* will be referred to as disorder ratios.

3.3. Raman Spectroscopy (RS)

While FT-IR provides information about the order of the amorphous network indirectly by the ratios of absorption strengths, RS is based on the interaction of photons with excitations in the material and thus constitutes a rather direct measurement of the microstructure. Monochromatic light from a laser is directed towards the sample where most of this light is reflected by elastic Rayleigh scattering. Yet, a small fraction of the incoming photons is reflected inelastically by Raman scattering. The effect relevant for the investigations of this thesis is Raman scattering at phonons. The intense light of the Rayleigh scattering at the laser wavelength is filtered out while the Raman scattered light is shifted in wavelength and spectrally analyzed. This Raman shift is typically specified in wavenumber units ω whereby a positive shift is attributed to the Stokes scattering and a negative shift to the anti-Stokes scattering with significantly lower intensities. More details about RS can be found in [119].

In this thesis, a confocal Raman spectrometer[25] was operated at a laser wavelength of 488 nm with a low power of 1 mW to avoid laser induced crystallization of initially amorphous layers. The scattered light was analyzed by a spectrometer over the Raman shift range from $\omega = -260 - 1200$ cm^{-1} whilst only the Stokes part of the spectrum was analyzed for $\omega > 50$ cm^{-1}.

[25]Technical details can be found in the Appendix A.1.

Fig. 3.8 a) shows representative RS spectra of PECVD as-deposited (i) a-Si:H[26] and (i) nc-Si:H[27] layers, of initially MSD deposited and crystallized (i) poly-Si, of a c-Si monocrystal substrate and of a FS substrate. According to the literature, the Raman scattering originating from the transverse optical phonon in a-Si is expected at $\omega_{a-Si} \approx 480$ cm^{-1} and in c-Si at $\omega_{c-Si} \approx 521$ cm^{-1} [120] (Fig. 3.8 a). The broad peak around $\omega \approx 650$ cm^{-1} in the a-Si:H and nc-Si:H spectra is attributed to Si-H bonds and to two-phonon scattering [121].

In Sec. 2.3.1 it was stated that an increase of the hydrogen gas flow ratio R_{H2} during PECVD deposition promotes the direct deposition of nc-Si:H. This statement is verified here by an increase from $R_{H2} = 0\%$ for the a-Si:H layer to $R_{H2} = 99\%$ for the nc-Si:H layer. The coexistence of the amorphous and crystalline phase can be seen in the nc-Si:H spectrum as a superposition of the a-Si:H and c-Si spectrum in Fig. 3.8 a). For the poly-Si layer the amorphous part of the spectrum is reduced so that it lies in between the nc-Si:H and the c-Si spectrum. This observation supports the notion of poly-Si consisting of individual grains surrounded by an amorphous like matrix (Sec. 2.4.3).

Without normalization the intensity of the peak at 521 cm^{-1} from a c-Si substrate is more than one order of magnitude higher compared to the one of a nc-Si:H or poly-Si layer and hence precludes the analysis of such spectra on c-Si substrate. Therefore, all measurements were performed on FS substrates. As the broad band of the FS spectrum overlays all other reference spectra in Fig. 3.8 a), a substrate correction was performed for each recorded spectrum following the procedure in [122]. The raw spectrum, the fitted and subtracted spectra as well as the substrate corrected spectrum resulting solely from the layer itself are shown exemplarily for the nc-Si:H spectrum in Fig. 3.8 b). The small peak in the FS substrate spectrum at $\omega \approx 490$ cm^{-1} appears also in the raw spectrum, but not in the corrected spectrum as desired. However, this substrate correction fails if applied for a layer deposited on a c-Si substrate.

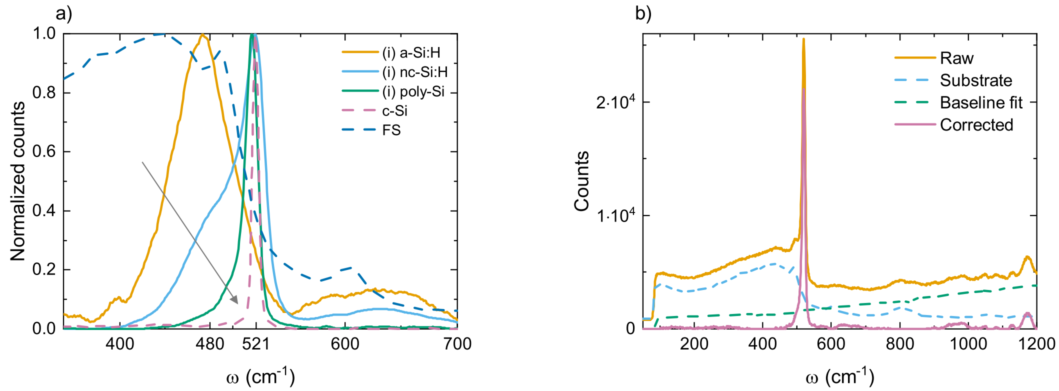

FIGURE 3.8. a) Representative Raman spectra of intrinsic a-Si:H, nc-Si:H and poly-Si layers as well as of a c-Si and FS substrates normalized to each maximum count value. The arrow indicates the transition from the amorphous phase ($\omega_{a-Si} \approx 480$ cm^{-1}) to the crystalline phase ($\omega_{c-Si} \approx 521$ cm^{-1}). b) Demonstration of the substrate correction with the substrate spectrum and baseline fit subtracted from the raw spectrum.

[26] PECVD deposition parameters: $P = 10$ W, $p = 400$ mTorr, $T_{set} = 225$°C, $R_{H2} = 0\%$, $t = 1800$ s.
[27] PECVD deposition parameters: $P = 20$ W, $p = 400$ mTorr, $T_{set} = 225$°C, $R_{H2} = 99\%$, $t = 3600$ s.

3.3.1. Crystallinity χ_c

In Fig. 3.8 a) the differences between pure a-Si, c-Si and mixed-phases in the Raman spectrum are shown qualitatively. For a quantitative description the Raman crystallinity χ_c is used as a measure for the crystalline volume fraction by fitting the spectrum. Most commonly, a fit with three Gaussian and/or Lorentzian peak functions is performed with start values for the position of $\omega_{a-Si} \approx 480$ cm^{-1} for the amorphous phase, of $\omega_{c-Si} \approx 521$ cm^{-1} for the crystalline phase and of $\omega_{inter} \approx 500$ cm^{-1} for an intermediate phase [123, 124]. Apart from better fit results, a justification for utilizing a third peak is a hexagonal silicon structure at the boundary between two crystallites according to [123] while others argue against its usage [125]. In [120] the authors suggested a procedure where a common a-Si:H spectrum is subtracted from an as-recorded mixed-phase spectrum, resulting in the crystalline part of the spectrum. This procedure rests on the assumption that all a-Si:H spectra are identical except for a scaling factor. As this assumption could not be verified for the layers investigated in this thesis, the standard three Gaussian fit procedure was applied where the crystallinity is defined as the ratio between the crystalline part of the spectrum and the full spectrum

$$\chi_c = \frac{I_{500} + I_{521}}{I_{480} + I_{500} + I_{521}} \tag{3.17}$$

with the integral under a Gauss curve I_x and x being one of the three position start values mentioned above. Since the authors in [123] reported significant deviations in the absolute values between the crystallinities obtained via eq. 3.17 and via x-ray diffractometry (XRD) and transmission electron microscopy (TEM), they suggested to interpret the Raman crystallinity rather as a lower limit than as an absolute value. Nevertheless, for values measured with the same tool in the context of a similar application χ_c offers an easily accessible quantity for relative comparisons.

Fig. 3.9 exemplarily shows the fitted spectrum for the nc-Si:H layer presented above in Fig. 3.8 a) with a resulting crystallinity of $\chi_c = 36.3 \pm 0.1\%$. The crystallinity of the poly-Si layer in the same figure was found to be $\chi_c = 81.9 \pm 6.8\%$. For the a-Si:H layer and the c-Si substrate the fit procedure usually fails and thus the expected crystallinites of 0 and 1 were set manually.

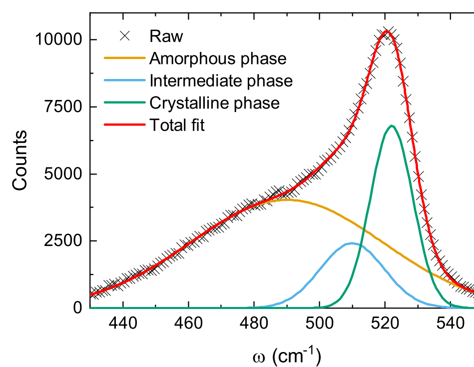

FIGURE 3.9. Demonstration of the fit procedure for the determination of the crystallinity according to eq. 3.17 by means of a representative (i) nc-Si:H layer with a crystallinity of $\chi_c = 36.3\%$. The three Gauss fits represent the amorphous ($\omega_{a-Si} \approx 480$ cm^{-1}), crystalline ($\omega_{c-Si} \approx 521$ cm^{-1}) and intermediate ($\omega_{inter} \approx 500$ cm^{-1}) phase and reproduce the raw spectrum.

Uncertainty Determination

Similar to the uncertainty determination of the FT-IR absorption strengths in Sec. 3.2, the Gauss functions, which aires if each fit parameter is enlarged by its uncertainty resulting from the fit procedure, were integrated. The absolute difference to the original integral I_x was taken as its uncertainty. Subsequently, the uncertainty of χ_c was determined by Gaussian uncertainty propagation of eq. 3.17.

3.3.2. Crystallite Diameter d_c and Internal Stress σ

Apart from the ratios of the peak integrals, a shift $\Delta\omega_{521}$ in the position of the crystalline peak located around $\omega_{c-Si} \approx 521$ cm^{-1} may appear. Shifts to lower wavenumbers are often connected to quantum confinement in the presence of small crystallites on the nanometer scale as present in mixed-phase nc-Si:H. In the context of this quantum confinement the term *crystallite* is used as opposed to the term *grain* used in Sec. 2.4.3 for the description of a poly-Si structure with significantly larger grains. Several models for an analytical relation between $\Delta\omega_{521}$ and the crystallite diameter d_c have been suggested and are compared in [126]. However, none of these is able to reproduce all available data in the literature.

A different and rather simple approach is to derive the crystallite diameter via its relation to the uncertainty of the wave vector assuming spherically shaped crystallites [127]. This approach leads to

$$d_c = 2\pi\sqrt{\frac{B}{\Delta\omega_{521}}} \tag{3.18}$$

with an empirically determined constant $B = 2.24$ cm^{-1}nm^2. Even if crystallite diameters determined in this way were reported to agree with TEM data for nc-Si [128], also doubts regarding the accuracy were raised [129].

Since this model relies on quantum effects, it is only valid for small crystallite diameters and is therefore not applicable to poly-Si as defined in Sec. 2.4.3. For poly-Si with grains too large for quantum confinement the shift $\Delta\omega_{521}$ is rather linked to internal stress σ induced by SPC [130]. This stress can be quantified via the empirical relation [131]

$$\sigma = C \cdot \Delta\omega_{521} \tag{3.19}$$

with an experimentally determined constant of $C = -522.5$ MPa/cm^{-1} whilst the original value in [131] was adjusted by the authors in [132]. Compressive stress results in a positive and tensile stress in a negative shift. According to [130], tensile stress is expected in the magnitude of GPa for poly-Si layers obtained from initially amorphous layers due to layer shrinkage during SPC under mechanical constraint of the substrate.

Uncertainty Determination

As $\Delta\omega_{521}$ is a single fit parameter, the uncertainty on both d_c and σ was determined by Gaussian uncertainty propagation of eq. 3.18 or 3.19, using the uncertainty of this fit parameter and an uncertainty of 0.1 cm^{-1}cm^2 for the constant B and 0.1 MPa/cm^{-1} for the constant C.

3.4. Spectroscopic Ellipsometry (SE)

Characterization of the poly-Si layers in terms of optical losses requires knowledge of the exact layer thickness as well as of the optical constants which was measured by SE. Monochromatic linearly polarized light is directed towards a layer stack on a substrate and the reflected light is then analyzed. During the transition of the layer stack the polarization changes due to interactions with the materials which is expressed by the complex reflectance of the parallel r_p and the perpendicular r_s polarized light. The ratio of both can be expressed as

$$\frac{r_p}{r_s} = \tan(\Psi)\, e^{i\Delta} \tag{3.20}$$

with the ratio of the diminished amplitudes $\tan(\Psi) = |r_p| / |r_s|$ and the phase difference between both polarizations Δ. A spectroscopic ellipsometer measures the ellipsometric parameter $\Psi(\lambda)$ and $\Delta(\lambda)$ as functions of the wavelength. The link to the optical properties of the layer stack is provided by modeling the complex dielectric functions of each layer $\varepsilon(\lambda) = \varepsilon_1(\lambda) + i\varepsilon_2(\lambda)$ as they jointly contribute together with the incident angle θ to the reflectances $r_{p/s}(\theta, \varepsilon)$ of each interface [133]. Based on these reflectances and eq. 3.20, the dielectric function models are fitted to the measured data by minimizing the standard mean-squared error (MSE). The resulting optimized dielectric functions are in turn linked to the optical constants via

$$n^2 = \frac{1}{2}\left(\sqrt{\varepsilon_1 + \varepsilon_2} + \varepsilon_1\right) \tag{3.21}$$

$$k^2 = \frac{1}{2}\left(\sqrt{\varepsilon_1 + \varepsilon_2} - \varepsilon_1\right). \tag{3.22}$$

Modeling the reflectances at each interface in the layer stack requires all layer thicknesses d_i as additional parameters which may also be fitted. Assuming a proper measurement, Ψ and Δ are expected to be exact values and the uncertainty mostly arises from the choice of an appropriate model describing the physical nature of the layer stack. Further details regarding SE measurement and data analysis can be found in [133, 134].

In this thesis, a spectroscopic rotating analyzer ellipsometer[28] was used for measurements at different incident angles with a spectral range of 240 – 2000 nm in reflectivity mode and an irradiated area in the range of mm^2. In addition to FS substrates, only layers on FZ silicon substrates were used as the rough surface of Cz substrates leads to a poor signal to noise ratio. Backside reflections on the FS substrate during measurement were avoided by attaching a black strip on the rear side. Model implementation and fitting to the experimental data were performed with the WVASE software[29]. If not stated otherwise, all spectra were recorded under 75° incidence angle in a spectral range of 240 – 1500 nm with a data point each 10 nm averaged over 40 measurements.

3.4.1. Modeling

The selection of an appropriate model for the dielectric functions is essential for SE. A poor model easily causes misleading interpretations even though the measurement itself was correct. One can rely on experiences documented in the literature for many materials and layer stacks, but also attempts for a systematical model selection were made [135].

[28] Technical details can be found in the Appendix A.1.
[29] Version 3.774, J.A. Woollam Co., 2012.

There are at least two distinct methods to model the dielectric function of a material. First, direct analytical expressions for the complex dielectric function $\varepsilon(\lambda, a_i)$ with fit parameters a_i can be applied and second, empirically determined tabulated data of the optical constants $n(\lambda)$ and $k(\lambda)$ can be utilized which are linked to the complex dielectric function via eq. 3.21 and 3.22. The former method was used for modeling of a-Si, a-Si:H, poly-Si and SiN_x:H layers while the latter was used for the interfacial oxide as well as the FZ and FS substrates as indicated in Table 3.4. In some cases the dielectric function of the FZ substrate was individually determined by a separate measurement of a reference sample without a layer stack.

Depending on the stage of the process flow (Chapter 2, Fig. 2.1), one of the three models shown in Fig. 3.10 a) was applied. In order to build a fully applicable model, a substrate material has to be chosen which is characterized by only one reflection at the interface to the layer above. In particular, all light transmitted at this interface is assumed to be subsequently absorbed in the substrate and thus no reflections at the rear side of the substrate are considered in the model. The interfacial oxide was included with a fixed thickness of 2.5 nm in the model for the FZ substrate but not in the model for

TABLE 3.4. List of all SE models applied in this thesis for each layer type with corresponding references to literature and total number of fit parameters.

Material	Model type	Number of fit parameters
FZ substrate	Tabulated data from [136]	1
FS substrate	Tabulated data from [136]	1
Interfacial / Native SiO_x	Tabulated data from [136]	1
a-Si	ε_2: 1 Tauc-Lorentz oscillator [137, 138] ε_1: Kramers-Kronig relation	6
poly-Si	ε_2: 2 Tauc-Lorentz oscillators [137, 138] ε_1: Kramers-Kronig relation	10
SiN_x:H	ε_2: 1 Tauc-Lorentz oscillator [137–139] ε_1: Kramers-Kronig relation	6

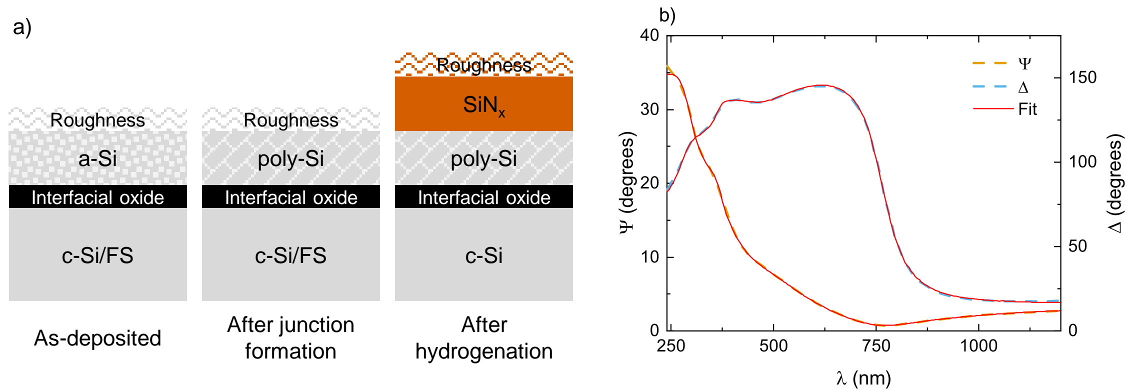

FIGURE 3.10. a) Sketches of the SE models used for samples at different stages during fabrication. No interfacial oxides and SiN_x on FS substrates. b) SE measured raw ellipsometric parameters as functions of the wavelength $\Psi(\lambda)$ and $\Delta(\lambda)$ of a (p) poly-Si layer on FZ substrate as well as the fit resulting from the corresponding model.

the FS substrates in accordance with the process flow. This thickness was determined separately by SE measurements of the interfacial oxide on FZ substrates without a deposited layer on top and kept at a fixed value. The surface roughness was modeled by a layer containing 50% underlying material and 50% voids, consequently reducing the refractive index of this roughness layer compared to the underlying material [140]. Fig. 3.10 b) exemplarily shows the fit of a PECVD deposited[30] in-situ doped (p) poly-Si layer on FZ substrate after SPC in good agreement with the experimental data yielding a MSE of 3. Further improvement of the fit could be expected for measurements at multiple incident angles which was not applied for all measurements due to impractical long measurement durations.

Uncertainty Determination

The uncertainty of the optical constants $n(\lambda)$ and $k(\lambda)$ was estimated starting from a complex dielectric function calculated according to the applied model from the fit parameter enlarged by its uncertainty $\varepsilon(\lambda, a_i + \sigma_{a_i})$. This function was then used to determine optical constants $n_\sigma(\lambda)$ and $k_\sigma(\lambda)$ whose absolute difference to the actual functions were taken as the uncertainties. Since the uncertainty of the fit parameter representing the layer thickness is usually unrealistically small, the previously discussed thickness inhomogeneities of the as-deposited layers were taken as relative uncertainties, namely 7% for PECVD (Sec. 2.3.1) and 9% for MSD (Sec. 2.3.2) deposited layers.

3.4.2. Optical Band Gap E_{gap} and E_{04}

Determination of the optical band gap is important for both the charge carrier selectivity and the parasitic absorption in a poly-Si/SiO_x contact. Based on the SE determined extinction coefficient $k(\lambda)$ the absorption coefficient is calculated via

$$\alpha(\lambda) = 4\pi \frac{k(\lambda)}{\lambda}. \tag{3.23}$$

According to the so-called Tauc-method [141], the optical band gap $E_{gap,tauc}$ of indirect amorphous semiconductors is the x-axis intercept of a linear fit in an E_{ph}-$\left(\alpha E_{ph}\right)^{1/2}$ plot with the single photon energy E_{ph}. It should be emphasized that the band gap of an amorphous semiconductor is not clearly defined due to the continuous decay of the band tail state density (Sec. 2.3.3). Nevertheless, $E_{gap,tauc}$ is commonly accepted as an approximation for the band gap in semiconductors. Alternatively, the fit parameter in the Tauc-Lorentz oscillator used for modeling of the a-Si and poly-Si layers (Table 3.4) can be used as measure for the optical band gap, indicated as $E_{gap,fit}$. Unfortunately, neither of the fit parameters from both Tauc-Lorentz oscillators of the poly-Si model provided meaningful values. Furthermore, the validity of the Tauc-method applied to polycrystalline semiconductors is seriously doubted in the literature [142, 143]. In order to provide a guess for the poly-Si band gap anyway, the photon energy E_{04} corresponding to an absorption coefficient of $\alpha(E_{04}) = 10^4$ cm^{-1} was determined as rough but robust estimate [144].

Uncertainty Determination

The uncertainty of $E_{gap,Tauc}$ and $E_{gap,fit}$ were taken from the corresponding fit parameter uncertainties. Regarding E_{04} and based on the uncertainty enlarged extinction coefficient $k_\sigma(\lambda)$ as introduced

[30]PECVD deposition parameters: $P = 20$ W, $p = 400$ mTorr, $T_{set} = 400$°C, $R_{B2H6} = 1.2\%$, $R_{H2} = 99\%$, $t = 1200$ s.

in the previous section, a similar absorption coefficient $\alpha_\sigma(\lambda)$ was calculated via eq. 3.23. E_{04} was determined also for this absorption coefficient and the absolute difference between both values was taken as uncertainty.

3.4.3. Parasitic Absorption Current Density J_{PA}

For a given stack of materials it is possible to determine a photocurrent density induced by irradiation for each photoactive layer using a transfer matrix method for which SE provides all necessary input parameters. Under knowledge of the optical constants or dielectric functions and all layer thicknesses, the formalism described in [145] can be applied to calculate the electric field resulting from an incident light spectrum as function of the position in the layer stack parallel to the surface normal $|E(z)|^2$. Following [145], the energy dissipation per volume as function of the position in the layer stack z and the wavelength λ is determined via

$$Q(z,\lambda) = \frac{1}{2} c\, \varepsilon_0\, \alpha(\lambda)\, n(\lambda)\, |E(z)|^2 \tag{3.24}$$

with the speed of light c, the vacuum permittivity ε_0, the refractive index $n(\lambda)$ and the absorption coefficient $\alpha(\lambda)$ as defined in eq. 3.23 for the layer corresponding to the position z. The total electron-hole pair generation rate per second and volume as function of the position in the layer stack is received by division of the single photon energy $E_{ph} = hc/\lambda$ and by integration over a suited spectral range (λ_1, λ_2) via

$$G(z) = \int_{\lambda_1}^{\lambda_2} Q(z,\lambda)\, \frac{\lambda}{h\,c}\, \mathrm{d}\lambda \tag{3.25}$$

with the Planck constant h. Finally, the parasitic absorption current density is determined by the integral over the z-range corresponding to the layer responsible for the parasitic absorption

$$J_{PA} = q \int_{z_1}^{z_2} G(z)\, \mathrm{d}z \tag{3.26}$$

with the elementary charge q.

All J_{PA} values for the poly-Si layers investigated in this thesis were calculated for a layer stack as shown in Fig. 3.11 a) representing the application of these layers on the front side of a solar cell and neglecting parasitic absorption on the rear side. The optical constants were SE determined as described above. Throughout this thesis all J_{PA} values were calculated for a spectral range of $\lambda = 240 - 1000$ nm with a step size of 1 nm. All layer thicknesses were kept constant at 2.5 nm for the interfacial oxide, at 100 nm for the poly-Si layer as guess for an industrially relevant thickness enabling screen printing (Sec. 1.3) and at 75 nm for the SiN_x:H layer as a typical thickness if applied as ARC on c-Si. Similar to the SE model, the substrate was seen as to absorb all light transmitted at the interface between the layer above and hence the substrate thickness did not influence J_{PA} of the poly-Si layer. All calculations were done with the standardized AM1.5 solar spectrum using the Matlab script provided in [146] whilst the substrate thickness was set to the maximum allowed value of 5 µm.

Fig. 3.11 b) exemplarily shows the AM1.5 solar spectrum in units of spectral irradiance F and the absorbed fractions of the poly-Si layer and of the c-Si substrate for a layer stack according to

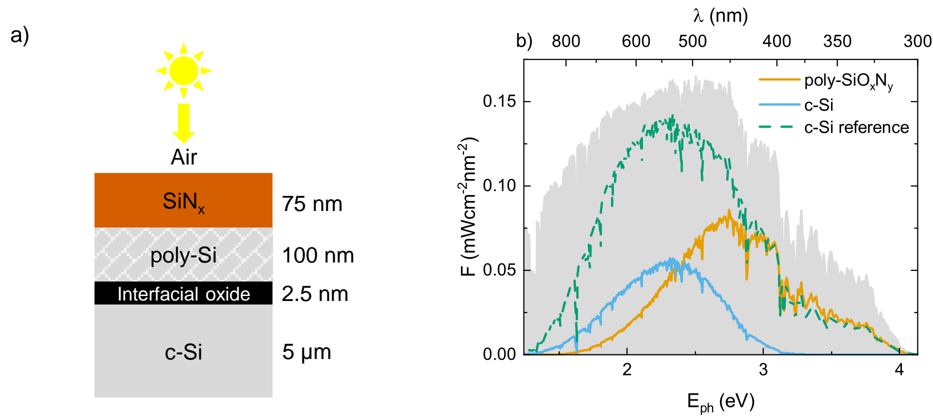

FIGURE 3.11. a) Model for J_{PA} determination with thicknesses for each layer and irradiation by the AM1.5 solar spectrum. b) Absorbed fractions of the (p) poly-SiO_xN_y layer and the c-Si substrate for an AM1.5 solar spectrum in terms of spectral irradiance as function of the photon energy $F(E_{ph})$. Additionally, absorbed fraction of a reference c-Si substrate without a poly-Si layer on top.

Fig. 3.11 a) with the dielectric functions taken from a SE fit of a PECVD deposited[31] (p) poly-SiO_xN_y layer on FS substrate. To allow for comparison, the absorbed fraction of the spectrum for a calculation without a poly-Si layer and thus without parasitic absorption is given as dashed line. The parasitic absorption current density of the (p) poly-SiO_xN_y layer according to eq. 3.26 is $J_{PA} = 5.67 \pm 0.34$ mA/cm^2, qualitatively described by the area under the corresponding curve in Fig. 3.11. It should be noted that the absorbed fraction of the c-Si substrate would be closer to the AM1.5 solar spectrum for a substrate thickness of ~ 200 µm typically used in solar cells without influencing J_{PA}.

Uncertainty Determination

The uncertainty was determined by repeating the same analysis for J_{PA} with the uncertainty enlarged extinction coefficient $k_\sigma(\lambda)$ (Sec. 3.4.1). The absolute difference between this and the actual J_{PA} value was taken as uncertainty.

3.5. Hall-Effect Measurement (HE)

Hall-effect measurements were utilized to measure the resistivity, the charge carrier concentration and the mobility of the poly-Si layers following the Van-der-Pauw method [147]. The sample of interest was contacted with four metal pins $A-D$ on the surface. A current was directed between two of these pins, e.g. I_{AB}, and the voltage between the other two pins was measured, e.g. V_{CD}, leading to the resistance $R_{AB,CD}$. Under reverse current the corresponding indices are switched, e.g. $R_{BA,CD}$. If a static magnetic field B is applied perpendicular to the samples surface, the measured voltages change compared to the case without magnetic field due to the Hall-effect. Even though the original theory introduced in [147] is independent of the specific sample shape and pin placement schemes, in practice an approximation of this theory is applied where the sample shape and the pin placement scheme are indeed a source of uncertainty. It was reported that one or the other pin placement scheme

[31]PECVD deposition parameters: $P = 100$ W, $p = 600$ mTorr, $T_{set} = 300$°C, $R_{N2O} = 20\%$, $R_{B2H6} = 1.8\%$, $R_{H2} = 0\%$, $t = 60$ s.

promotes the measurement of either quantity of interest [148]. To correct for asymmetrical sample shapes, the correction factor f is used as function of the determined resistances [149]. More details about HE measurements can be found in [31].

In this thesis, the sample shape of a 2 x 2 cm^2 square was chosen to easily fit in the Hall-effect measurement device[32] and the pins were placed directly on the layer in each corner as close to the edge as possible and labeled clock-wise from $A-D$. Only layers on FS substrates were measured to make sure that the results originate solely from the layer without a contribution of the substrate.

3.5.1. Resistivity ρ_{HE}

After the pin placement ohmic contacts between each pin and layer were verified by measuring the $I-V$ curves between all pin combinations. For high resistivities and/or very thin layers this verification might fail. The sheet resistance was obtained from the resistivities of two either vertically or horizontally opposing pin combinations in both current directions via

$$R_s = f\frac{\pi}{\ln(2)}\left(\frac{R_{AB,CD}+R_{BA,CD}+R_{CD,AB}+R_{DC,AB}}{4}\right) \tag{3.27}$$

while the symmetry correction factor was set to $f=1$ due to the symmetry of the quadratic FS substrate shape. R_s was determined solely from this measurement without externally determined input parameters but implicitly depends on the layer thickness d. In particular, for a thicker layer with identical electrical properties the measured R_s would be lower. For the characterization of the material itself the resistivity

$$\rho_{HE} = R_s\, d \tag{3.28}$$

is more suited at the expense that the layer thickness has to be determined externally, which was done by SE throughout this thesis (Sec. 3.4). It is important to state that ρ_{HE} contributes to the contact resistance ρ_c of a poly-Si/SiO_x contact via eq. 1.7 and thus to the selectivity S_{10} via eq. 1.9. As the current flow between two pins is directed in the plane parallel to the substrates surface, the HE measured resistivity can be seen as a measure for the lateral conductivity which is a critical parameter for a low contact resistance of a poly-Si/SiO_x structure with local metal contacts (Sec. 1.3).

Uncertainty Determination

The uncertainty was determined by the standard deviation of five to twenty repetitions of each measurement and by a sum of squares of this standard deviation with the uncertainty of the layer thickness according to Sec. 3.4.1.

3.5.2. Charge Carrier Concentration $n_{e/h}$ and Mobility $\mu_{e/h}$

During a measurement in presence of a static magnetic field B a current was directed between two diagonally opposing pins and the voltage was measured between the other two pins. The direction of the magnetic field is marked by a $+$ or $-$ sign in the determined resistances, e.g. $R^{+}_{AC,BD}$. Based on these measurements the charge carrier sheet concentration was determined by

$$n_s = \frac{B}{q}\left(\frac{8}{R^{+}_{AC,BD}-R^{-}_{AC,BD}+R^{+}_{CA,BD}-R^{-}_{CA,BD}+R^{+}_{BD,AC}-R^{-}_{BD,AC}+R^{+}_{DB,AC}-R^{-}_{DB,AC}}\right) \tag{3.29}$$

[32]Technical details can be found in the Appendix A.1.

with opposite signs for electrons and holes, respectively. Similar to R_s, n_s was determined solely from the HE measurements but implicitly depends on the layer thickness d. External determination of the layer thickness allowed for the calculation of the charge carrier concentration

$$n_{e/h} = \frac{n_s}{d}. \tag{3.30}$$

A combination of the measurements with (eq. 3.29) and without (eq. 3.27) magnetic field eventually led to the charge carrier mobility

$$\mu_{e/h} = (q\, n_s\, R_s)^{-1}. \tag{3.31}$$

It is worth mentioning that $\mu_{e/h}$ was not only determined solely from the HE measurement but is also independent of the layer thickness as its influence on n_s and R_s simply cancels out. It was found that HE measures the mobility only within the grains of a polycrystalline material if the conductivity at the grain boundaries is significantly lower [87].

Uncertainty Determination

The uncertainty of $n_{e/h}$ was determined analogous to the resistivity by the standard deviation of five to twenty repetitions of each measurement and by a sum of squares of this standard deviation with the uncertainty of the layer thickness according to Sec. 3.4.1. In contrast, $\mu_{e/h}$ was determined by the standard deviation of five to twenty repetitions of each measurement only since it is independent of the layer thickness.

3.6. Photoconductance Decay Measurement (PCD)

Contrary to the structural and electrical characterization methods introduced above, PCD aims at the determination of parameters that directly influence the solar cell performance [150]. In a test sample without metallization an excess charge carrier density Δn was generated by a light flash inducing a photogenerated current density J_{ph}. These additional charge carriers change the excess photoconductance ΔC in the sample, which was measured with an induction coil. The excess charge carrier concentration was then determined by

$$\Delta n = \frac{\Delta C}{qW\left(\mu_{e,c-Si} + \mu_{h,c-Si}\right)} \tag{3.32}$$

with the elementary charge q, the sample thickness W and the electron and hole mobilities in crystalline silicon $\mu_{e/h,c-Si}$. The effective minority carrier lifetime τ_{eff} is defined by

$$\tau_{eff}^{-1} = \sum_i \tau_i^{-1} \tag{3.33}$$

with τ_i being characteristic lifetimes for each recombination mechanism, namely radiative recombination, Auger recombination, SRH recombination via defects and recombination at the surface (Sec. 1.1). For PCD measurements an effective minority carrier lifetime can be determined with Δn from eq. 3.32 via

$$\tau_{eff} = \frac{\Delta n}{G - \frac{\partial \Delta n}{\partial t}}. \tag{3.34}$$

Therein, the charge carrier generation rate G was approximated by a typical photogenerated current density at one sun irradiance of $J_{ph,typ} = 38$ mA/cm^2 and the optical constant $\theta = J_{ph}/J_{ph,typ}$ as an adjustment to the actual photogenerated current density J_{ph} at one sun. The unit *sun* is in turn defined

by the photon flux generating a short circuit current density $J_{sc,ref}$ of a reference solar cell measured at standard test conditions in a solar spectrum simulator whereas the absolute value of this photon flux may differ for a specific measurement setup [151]. Altogether, the choice of θ seems somehow arbitrary but may be justified from empirical experience.

PCD measurements can be operated at two extreme conditions of eq. 3.34. First, the transient mode with a short light flash where τ_{eff} is long compared to the flash duration. In this case Δn decays in the dark with $G = 0$, leading to

$$\tau_{eff} = -\Delta n \left(\frac{\partial \Delta n}{\partial t} \right)^{-1} \tag{3.35}$$

which is independent of θ. Second, the quasi-steady-state (QSS) mode which utilizes a longer flash duration where τ_{eff} is small compared to the flash duration and hence $\frac{\partial \Delta n}{\partial t} = 0$ resulting in

$$\tau_{eff} = \frac{\Delta n}{G} \tag{3.36}$$

with the need for a specification of θ in order to determine the generation rate G.

In this thesis, symmetrical poly-Si/SiO_x test samples were measured by a lifetime tester[33] with a xenon flash lamp at a constant temperature of 30°C in both the transient and QSS mode. In absence of an ARC before hydrogenation, the optical constant was set to $\theta = 0.7$ and after SiN_x:H deposition during hydrogenation to $\theta = 0.9$ as empirically justified values. Besides the uncertainty arising from the choice of θ, the uncertainty regarding τ_{eff} using such a tool was found to be $< 10\%$ [152, 153].

3.6.1. Contact Recombination Current Density J_c

The saturation current density J_0 in the one-diode model (eq. 1.1) is typically interpreted as total recombination current density, which is composed of contributions from the bulk, the surface and, in case of diffused homojunction structures (Sec. 1.2.1), also from the emitter. PCD measurements provide the determination of the surface contribution if high quality bulk material such as FZ substrates is used. Based on the original method in [154] several refinements have been suggested. In this thesis, the analysis followed the method described in [155] which includes corrections for radiative and Auger recombination as well as for band gap narrowing and finite diffusion of charge carriers. Thereby the measured J_0 is corrected to larger values if Δn is large. The recombination current density can be written as

$$J_0 = \frac{qW}{2} \frac{\mathrm{d}}{\mathrm{d}\Delta n} \left(\frac{n_{i,eff}^2}{\tau_s - \frac{W^2}{D\pi^2}} \right) \tag{3.37}$$

with the injection dependent effective intrinsic carrier density $n_{i,eff}(\Delta n)$ at 25°C, the characteristic lifetime for recombination at the surface τ_s and the ambipolar diffusion coefficient of the injected carriers D. Reordering of eq. 3.33 reveals the link between τ_s and the PCD measured τ_{eff} via

$$\tau_s^{-1} = \tau_{eff}^{-1} - \sum \tau_i^{-1}. \tag{3.38}$$

Based on this relation and on eq. 3.37 it is evident, that the problem of J_0 determination reduces to a meaningful correction for the recombination mechanisms not related to the surface, characterized by their corresponding lifetimes τ_i.

[33]Technical details can be found in the Appendix A.1.

Following [155], this correction was done by an iterative procedure. As the initial condition it was assumed that

$$\tau_{corr}^{-1} \approx \tau_{eff}^{-1} - \tau_{intr}^{-1} \tag{3.39}$$

with τ_{intr} being the intrinsic lifetime limit for radiative and Auger recombination in the bulk from the parametrization in [156]. Each following iteration i consists of three steps:

I) Assuming $\tau_s = \tau_{corr,i}$, $J_{0,i}$ is determined from the slope of a linear fit of $\tau_{corr,i}(\Delta n)$ using eq. 3.37.

II) The contribution of SRH recombination is approximated by averaging $\tau_{SRH,i}^{-1}(\Delta n) = \tau_{corr,i}^{-1}(\Delta n) - \tau_{s,i}^{-1}(\Delta n, J_{0,i})$ over the fitted region with $\tau_{s,i}$ being calculated from eq. 3.37 using the $J_{0,i}$ value from step I).

III) τ_{corr} is refined using $\tau_{SRH,i}^{-1}$ from step II) via $\tau_{corr,i+1}^{-1} = \tau_{corr,i}^{-1} - \tau_{SRH,i}^{-1}$ and applied as input for step I).

This iteration procedure converges to a final J_0 value. Due to the consideration of SRH recombination in the bulk, this method enables J_0 measurements not only on FZ but also on Cz substrates.

For dopant diffused regions as applied in homojunction solar cells, the emitter saturation current density J_{0e} is the quantity measured by PCD and typically used to quantify the recombination current near the surface. The authors in [8] argue that PCD measures a similar saturation current density near the surface J_{0s} also for non-diffused surfaces. In the context of poly-Si/SiO_x contacts the slight in-diffusion of dopants (Sec. 1.3.1) causes the PCD measured saturation current density to be a mixture of J_{0e} and J_{0s} while the exact interpretation is not clear yet. For the purpose of simplicity, throughout this thesis the quantity measured by PCD is referred to as the recombination current density into the selective contact J_c in line with the authors in [7] and in line with the definition of the selectivity in eq. 1.9.

Uncertainty Determination

As the uncertainty of the fit during J_c determination is assumed to be too small to represent an actual uncertainty, a constant relative uncertainty of 8% was chosen following the uncertainty determined within a round-robin experiment of PCD measurements [152].

3.6.2. Implied Open Circuit Voltage iV_{oc}

Besides the recombination current density, the implied open circuit voltage iV_{oc} is also commonly used to quantify the passivation quality of a test sample. Metallization of samples increases the total recombination current density and thus decreases the open circuit voltage V_{oc} according to eq. 1.2. As PCD measurements are performed before metallization, iV_{oc} can be seen as an upper limit for V_{oc} of a finalized solar cell. It is determined directly from Δn via

$$iV_{oc} = V_{th} \ln \left[\frac{\Delta n \left(\Delta n + N_{D/A} \right)}{n_i^2} \right] \tag{3.40}$$

with the dopant concentration in n/p-type substrate $N_{D/A}$ and the intrinsic carrier concentration n_i at 25°C. As the excess charge carrier density Δn is a function of the incoming photon flux density, iV_{oc} is specified as the value measured at one sun irradiance to ensure comparability. The determination of the point of one sun irradiation depends on the optical constant θ for the transient mode but is

independent of θ for the QSS mode [157]. In order to avoid uncertainties due to a bad choice of θ, iV_{oc} was measured in QSS mode throughout this thesis. In contrast to J_c, for iV_{oc} no corrections for recombination mechanisms were performed so that a J_c value calculated from a measured iV_{oc} value via the one-diode model (eq. 1.2)

$$J_c = J_{ph,typ}\, \theta\, e^{-\frac{iV_{oc}}{V_{th}}} \tag{3.41}$$

with the photogenerated current density $J_{ph,typ}\, \theta$ as an upper limit for the short circuit current will most likely yield a larger value than a directly measured and corrected J_c as described above.

Uncertainty Determination

For the implied open circuit voltage it was assumed that the largest uncertainty arises from the determination of the Δn value corresponding to one sun irradiance. Thus, for several samples the variation of iV_{oc} within the range of three data points around one sun was averaged and a value of 4 mV was found which was consequently used as absolute uncertainty.

3.6.3. Resistivity ρ_{PCD}

Besides the passivation quality, PCD can also be used to determine the resistivity of a surface layer by measuring the conductance in the dark C_{dark}. This measured conductance is composed of a contribution of both surface layers and of the substrate. For symmetrical test samples the contributions from the surface layers are equal and thus

$$C_{dark} = 2\, W\, \sigma_{layer} + W\, \sigma_{substrate} \tag{3.42}$$

with the conductivities σ for one layer and the substrate, respectively. If the substrate resistivity $\rho_{substrate}$ is known, e.g. from previous C_{dark} measurements without surface layers, the resistivity of one surface layer is obtained via

$$\rho_{PCD} = 2\, d \left(C_{dark} - \frac{W}{\rho_{substrate}} \right)^{-1} \tag{3.43}$$

with the layer thickness of one surface layer d. ρ_{PCD} of a poly-Si layer can be seen as a contribution to the contact resistance ρ_c of a poly-Si/SiO_x contact according to eq. 1.7. This is also the case for the HE measured resistivity ρ_{HE}. In order to compare this resistivity of two independent characterization methods, it should be stated that ρ_{PCD} is most likely related to an average value over all three dimensions while ρ_{HE} is rather a measure for the lateral conductivity.

Uncertainty Determination

The uncertainty of ρ_{PCD} was determined by a Gaussian uncertainty propagation of eq. 3.43 with the uncertainties of the layer thickness d according to Sec. 3.4.1 and the uncertainty of the wafer thickness W roughly chosen to be 5 µm. The uncertainty of the substrate resistivity $\rho_{substrate}$ was estimated to 0.01 Ωcm based on the standard deviation of three reference samples without a deposited layer after SPC. The uncertainty of C_{dark} was approximated by a standard deviation, if available, or otherwise by a relative uncertainty of 5% according to [152].

CHAPTER 4

As-Deposited Layers

The process flow described in Chapter 2 and applied throughout this thesis includes the deposition of initially amorphous layers which are subsequently crystallized during junction formation. Hence, the structure of the as-deposited layers is expected to influence the properties of the resulting poly-Si layer. In this chapter, PECVD deposition parameters are utilized to control for the microstructure of the as-deposited layers in terms of a more efficient SPC, avoidance of blistering and tuning of the optical band gap (Sec. 4.1). Influences of the dopant concentration on interface and layer properties are subsequently discussed (Sec. 4.2) before the incorporation of light elements and its effects on the microstructure and optical properties in light of blister avoidance are presented (Sec. 4.3). All uncertainties were determined according to the sections in Chapter 3 and a sum of squares was calculated with the standard deviation, if available.

4.1. Adjustment of PECVD Deposition Parameters

ABSTRACT. *Increasing R_{B2H6} during PECVD deposition of (p) nc-Si linearly decreased the crystallinity down to the pure amorphous phase for $R_{B2H6} > 1.5\%$. The disorder of PECVD deposited (i) a-Si:H as well as the hydrogen concentration continuously decreased with increasing deposition temperatures. A minimum of the optical band gap evolved at an intermediate deposition temperature of $T_{set} = 250°C$, which is rather described by the silicon monohydride bond density than by the disorder or hydrogen concentration as suggested in the literature.*

For the variation of PECVD deposition parameters, two approaches relevant for poly-Si/SiO_x contact formation were chosen and are described in this section. First, the direct deposition of (p) nc-Si:H for controlling the final grain size and for avoiding blistering during SPC is discussed (Sec. 4.1.1). Second, a variation of the deposition temperature T_{set} is described in order to control the hydrogen concentration and microstructure of (i) a-Si:H layers in relation to blistering during SPC. The deposition temperature was additionally utilized for tuning of the optical band gap (Sec. 4.1.2). The results belonging to the deposition temperature variation were already published in [118].

4.1.1. More Efficient SPC by nc-Si Deposition

In Sec. 2.4.1 SPC was described via the JMAK model consisting of a nucleation and growth phase with the nucleation rate determining the final grain size. Small crystallites in as-deposited nc-Si:H layers might act as nucleation centers during SPC and hence it should be possible to control the final grain size by a variation of the as-deposited layer structure. Furthermore, as will be shown in Sec. 5.1.1, blistering during SPC is intensified with higher boron concentrations in (p) a-Si:H and one could expect less blistering due to the additional crystalline phase in as-deposited (p) nc-Si:H layers. As described in Sec. 2.3.1, such nc-Si growth is promoted by a large gas flow ratio R_{H2} which

was already demonstrated for (i) nc-Si in Sec. 3.3. However, B_2H_6 addition to the PECVD plasma was observed to suppress nc-Si growth [158]. Based on this the question arises if nc-Si growth and a sufficient boron concentration for poly-Si/SiO_xcontact formation can be achieved at the same time.

In order to answer this question, PECVD (p) a-Si:H layers were deposited[34] on FS substrates with a large hydrogen gas flow ratio of $R_{H2} = 99\%$ and a diborane addition in the range of $R_{B2H6} = 0-1.5\%$. The RS measured spectra and the corresponding crystallinities χ_c are shown in Fig. 4.1. An approximately linear relation between R_{B2H6} and χ_c was observed while the crystallinity for $R_{B2H6} = 1.5\%$ yields a negligible value of $\chi_c = 2.8\%$. In the corresponding RS spectrum in Fig. 4.1 a) a crystalline contribution near 521 cm^{-1} is barely visible so that this layer may also be seen as fully amorphous. Consequently, the corresponding relative uncertainty was assumed to be 100% (Fig. 4.1 b).

For as-deposited nc-Si layers typically the crystallite diameter d_c is determined and thus shown in Fig. 4.1 b) with values around $d_c \approx 5$ nm. For the layer deposited at $R_{B2H6} = 0\%$ no shift of the peak corresponding to the crystalline phase was observed. The crystallite sizes for the layer deposited at $R_{B2H6} = 1.5\%$ seems to be not reliable as the barely visible crystalline phase in Fig. 4.1 a) resulted in a very small peak whose position is unlikely to be dominated by the underlying quantum confinement effect. Considering these two findings, no statement about a trend in d_c for a variation of R_{B2H6} can be given.

For the layer deposited at $R_{B2H6} = 0.6\%$ with an acceptable crystallinity of $\chi_c \approx 20\%$, the boron atomic density was roughly estimated by GD-OES. The measured boron signal was just $\sim 14\%$ above the dark current signals mean value (standard deviation of $\sim 2.5\%$). Even under the assumption that this signal is not a measurement artifact, a rough upper limit for the boron concentration can be derived from the GD-OES resolution of $\sim 10^{18}$ cm^{-3} (Sec. 3.1). As atomic densities in the range of $\sim 10^{19}$ cm^{-3} are required for functioning poly-Si/SiO_x contacts [19, 21], the approach of a direct (p) nc-Si deposition for poly-Si/SiO_x contacts was omitted.

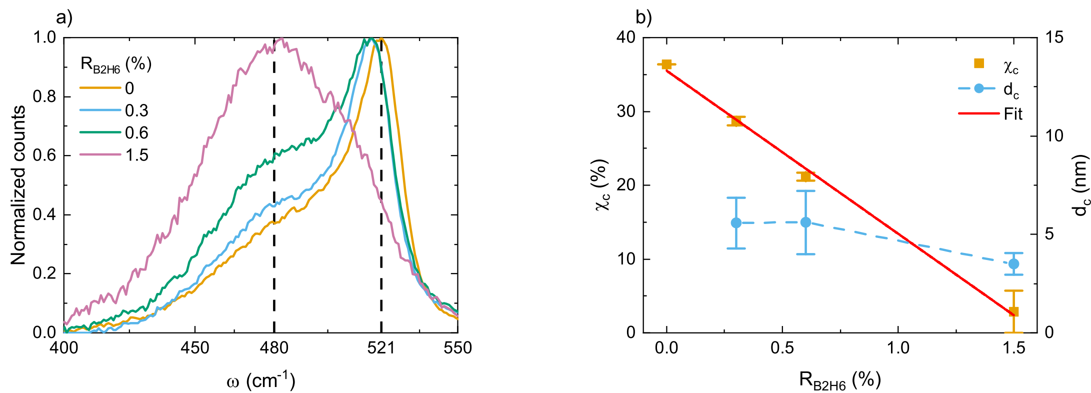

FIGURE 4.1. a) Normalized RS spectra of PECVD as-deposited (p) a/nc-Si:H layers under variation of R_{B2H6} during PECVD deposition. The vertical dashed lines mark the main peak positions of the amorphous phase at $\omega_{a-Si} = 480$ cm^{-1} and the crystalline phase at $\omega_{c-Si} = 521$ cm^{-1}. b) RS determined crystallinity χ_c and crystallite diameter d_c for the same layers as shown in a) as function of R_{B2H6}. The solid red line is a weighted linear fit and the dashed line a guide for the eye.

[34] PECVD deposition parameters: $P = 20$ W, $p = 400$ mTorr, $T_{set} = 225$°C, $R_{H2} = 99\%$, $R_{B2H6} = 0-1.5\%$.

4.1.2. Microstructure and Hydrogen Concentration in Relation to Blistering

During SPC in the context of PECVD deposited poly-Si/SiO_x contacts blistering of the a-Si:H layer may occur, which is commonly related to hydrogen trapped in voids within the layer (Sec. 2.4.2). Both the hydrogen content and the microstructure are strongly influenced by the deposition temperature and hence it should be possible to utilize T_{set} to control blistering. Therefore, it is useful to investigate the influence of the deposition temperature on the microstructure of the as-deposited layers. In this section, the results of a deposition temperature variation are presented in the range of $T_{set} = 100-400°C$ for PECVD deposited[35] (i) a-Si:H layers on FZ substrates without an interfacial oxide and deposited immediately after a short HF etching to remove the native oxide. These results have been published before in [118].

FT-IR analysis clearly revealed for higher deposition temperatures T_{set} a decrease in hydrogen concentration c_H, validated by NRA measurements on similar samples (Fig. 4.2 a), and a simultaneous decrease in structural disorder, expressed by the disorder ratios R^* and Q^* (Fig. 4.2 b). Both effects were expected and reported before [159, 160]. The gap between the c_H determination methods and the corresponding larger uncertainties are rather attributed to a systematical deviation from the real concentrations in the FT-IR analysis as the nuclear reaction based NRA measurements do not depend on the detailed structure of the material, which significantly changes under variation of the deposition temperature. Blistering during SPC is less pronounced for lower c_H (Sec. 2.4.2) and was observed to be stronger for lower microstructure factors R^* [161]. Based on this both trends in Fig. 4.2 show competing effects on blistering which will be discussed in more detail later in Sec. 5.1.2.

In order to gain more information about the relation between these trends and the blistering issue, according to [118, 162], a combination of the FT-IR, SE and NRA measurements allows for the determination of the microvoid density

$$N_{void} = \frac{N_{Si-H2}^3 \rho_{Si}^2}{4\pi \rho_S^3 \left[3\left(\rho_{Si} - \rho_{a-Si:H}\right) + 3\, m_H \left(N_{Si-H} + N_{Si-H2}\right) - m_{Si}\, N_{Si-H}\right]^2}, \tag{4.1}$$

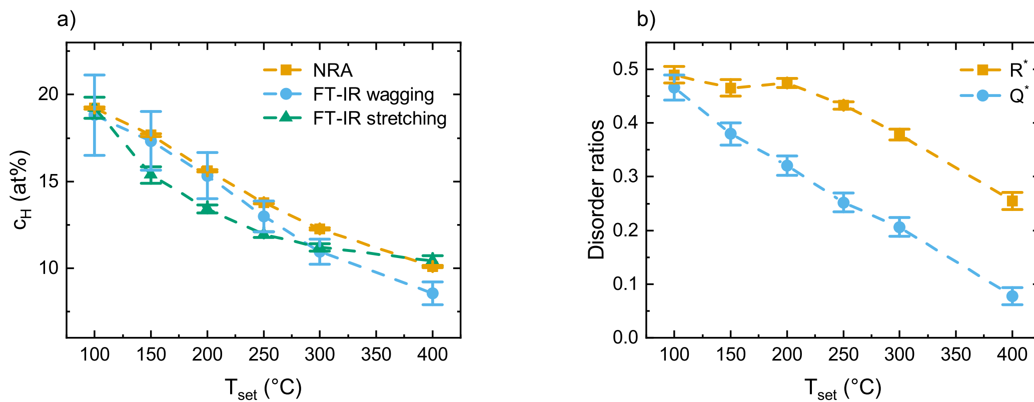

FIGURE 4.2. a) NRA and FT-IR determined hydrogen concentrations c_H and b) FT-IR determined disorder ratios R^* and Q^* of (i) a-Si:H layers as functions of the PECVD deposition temperature T_{set}. Dashed lines are a guide for the eye.

[35]PECVD deposition parameters: $P = 10$ W, $p = 1000$ mTorr, $T_{set} = 100-400°C$, $R_{H2} = 50\%$, $R_{Ar} = 95\%$, $t = 1500$ s and a previous ignition step with $P = 20$ W for $t = 10$ s.

the average microvoid diameter

$$D_{void} = \frac{2\,\rho_S\,[3\,(\rho_{Si} - \rho_{a-Si:H}) + 3\,m_H\,(N_{Si-H} + N_{Si-H2}) - m_{Si}\,N_{Si-H}]}{N_{Si-H2}\,\rho_{Si}} \tag{4.2}$$

and the volume fraction of microvoids

$$c_{void} = V_{void}\,N_{void} = \frac{4}{3}\pi\left(\frac{D_{void}}{2}\right)^2 N_{void} \tag{4.3}$$

with the bonded hydrogen density on the inner surfaces of a microvoid $\rho_S = 7.83 \cdot 10^{14}$ cm^{-2} and the crystalline silicon mass density $\rho_{Si} = 2.33$ g/cm^3. The a-Si:H mass density $\rho_{a-Si:H}\,(n_\infty, c_H)$ was determined according to [163] utilizing the refractive index n_∞ for $\lambda \rightarrow \infty$ from SE measurements under 70°, 75° and 80° incidence angles in a spectral range of $240 - 2000$ nm and the hydrogen concentration c_H from the NRA measurements. N_{Si-H} and N_{Si-H2} are the FT-IR determined bond densities corresponding to silicon monohydride and dihydride bonds, respectively, (Sec. 3.2)[36] and $m_{Si/H}$ are the atomic masses of a single atom.

In Fig. 4.3 a)−c) these three quantities are plotted as function of the deposition temperature T_{set}. With higher T_{set} the microvoid density N_{void} decreases while the microvoid diameter D_{void} increases

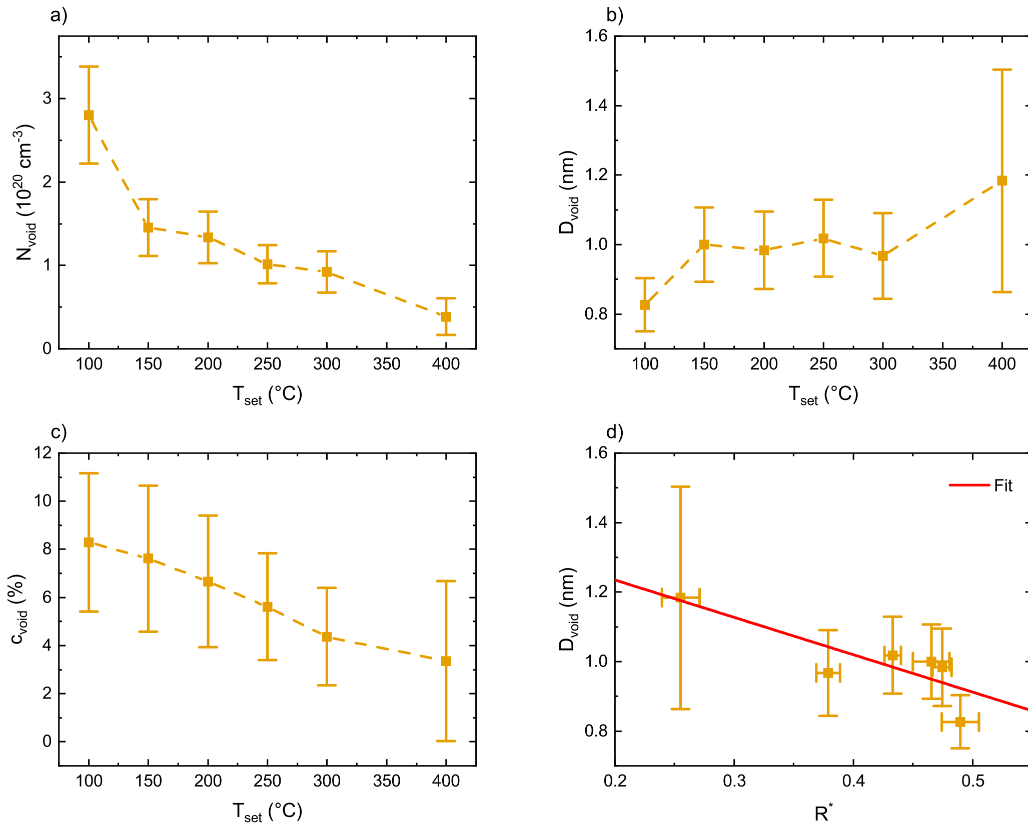

FIGURE 4.3. a) Microvoid density N_{void}, b) microvoid diameter D_{void} and c) volume fraction of microvoids c_{void} according to eq. 4.2−4.3 of (i) a-Si:H layers as functions of the PECVD deposition temperature T_{set}. Dashed lines are a guide for the eye. d) Microvoid diameter D_{void} as function of the microstructure factor R^* of the same layers. Solid red line is a weighted linear fit.

[36] For the purpose of clarity, the indices Si-H/Si-H2 were chosen instead of the corresponding literature peak values of 2000 cm^{-1} and 2080 cm^{-1} (Sec. 3.4).

at the same time. These unexpected oppositional trends are resolved by the combination of both quantities to the volume fraction of microvoids c_{void} which reveals a decreasing trend as it was also expected from the decreasing disorder concluded from the disorder ratios (Fig. 4.2 b).

The combination of lower c_H and lower c_{void} would allow the conclusion of a less pronounced blistering during SPC for layers deposited at higher temperatures. However, in the literature it is reported that blistering is even promoted by a lower microstructure factor R^* and hence reduced disorder [161]. One explanation for these observations could be the larger void diameter D_{void} for lower R^* values (Fig. 4.3 d) leading to larger cavities for hydrogen accumulation and subsequent blistering. Yet, it seems to be more likely that blistering is caused by large voids at the interface as described in Sec. 2.4.2.

4.1.3. Tuning of the Optical Band Gap for Reduced Parasitic Absorption

As mentioned before in Sec. 1.3, parasitic absorption may be reduced and selectivity may be enhanced by a wider band gap. The just discussed structural changes under variation of the deposition temperature T_{set} are expected to influence E_{gap} of the as-deposited layers and thus also of the crystallized poly-Si layers. Therefore, the influence of T_{set} on E_{gap} is discussed in the following with the aim to tune the optical band gap.

In the literature one line of publications argues that the structural disorder predominantly determines E_{gap} (disorder increase, E_{gap} decrease) [164, 165] whereas another line argues for the hydrogen concentration (c_H increase, E_{gap} increase) [166, 167]. Up to now this discussion is not fully resolved, probably due to the interdependency of both properties [168, 169]. Therefore, some authors concluded that rather the combination of both quantities determines E_{gap} [170, 171].

In Fig.4.4 a minimum of E_{gap} around $T_{set} = 250°C$ is visible which is not in line with previous reports of monotonic relations for both deposition and post-deposition anneal temperature variations [160, 164, 166, 172]. An important difference between those anneals is that an increase of temperature during post-deposition anneals decreases the hydrogen concentration and increases the structural disorder [57] while the increase of the temperature during deposition decreases the hydrogen concentration but at the same time also decreases the disorder (Fig. 4.2 / 4.3). Hence, in the case of a

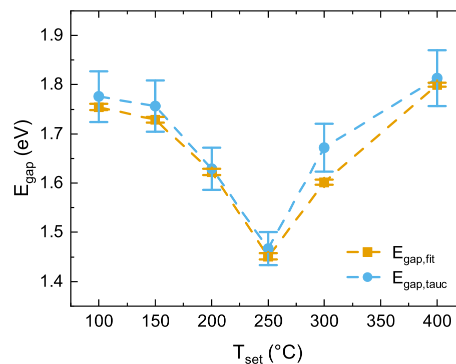

FIGURE 4.4. Optical band gaps of (i) a-Si:H layers as function of the PECVD deposition temperature T_{set} determined by the SE fit parameter ($E_{gap,fit}$) and the Tauc-method ($E_{gap,tauc}$). Dashed lines are a guide for the eye.

deposition temperature variation the hydrogen concentration and the structural disorder are assumed to influence E_{gap} in different directions, which could explain the observed local minimum of E_{gap}.

The hypothesis that neither the hydrogen concentration nor the structural disorder has an isolated influence on E_{gap} is supported by the presence of similar local minima of E_{gap} as function of c_H and c_{void} (Fig. 4.5 a, b). However, the only investigated quantity showing a similar local minimum for increasing T_{set} is the silicon monohydride bond density N_{Si-H} (Fig. 4.5 c). In Fig. 4.5 d) E_{gap} is plotted as function of this monohydride bond density and the resulting monotonic increasing relation was fitted using the following equation

$$E_{gap} = E_{max} - a\, e^{-b\, N_{Si-H}} \tag{4.4}$$

with standard fit parameters a, b and an asymptotic maximum optical band gap value E_{max} for large N_{Si-H}. As this fit only has three degrees of freedom it should be seen as rough estimate. Nevertheless, the hypothesis included in eq. 4.4 of an asymptotic maximum band gap value $E_{max} \approx 1.78$ eV for large monohydride bond densities N_{Si-H} can be utilized to explain previously observed constant E_{gap} values from both experimental [160] and simulation [171] studies. In both cases constant E_{gap}

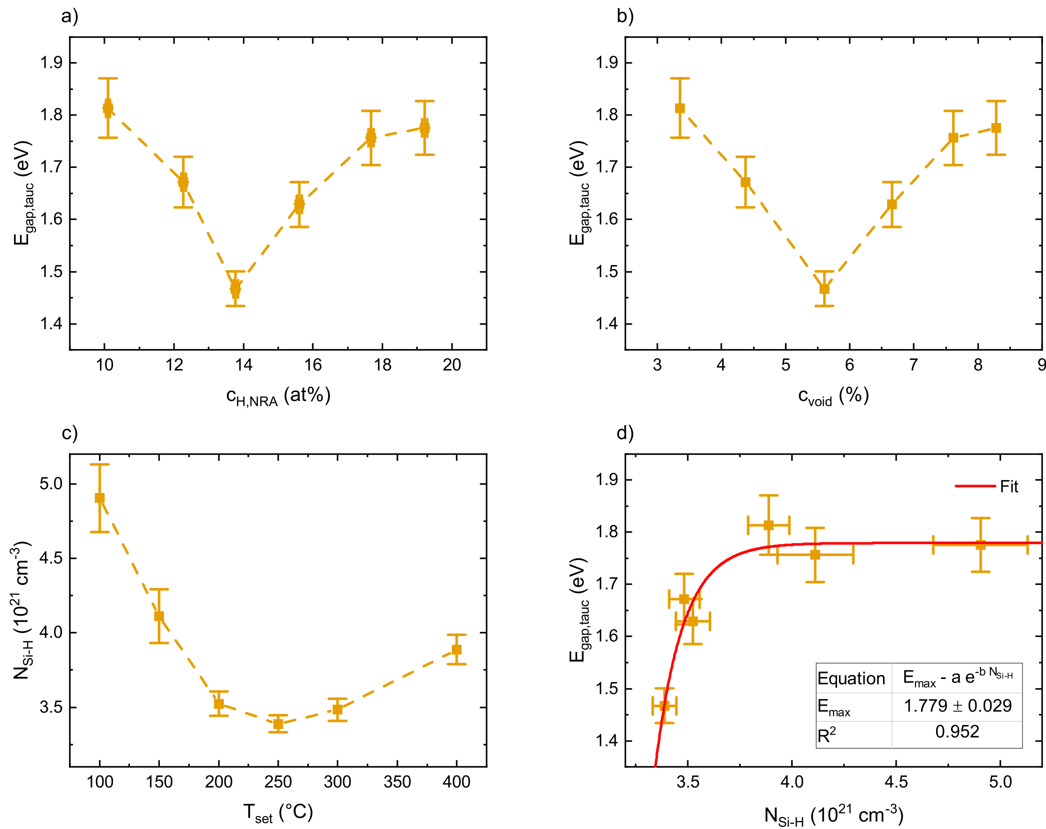

FIGURE 4.5. SE determined optical band gap $E_{gap,tauc}$ of PECVD deposited (i) a-Si:H layers as function of a) the NRA determined hydrogen concentration $c_{H,NRA}$ and b) the volume fraction of microvoids c_{void} according to eq. 4.3. c) FT-IR determined monohydride bond density N_{Si-H} as function of the deposition temperature T_{set}. d) Optical band gab $E_{gap,tauc}$ as function of the monohydride bond density N_{Si-H}. The solid red line is an exponential fit according to eq. 4.4 with the resulting fit parameter as depicted in the inset table. Dashed lines are a guide for the eye.

values were reported for large hydrogen concentrations and hence large monohydride bond densities in line with eq. 4.4.

4.2. Variation of the Dopant Concentration

ABSTRACT. *For increasing R_{B2H6} the disorder and the optical band gap in PECVD deposited (p) a-Si:H layers sightly decreased and a less dense region near the interfacial oxide was observed, which densifies with increasing R_{B2H6}. Peaks in the GD-OES boron signal shortly before the signal of the interfacial oxide were observed but could not definitely be related to these less dense regions.*

As stated in Sec. 1.3, the dopant concentration of the poly-Si layer has to be adjusted carefully for a functioning poly-Si/SiO$_x$ contact. In the case of in-situ doping, the boron concentration is determined by the diborane gas flow ratio R_{B2H6} during PECVD (p) a-Si:H deposition[37], which was varied in the range of $R_{B2H6} = 0.6-2.3\%$. Depth profiles of both the boron concentration and the refractive index are discussed in Sec. 2.3.3 with a focus on the interface properties, which might influence both the blister sensitivity during SPC and the passivation quality of the resulting poly-Si layers. Subsequently, layer properties are considered in Sec. 2.3.3 in terms of blister related microstructure and tuning of the optical band gap. Since phosphorus doping was achieved only during SPC by POCl$_3$-diffusion, a dopant variation of amorphous as-deposited layers was only possible for boron doping.

4.2.1. Influence of the Diborane Gas Flow Ratio on Interface Properties

The solid lines in the GD-OES profiles in Fig. 4.6 a) correspond to the boron signal and reveal a clear increase of the boron concentration for higher R_{B2H6}. The dashed lines correspond to the oxygen signal and the interfacial oxides appear as similar peaks in all layers as expected. In the boron profiles a pile-up can be seen close to but shortly before the interfacial oxides peak positions which is evident

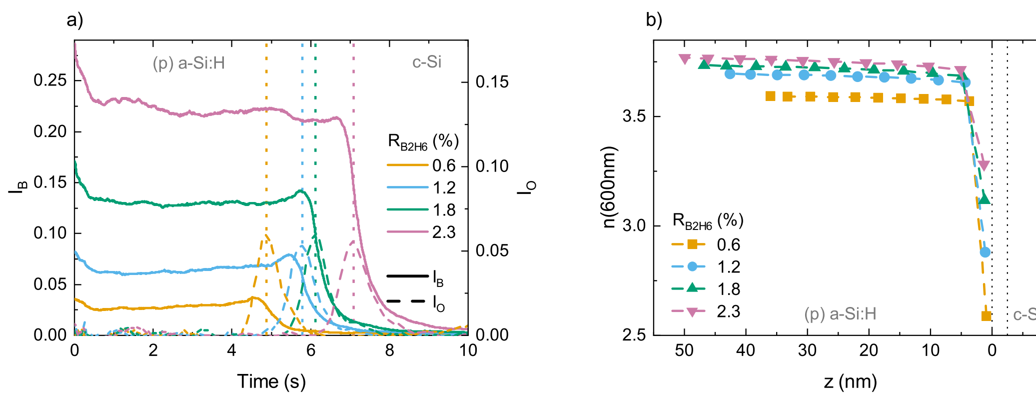

FIGURE 4.6. a) GD-OES measured raw depth profiles $I_B(s)$ (left axis, solid lines) and $I_O(s)$ (right axis, dashed lines). Vertical dotted lines mark the positions of the oxygen peaks originating from the interfacial oxides.b) SE determined refractive index n at a wavelength of $\lambda = 600$ nm as function of the position in the layer parallel to the surface normal z with $z = 0$ nm being the position of the (p) a-Si:H/SiO$_x$ interface for several R_{B2H6} during PECVD deposition. Vertical dotted lines mark the rough range of the interfacial oxide.

[37]PECVD deposition parameters: $P = 20$ W, $p = 400$ mTorr, $T_{set} = 100°$C, $R_{H2} = 99\%$, $R_{B2H6} = 0.6-2.3\%$, $t = 1800$ s.

from the vertical dotted lines. Such an increased interface signal could originate from a non steady-state growth during the first seconds of the deposition. A larger boron concentration at the interface may in turn lead to poor adhesion between the layer and the interfacial oxide and thereby increase the blister sensitivity. Furthermore, it would intensify detrimental boron in-diffusion during SPC degrading the passivation quality of the resulting poly-Si/SiO_x contact.

Contrary, the boron pile-up could also be a result of an increased sputter rate during GD-OES measurement. This conclusion was drawn before from secondary ion mass spectroscopy (SIMS) measurements of (p) poly-Si/SiO_x contacts which rely on a sputter process similar to the one of GD-OES [20]. However, an increased boron concentration within the interfacial oxide was also reported before from laser-assisted 3D atom probe measurements which are not influenced by a sputter process. This point of view supports the interpretation of the boron peak as real concentration pile-up [173]. Since the investigated layers here are in the as-deposited state and segregation into the interfacial oxide might occur only later in the process flow by thermal activation during junction formation, both references have to be taken with care. Thus, no definite statement regarding the origin of the boron peak can be given at this point. The authors in [20] interpreted the increased boron signal near the surface also as a sputter rate related measurement artifact. Similar GD-OES profiles of crystallized (p) poly-Si layers will be discussed later in Sec. 5.2.

SE measurements were recorded in the spectral range of $300 - 1500$ nm and fitted with the model described in Sec. 3.4.1. Additionally, the a-Si layer was divided into eleven sublayers with equal thicknesses but separate refractive indices following the approach in [174]. Thereby the refractive index as function of the position in the layer parallel to the surface normal z with $z = 0$ nm being the position of the interfacial oxide was modeled by an exponential function with two additional fit parameters.

The resulting refractive index profiles $n(z)$ at a wavelength of $\lambda = 600$ nm are depicted in Fig. 4.6 b). A nearly constant refractive index throughout the whole layer was observed except for a reduced value in the first sublayer at the interface to the substrate. Based on this observation a distinction is made in the following between the *bulk* and *interfacial* refractive index. It can be seen that the bulk refractive index increases with R_{B2H6} and hence with the boron concentration in the layer which was also reported before [175].

In general, the lower value of the interfacial refractive index compared to the bulk refractive index may be attributed to a less dense microstructure in the first nanometers of the layer [162], which could be a result of a non steady-state growth during deposition. Such a less dense microstructure would support the interpretation of the boron peak in the GD-OES profiles (Fig. 4.6 a) as an artifact due to an increased sputter rate and also support the assumption of a poor adhesion between the layer and the interfacial oxide. For higher R_{B2H6} the interfacial refractive index increases faster than the bulk refractive index does. This could be explained by a higher boron concentration near the interface raising the interfacial refractive index similar to the bulk refractive index. However, this suggestion would support the interpretation of the boron peak in the GD-OES profiles as a real concentration pile-up.

4.2.2. Influence of the Diborane Gas Flow Ratio on Layer Properties

FT-IR measurements of the (p) a-Si:H layers revealed a clear decrease in disorder with increasing R_{B2H6} as is evident from both decreasing disorder ratios R^* and Q^* in Fig. 4.7 a). A similar decreasing microstructure factor for higher R_{B2H6} was reported before [158]. Following [161], intensified blistering could be expected for higher boron concentrations due to the lower R^* values. This notion will be discussed in more detail in Sec. 5.1.1.

In contrast to the more compact microstructure deduced from the lower disorder ratios and as stated in Sec. 2.3.3, doping of a-Si:H layers increases the defect density by creating dangling bonds and thus one would expect an increased disorder. One hypothesis to explain this discrepancy could be that most of the induced dangling bonds belong to boron atoms and thus hydrogen saturated defects would appear as separate B-H absorption peaks in the FT-IR spectrum. In particular, the disorder ratios do not consider dangling bonds from non-silicon atoms and therefore describe the disorder of the silicon network only. However, absorption peaks belonging to B-H bonds were not found in the recorded spectra.

Fig. 4.7 b) shows the optical band gap obtained from the fit parameter during SE modeling. A clear reduction of E_{gap} is visible and is in line with previous publications which explain this effect either by a larger general disorder [175] similar to the discussion about (i) a-Si:H layers in Sec. 4.1.3 or by boron induced states within the band gap but close to the edges [176]. On the one hand, the FT-IR results presented in the previous section suggest a decrease in disorder and hence the former explanation should be excluded. But on the other hand, as also discussed above, the disorder ratios only describe the disorder of the silicon network. An increased disorder due to boron induced defect states could still account for the decrease in E_{gap}. In fact, this would be in line with the second explanation.

For poly-Si the higher doping would shift the Fermi level closer to the band edge and induce a larger band offset. Assuming that the observation of an E_{gap} reduction with higher doping of (p) a-Si:H layers can be transferred to (p) poly-Si layers after SPC, such a band gap narrowing would reduce the band offset and as such compete with the effect of the Fermi level shift. Furthermore, a reduced

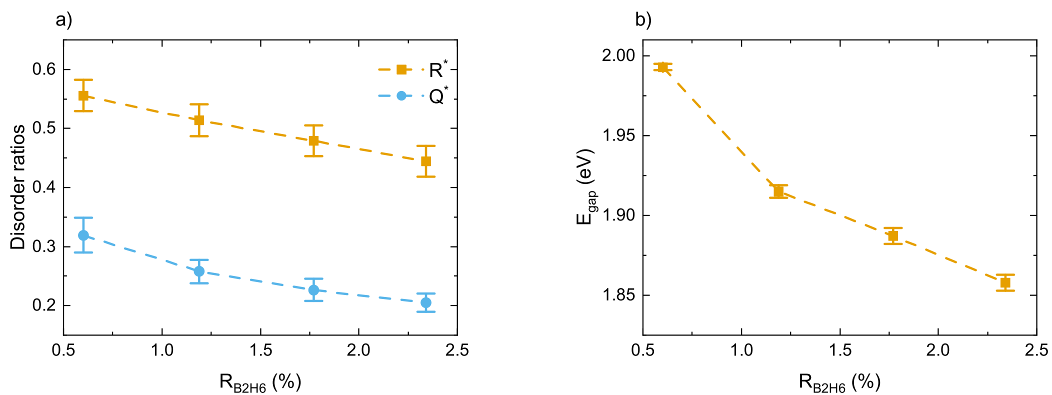

FIGURE 4.7. a) FT-IR determined disorder ratios R^* and Q^* of (p) a-Si:H layers as function of R_{B2H6} during PECVD deposition. b) Optical band gap E_{gap} determined from the fit parameter of the SE model as function of R_{B2H6} for the same layers as shown in a). Dashed lines are a guide for the eye.

band gap would also be detrimental for the desired reduction of the parasitic absorption within the poly-Si layer. Thus, tuning of E_{gap} towards a preferably large band gap favors low R_{B2H6} as was also concluded above with regard to possible blistering.

4.3. Incorporation of Light Elements

ABSTRACT. *With increasing R_{N2O} and R_{CO2} the normalized bond densities of the corresponding light elements as well as the structural disorder continuously increased while the bulk as well as the interfacial refractive index were reduced at the same time. A deviation of this trend and an increased interstitial oxygen concentration as well as an increased microstructure factor at a gas flow ratio of $R_{CO2} = 7\%$ revealed a relation between those quantities.*

The incorporation of light elements in a poly-Si/SiO_x contact is expected to reduce the parasitic absorption. In order to control the properties of the poly-Si layer it is useful to investigate the influence of the corresponding gas flow ratios R_X on the as-deposited layers similar to the investigation in the previous section regarding R_{B2H6}. a-SiO_x:H and a-SiO_xN_y:H layers with a thickness > 100 nm were PECVD deposited[38] on 2 Ωcm FZ substrates without an interfacial oxide immediately after a short dip in HF to remove the native oxide with a variation range of $R_{CO2} = 4.8 - 9.1\%$ and $R_{N2O} = 4.8 - 16.6\%$. The layers were analyzed in terms of their composition and microstructure with regard to avoid blistering during SPC (Sec. 4.3.1) as well as in terms of optical properties for a reduction of the optical losses (Sec. 4.3.2). The lower variation range for CO_2 was chosen as this molecule provides twice as much oxygen atoms as N_2O does. All results presented in this section were already published in [65] but were partly re-evaluated for this thesis.

4.3.1. Larger Disorder to Avoid Blistering

As stated in Sec. 2.3.1, a linear relationship between the concentration of light elements in the resulting layer and the gas flow ratio R_X was observed. However, the incorporation of carbon for increasing R_{CO2} did not result in an observable FT-IR absorption peak. Utilizing the data in [177] allows for a rough estimate of a carbon concentration to $c_C \approx 1.4 \cdot 10^{-2}$ at% for $R_{CO2} = 9.1\%$. It is reasonable that for this low concentration no carbon signal was detected by FT-IR measurements on samples with layer thicknesses of less than 120 nm.

From the FT-IR absorption strengths bond densities N_x can be determined via eq. 3.14 which in turn yield the corresponding elemental concentrations by division of the atomic density of crystalline silicon $n_{Si} = 5 \cdot 10^{22}$ cm^{-1}. The experimentally determined proportionality constants A_x in eq. 3.14 are typically taken from literature but are only valid for specific materials and deposition methods. The constants for silicon hydride bonds in pure a-Si:H are well-known. Unfortunately this is not the case for all bonds in a-SiO_x:H and a-SiO_xN_y:H, especially under the expected microstructure variations. To avoid misleading absolute concentration values from a bad choice of A_x, all bond densities N_x presented in the following are normalized to the bond density corresponding to the maximum gas flow ratio of either $R_{CO2} = 9.1\%$ or $R_{N2O} = 16.6\%$. Hereby the unknown proportionality constant A_x simply cancels out.

[38]PECVD deposition parameters: $P = 100$ W, $p = 450$ mTorr, $T_{set} = 175$°C, $R_{CO2} = 4.8 - 9.1\%$ or $R_{N2O} = 4.8 - 16.6\%$, $t = 150$ s.

The normalized bond densities for bonds according to Table 3.3 are presented in Fig. 4.8. For both gas flow ratio variations all normalized bond densities of oxygen bonded to two silicon atoms (Si-O-Si) increase linearly. This linear relationship suggests a constant ratio of the number of molecules present in the plasma to the incorporated light elements and corresponds to the linear element incorporation observed by GD-OES (Sec. 2.3.1). The same holds for the Si-N bonds with a similar linear relationship. In contrast, the normalized bond density of interstitial oxygen (O_i) shows a linear increase only for $R_{N2O} > 9\%$ and no clear trend at all for R_{CO2}.

Fig. 4.9 a) presents the microstructure factor R^*as function of the gas flow ratios R_X. From an initial microstructure factor for the pure a-Si:H reference layer of $R^* = 0.35$ it increases with both gas flow ratios up to a value of 0.72 for CO_2 and 0.94 for N_2O addition while it is always larger for CO_2 addition at equal R_X. As discussed before, this increase of R^* can be interpreted as an increase in structural disorder. Under variation of the deposition temperature of (i) a-Si:H layers the maximum absolute variation in R^* was 0.2 and under variation of R_{B2H6} it was 0.1. The variation of R^* for the

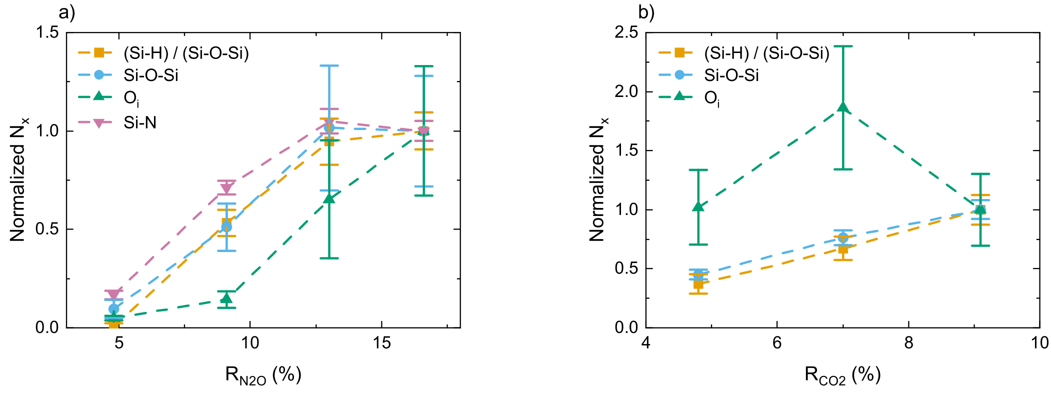

FIGURE 4.8. FT-IR determined bond densities N_x of bonds according to Table 3.3 normalized to the value of the corresponding maximum gas flow ratio R_X during PECVD deposition for a) a-SiO_xN_y:H (X =N_2O and b) a-SiO_x:H (X =CO_2) layers. Dashed lines are a guide for the eye.

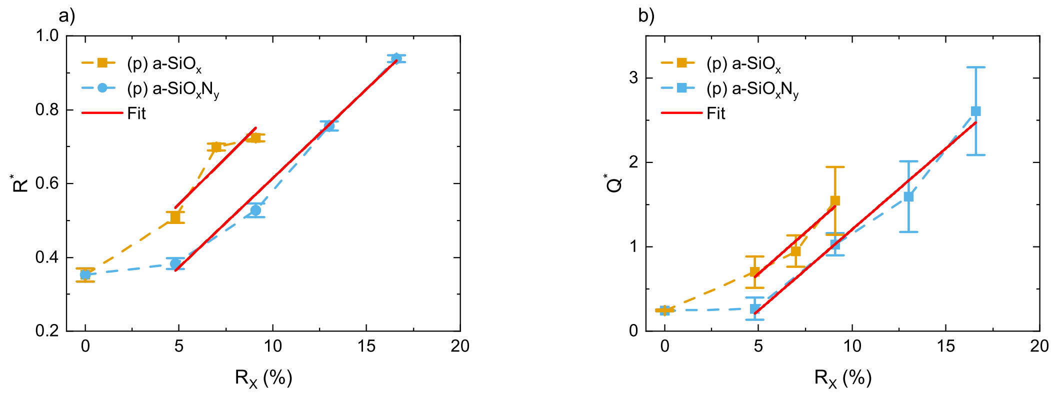

FIGURE 4.9. FT-IR determined disorder ratios a) R^* and b) Q^* for (p) poly-SiO_x and (p) poly-SiO_xN_y layers as function of the corresponding gas flow ratios R_X during PECVD deposition with X being either CO_2 or N_2O. The solid red lines are linear fits and the dashed lines a guide for the eye.

light elements incorporation is much stronger with 0.6. Following [161], the increase in R^* should be beneficial for the avoidance of blistering during SPC as will also be discussed later in Sec. 5.1.

Similarly to R^*, the ratio Q^* presented in Fig. 4.9 b) increases with the values for CO_2 addition being larger than for N_2O addition for equal R_X. The interpretation of high Q^* values as indicator for the presence of microvoids is in accordance with the large values of R^*. It should be noted that from the definitions in Sec. 3.2.1, R^* is limited to values between zero and one while Q^* could principally be any positive real number. In [109] it is stated that values $Q^* > 1$ occur in the presence of large hydrogen concentrations. This is in line with the rather low deposition temperature of $T_{set} = 175°C$ used here. The uncertainties in both quantities arise from the fit procedure of the absorption peaks while the larger uncertainties for Q^* are explained by a much weaker absorption of the corresponding bonds and thus larger relative uncertainty during the fit procedure.

Interestingly, for $R_X \gtrsim 5\%$ a similar slope evolved in the trends for both N_2O and CO_2 addition in both disorder ratios. Considering that the shared element of both gases is oxygen, one could speculate that this slope is rather connected to oxygen incorporation in the amorphous matrix and that nitrogen or carbon incorporation plays a minor role regarding the structural disorder. Furthermore, the increase in both disorder ratios did not start before $R_{N2O} \gtrsim 5\%$, leading to the shift of the linear relation to larger gas flow ratios. A similar shift was observed for the normalized bond densities of the interstitial oxygen for $R_{N2O} \lesssim 9\%$ (Fig. 4.8 a). Likewise, the pronounced maximum of the normalized bond density of interstitial oxygen arose at a gas flux density of $R_{CO2} = 7\%$ which also led to a similar maximum in the microstructure factor visible in Fig. 4.8 a) as deviation from the fit line. These observations suggest a linear relationship between the degree of disorder and the density of interstitial oxygen which could be explained with a strongly disordered material offering more sites for interstitial oxygen incorporation. This larger disorder in turn is expected to suppress blistering during SPC.

4.3.2. Tuning of the Optical Properties for Reduced Optical Losses

As it was the case for the variation of R_{B2H6} above, these just described structural differences are assumed to also influence the optical properties of the layers. For the incorporation of light elements this influence is expected to be even stronger and eventually beneficial with regards to a reduced parasitic absorption in a poly-Si/SiO_x contact.

The standard SE model for as-deposited layers described in Sec. 3.4.1 was not able to reproduce the experimental data. The reason for this failure are most likely the large nitrogen and oxygen contents of up to ~ 20 at% and ~ 5 at%, respectively, as obtained by an adjusted multi-matrix calibration of GD-OES measurements (Sec. 3.1.1). Hence, a slightly adapted model was developed for measurements in a different spectral range of $500 - 2000$ nm wherein the optical constants of the a-SiO_x:H and a-SiO_xN_y:H layer were modeled by a Cauchy-relationship [133]. Furthermore, the layers were divided into 21 sublayers similarly to the procedure described in Sec. 4.2.2 above but with more sublayers due to the larger layer thickness.

The resulting refractive index profiles $n(z)$ at a wavelength of $\lambda = 600$ nm are depicted in Fig. 4.10. For the bulk refractive indices a reduction with higher gas flow ratios R_X was observed except for $R_{CO2} = 7\%$. Such a reduction in the refractive index should be accompanied by the desired reduction of the parasitic absorption. As the bulk refractive indices of $n > 3$ are closer to the one of the a-Si:H

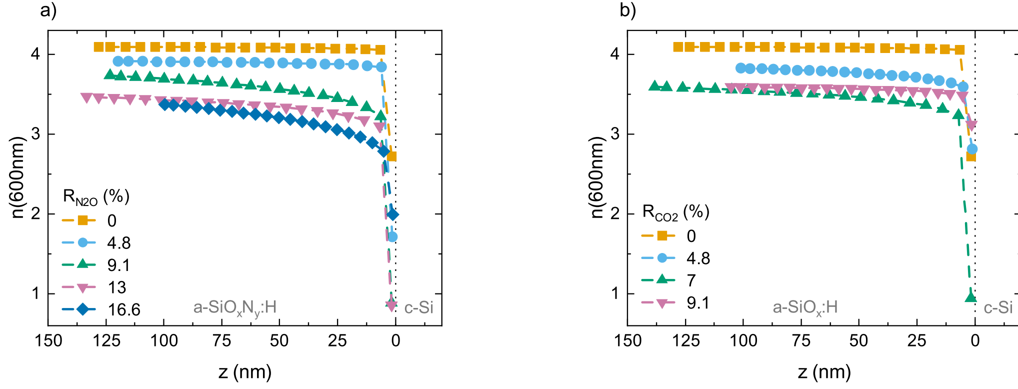

FIGURE 4.10. SE determined refractive index profiles $n(z)$ at a wavelength of $\lambda = 600$ nm as function of the position in the layer parallel to the surface normal z with $z = 0$ nm being the position of the interface to the c-Si substrate (vertical dotted line) for several R_X during PECVD deposition of a) a-SiO_xN_y:H (X =N_2O and b) a-SiO_x:H (X =CO_2) layers. Dashed lines are a guide for the eye.

reference layer than to literature values of $n_{Si3N4} \approx 2.0$ and $n_{SiO2} \approx 1.5$ at $\lambda = 600$ nm [178], the materials have to be considered as non-stoichiometric.

For large R_X no constant bulk refractive index evolved but rather continuously increases up to the layer surface. This might be a hint that during deposition steady-state growth was not reached. With regard to an application in a poly-Si/SiO_x contact, such an inhomogeneous bulk refractive index might be detrimental in terms of coupling of light into the c-Si substrate due to the large difference to the silicon refractive index at $\lambda = 600$ nm of $n_{Si} = 3.9$ [136]. However, an inverted profile with an increasing refractive index from the surface to the substrate could enhance the coupling of light by a rough index matching from the overlying SiN_x:H layer to the c-Si substrate [179].

Lastly, the bulk refractive index of the layer deposited with $R_{CO2} = 7\%$ is lower than for the layer deposited with $R_{CO2} = 9.1\%$, which is even more pronounced for the interfacial refractive index. As the latter layer also showed deviations from the overall trend in the FT-IR results that were discussed in the previous section, this observation supports the suggested relations between disorder, interstitial oxygen and the presence of the interfacial refractive index.

CHAPTER 5

Crystallized poly-Si Layers

In this chapter, the properties of the crystallized poly-Si layers are discussed, starting with a description of strategies for a reduction of blistering during SPC of PECVD deposited in-situ doped (p) poly-Si layers in Sec. 5.1. Afterwards, dependencies between the poly-Si layer composition and the solar cell efficiency are discussed as explored by varying the following three parameter groups, whereas each variation will be described in one section of this chapter:

I) Sec. 5.2: The dopant concentrations of either boron or phosphorus ($c_{B/P}$)

II) Sec. 5.3: The incorporation of light elements, either oxygen and nitrogen or carbon ($c_{O/N/C}$)

III) Sec. 5.4: The temperature and duration of the SPC (T_{SPC} / t_{SPC})

Fig. 5.1 summarizes all dependencies between these parameter groups I)−III) and the three parameters contact recombination current density J_c, contact resistance ρ_c and parasitic absorption current density J_{PA} as they were discussed throughout Chapter 1. These three parameters in turn influence the solar cell efficiency η which will be discussed in more detail in Chapter 6. It should be noted that Fig. 5.1 is a simplified overview with no claim of completeness. All expected dependencies depicted in Fig. 5.1 are described in the following.

I): For increasing dopant concentrations $c_{B/P}$ four effects are expected. For moderate dopant concentrations, ρ_c decreases and the increased band offset reduces J_c, both raising η. For high dopant concentrations detrimental strong in-diffusion increases J_c and FCA within the poly-Si raises J_{PA}, both diminishing η. Therefore, an optimization of the dopant concentrations is required and will be discussed in Sec. 5.2.

II): Incorporation of light elements, thus increasing $c_{O/N/C}$, widens the optical band gap E_{gap} and in turn decreases J_{PA} and by the larger band offset also J_c. In contrast, both J_{PA} and ρ_c increase due to a decreasing crystallinity χ_c. Both effects have opposing influences on η and so also an optimization of the concentration of light elements is required. Special attention has to be paid to the direct effect of $c_{O/N/C}$ on ρ_c as it decreases for oxygen and nitrogen but increases for carbon incorporation. ρ_c is also expected to increase for large oxygen and nitrogen concentrations and so the efficiency η is influenced in different ways depending on the specific material (arrow in both directions in Fig. 5.1). The investigations regarding incorporation of light elements are discussed in Sec. 5.3.

III): An increase of either the temperature T_{SPC} or the duration t_{SPC} of the SPC decreases J_{PA} and ρ_c by a higher crystallinity χ_c but increases J_c due to detrimental strong dopant in-diffusion which have opposing influences on η. Hence, also for the SPC parameter group an optimization is required and will be discussed in Sec. 5.4.

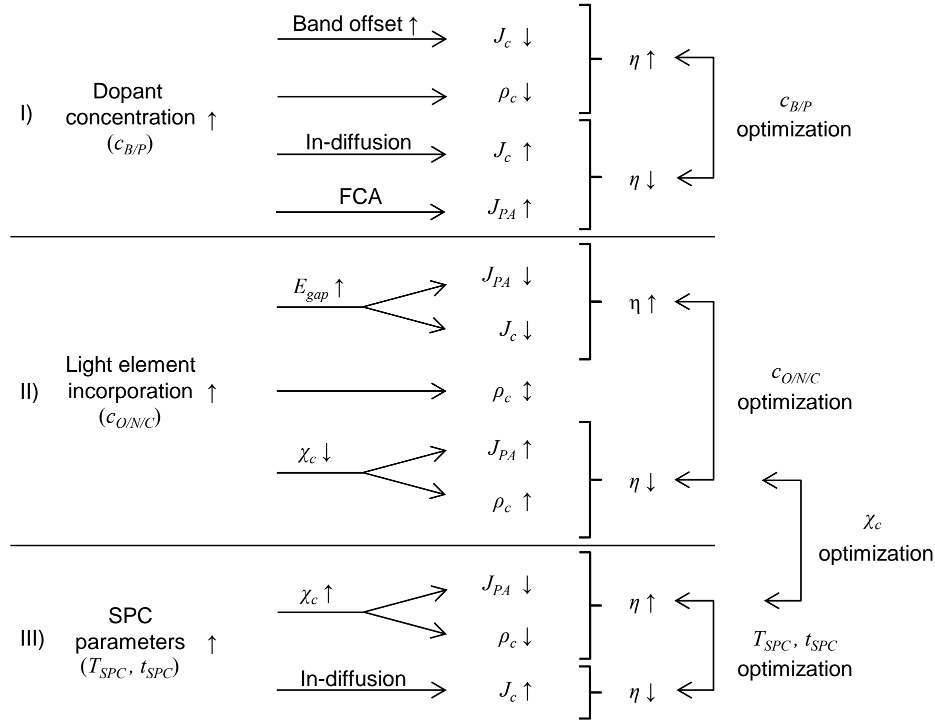

FIGURE 5.1. Dependencies between process parameter groups I)−III) and solar cell efficiency η indicated by arrows and mediated by the contact recombination current density J_c, the contact resistance ρ_c and the parasitic absorption current density J_{PA}. Four parameter optimizations were found regarding the dopant concentration $c_{B/P}$, the concentration of light elements $c_{O/N/C}$, the SPC parameters T_{SPC}, t_{SPC} and the crystallinity χ_c.

A fourth optimization is indicated in Fig. 5.1 regarding the crystallinity χ_c. The loss in η due to a decreased crystallinity χ_c for larger $c_{O/N/C}$ could be avoided by larger T_{SPC} and/or t_{SPC} and thus higher χ_c. Unfortunately, this could in turn increase J_c due to detrimental strong dopant in-diffusion. Therefore, the optimization of χ_c is considered throughout all sections 5.2−5.4. In general, none of the parameter groups I)−III) can be examined completely in isolation. The crystallinity is just one example of more complex interdependencies influencing the solar cell efficiency η.

Apart from Sec. 5.1 on the avoidance of blistering, all sections in this chapter are arranged in the same order: Starting from the GD-OES determined composition, the microstructure is discussed as measured by RS, followed by the SE determined optical properties. Afterwards, both quantities constituting the selectivity of a poly-Si/SiO_x contact S_{10} (eq. 1.9) are discussed, namely the HE and PCD determined resistivities as measures for ρ_c via eq. 1.7 and the PCD determined passivation quality of symmetrical test samples in terms of J_c and iV_{oc}, followed by a short summary. All uncertainties presented in this chapter were determined according to the sections in Chapter 3 and a sum of squares was calculated with the standard deviation, if available.

All processes and data acquisitions regarding the poly-SiO_x and poly-SiO_xN_y layers were executed by Raphael Glatthaar in the context of his master's thesis [180] under my supervision. As the applied process flow, characterization and data analysis methods as well as deposition parameters are based on my previous investigations of pure poly-Si layers, the results are presented also within this thesis. However, all raw data were re-evaluated in order to match the methods described in Chapter 3 and

may therefore differ from the master's thesis in absolute values. All processes and data acquisitions regarding the polycrystalline silicon carbide (poly-SiC_x) layers were executed by Swetlana Weit whereas the main data evaluation and interpretation was done by myself and will be published [181]. Both colleagues approved the publication of their data within this thesis.

5.1. Strategies to Avoid Blistering

ABSTRACT. *Blistering is promoted with increasing R_{B2H6} whilst it is suppressed for higher R_{N2O} and R_{CO2}. Blistering was found to be most pronounced for an intermediate deposition temperature range of $T_{set} = 200-250°C$. A clear relation for less blistering with larger microstructure factors R^* was identified.*

As stated in Sec. 2.4.2, in the context of poly-Si/SiO_x contacts blistering was predominantly observed on PECVD deposited in-situ boron doped (p) a-Si:H layers as also prepared in this thesis. Therefore, the characterization and development of strategies for an avoidance of blistering constituted a significant part of the process flow optimization and will hence be described in the following sections. The avoidance of blistering utilizing the gas flow ratios R_X during PECVD deposition and as such the dopant and light elements concentrations is described in Sec. 5.1.1. The deposition temperature T_{set} significantly influences the hydrogen concentration as well as the microstructure of the as-deposited layers which both are critical parameters for blister occurrence. Therefore, the influence of T_{set} on blistering is discussed in Sec. 5.1.2. Since the thickness of the as-deposited layer has a strong impact on blistering it was approximately kept constant for all layers within each parameter variation.

5.1.1. Adjustment of the PECVD Gas Flow Ratios

Influence of R_{B2H6}

Fig. 5.2 shows OM images of (p) poly-Si layers[39] on FZ substrates under variation of R_{B2H6}. It is

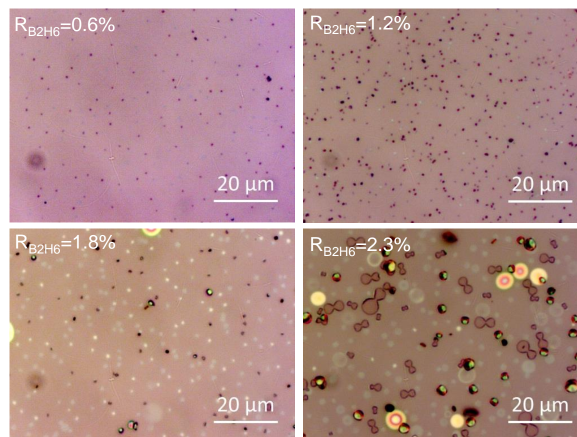

FIGURE 5.2. OM images of blistered surfaces after SPC of (p) poly-Si layers under variation of R_{B2H6} during PECVD deposition.

[39]PECVD deposition parameters: $P = 20$ W, $p = 400$ mTorr, $T_{set} = 100°C$, $R_{H2} = 99\%$, $R_{B2H6} = 0.6-2.3\%$, $t = 1800$ s.

clearly evident that the number and diameter of blister structures increases with R_{B2H6} from sub-micrometer range up to a few micrometers. For $R_{B2H6} = 1.8\%$ isolated dome-shaped surface elevations appear whereas at $R_{B2H6} = 2.3\%$ delamination occurs as identified by the barbell structures.

As stated in Sec. 2.4.2, blistering may be attributed to a high pressure caused by hydrogen accumulation below local uplifts of the whole poly-Si layer during SPC. From the investigations in Sec. 4.2.1 regarding the as-deposited layers, a decreasing microstructure factor R^* and ratio Q^* with increasing R_{B2H6} was observed on the (p) a-Si:H layers which corresponds to a denser microstructure. Stress caused by an increasing pressure during SPC below these uplifts could be less efficiently relaxed by this denser amorphous network and hence promote blistering in form of larger structures and intensified layer delamination. A correlation between blistering and low R^* values was discussed before throughout Chapter 4 and also suggested in [161].

A second line of explanation for the more pronounced blistering for higher R_{B2H6} follows the observation of a less dense microstructure of the (p) a-Si:H layer at the interfacial oxide in the context of a decreased interfacial refractive index as discussed in Sec. 4.2.1. The interfacial refractive index increases with higher R_{B2H6}, which in turn increases the difference in the microstructure between the interfacial oxide and the (p) a-Si:H layer since the interfacial oxide has a lower refractive index. Eventually, this difference could promote the local uplifts of the layer due to interface strain (Sec. 2.4.2).

Influence of R_{N2O} and R_{CO2}

In contrast to a B_2H_6 addition to the PECVD deposition plasma, light element incorporation decreases the blistering as was observed by OM with increasing gas flow ratios R_{N2O} for (p) poly-SiO_xN_y[40] (Fig. 5.3 a) and R_{CO2} for poly-SiO_x[41] layers (Fig. 5.3 b) on FZ substrates. The background structures of the OM images of non-blistered layers correspond to the FZ surface and are not visible

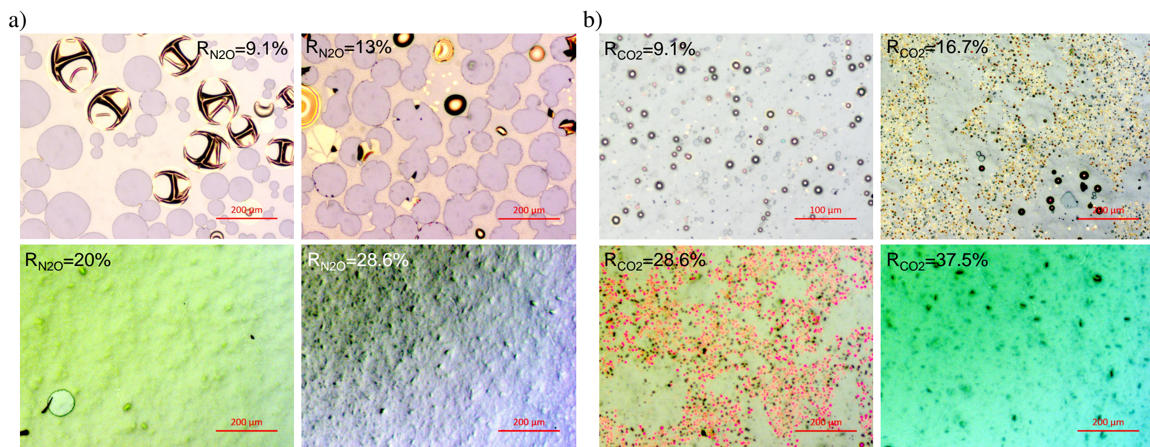

FIGURE 5.3. OM images of blistered surfaces after SPC of a) (p) poly-SiO_xN_y layers under variation of R_{N2O} and b) (p) poly-SiO_x layers under variation of R_{CO2} during PECVD deposition. Note the different scale for $R_{CO2} = 9.1\%$ in b).

[40]PECVD deposition parameters: $P = 20$ W, $p = 400$ mTorr, $T_{set} = 300$°C, $R_{B2H6} = 0.6\%$, $R_{H2} = 0\%$, $R_{N2O} = 9.1-28.6\%$, $t = 75$ s.

[41]PECVD deposition parameters: $P = 20$ W, $p = 400$ mTorr, $T_{set} = 400$°C, $R_{B2H6} = 0.6\%$, $R_{H2} = 99\%$, $R_{CO2} = 9.1-37.5\%$, $t = 2400$ s.

in the images of blistered layers as the microscope was focused on the layer's surface in the blistered case and unintentionally focused on the substrate's surface in the non-blistered case. The reason for this was that no structures were present on the layer's surface to focus on.

For $R_{N2O} \leq 13\%$ strong blistering occurred with area diameters of up to 100 µm and a fraction of intact surface area below 30%. For $R_{N2O} = 20\%$ only isolated blisters were observed and eventually completely disappeared for $R_{N2O} = 28.6\%$. The blister diameter for the (p) poly-SiO_x layers was much lower with a few µm at $R_{CO2} = 9.1\%$ and reduced to even smaller diameters for $R_{CO2} = 16.7 - 29.6\%$. For $R_{CO2} = 37.5\%$ all blister structures disappeared.

The sizes of the blister structures during R_{N2O} variation were two orders of magnitude larger compared to the ones during R_{CO2} and R_{B2H6} variation (Fig. 5.2). This difference could be attributed to the hydrogen gas flow ratio, which was $R_{H2} = 99\%$ for the R_{B2H6} and R_{CO2} variation and $R_{H2} = 0\%$ for the R_{N2O} variation, since hydrogen addition promotes nanocrystalline growth and hence a rather compact microstructure of the resulting layers. Within the picture of interface voids as a reason for blistering (Sec. 2.4.2), this compact microstructure hinders the growth of these voids resulting in smaller structures for similar SPC parameters.

In Sec. 4.3.1 an increase of the microstructure factor R^* and the ratio Q^* of as-deposited a-SiO_xN_y layers was observed for higher R_{N2O} and R_{CO2}. Hence, a less pronounced blistering was observed for higher microstructure factors R^*, which is in line with the discussion above and with [161]. It seems that the microstructure factor of the as-deposited amorphous layers is a useful measure to control and predict the blistering behavior during SPC regardless of the incorporation of foreign elements.

An additional explanation for reduced blistering by incorporation of oxygen and nitrogen in the amorphous network could be the hydrogen bond energies of these elements. According to [182], O-H (4.43 eV) and N-H (3.69 eV) bonds are stronger than Si-H bonds (3.25 eV) and hence hydrogen diffusion and consequently accumulation below the local uplifts of the layers is suppressed. A similar reduction of blistering was observed for higher carbon incorporation in (p) poly-SiC_x layers (not shown here) and could be explained similarly by the C-H bond energy (3.51 eV) according to [182]. However, this argumentation via the bond energies can only partly explain the results since the B-H bond (3.43 eV) is also stronger than the Si-H bond, but blistering was observed to be enhanced with increasing boron concentration as discussed above (Fig. 5.2).

5.1.2. Adjustment of the PECVD Deposition Temperature

As stated in Sec. 2.4.2, blistering during SPC is commonly linked to hydrogen accumulation below local uplifts of the poly-Si layer and to the microstructure. Both the hydrogen concentration and the microstructure are influenced by the deposition temperature during PECVD deposition, as discussed before in Sec. 4.1.2. While the temperature variation therein was performed for intrinsic (i) a-Si:H layers, the blister related temperature variation in this section was carried out with (p) a-Si:H layers[42] on FZ substrates in the range of $100 - 400°C$, since the doped (p) poly-Si layers additionally allow for an investigation in terms of passivation quality.

Fig. 5.4 shows OM images of these blistered surfaces. For $T \leq 150°C$ only small bubbles and swales are visible with isolated dome-shaped surface elevations. With increasing deposition temperatures

[42]PECVD deposition parameter: $P = 20$ W, $p = 400$ mTorr, $T_{set} = 100 - 400°C$, $R_{H2} = 99\%$, $R_{B2H6} = 1.2\%$, $t = 1800$ s.

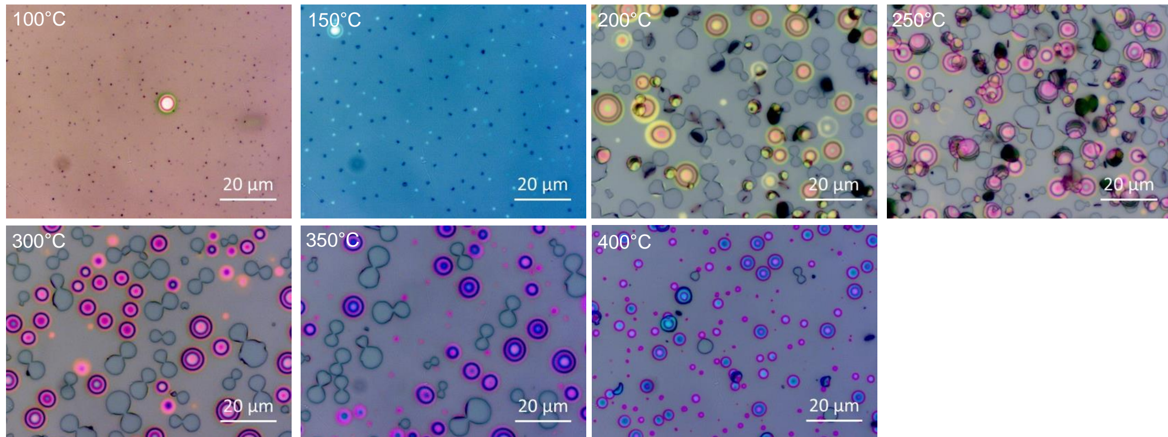

FIGURE 5.4. OM images of blistered surfaces after SPC of (p) poly-Si layers under variation of the deposition temperature T during PECVD deposition.

strong blistering occurred with intact surface elevations and delaminated barbell shaped areas, while for the temperature range of $200-250$°C also the delaminated layer pieces became apparent. For even higher temperatures the blister strength and delaminated area fraction decreased again from $300-400$°C. The hydrogen gas flow ratio during deposition was $R_{H2} = 99\%$ and the size of the blistered structures was similar to the one observed during R_{B2H6} and R_{CO2} variation. This observation supports the above proposed relation between large R_{H2} and small blister structures.

Following the interpretation of a correlation between low microstructure factors R^* of the as-deposited layers and the occurrence of blistering, one would expect a minimum in R^* of the corresponding as-deposited layers in the range of $200-250$°C. In contrast, after a nearly constant plateau between $100-200$°C, R^* decreased linearly up to 400°C as discussed before in Sec. 4.1.2. This discrepancy between the blister intensity observed in the OM images and the microstructure factor R^* of the as-deposited layers can be explained by a decreasing hydrogen concentration with increasing T_{set}, which reduces the amount of hydrogen available for accumulation below the local uplifts of the layer or at the interface to the substrate. Therefore, a strict relation between the microstructure factor R^* and strength of blistering is only valid for similar hydrogen concentrations.

The strength of blistering as function of T_{set} showed a maximum around $200-250$°C. Interestingly, the presence of this maximum is similar to the local minimum of the optical band gap and monohydride bond density at 250°C, as discussed in Sec. 4.1.3 and in [118]. A similar minimum also appeared for the passivation quality of the corresponding (p) poly-Si layers after SPC as a minimum of iV_{oc} and as a maximum of J_c (Fig. 5.5). Moreover, temperatures around 200°C are typically utilized to deposit a-Si:H layers with a high chemical passivation ability in the context of SHJ solar cells (Sec. 1.2.2). Thus, it seems that this temperature range between $200-250$°C provides a prominent relation between the microstructure and the hydrogen concentration. This notion is supported at least for the microstructure for which a minimum of the defect density in a-Si:H is known to be located around 250°C [57].

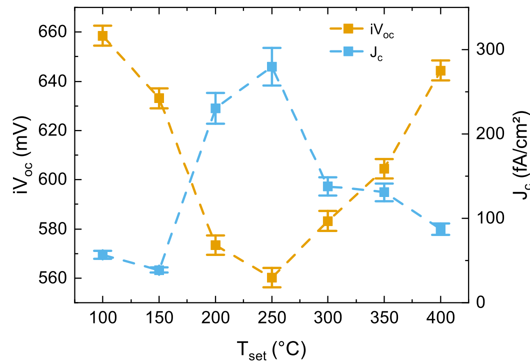

FIGURE 5.5. PCD determined passivation quality in terms of implied open circuit voltage iV_{oc} and contact recombination current density J_c as function of the deposition temperature T_{set}. Dashed lines are a guide for the eye.

5.1.3. Section Summary

The most promising strategy for avoidance of blistering was identified to be an increase of the microstructure factor R^* of the as-deposited layers before SPC. This was achieved by low boron concentrations, by the incorporation of light elements and by low deposition temperatures. In addition, high deposition temperatures also reduced blistering due to a lower hydrogen concentration. Unfortunately, the successful tuning of the optical band gap of the as-deposited layers was not preserved during SPC to poly-Si.

5.2. Variation of the Dopant Concentration

ABSTRACT. *A pile-up of dopant concentration shortly before the interfacial oxide and a significant difference in total and electrically active dopant concentration were observed for both dopant types and deposition methods. With higher R_{B2H6} during PECVD deposition of (p) poly-Si and (p) poly-SiO_xN_y layers a slight increase in crystallinity and internal stress was revealed whereas no clear trend was found neither for the parasitic absorption current density nor the optical band gap. Nevertheless, an overall wider band gap and a reduced parasitic absorption of (p) poly-SiO_xN_y layers compared to (p) poly-Si was confirmed, accompanied by a higher resistivity which reduced for both layer types with increasing R_{B2H6}. A difference of two orders of magnitude was observed between PCD and HE determined resistivities only of the (p) poly-SiO_xN_y layers. For a lower dopant concentration of MSD deposited (n) poly-Si layers a reduction of parasitic free carrier absorption was found with the drawback of a higher resistivity and a lower passivation quality. Hydrogenation decreased the resistivity of MSD deposited (p) poly-Si layers, saturated interface defects induced by SPC of PECVD deposited (p) poly-SiO_xN_y layers and also saturated bulk defects induced during SPC of MSD deposited (p) poly-Si layers. A sputter damage to the interfacial oxide during MSD deposition was observed but compensated within the standard process flow during hydrogenation.*

The dopant concentration was varied on the one hand by the diborane gas flow ratio during PECVD deposition of in-situ doped (p) poly-Si and (p) poly-SiO_xN_y layers in the range of $R_{B2H6} = 0.6 - 2.9\%$, which were partly compared to MSD deposited in-situ doped (p) poly-Si layers. On the other hand, the phosphorus concentration was varied by an adjusted $POCl_3$-diffusion of MSD deposited

(i) a-Si layers. Furthermore, differences between both dopants boron and phosphorus were examined. For each variation all other parameters were kept constant at $R_{N2O} = 20\%$ and at the standard SPC parameters $T_{SPC} = 920°C$ and $t_{SPC} = 30$ min. Parts of this section were already published in [61].

5.2.1. Composition

Representative Dopant Profiles

Fig. 5.6 a) shows GD-OES raw profiles of the dopant, either boron or phosphorous, and the oxygen signal normalized to the maximum measured value for several representative poly-Si layer types on the interfacial oxide. Similar boron profiles of as-deposited (p) a-Si:H layers were discussed before in Sec. 4.2.1. Therein, no definite statements could be given regarding the question if the peaks in the dopants signals shortly before the interfacial oxide and the increased signal at the surface were measurement artifacts or signals originating from real concentration pile-ups. Here, the comparison of several layer types at different stages in the process flow allowed to partly answer this question. In this context three main observations are highlighted:

I) The higher surface signal of the dopant profiles does not appear in the profile of the MSD in-situ doped (p) poly-Si layer after hydrogenation and thus with a SiN_x:H layer on top.

II) The peaks in the dopant signals appear shortly before the oxygen peaks, which is marked by the vertical dotted lines, independent of the overall course of the dopant profile.

III) The peak in the only phosphorus profile of the MSD deposited ex-situ doped (n) poly-Si layer is more pronounced in relation to the surrounding signal than it is the case for all boron profiles of all other layers.

Following observation I), the higher surface signal is assumed to be a measurement artifact as no such increased surface signal is observed after measuring through the SiN_x:H of the MSD deposited

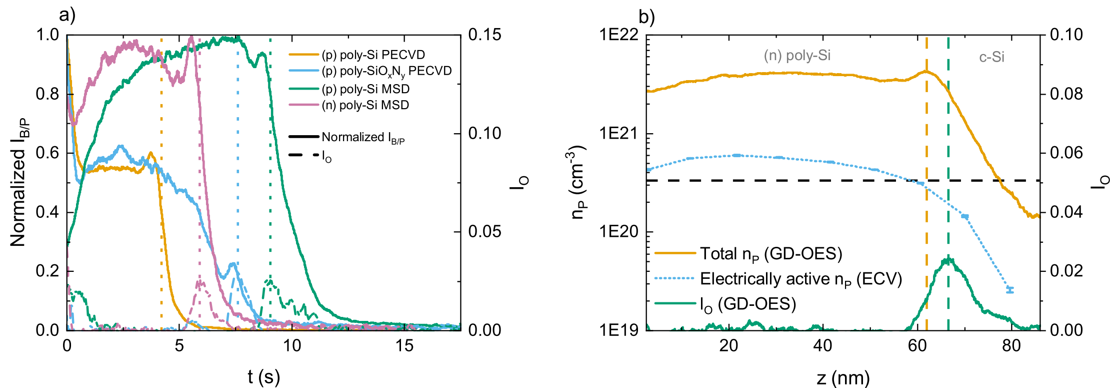

FIGURE 5.6. a) GD-OES measured representative dopant raw data depth profiles $I_{B/P}(s)$ for different layer types normalized to the corresponding maximum and b) calibrated phosphorus atomic density depth profiles $n_P(z)$ of a MSD deposited (n) poly-Si layer measured by GD-OES (total n_P) and ECV (electrically active n_P). Additionally, in both figures the GD-OES measured oxygen semi-quantized depth profile $I_O(z)$ is plotted. All vertical lines mark positions of corresponding peaks in either $I_{B/P}$, I_O or n_P. The horizontal line in b) corresponds to the solubility limit of electrically active phosphorus in silicon equilibrated at 900°C according to [183].

(p) poly-Si layer. The same observation was made on other hydrogenated samples (not shown here). Based on observation II) and in particular on the peak close to the interface in the boron profile of the PECVD deposited (p) poly-SiO_xN_y layer, it can be concluded that these peaks are related to a sputter rate effect during the GD-OES measurement. Furthermore, peaks are also visible in the silicon signals close to the interface (not shown here), supporting the conclusion of a sputter rate effect. These two hypotheses are consistent with the discussion in [20] for SIMS measured dopant profiles of (p) and (n) poly-S/SiO_x contacts.

It is important to note that the presence of a sputter rate effect does not exclude a real concentration pile-up, as it is also stated by the authors in [20]. In fact, an increased boron concentration within the interfacial oxide was reported before from laser-assisted 3D atom probe measurements which are not influenced by a sputter process [173]. Therein, also a phosphorus pile-up before the interfacial oxide was observed which was formerly reported by the authors in [184]. In combination with observation III) it is concluded that at least for the (n) poly-Si layers investigated in this thesis the dopant peak in the GD-OES profile is partly caused by a real concentration pile-up.

Calibrated Phosphorus Concentrations

In Fig. 5.6 b) a GD-OES phosphorus profile obtained by the calibration described in Sec. 3.1.3 is plotted together with an ECV measured phosphorus depth profile as well as a raw GD-OES measured oxygen profile of a MSD deposited ex-situ doped (n) poly-Si layer on an interfacial oxide. These profiles were published before in [61]. The shapes of the GD-OES measured profiles are similar to the ones presented in Fig. 5.6 a) whilst no phosphorus pile-up is observable in the ECV profile. As ECV measures the electrically active and GD-OES the total phosphorus concentration, the real phosphorus pile-up consists of electrically inactive phosphorus only. In [183] the authors reported solubility limits for phosphorus in c-Si which should also hold for poly-Si according to [185]. Therein, the limit for the total phosphorus concentration equilibrated at 900°C is $5.34 \cdot 10^{20}$ cm^{-3} and for the electrically active phosphorus concentration it is $3.35 \cdot 10^{20}$ cm^{-3}. Both the GD-OES and ECV determined concentrations in Fig. 5.6 b) are above these limits. Similar values above these limits were also published by other authors [183, 186, 187].

In [183] the exceeding of the total phosphorus concentration limit is explained by the formation of monoclinic SiP precipitates. This hypothesis was not tested for the layers investigated in this thesis. However, the ECV determined electrically active phosphorus concentration above the corresponding limit can be attributed to a measurement artifact. A possible explanation for this artifact could be that the etch process etches faster at grain boundaries and consequently the effectively etched area is increased. A correction for this larger etched area would lower the measured atomic densities but was not applied due to lack of clear evidence.

Starting from the PCD determined sheet resistance R_s, the HE determined electron mobility μ_e and the SE determined layer thickness d, a concentration of electrically active phosphorus can be determined via a combination of eq. 3.30 and 3.31 via

$$n_P = (q\, d\, R_s\, \mu_e)^{-1} \tag{5.1}$$

with the elemental charge q. The resulting concentration of $n_P = 3.18 \cdot 10^{20}$ cm^{-3} is closely below the limit stated above and hence directly supports the hypothesis of the presence of an ECV measurement

artifact. Even if such concentrations close to both limits might be limited by detrimental strong dopant in-diffusion, if applied in a poly-Si/SiO_x contact, a sufficient passivation quality of J_c = 7.9 fA/cm^2 was measured on similar samples as will be shown later in Sec. 5.2.5. This finding and the phosphorus pile-up at the interfacial oxide allow to conclude that the oxide thickness of $\sim$ 2.5 nm used throughout this thesis is large enough to act as efficient phosphorus diffusion barrier for concentrations up to the solubility limits, at least for the standard SPC parameters.

Calibrated Boron Concentrations

The boron concentration under variation of the gas flow ratio R_{B2H6} for PECVD deposited[43] (p) poly-SiO_xN_y layers, determined by an adjusted multi-matrix calibration[44] of GD-OES measurements (Sec. 3.1.1) on Cz substrates, and by HE on FS substrates is shown in Fig. 5.7. For both measurement techniques an increase of the boron concentration for higher R_{B2H6} is observed. The rather large difference of two orders of magnitude occurred since GD-OES measures the total boron concentration while HE measures only the hole density and as such the electrically active boron concentration, similar to the ECV technique discussed above. Furthermore, GD-OES calibrations yield atomic concentrations which were transferred into atomic densities by multiplying the silicon monocrystal atomic density of $n_{Si} = 5 \cdot 10^{22}$ cm^{-3}. As will be shown later in Sec. 5.3.1, the used gas flow ratio of $R_{N2O} = 20\%$ resulted in a nitrogen concentration of $c_N \approx 28$ at% and an oxygen concentration of $c_O \approx 10$ at%. Therefore, the usage of the silicon monocrystal atomic density is assumed to induce a large offset to the absolute values presented in Fig. 5.7. Thus, even if absolute values in the order of 10^{21} cm^{-3} were reported to be too large for functioning (p) poly-Si/SiO_x contacts [19], the layers presented here may have a lower boron concentration and hence are indeed applicable in poly-SiO_xN_y/SiO_x contacts as will be further demonstrated throughout this chapter.

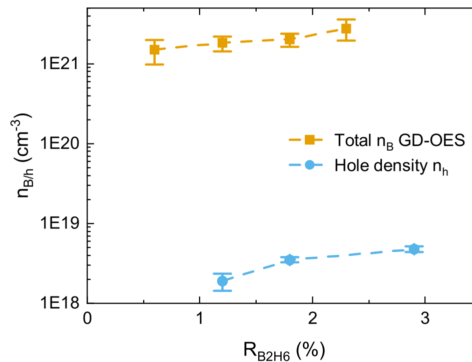

FIGURE 5.7. GD-OES determined total boron atomic densities n_B and HE determined hole densities n_h of electrically active boron of (p) poly-SiO_xN_y layers as function of R_{B2H6} during PECVD deposition. Dashed lines are a guide for the eye.

[43]PECVD deposition parameters: $P = 100$ W, $p = 600$ mTorr, $T_{set} = 300$°C, $R_{N2O} = 20\%$, $R_{H2} = 0\%$, $R_{B2H6} = 0.6 -$ 2.9%, $t = 60$ s.

[44]Details regarding the used calibration standards can be found in the Appendix A.2.

5.2.2. Microstructure

In the context of (p) nc-Si deposition the crystallinity χ_c was observed to decrease for higher R_{B2H6} as discussed in Sec. 4.1.1. This should not be confused with an increased boron concentration during SPC of (p) a-Si:H, which is expected to increase the grain growth velocity (Sec. 2.4.1). Thus, if the resulting (p) poly-Si layer is not fully crystallized, χ_c is expected to increase for higher R_{B2H6}. Such an increase was observed for the same PECVD deposited[45] (p) poly-SiO_xN_y layers as discussed in the previous section on FS substrates only for $R_{B2H6} \gtrsim 1\%$, as shown in Fig. 5.8. For $R_{B2H6} > 2.3\%$ a plateau at $\chi_c \approx 51\%$ evolved which might correspond to a maximum achievable crystallinity for $R_{N2O} = 20\%$ and the standard SPC parameters which both were kept constant during the variation of R_{B2H6}. The crystallinity at $R_{B2H6} = 0.6\%$ deviated from the overall trend but also fits to this maximum crystallinity of $\chi_c \approx 51\%$. Hence, an adjustment of the SPC parameters to increase this maximum achievable crystallinity is mandatory and will be discussed in Sec. 5.4.

In comparison, PECVD[46] as well as MSD[47] deposited in-situ doped (p) poly-Si layers without incorporated light elements showed much higher crystallinities which was even exceeded by MSD deposited ex-situ doped (n) poly-Si layers as depicted in Table 5.1. This even larger crystallinity for similar temperature profiles in both SPC steps may be explained by the larger grain size for phosphorus compared to boron doped poly-Si layers (Sec. 2.4.1).

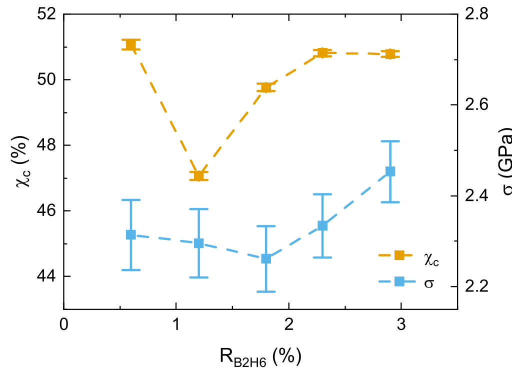

FIGURE 5.8. RS determined crystallinity χ_c and internal stress σ of (p) poly-SiO_xN_y layers as function of R_{B2H6} during PECVD deposition. Dashed lines are a guide for the eye.

TABLE 5.1. RS determined crystallinity χ_c and internal stress σ of different layer types.

Layer type	Deposition technique	χ_c (%)	σ (GPa)
(p) poly-Si	PECVD	81.1 ± 14.2	2.57 ± 0.15
(p) poly-Si	MSD	80.3 ± 2.8	1.43 ± 0.04
(n) poly-Si	MSD	94.6 ± 1.9	0.98 ± 0.05

[45]PECVD deposition parameters: $P = 100$ W, $p = 600$ mTorr, $T_{set} = 300°C$, $R_{N2O} = 20\%$, $R_{H2} = 0\%$, $R_{B2H6} = 0.6-2.9\%$, $t = 60$ s.

[46]PECVD deposition parameters: $P = 50$ W, $p = 350$ mTorr, $T_{set} = 400°C$, $R_{B2H6} = 1.4\%$, $R_{H2} = 50\%$, $t = 200$ s.

[47]MSD deposition parameters: $P_{Si} = 300$ W, $P_B = 250$ W, $p = 2$ mTorr, $Q_{Ar} = 80$ sccm, $T_{set} = 450°C$, $d_{target} = 17$ cm, $t = 2000$ s. In order to protect the quartz tube furnace from iron contamination originating from the boron sputter target, a ~30 nm (i) a-Si capping layer was deposited with equal parameters except of $P_B = 0$ W and $t_{cap} = 750$ s.

Regarding the internal stress σ, no clear trend was found for the (p) poly-SiO_xN_y layers in Fig. 5.8. If the value at $R_{B2H6} = 0.6\%$ is neglected, a continuous increase in σ is possible within the uncertainties but not very likely. While σ of the PECVD deposited (p) poly-Si layer without incorporated light elements was comparable to the values of the (p) poly-SiO_xN_y layers, the internal stresses of the MSD deposited layers were significantly lower (Table 5.1). This finding reveals a fundamental difference between both deposition techniques regardless of the actual crystallinity. The reason for this difference is most likely the involvement of hydrogen in processing of the PECVD layers during growth and effusion during SPC while no hydrogen at all is involved in processing of the MSD layers. At least an increase in structural disorder during hydrogen effusion was observed before [57] and might simultaneously increase the internal stress.

5.2.3. Optical Properties

Variation of R_{B2H6}

A variation of the dopant concentration is not expected to have a strong influence on the optical properties. Indeed, no clear trends were observed for a R_{B2H6} variation during the deposition of PECVD (p) poly-Si layers[48] and the same (p) poly-SiO_xN_y layers[49] as discussed in the previous section on FS substrates. Fig. 5.9 a) shows the parasitic absorption current density J_{PA} determined from SE measurements in a spectral range of $270-1000$ nm. The slight decrease with R_{B2H6} for the (p) poly-SiO_xN_y layers could be attributed to the increased crystallinity, as discussed in the previous section, since a-Si absorbs a larger fraction of the AM1.5 spectrum compared to poly-Si. However, the rather large uncertainties exclude a definite statement. Nevertheless, all J_{PA} values of the poly-SiO_xN_y layers were lower than the ones of the (p) poly-Si layers for equal R_{B2H6} and thus similar dopant concentrations which directly reflects the desired reduced parasitic absorption by incorporation of light elements.

Regarding E_{04} in Fig. 5.9 b) also no clear trend with increasing R_{B2H6} was observed. In particular the band gap narrowing of the as-deposited (p) a-Si:H layers with higher R_{B2H6} (Sec. 4.2.2) disappeared

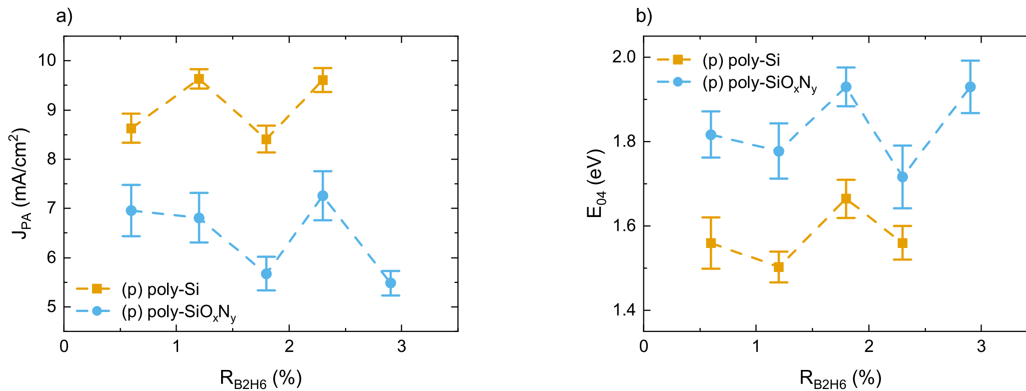

FIGURE 5.9. SE determined a) parasitic absorption current density J_{PA} and b) optical band gap E_{04} of (p) poly-Si and (p) poly-SiO_xN_y layers as function of R_{B2H6} during PECVD deposition. Dashed lines are a guide for the eye.

[48] PECVD deposition parameters: $P = 20$ W, $p = 400$ mTorr, $T_{set} = 100$°C, $R_{H2} = 99\%$, $t = 1800$ s.
[49] PECVD deposition parameters: $P = 100$ W, $p = 600$ mTorr, $T_{set} = 300$°C, $R_{N2O} = 20\%$, $R_{H2} = 0\%$, $t = 60$ s.

after junction formation. Therefore, it can be concluded that the tuning of the optical band gap of the as-deposited layers cannot simply be transferred to the crystallized poly-Si layers. Admittedly, the approximate character of E_{04} compared to the E_{gap} determination from the SE fit parameter causes the total uncertainty range of E_{04} in Fig. 5.9 b) of ~ 0.13 eV to be in the same range as the band gap narrowing of the as-deposited layers of ~ 0.15 eV (Sec. 4.2.2). Nonetheless, the desired optical band gap widening by incorporation of light elements is observable in the larger E_{04} values of the poly-SiO_xN_y layers.

Free Carrier Absorption

Contrary to the just discussed absence of changing optical properties with R_{B2H6}, FCA may increase parasitic absorption for heavily doped poly-Si layers. This effect was observed for a variation of the $POCl_3$-diffusion of ex-situ doped MSD deposited (n) poly-Si layers on FS substrates. In Sec. 5.2.1 a large phosphorus concentration of up to $n_P = 3 \cdot 10^{21}$ cm^{-3} was determined with the standard $POCl_3$-diffusion profile. A lower phosphorus concentration with minor changes to the crystallinity was achieved by using the same temperature profile as in the standard process but activating the $POCl_3$-N_2 flow only during cooling. For an approximate quantification of the phosphorus concentration the GD-OES and SE determined quantity ξ_P was used (eq. 3.10) which revealed roughly a factor of two between both concentrations.

FCA was observed in the corresponding FT-IR absorbance spectra for both concentrations as a strong bending of the baseline at lower wavenumbers with respect to an intrinsic (i) poly-Si layer reference to remarkably larger absorbances A close to unity (Fig. 5.10 a). The FCA induced bending of the baseline was significantly reduced for the lower concentration ξ_P and J_{PA} was simultaneously reduced as indicated in Fig. 5.10 b). Therein, the fraction of the solar spectrum, which is absorbed by the corresponding poly-Si layer, is plotted similarly to the spectrum discussed in Sec. 3.4.3. A clearly larger fraction was absorbed by the layer with higher ξ_P for longer wavelengths as it is typical for FCA [46, 188]. The authors in [46] stated that optical losses in poly-Si are dominated by the absorption of light with short wavelengths and that FCA plays a secondary role. This is partly consistent with the data in Fig. 5.10 b) as a significant fraction of the additional absorption at larger

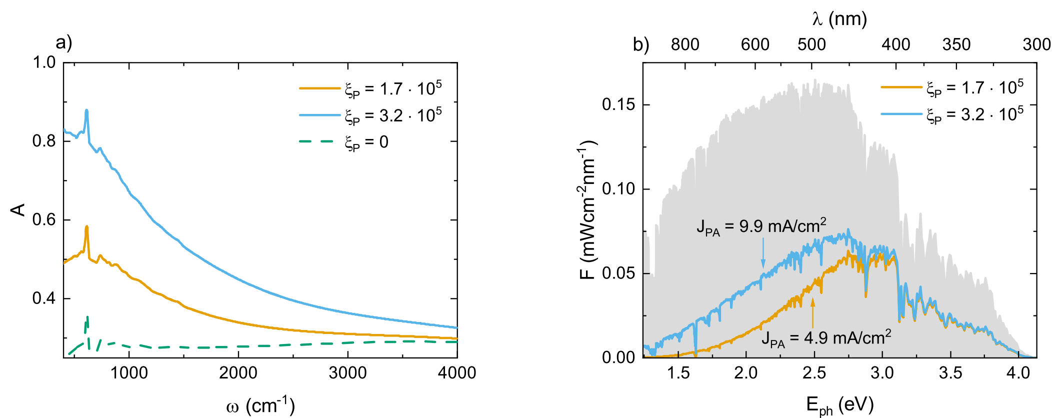

FIGURE 5.10. a) FT-IR determined absorbance spectrum $A(\omega)$ of MSD deposited (n) poly-Si layers with different phosphorus concentrations expressed as ξ_P and of an intrinsic (i) poly-Si reference. b) Corresponding absorbed fractions of an AM1.5 solar spectrum in terms of spectral irradiance as function of the photon energy $F(E_{ph})$ and resulting parasitic absorption current densities J_{PA}.

ξ_P is also present for intermediate wavelengths. Nevertheless, the corresponding electrically active phosphorus concentration was found to be close to the solubility limit (Sec. 5.2.1) and thus FCA is assumed to dominate the parasitic absorption in this case.

It should be noted that J_{PA} of the MSD deposited (n) poly-Si layer with the lower ξ_P was smaller than all values shown in Fig. 5.9 a) for the PECVD deposited layers while J_{PA} of the layer with larger ξ_P was in the same range. This could be a hint that FCA also influences the boron doped PECVD layers. However, the higher crystallinity of MSD deposited (n) poly-Si layers (Table 5.1) might also contribute to the lower J_{PA}.

5.2.4. Resistivity

PECVD Deposited poly-Si and poly-SiO$_x$N$_y$

Higher dopant concentrations are expected to decrease the resistivity of the layers for both the amorphous and crystalline phase. The PCD determined resistivities ρ_{PCD} of the same PECVD deposited (p) poly-Si layers[50] and (p) poly-SiO_xN_y layers[51] as discussed in the previous section on FZ and Cz substrates, respectively, under variation of R_{B2H6} are presented in Fig. 5.11 a). The overall resistivity was higher for the (p) poly-SiO_xN_y layers compared to the (p) poly-Si layers. Even though small amounts of nitrogen and oxygen might decrease the resistivity in poly-Si (Sec. 2.4.3), the low crystallinities of $\chi_c \approx 50\%$ (Sec. 2.3.3) overcompensate this effect by inefficient carrier transport through domains of amorphous material via extended or band tail states resulting in an increased resistivity (Sec. 2.3.3).

For the (p) poly-Si layers ρ_{PCD} decreased continuously with increasing R_{B2H6} while for the (p) poly-SiO_xN_y layers a slight increase for higher R_{B2H6} was observed. As the uncertainties are rather large due to the usage of Cz substrate and a horizontal line could be drawn within all uncertainty ranges, it is not clear if a trend similar to the one of ρ_{PCD} of the (p) poly-Si layers is present. An argument

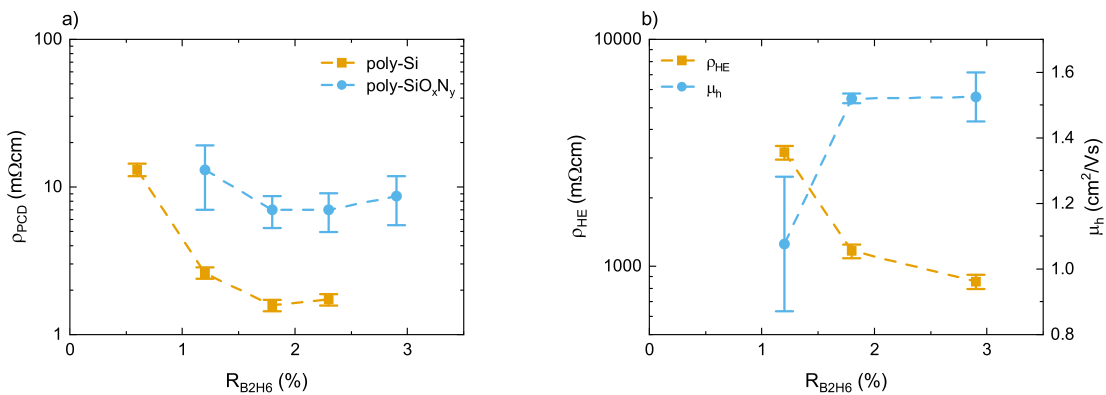

FIGURE 5.11. a) PCD determined resistivities ρ_{PCD} of (p) poly-Si layers on FZ substrate and (p) poly-SiO_xN_y layers on Cz substrates. b) HE determined resistivities ρ_{HE} and hole mobilities μ_h of the same (p) poly-SiO_xN_y layers on FS substrates as function of R_{B2H6} during PECVD deposition. Note the difference of two orders of magnitude between ρ_{PCD} and ρ_{HE}. Dashed lines are a guide for the eye.

[50] PECVD deposition parameters: $P = 20$ W, $p = 400$ mTorr, $T_{set} = 100°$C, $R_{H2} = 99\%$, $R_{B2H6} = 0.6 - 2.3\%$, $t = 1800$ s.
[51] PECVD deposition parameters: $P = 100$ W, $p = 600$ mTorr, $T_{set} = 300°$C, $R_{N2O} = 20\%$, $R_{H2} = 0\%$, $R_{B2H6} = 1.2 - 2.9$ $t = 60$ s.

for a similar trend are the HE measured resistivities ρ_{HE} of the same (p) poly-SiO_xN_y layers on FS substrates with a continuously decreasing trend in the same R_{B2H6} range similar to the one of the (p) poly-Si layers (Fig. 5.11 b).

It is important to note the difference between PCD and HE determined absolute resistivity values of two orders of magnitude in Fig. 5.11. This difference was observed on the (p) poly-SiO_xN_y layers only but not on the other layers types. Exemplarily, for a MSD deposited (p) poly-Si layer similar values were determined by PCD and HE (Fig. 5.12 a). Thus, a systematic deviation between both measurement techniques such as the different underlying substrates (crystalline silicon for PCD and and FS for HE) can be excluded. A possible source of uncertainty could be the calibration of the PCD measured conductance to resistivity which is strictly speaking only valid for pure silicon and does not necessarily hold for the (p) poly-SiO_xN_y layers. However, a deviation of two orders of magnitude cannot be explained solely by this calibration uncertainty.

The following rather speculative interpretation would offer an additional explanation for the large difference between ρ_{HE} and ρ_{PCD} and also allows to draw a conclusion regarding the microstructure of the layer. During HE measurements the applied current has to flow in lateral direction from one pin to another (Sec. 3.5). In contrast, PCD measures conductances via an induction coil and hence no directed current has to flow. As stated in Sec. 2.4.3, a higher lateral resistivity is expected if the density of grain boundaries is larger in the lateral direction compared to the direction parallel to the surface normal. Additionally, the low crystallinity of the (p) poly-SiO_xN_y layers is accompanied by amorphous domains with higher resistivities. Therefore, one could conclude that HE strictly measures the lateral resistivity with a current over grain boundaries and amorphous domains while during PCD mostly the resistivities within the crystallized grains are measured avoiding the potential barriers of the grain boundaries and the amorphous domains. For poly-Si/SiO_x contacts the lateral conductivity is important for an application of local metal contacts. Hence, a larger ρ_{HE} value compared to ρ_{PCD} would be detrimental but would still allow a functioning poly-Si/SiO_x contact with full area metallization on the rear side of a solar cell. Following this interpretation, the above discussed (p) poly-SiO_xN_y layers should only be applied in a poly-Si/SiO_x contact with full area metallization.

Besides ρ_{HE} the hole mobility μ_h as function of R_{B2H6} is presented in Fig. 5.11 b) and shows an inverted trend compared to ρ_{HE}. In order to set the absolute values of μ_h in context, the silicon bulk hole mobility as function of the acceptor concentration N_A at 300 K was calculated according to [31] via

$$\mu_{h,bulk} = \mu_{min} + \frac{\mu_0}{1+(N_A/N_{ref})^{\alpha}} \tag{5.2}$$

with $\mu_{min} = 54.3$ cm^2/Vs, $\mu_0 = 406.9$ cm^2/Vs, $N_{ref} = 2.35 \cdot 10^{17}$ cm^{-3} and $\alpha = 0.88$. Inserting the HE determined hole densities in the order of $n_h \approx 10^{18}$ cm^{-3} (Sec. 5.2.1) as an approximation for the acceptor density N_A leads to silicon bulk hole mobilities in the range of $\mu_{h,bulk} = 80 - 115$ cm^2/Vs. This value is two orders of magnitude larger than the mobilities of the (p) poly-SiO_xN_y layers presented in Fig. 5.11 b). Even if it is considered that the hole mobility of boron doped pure (p) poly-Si without light elements is not expected to reach $\mu_{h,bulk}$ of a silicon monocrystal, the determined mobilities are still one order of magnitude lower than previously reported hole mobilities for (p) poly-Si

with a similar boron concentration after annealing at 900°C [189]. The low μ_h values for (p) poly-SiO_xN_y are attributed to the lower crystallinity in line with the discussion on the increased resistivity above.

In Sec. 2.4.3 it was mentioned that a sharp drop in the resistivity in poly-Si over five orders of magnitude down to 10^{-2} Ωcm for increasing dopant concentrations in the rough range between $N_D \approx 10^{17} - 10^{19}$ cm^{-3} was reported in the literature (Fig. 2.13). The previously discussed GD-OES measurement of a (p) a-Si:H layer deposited with the minimum possible diborane flow ratio of $R_{B2H6} = 0.6\%$ (Fig. 4.6 a) showed a boron signal close to the dark currents signal. Since the corresponding GD-OES resolution limit is $\sim 10^{18}$ cm^{-3}, the boron concentration falls in the range of the tail of this sharp drop. In Fig. 5.11 a reduction of ρ_{PCD} is visible between $R_{B2H6} = 0.6 - 1.2\%$. As also the absolute values are in the range of the literature values, it can be concluded that the tail of this sharp drop is apparent in Fig. 5.11. In the context of optimizing a poly-Si/SiO_x contact this finding means that for $R_{B2H6} \geq 1.2\%$ no significant reduction of the poly-Si resistivity is expected and thus the doping level can be adjusted for an optimized passivation quality within this range without considering the resistivity.

MSD Deposited poly-Si

Fig. 5.12 a) shows ρ_{PCD} values of MSD deposited in-situ doped (p) poly-Si layers[52] on FZ substrates tracked after each hydrogenation step together with the HE measured resistivity ρ_{HE} only after SPC on FS substrates since hydrogenation was not performed on FS substrates according to the process flow (Chapter 2). During hydrogenation ρ_{PCD} was reduced by a factor of four which was only observed for in-situ doped MSD (p) poly-Si layers but not for the in-situ doped PECVD deposited (p) poly-Si layers (not shown here). An explanation for this reduction could be the supplement of hydrogen to the poly-Si layer by the SiN_x:H deposition where it may saturate defects at the grain boundaries. This in turn would reduce the potential barrier height and thereby decrease the resistivity

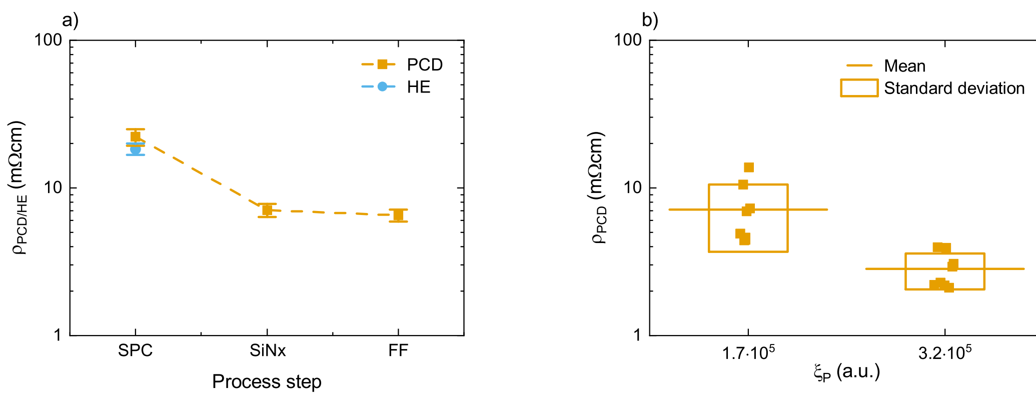

FIGURE 5.12. a) PCD and HE determined resistivities $\rho_{PCD/HE}$ of MSD deposited (p) poly-Si layers after each hydrogenation step. Dashed line as guide for the eye. b) PCD determined resistivities ρ_{PCD} of MSD deposited (n) poly-Si layers for different phosphorus concentrations expressed as ξ_P. Horizontal lines mark the mean values and boxes the standard deviation ranges.

[52] MSD deposition parameters: $P_{Si} = 300$ W, $P_B = 250$ W, $p = 2$ mTorr, $Q_{Ar} = 80$ sccm, $T_{set} = 450$°C, $d_{target} = 17$ cm, $t = 2000$ s. In order to protect the quartz tube furnace from iron contamination originating from the boron sputter target, a ~30 nm (i) a-Si capping layer was deposited with equal parameters except of $P_B = 0$ W and $t_{cap} = 750$ s.

as described in Sec. 2.4.3. As this reduction was not observed for PECVD deposited layers, it can be concluded that the MSD deposited (p) poly-Si layers initially show a higher defect density at the grain boundaries. A reason for this could be on the one hand the large iron impurity in the boron sputter target (Sec. 2.3.2) and on the other hand the different quartz tube used for SPC which is assumed to have more impurities on the tube walls.

Fig. 5.12 b) shows the PCD determined resistivity ρ_{PCD} of the same MSD deposited ex-situ doped (n) poly-Si layers on FZ substrates as discussed in the previous section with different phosphorus concentrations expressed as ξ_P (eq. 3.10) for eight samples at each concentration. The measured resistivities ρ_{PCD} were lower for the higher phosphorus concentration ξ_P as expected. This observation reveals a trade-off between parasitic absorption and resistivity as the former one is improved by a lower phosphorus concentration and the latter one by a larger phosphorus concentration.

5.2.5. Passivation Quality

PECVD Deposited poly-Si and poly-SiO$_x$N$_y$

A variation of the doping level might increase the strength of the field-effect passivation but might also induce detrimental strong dopant in-diffusion. The passivation quality in terms of both implied open circuit voltage iV_{oc} and contact recombination current density J_c under variation of R_{B2H6} during PECVD deposition[53] of the same (p) poly-Si layers as discussed in the previous section on FZ substrates after SPC is plotted in Fig. 5.13 a). In Fig. 5.13 b) the passivation quality in terms of iV_{oc} after each hydrogenation step is plotted for the same PECVD deposited[54] (p) poly-SiO$_x$N$_y$ layers as discussed in the previous section without J_c values since its evaluation failed on the Cz substrates. The overall low passivation quality of the (p) poly-Si layers is attributed to unintentionally left out process steps, namely the plasma pre-cleaning of the interfacial oxide immediately before deposition

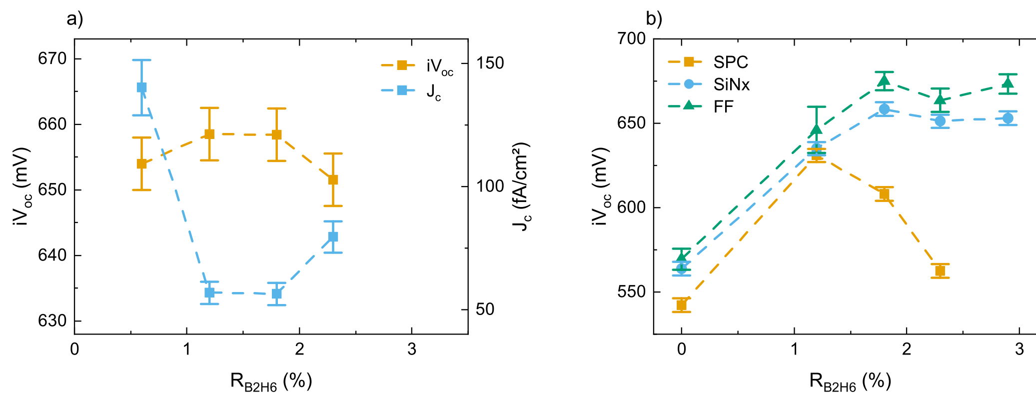

FIGURE 5.13. PCD determined passivation quality in terms of implied open circuit voltage iV_{oc} and contact recombination current density J_c of a) (p) poly-Si layers on FZ substrates and b) (p) poly-SiO$_x$N$_y$ layers on Cz substrate as function of R_{B2H6} during PECVD deposition. In b) iV_{oc} after each hydrogenation step, but no J_c values are shown due to the Cz substrate. Dashed lines are a guide for the eye.

[53] PECVD deposition parameters: $P = 20$ W, $p = 400$ mTorr, $T_{set} = 100$°C, $R_{H2} = 99\%$, $R_{B2H6} = 0.6 - 2.3\%$, $t = 1800$ s.
[54] PECVD deposition parameters: $P = 100$ W, $p = 600$ mTorr, $T_{set} = 300$°C, $R_{N2O} = 20\%$, $R_{H2} = 0\%$, $R_{B2H6} = 0 - 2.9\%$, $t = 60$ s.

(Sec. 2.3.1), the wet-chemical pre-cleaning immediately before SPC (Sec. 2.4.1) and the hydrogenation as a whole (Sec. 2.5). In comparison, a similar PECVD in-situ doped (p) poly-Si layer with slightly different deposition parameters[55] and also without wet-chemical pre-cleaning before SPC showed a passivation quality of $iV_{oc} = 716$ mV and $J_c = 9.2$ fA/cm^2 after hydrogenation.

In Fig. 5.13 a maximum in iV_{oc} around $R_{B2H6} \approx 1.5\%$ is visible for both the (p) poly-Si layers and the (p) poly-SiO_xN_y layers but is not significant for the former ones when considering the uncertainties and the small absolute variation of a few millivolts. In contrast, the corresponding minimum in J_c is a factor of two lower than the maximum value and thus should be seen as significant. Based on this finding the question arises if these maxima correspond to an optimal dopant concentration which evolved due to a too low field-effect passivation for lower concentrations and a detrimental strong dopant in-diffusion for higher concentrations. The answer can be found in the passivation quality tracked after each hydrogenation step for the (p) poly-SiO_xN_y layers as shown in in Fig. 5.13 b). After SiN_x:H deposition and FF the iV_{oc} values increased up to a plateau for $R_{B2H6} > 1.5\%$ and no decreasing trend was observed for the layers measured after SPC. This observation directly excludes the interpretation of detrimental strong in-diffusion as this should also lower the passivation quality after hydrogenation. The decrease after SPC is rather attributed to induced defects at the SiO_x/c-Si interface due to boron penetration (Sec. 1.3.1) which were in turn saturated during hydrogenation. Transferred to the (p) poly-Si layers, this interpretation would also explain the minimum of J_c in Fig. 5.13 a) which should also form a plateau at lower values after hydrogenation. Altogether it is concluded that the poly-Si/SiO_x contacts based on in-situ doped PECVD deposited layers in this thesis were not limited by detrimental strong in-diffusion within the investigated boron concentration range, at least for the standard SPC parameters.

MSD Deposited (p) poly-Si

Fig. 5.14 a) shows the passivation quality in terms of iV_{oc} and J_c of the same MSD deposited[56] in-situ doped (p) poly-Si layers as discussed in the previous section on FZ substrates tracked after each hydrogenation step. Typically most of the gain in passivation quality is achieved already by the SiN_x:H deposition as it was also the case here for J_c. In contrast, iV_{oc} increased only marginally after SiN_x:H deposition whereas it increased significantly by ~ 40 mV after FF. This might be a hint for bulk defect passivation since the corrected J_c, evaluated as described in Sec. 3.6.1, describes the recombination near the surface only. In contrast, iV_{oc} is indeed affected also by the bulk quality. Therefore, one may argue that surface defects might be passivated already after SiN_x:H deposition (strong J_c reduction) and bulk defects only subsequently by hydrogen diffusion into the silicon substrate during FF (strong iV_{oc} increase) which did not occur during the lower temperature of the SiN_x:H deposition. For all other doping methods most of the gain in passivation quality took place already after SiN_x:H deposition. Such bulk defects could originate from the large iron impurity in the boron sputter target which was only used for the in-situ doped (p) poly-Si layers (Sec. 2.3.2). These iron impurities could eventually diffuse into the substrate during SPC. The hypothesis of bulk defects is further supported by the fit intercept during J_c evaluation which can be interpreted as an indicator

[55] PECVD deposition parameters: $P = 20$ W, $p = 400$ mTorr, $T_{set} = 400$°C, $R_{B2H6} = 1.2\%$, $R_{H2} = 99\%$, $t = 1200$ s.

[56] MSD deposition parameters: $P_{Si} = 300$ W, $P_B = 250$ W, $p = 2$ mTorr, $Q_{Ar} = 80$ sccm, $T_{set} = 450$°C, $d_{target} = 17$ cm, $t = 2000$ s. In order to protect the quartz tube furnace from iron contamination originating from the boron sputter target, a ~30 nm (i) a-Si capping layer was deposited with equal parameters except of $P_B = 0$ W and $t_{cap} = 750$ s.

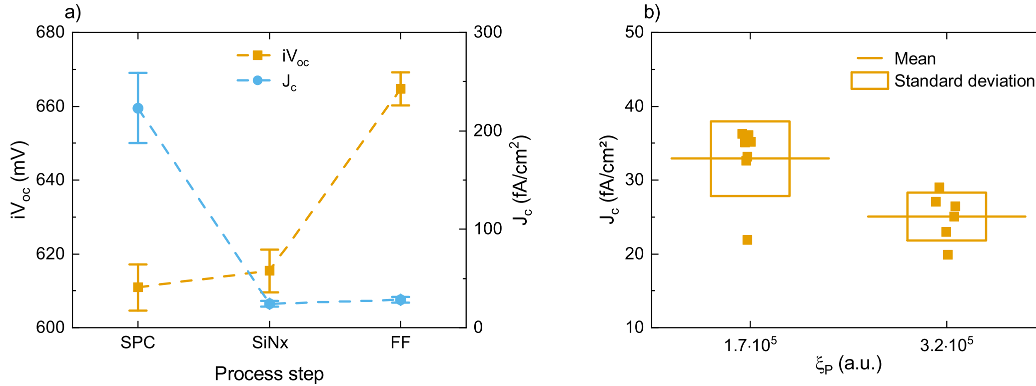

FIGURE 5.14. PCD determined passivation quality in terms of implied open circuit voltage iV_{oc} and contact recombination current density J_c of a) MSD deposited (p) poly-Si layers after each hydrogenation step. Dashed lines are a guide for the eye. b) J_c of MSD deposited (n) poly-Si layers for different phosphorus concentrations expressed as ξ_P. Horizontal lines mark the mean values and boxes the standard deviation ranges.

for the bulk lifetime [157]. The value of 100 µs after SiN_x:H deposition is far too low for 200 Ωcm FZ material indicating the presence of bulks defects. This low value was increased to 500 µs after FF indicating the bulk defect saturation during FF. Furthermore, a large $J_c > 1000$ fA/cm^2 is obtained if calculated from the measured $iV_{oc} = 615$ mV after SiN_x:H deposition via eq. 3.41.

Based on this it is concluded that the iron impurities indeed affect the passivation quality as suspected but the loss is at least partly compensated by hydrogenation induced defect saturation. However, the boron concentration can be approximated qualitatively by the GD-OES and SE determined quantity ξ_B (eq. 3.10). It was with $\xi_B \approx 1.4 \cdot 10^6$ roughly one order of magnitude larger for the MSD deposited in-situ doped (p) poly-Si layers compared to PECVD deposited (p) poly-Si. Hence, it is not clear if the rather low overall passivation quality compared to all other layer types is a consequence of these iron induced bulk defects or of a detrimental strong boron in-diffusion caused by a too large dopant concentration. Either way these layers have to be further optimized to be considered for application in an actual solar cell.

MSD Deposited (n) poly-Si

Fig. 5.14 b) shows the passivation quality in terms of iV_{oc} for the same MSD deposited ex-situ doped (n) poly-Si layers on FZ substrates after hydrogenation as discussed in the previous section with different phosphorus concentrations expressed as ξ_P (eq. 3.10) for eight samples at each concentration. As these samples were prepared early in the stage of MSD deposition development, no wet chemical pre-cleaning before SPC was performed, leading to the low overall iV_{oc} values, which were expected to ba larger in face of the used FZ substrates after hydrogenation. Even if the scattering is larger compared to the corresponding ρ_{PCD} data in Fig. 5.12 b), the passivation quality was higher for the layer with larger phosphorus concentration. As this concentration originated from the standard $POCl_3$-diffusion, which was determined to be close to both solubility limits as discussed in Sec. 5.2.1, the optimal dopant concentration should be expected between the concentrations presented in Fig. 5.14 b).

A sputter damage during MSD a-Si deposition might be an issue for a high passivation quality of poly-Si/SiO_x contacts. As previously discussed in Sec. 2.3.2, the sputter parameter can be adjusted to minimize the sputter damage in the first place. Using the optimized standard parameter set therein, the passivation quality was tracked after each process flow step (Chapter 2, Fig. 2.1) starting from the thermal oxidation and the subsequent (i) a-Si MSD deposition. The following SPC was performed with the standard $POCl_3$-diffusion and also in N_2 atmosphere as an intrinsic reference without field-effect passivation, followed by the hydrogenation whereas the SiN_x:H deposition and FF were not tracked individually. For the $POCl_3$ diffused sample set after hydrogenation one sample was removed from the analysis as its passivation quality was even worse than before hydrogenation. All results are depicted in terms of iV_{oc} (Fig. 5.15 a) and J_c (Fig. 5.15 b). The overall trend is the same for both quantities while the logarithmic scale for J_c reflects the exponential relation between J_c and iV_{oc} according to the one-diode model (eq. 3.41). Therefore, only the trend in iV_{oc} is discussed in the following and was published before in [61].

The sputter damage can be seen in a decrease in iV_{oc} of $\sim$ 10 mV during (i) a-Si deposition which was quiet low since the sputter parameters were previously optimized for a low sputter damage (Sec. 2.3.2). The following SPC in inert N_2 atmosphere further decreased iV_{oc} to values below 600 mV. This could be attributed to pinhole formation inducing local intrinsic (i) poly-Si/c-Si interfaces which were not passivated and hence defect-rich. In contrast, the $POCl_3$ diffused samples showed higher iV_{oc} values compared to the initial passivation quality of the as-grown interfacial oxide reference. This observation is directly explained by the additional field effect passivation. During hydrogenation interface defects were saturated by hydrogen for both the intrinsic and phosphorus doped poly-Si layers and leading to a maximum passivation quality of $iV_{oc} = 719$ mV and $J_c = 7.9$ fA/cm^2. As the iV_{oc} values of the intrinsic layers are comparable to or higher than the ones of the as-grown interfacial oxide reference, it can be concluded that during hydrogenation the sputter damage as well as the defects at the local (i) poly-Si/c-Si interfaces were compensated. Hence, for optimized sputter parameters the sputter damage during MSD deposition of (i) a-Si layers can be neglected in the context of poly-Si/SiO_x contacts.

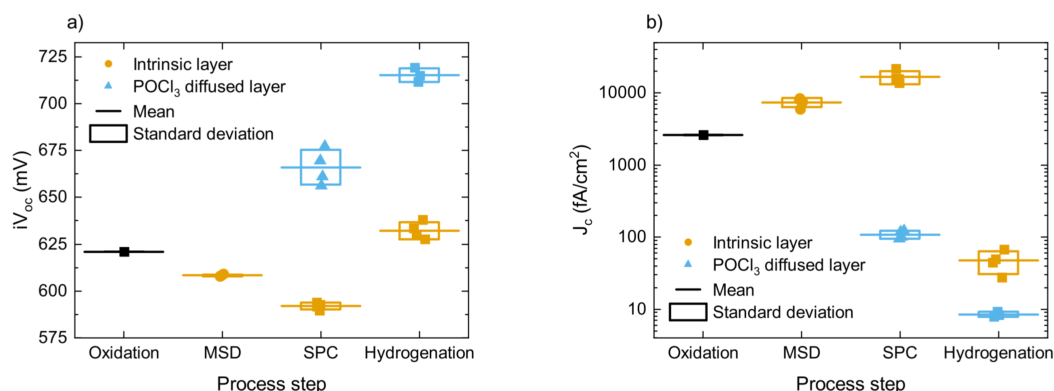

FIGURE 5.15. PCD determined passivation quality in terms of a) implied open circuit voltage iV_{oc} and b) contact recombination current density J_c of MSD deposited intrinsic (i) poly-Si and $POCl_3$-diffused (n) poly-Si layers after each process step. Horizontal lines mark the mean values and boxes the standard deviation ranges.

5.2.6. Section Summary

For all layer compositions a difference between total and electrically active dopant concentration was found as well as a concentration pile-up close to or within the interfacial oxide for both dopant polarities while the phosphorus pile-up was more pronounced. Another identified asymmetry between both dopant polarities for the pure poly-Si layers without incorporated light elements was an efficiency limitation by FCA for phosphorus doping and by detrimental strong in-diffusion for boron doping. Additionally, MSD deposited (p) poly-Si layers were limited by bulk defects which were only partly saturated during hydrogenation. A similar asymmetry was revealed between both deposition techniques with significantly lower internal stress σ for MSD compared to PECVD deposited poly-Si.

5.3. Incorporation of Light Elements

ABSTRACT. *All light elements were incorporated linearly with the corresponding gas flow ratio R_X while the boron concentration was slightly increased at the same time even though R_{B2H6} was kept constant. For increasing R_{N2O} and c_C the crystallinity decreased whilst the internal stress followed this decreasing trend for nitrogen and oxygen incorporation but followed an inverted trend for carbon incorporation. With higher c_C the parasitic absorption and the resistivity increased linearly due to the decreasing crystallinity. For higher R_{N2O} a minimum of the parasitic absorption and a continuous increase in the resistivity was observed. A degradation of the passivation quality was found for both larger R_{N2O} and R_{CO2}. In contrast, for a variation of c_C the passivation quality was found to be rather determined by the unintentionally varied boron concentration.*

The incorporation of light elements changed the layer composition by a variation of the three gas flow ratios during PECVD deposition R_{CO2}, R_{N2O} and R_{CH4} leading to (p) poly-SiO_x, (p) poly-SiO_xN_y and (p) poly-SiC_x. The (p) poly-SiO_x layers were studied in less detail due to significantly reduced deposition rates and hence practical limitations during fabrication. The gas flow ratios were varied in the range of $R_{CO2} = 4.8 - 20\%$ and $R_{N2O} = 4.8 - 28.6\%$. Regarding the (p) poly-SiC_x layers, not only R_{CH4} was varied but also the plasma power P, chamber pressure p and deposition temperature T_{set} during PECVD deposition[57]. In order to avoid a discussion about numerous parameter dependencies, all variations are presented with respect to the Rutherford backscattering spectrometry (RBS)[58] determined carbon concentration c_C instead of R_{CH4}. Details about the RBS measurement technique can be found in [190]. For an isolated study of the incorporation of light elements all other parameters were kept constant during each variation and the standard SPC parameters were used ($T_{SPC} = 920°C$ and $t_{SPC} = 30$ min). The results on the (p) poly-SiO_x and (p) poly-SiO_xN_y layers were already reported in the master's thesis of Raphael Glatthaar [180] and the results on the (p) poly-SiC_x layers will be published [181].

5.3.1. Composition

In order to interpret changes in material properties due to the incorporation of light elements it is useful to determine the actual concentration of these elements $c_{O/N/C}$. Under variation of the gas

[57] A complete list of all deposition parameter variations can be found in the Appendix A.3.

[58] RBS measurements were performed by Sören Möller at the Institute of Energy and Climate Research - Plasma Physics IEK-4, Forschungszentrum Jülich.

flow ratio R_{N2O} this determination was done for nitrogen and oxygen in (p) poly-SiO_xN_y layers by GD-OES adjusted multi-matrix calibrations[59] (Sec. 3.7) and under variation of R_{CH4} for carbon in (p) poly-SiC_x layers by RBS. For these three elements a linear relation was found between the atomic concentrations and the gas flow ratio R_X for PECVD deposited (p) poly-SiO_xN_y layers[60] on FZ substrates and (p) poly-SiC_x layers[61] on FS substrates, as presented in Fig. 5.16 a).

The slope corresponding to the nitrogen concentration is roughly a factor of three larger than the slope of the oxygen concentration. Even though this does not reflect the ratio of these elements in the initial N_2O molecule, it implies a constant nitrogen to oxygen ratio which significantly influences the properties of oxynitride layers if not constant [191]. As the uncertainties of the nitrogen and oxygen concentrations are rather large, they should be seen as a rough orientation instead of precise determinations. Therefore, variations of the gas flow ratio R_{N2O} are discussed in the following which is linearly connected to both the oxygen and nitrogen concentrations.

As stated above, the idea behind this section is to vary only the light elements concentration while keeping the dopant concentration constant. This was attempted by a constant diborane gas flow ratio R_{B2H6}. However, an increase in the boron concentrations expressed as ξ_B (eq. 3.10) with increasing gas flow ratios R_X was observed for PECVD deposited (p) poly-SiO_x layers[62] and (p) poly-SiO_xN_y layers[63] as well as the same (p) poly-SiC_x layers as shown in Fig. 5.16 a) on Cz substrates and is shown in Fig. 5.16 b). Addition of the gases CO_2, N_2O and CH_4 changed the plasma composition and as such the formed radicals and growth mechanisms due to additional surface atom and bond configurations. A detailed investigation on this matter was not performed.

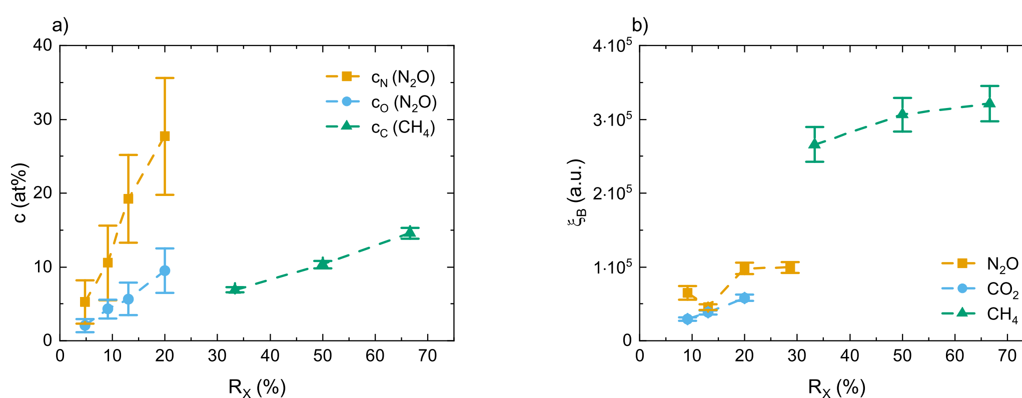

FIGURE 5.16. a) Calibrated concentrations of nitrogen c_N and oxygen c_O for poly-SiO_xN_y layers determined by GD-OES and of carbon c_C for poly-SiC_x layers determined by RBS and b) GD-OES and SE determined boron concentrations expressed as ξ_B as function of the corresponding gas flow ratios R_X during PECVD deposition with X being either N_2O or CH_4. Dashed lines are a guide for the eye.

[59] Details regarding the used calibration standards can be found in the Appendix A.2.

[60] PECVD deposition parameters: $P = 50$ W, $p = 600$ mTorr, $T_{set} = 300°C$, $R_{B2H6} = 0.6\%$, $R_{N2O} = 4.8 - 20\%$, $t = 75$ s.

[61] PECVD deposition parameters: $P = 20$ W, $p = 800$ mTorr, $T_{set} = 400°C$, $R_{B2H6} = 1.4\%$, $R_{CH4} = 33/50/66\%$, $t = 300/420/510$ s.

[62] PECVD deposition parameters: $P = 20$ W, $p = 400$ mTorr, $T_{set} = 400°C$, $R_{B2H6} = 0.6\%$, $R_{H2} = 99\%$, $R_{CO2} = 4.8 - 20\%$, $t = 2400$ s.

[63] PECVD deposition parameters: $P = 100$ W, $p = 450$ mTorr, $T_{set} = 300°C$, $R_{B2H6} = 0.6\%$, $R_{N2O} = 4.8 - 28.6\%$, $t = 75$ s.

5.3.2. Microstructure

Besides the desired beneficial optical effects, the incorporation of light elements is expected to decrease the crystallinity χ_c for constant SPC parameters which in turn increases the resistivity and parasitic light absorption. All crystallinities shown in Fig. 5.17 for PECVD deposited[64] (p) poly-SiO_xN_y as well as for all (p) poly-SiC_x layers on FS substrates are $< 50\%$ which is significantly lower than the crystallinity of the (p) poly-Si layer of $\chi_c = 80.3\%$ without light elements (Table 5.1). Interestingly, the crystallinity in Fig. 5.17 does not exceed the hypothetical maximum crystallinity achievable with the standard SPC parameters as suggested above in Sec. 5.2.2. Besides the expected decreasing trend for $R_{N2O} \geq 13\%$, an increase in crystallinity up to $R_{N2O} = 13\%$ was observed so that a maximum crystallinity evolved. A similar minimum is visible for the boron concentration ξ_B at the same gas flow ratio of $R_{N2O} = 13\%$ in Fig. 5.16 b). In contrast, a clear linear decrease in χ_c with increasing carbon concentration c_C was observed as depicted in Fig. 5.17 b) for the PECVD deposited (p) poly-SiC_x layers[65]. This trend implies that the crystallinity might even exceed $\chi_c > 60\%$ for $c_C < 5$ at% which should be beneficial for a reduction of both the parasitic absorption and the resistivity.

As described in Sec. 3.3.2, on the one hand the shift of the RS determined peak corresponding to the crystalline phase $\Delta\omega_{521}$ may be interpreted as caused by either quantum confinement from small crystallites with diameter d_c in the nanometer range or by internal stress σ. For poly-Si layers with a large crystallinity the grains are assumed to be too large for quantum confinement as the cause for the shift and thus $\Delta\omega_{521}$ should be attributed to internal stress via eq. 3.19. On the other hand, for as-deposited nc-Si layers with a low crystallinity the shift $\Delta\omega_{521}$ is typically attributed to this quantum confinement. However, as the crystallinities presented in Fig. 5.17 mostly lie in the intermediate range the interpretation of the observed shift $\Delta\omega_{521}$ is ambiguous. Due to lack of clear evidence and

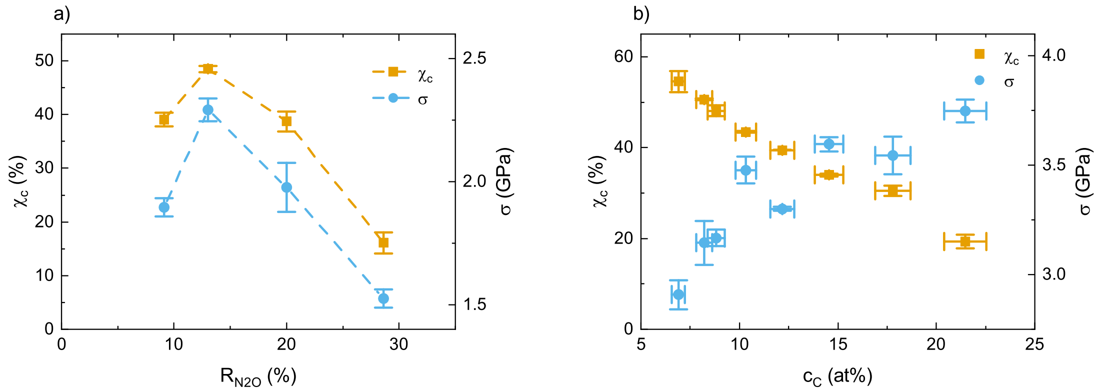

FIGURE 5.17. RS determined crystallinity χ_c and internal stress σ for a) (p) poly-SiO_xN_y layers as function of R_{N2O} during PECVD deposition and for b) PECVD deposited (p) poly-SiC_x layers as function of the RBS determined carbon concentration c_C. Dashed lines are a guide for the eye.

[64] PECVD deposition parameters: $P = 100$ W, $p = 450$ mTorr, $T_{set} = 300°$C, $R_{B2H6} = 0.6\%$, $R_{H2} = 0\%$, $t = 75$ s.

[65] As the layer thicknesses were in the range of $120 - 260$ nm, the RS signal from the substrate was absorbed within these layers. Therefore, a standard baseline correction of the RS spectra was performed instead of the FS substrate correction described in Sec. 3.3.

for reasons of consistency, $\Delta\omega_{521}$ is depicted as internal stress σ via eq. 3.19 in Fig. 5.17 for both the (p) poly-SiO_xN_y and (p) poly-SiC_x layers.

As-deposited amorphous layers were reported to show compressive stress with negative σ values for both a-SiO_xN_y [191] and a-SiC_x [192] layers, which during SPC converts into tensile stress with positive σ values. A reason for this might be hydrogen effusion leaving silicon dangling bonds behind, which form bonds with the light elements and thereby induce a film shrinkage and in turn a rather tensile than compressive stress [191]. The corresponding shift $\Delta\omega_{521}$ occurs in the same direction as the shift caused by quantum confinement and hence both effects would add up.

In Fig. 5.17 a) σ follows the trend of the crystallinity under variation of R_{N2O} and thus $c_{O/N}$ which is in line with the notion of a SPC induced change from compressive to tensile stress for (p) poly-SiO_xN_y layers. At least for as-deposited (i) a-SiO_xN_y layers a stress reduction with increasing oxygen concentration was observed [191, 193]. Furthermore, in [191] also a stress maximum with increasing oxygen concentration was reported similar to the one depicted in Fig. 5.17 a). In contrast, for the (p) poly-SiC_x layers the trend of σ was inverted with respect to χ_c (Fig. 5.17 b). Following the picture of hydrogen effusion induced formation of bonds of silicon with the light elements in [191] these observations can be explained as follows. The twofold Si-O-Si bonds in (p) poly-SiO_xN_y can be assumed to be more flexible than the fourfold Si=C=Si bonds in (p) poly-SiC_x leading to a stress relaxation for larger oxygen concentrations and a stress enhancement for larger carbon concentrations.

5.3.3. Optical Properties

The main concern regarding incorporation of light elements in the poly-Si layer is a reduced parasitic absorption by widening the band gap. This was already discussed in Sec. 5.2.3 for a comparison of pure (p) poly-Si and (p) poly-SiO_xN_y deposited at $R_{N2O} = 20\%$. In Fig. 5.18 J_{PA} and E_{04} are presented for the same PECVD deposited[66] (p) poly-SiO_xN_y layers as discussed in the previous section on FS substrates under variation of R_{N2O}. Up to $R_{N2O} = 20\%$ J_{PA} reduced and E_{04} increased with

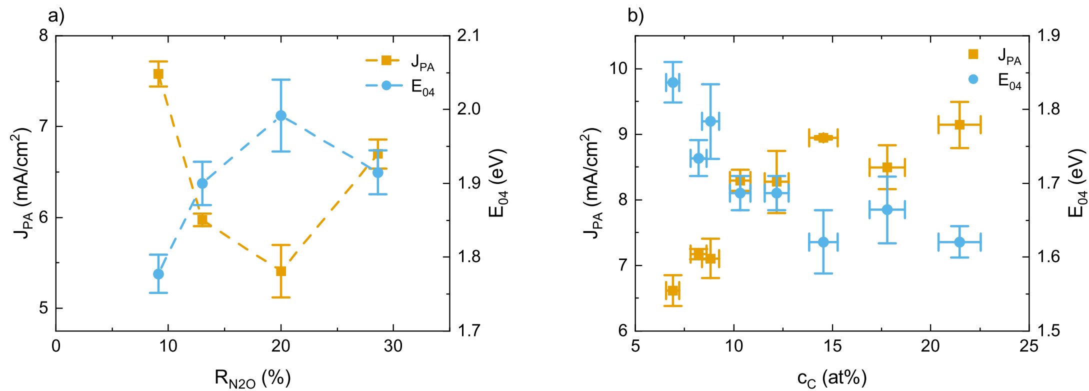

FIGURE 5.18. SE determined parasitic absorption current density J_{PA} and optical band gap E_{04} for a) (p) poly-SiO_xN_y layers as function of R_{N2O} during PECVD deposition and for b) PECVD deposited (p) poly-SiC_x layers as function of the RBS determined carbon concentration c_C. Dashed lines are a guide for the eye.

[66]PECVD deposition parameters: $P = 100$ W, $p = 450$ mTorr, $T_{set} = 300°$C, $R_{B2H6} = 0.6\%$, $R_{N2O} = 4.8-28.6\%$, $t = 75$ s.

increasing R_{N2O}. For $R_{N2O} > 20\%$ both trends were inverted which can be explained by the significantly reduced crystallinity for $R_{N2O} = 28.6\%$ that was shown in the previous section. This explanation is further supported by the failure of the standard SE poly-Si fit procedure (Sec. 3.4.1) for $R_{N2O} \geq 20\%$ which resulted in large uncertainties of one of the two Tauc-Lorentz oscillators. Therefore, only one Tauc-Lorentz oscillator was applied which in turn corresponds to the standard SE fit procedure for a-Si (Sec. 3.4.1). However, the narrowing of the optical band gap for $R_{N2O} \geq 20\%$ is rather unexpected. Altogether, the decrease in parasitic absorption by incorporation of light elements and the opposing increase by a lower crystallinity are competing effects whereas a minimum parasitic absorption was observed around $R_{N2O} = 20\%$.

For all PECVD deposited (p) poly-SiC_x layers on FS substrates[67] a continuous increase in J_{PA} for higher carbon concentrations c_C was found as depicted in Fig. 5.18 b). Analogous to the oxygen and nitrogen incorporation it was most likely caused by the linearly decreasing crystallinity (Fig. 5.17 b). In this sense, the desired reduced parasitic absorption by carbon incorporation was compensated by the lower crystallinity within the investigated concentration range. This conclusion was also reached before in the context of (n) poly-SiC_x/SiO_x contacts in [45]. However, the clear continuous relation to the carbon concentration suggests an even reduced J_{PA} for $c_C < 5$ at% by an increased crystallinity.

In the literature it was reported that carbon incorporation widens the band gap [45, 67]. Though, the optical band gap E_{04} decreased for higher c_C within the range of typical a-Si:H band gap values (Sec. 4.1.3). This contradiction is somehow unexpected but might be related to the lower crystallinity which increased the parasitic absorption J_{PA} opposed to the desired reduction. However, for lower crystallinities E_{04} should approach the a-Si:H band gap range from lower values with an increasing trend. The observed inverted trend is a hint for more complex interdependencies between the carbon incorporation and the crystallinity than would be expected for pure a-Si:H ($c_C = 0$ at%). Nevertheless, E_{04} showed inverted trends for the (p) poly-SiO_xN_y and (p) poly-SiC_x layers similar to the RS shift $\Delta\omega_{521}$ as was discussed in the previous section.

5.3.4. Resistivity

On the one hand, nitrogen and oxygen might act as donors and saturate defects at grain boundaries, which reduces the potential barrier height and thus decreases the resistivity (Sec. 2.4.3). On the other hand, a low crystallinity implies domains of amorphous material with inefficient carrier transport via extended or band tail states as was also discussed in the context of the dopant variation above in Sec. 5.2.4 and in Sec. 2.3.3. Both resistivities ρ_{HE} and ρ_{PCD} of the same (p) poly-SiO_xN_y layers[68] as discussed in the previous section on FS (HE[69]) and on FZ (PCD) substrates increased with higher R_{N2O} as is evident from Fig. 5.19 a). The difference of two orders of magnitude between HE and PCD determined resistivities can be explained analogous to the discussion above in Sec. 5.2.4. Furthermore, ρ_{PCD} values for $R_{N2O} < 20\%$ are missing as blistering occurred on the FZ but not on the FS substrates.

---

[67] In order to account for a thickness inhomogeneity within the light spot during SE measurements one fit parameter was added to the standard poly-Si model described in Sec. 3.4.1.

[68] PECVD deposition parameters: $P = 100$ W, $p = 450$ mTorr, $T_{set} = 300$°C, $R_{B2H6} = 0.6\%$, $R_{N2O} = 4.8 - 28.6\%$, $t = 75$ s.

[69] For these HE measurements only, a centrally aligned square of 1 x 1 cm^2 was separated from the surrounding layers by laser ablation.

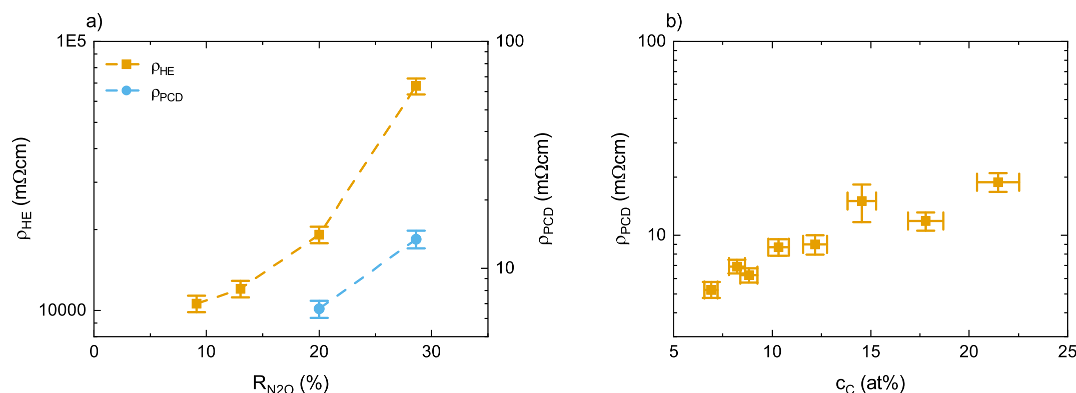

FIGURE 5.19. HE and PCD determined resistivities ρ_{HE} and ρ_{PCD} for a) (p) poly-SiO$_x$N$_y$ layers on FZ substrates (PCD) and FS substrates (HE) as function of R_{N2O} during PECVD deposition and for b) PECVD deposited (p) poly-SiC$_x$ layers as function of the RBS determined carbon concentration c_C. Dashed lines are a guide for the eye.

Assuming a strict correlation between the resistivity ρ_{HE} and the crystallinity χ_c, one would expect a minimum in ρ_{HE} for $R_{N2O} = 13\%$ as it was observed for χ_c (Fig. 5.17 a). Since no such minimum is visible in Fig. 5.19 a), an additional effect increasing the resistivity must exist. Based on the data in Fig. 5.16 a), the nitrogen concentration exceeded $c_N = 10$ at% already for $R_{N2O} = 9.1\%$ being the lowest gas flow ratio in Fig. 5.19 a). Together with an oxygen concentration of $c_O \approx 5$ at% these concentrations are too large to show the beneficial doping effect. Rather, the insulating property of stoichiometric silicon Si_3N_4 or SiO_2 seems to dominate the resistivity over the doping effect which can be seen as the additional effect increasing ρ_{HE} for higher R_{N2O}. Interestingly, the observed increase in boron concentration for higher R_{N2O} (Sec. 5.3.1) seems to play a minor role within this context.

For all (p) poly-SiC$_x$ layers the resistivity was only determined by PCD on Cz substrates as no ohmic contact was achievable between two pins during HE measurements. Hence, similar to the discussion above in Sec. 5.2.4 regarding the (p) poly-SiO$_x$N$_y$ layers, also the (p) poly-SiC$_x$ layers show an insufficiently high lateral resistivity. In Fig. 5.19 b) a basically linear increase for higher carbon concentrations c_C is visible, which can be explained by the decreasing crystallinity that was presented before in Fig. 5.17 b). This observation again emphasizes the key role of the crystallinity for light elements incorporation in the context of poly-Si/SiO$_x$ contacts. As it was the case for the discussion regarding the parasitic absorption in the previous section, the clear continuous relation to the carbon concentration suggests a further reduced resistivity for even lower concentrations $c_C <$ 5 at%.

5.3.5. Passivation Quality

A band gap widening by light element incorporation might increase the band offset and as such the field-effect passivation, which should lead to higher iV_{oc} and lower J_c values. The corresponding results of the same PECVD deposited (p) poly-SiO$_x$[70] and (p) poly-SiO$_x$N$_y$ layers[71] layers as

[70]PECVD deposition parameters: $P = 20$ W, $p = 400$ mTorr, $T_{set} = 400°$C, $R_{B2H6} = 0.6\%$, $R_{H2} = 99\%$, $R_{CO2} = 20 - 28.6\%$, $t = 2400$ s.

[71]PECVD deposition parameters: $P = 100$ W, $p = 450$ mTorr, $T_{set} = 300°$C, $R_{B2H6} = 0.6\%$, $R_{N2O} = 9.1 - 20\%$, $t = 75$ s.

discussed in the previous sections on FZ substrates after hydrogenation are presented in Fig. 5.20. Since blistering occurred for $R_{N2O} < 20\%$ and $R_{CO2} < 9.1\%$ (Sec. 5.1.1), measurements were only possible for layers deposited at higher gas flow ratios. The layer deposited with $R_{CO2} = 13\%$ was processed separately at a different time and hence it is not possible to identify the lower passivation quality as a systematic effect or as an individual process flow related degradation. An unexpectedly lower oxygen content for this sample compared to the sample deposited at $R_{CO2} = 9.1\%$ was observed by GD-OES measurements which is a hint for a dysfunctional CO_2 gas supplement during this deposition. If this data point is neglected, a decrease in passivation quality for the higher gas flow ratios was observed for both CO_2 and N_2O.

Two possible explanations can be put forward. First, the dopant concentration might be insufficient to shift the Fermi energy level close enough to the band edge to make use of the stronger field-effect by a wider band gap (Sec. 1.3). Second, diffusion of nitrogen into the interfacial oxide could degrade its chemical passivation ability by inducing electrically active defects as it was observed for a deliberate nitridation of the interfacial oxide [20]. This second explanation would provide a reason for the huge loss in iV_{oc} of ~ 70 mV for the (p) poly-SiO_xN_y compared to the rather small loss of ~ 10 mV for the (p) poly-SiO_x layer where no nitrogen is present at all. Interestingly, the maximum in passivation quality appeared for equal deposition parameters and at the same gas flow ratio $R_{N2O} = 20\%$ where also the minimum of the parasitic absorption was found (Fig. 5.18 a). Even if the question of an underlying mechanism is not answered at this point, the corresponding PECVD parameter set seems to be adequate for a functioning poly-SiO_xN_y/SiO_x contact.

Regarding carbon incorporation, the J_c values as function of the carbon concentration c_C are shown in Fig. 5.21 a) for all PECVD deposited (p) poly-SiC_x layers on Cz substrates after hydrogenation. First of all the excellent passivation quality with most values of $iV_{oc} > 700$ mV and $J_c < 10$ fA/cm^2 should be highlighted as they were achieved on Cz substrates and are comparable to the values of the (p) poly-SiO_x and (p) poly-SiO_xN_y layers on FZ substrates (Fig. 5.20). Ignoring the data point with the largest uncertainty at $c_C = 6.9$ at%, the J_c values show a parabolic relation for increasing c_C with a maximum around $c_C = 15$ at% as is evident from the weighted parabolic fit in Fig. 5.21 a).

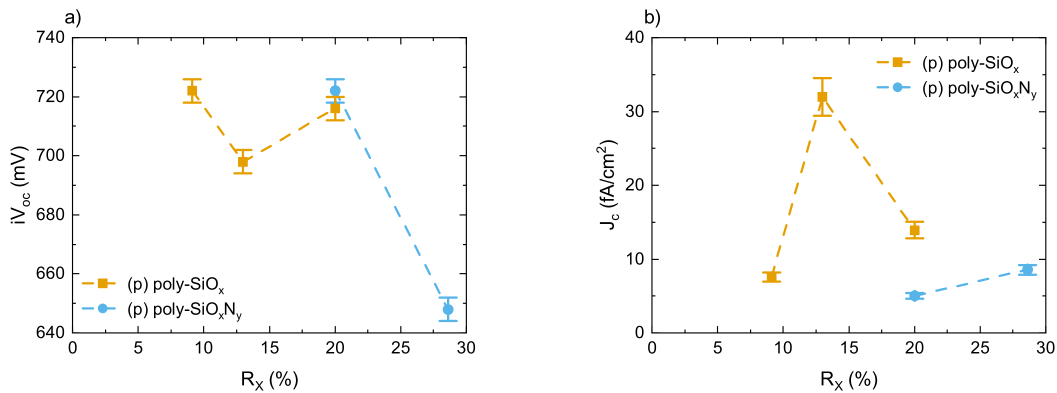

FIGURE 5.20. PCD determined passivation quality in terms of a) implied open circuit voltage iV_{oc} and b) contact recombination current density J_c for (p) poly-SiO_x and (p) poly-SiO_xN_y layers as function of the corresponding gas flow ratios R_X during PECVD deposition with X being either CO_2 or N_2O. Dashed lines are a guide for the eye.

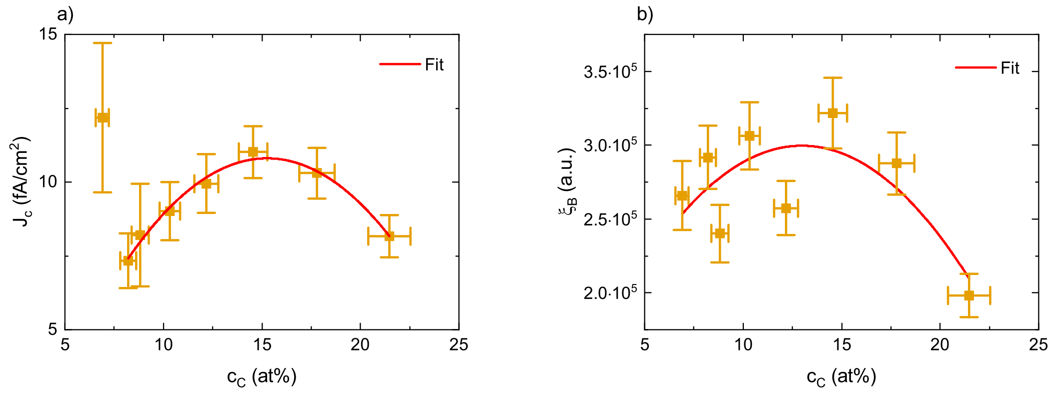

FIGURE 5.21. a) PCD determined contact recombination current density J_c and b) GD-OES and SE determined boron concentration expressed as ξ_B for PECVD deposited (p) poly-SiC$_x$ layers on Cz substrates as function of the RBS determined carbon concentration c_C. The solid red lines are parabolic weighted fits.

As stated above in Sec. 5.3.1, the boron concentration increased for higher R_{CH4} even if $R_{B2H6} = 1.6\%$ was kept constant. As several parameters were varied for the deposition of the (p) poly-SiC$_x$ layers, no linear relationship between c_C and R_{CH4} was found and thus also no linear relation between c_C and the boron concentration is expected. Indeed, Fig. 5.21 b) shows the boron concentration expressed as ξ_B (eq. 3.10) as function of c_C and a parabola can be fitted here similar to Fig. 5.21 a). The fit should be understood only as illustration of a trend considering the uncertainties and no underlying physical relation is claimed. Based on this similarity between $J_c\,(c_C)$ and $\xi_B\,(c_C)$ it can be concluded that the boron concentration is responsible for the variation of $J_c\,(\xi_B)$ in Fig. 5.21 a). This implies in particular that no relation between c_C and a higher passivation quality was found for $c_C \gtrsim 6\%$ as could have been expected from an increased band gap by carbon incorporation. Since these layers were measured after hydrogenation, which was observed to compensate defects induced by boron penetration of the SiO$_x$/c-Si interface (Sec. 5.2.5), the relation between ξ_B and J_c should rather be attributed to a detrimental strong in-diffusion of boron through the interfacial oxide into the Cz substrate.

Altogether, the low J_c values in the range of $c_C = 8 - 10$ at% correspond to the lowest ρ_{PCD} values and therefore this concentration range is identified as promising for an application in a (p) poly-SiC$_x$/SiO$_x$ contact in an actual solar cell. As mentioned several times before, a larger crystallinity is expected for even lower $c_C < 5$ at% which would in turn further decrease ρ_{PCD}. A simultaneous significant degradation of the passivation quality is not expected according to the small absolute variation range in J_c of ~ 5 fA/cm^2.

5.3.6. Section Summary

Most importantly the crystallinity χ_c was identified as a key parameter determining all properties of the layers relevant for an application in a solar cell. For larger concentrations of light elements the crystallinity decreases and thus raises the parasitic absorption as well as the resistivity. Several differences between the (p) poly-SiO$_x$N$_y$ and (p) poly-SiC$_x$ layers were identified. For the former ones optimal oxygen and nitrogen concentrations $c_{O/N}$ were found regarding the parasitic absorption and passivation quality while for the latter ones these properties could be further optimized by

decreasing the carbon concentration c_C and thus increasing the crystallinity χ_c. An exception to this is the passivation quality J_c of the (p) poly-SiC_x layers which was found to be determined by the unintentionally varied boron concentration ξ_B and as such being independent of the carbon concentration c_C in the investigated range. Regarding the resistivities ρ_{PCD} both layer types showed a continuous increase for larger concentrations of light elements whilst an internal stress σ relaxation was observed for the (p) poly-SiO_xN_y layers and a stress enlargement for the (p) poly-SiC_x layers. Altogether the desired band gap widening was observed for incorporation of light elements. This in turn led only to a reduced parasitic absorption current density J_{PA} whereas an increased passivation quality was not clearly identified.

5.4. Adjustment of the SPC Parameters for Larger Crystallinity

ABSTRACT. *Higher temperatures T_{SPC} were shown to increase both the crystallinity and the internal stress while the parasitic absorption and resistivity were reduced as a consequence of the higher crystallinity. Longer durations t_{SPC} also increased the crystallinity but decreased the internal stress. Only the resistivity was reduced due to the higher crystallinity whereas the parasitic absorption remained constant within the uncertainties when applying longer durations t_{SPC}. While no significant influence of T_{SPC} on the passivation quality was observed, it strongly degraded for longer durations t_{SPC}. The standard SPC parameter were found to be the passivation quality optimum within the investigated SPC parameter ranges.*

A variation of the SPC parameters was only performed on PECVD deposited[72] (p) poly-SiO_xN_y layers with the optimal parameter set that was found in the previous sections. The temperature was varied in the range of $T_{SPC} = 850-1000$°C for a constant duration of $t_{SPC} = 180$ min and the duration was varied in the range of $t_{SPC} = 30-300$ min for a constant temperature of $T_{SPC} = 920$°C. Hence, the parameter combination of $T_{SPC} = 920$°C and $t_{SPC} = 180$ min is included in both variations. Note that the standard SPC parameters, as described in Sec. 2.4.1, were only considered in the variation of t_{SPC}. The gas flow ratios R_{B2H6} and R_{N2O} were kept constant ensuring an isolated study of the influence of the SPC parameters without a change in dopant or light elements concentration.

5.4.1. Microstructure

In Sec. 5.3.2 a clear decrease in the crystallinity χ_c with increasing gas flow ratio R_{N2O} was found which in turn significantly increased the resistivity of the (p) poly-SiO_xN_y layers. Based on this observations the question arises if a variation of the SPC temperature T_{SPC} and duration t_{SPC} is able to raise the crystallinity. In order to answer this question the (p) poly-SiO_xN_y layers were deposited on FS substrates and χ_c was determined under variation of T_{SPC} (Fig. 5.22 a) and under variation of t_{SPC} (Fig. 5.22 b). χ_c clearly increased with both T_{SPC} and t_{SPC}. Thus, it is possible to increase the crystallinity as desired with adjusted SPC parameters. However, even if the maximum value at $t_{SPC} = 300$ min exceeded the maximum crystallinity for the standard SPC parameters, it is still $\sim 20\%_{abs}$ below the crystallinity of pure (p) poly-Si without light elements of $\chi_c = 80.3\%$ (Table 5.1).

[72]PECVD deposition parameters: $P = 100$ W, $p = 450$ mTorr, $T_{set} = 300$°C, $R_{B2H6} = 0.6\%$, $R_{N2O} = 20\%$, $t = 75$ s.

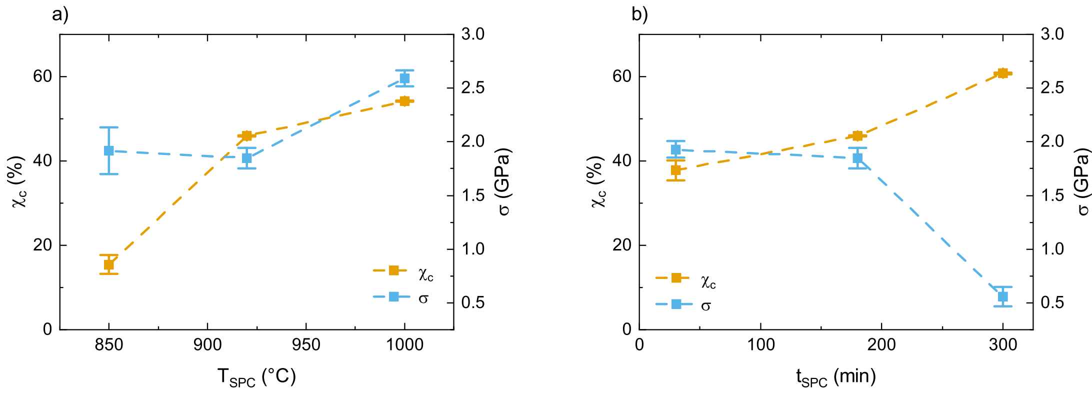

FIGURE 5.22. RS determined crystallinity χ_c and internal stress σ for PECVD deposited (p) poly-SiO_xN_y layers as function of a) the SPC temperature T_{SPC} at a constant duration of $t_{SPC} = 180$ min and of b) the SPC duration t_{SPC} at a constant temperature of $T_{SPC} = 920°C$. Dashed lines are a guide for the eye.

Within the uncertainties the internal stress σ also increased with T_{SPC} as was previously reported for a-SiO_xN_y layers for a lower temperature range [194]. In contrast, σ decreased with the duration t_{SPC}. Such an inverted trend of σ with respect to χ_c was already discussed above within the context of (p) poly-SiC_x layers (Sec. 5.3.2). Therein it was stated that the interpretation of the shift $\Delta\omega_{521}$ is ambiguous and could be seen as a result of internal stress (eq. 3.19), of quantum confinement caused by small crystallites with diameter d_c (eq. 3.18) or of a combination of both. According to eq. 3.18, a trend in σ is translated into an inverted trend in d_c, thus increasing crystallite diameter. This would be in accordance with the simultaneously increasing χ_c values (Fig. 5.22 b) but not with the T_{SPC} variation with an inverted trend (Fig. 5.22 a). Since the crystallinities for $T_{SPC} > 900°C$ were in the same range as for the t_{SPC} variation, these observations cannot be definitely interpreted without further microscopic investigations.

5.4.2. Optical Properties

For higher T_{SPC} and t_{SPC} a decrease in the parasitic absorption current density J_{PA} is expected due to the increased crystallinity (Fig. 5.22). Fig. 5.23 presents J_{PA} and E_{04} values determined from SE measurements in the spectral range of 240 – 1000 nm of the (p) poly-SiO_xN_y layers on FS substrates under variation of the SPC parameters. Indeed, J_{PA} decreased continuously with increasing T_{SPC} as can be seen in Fig. 5.23 a). In contrast, J_{PA} was constant within the uncertainties or even slightly increased for longer durations t_{SPC} (Fig. 5.23 b). In the previous section a similar opposing trend under T_{SPC} or t_{SPC} variation was found for the internal stress σ, indicating a relation between the optical property J_{PA} and the microstructural property σ.

E_{04} in Fig. 5.23 follows an inverted trend with respect to J_{PA} for both the T_{SPC} and t_{SPC} variations while for the latter also no change in both optical properties can be assumed within the uncertainty ranges. However, it is difficult to clearly identify the origin of these trends in E_{04} as the crystallinity changed simultaneously. This is particularly true for the rather large crystallinity variation ranges of $\sim 40\%_{abs}$ for T_{SPC} and $\sim 20\%_{abs}$ for t_{SPC}. Anyway, the expected relation of a lower parasitic absorption and a wider band gap is observable for the T_{SPC} parameter variation and additionally correlates with higher crystallinities as presented in the previous section.

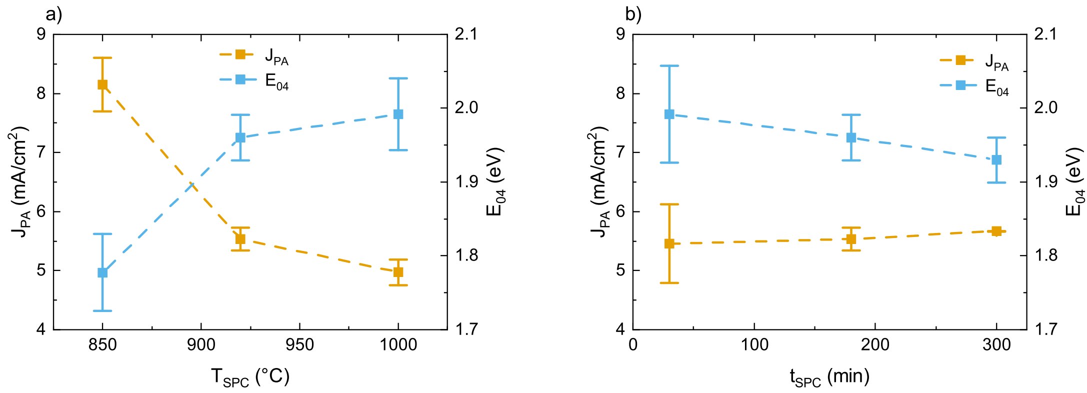

FIGURE 5.23. SE determined parasitic absorption current density J_{PA} and optical band gap E_{04} for PECVD deposited (p) poly-SiO_xN_y layers as function of a) the SPC temperature T_{SPC} at a constant duration of $t_{SPC} = 180$ min and of b) the SPC duration t_{SPC} at a constant temperature of $T_{SPC} = 920$°C. Dashed lines are a guide for the eye.

5.4.3. Resistivity

In Sec. 5.19 higher resistivities for an increasing gas flow ratio R_{N2O} were observed, which is detrimental for an application in a poly-Si/SiO_x contact. The increased crystallinity by variation of the SPC parameters (Sec. 5.4.1) should reverse this effect and decrease the resistivity. In Fig. 5.24 ρ_{PCD} under variation of the SPC parameters is shown for the (p) poly-SiO_xN_y layers on FZ substrate. HE measurements failed as no ohmic contact could be established between the pins and the layer. Likewise, the PCD resistivity measurement on the sample belonging to $T_{SPC} = 850$°C failed. The reason for this is most likely a too high resistivity on the high ohmic FZ substrate leading to a negative output value from the PCD calibration which is imprecise for high resistivities.

The remaining ρ_{PCD} values showed a decreasing trend for both increasing T_{SPC} and t_{SPC} down to values below the resistivities determined for similar layers and the standard SPC parameters and therefore followed the trend of the crystallinity. The slight increase in resistivity for $t_{SPC} > 180$ min should be attributed to process fluctuations or measurement artifacts as no mechanism is known

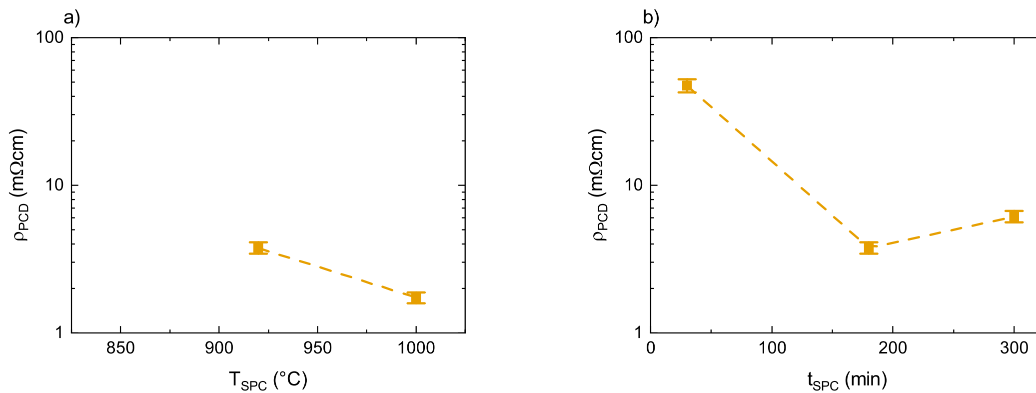

FIGURE 5.24. PCD determined resistivities ρ_{PCD} for PECVD deposited (p) poly-SiO_xN_y layers on FZ substrates as function of a) the SPC temperature T_{SPC} at a constant duration of $t_{SPC} = 180$ min and of b) the SPC duration t_{SPC} at a constant temperature of $T_{SPC} = 920$°C. Dashed lines are a guide for the eye.

which would increase the resistivity from a lower value after 180 min of thermal treatment to a higher value after 120 additional minutes. Since the lowest ρ_{PCD} value was found for an elevated temperature of $T_{SPC} = 1000°C$, the temperature rather than the duration should be increased for a reduction of the resistivity.

5.4.4. Passivation Quality

So far the SPC parameter variation revealed higher crystallinities and thereby lower parasitic absorption and resistivities for increasing T_{SPC} and t_{SPC} as desired. The main constraint for a SPC parameter range suitable for a poly-Si/SiO$_x$ contact is a detrimental strong in-diffusion of dopants. In Fig. 5.25 the passivation quality in terms of iV_{oc} and J_c is presented for both parameter variations on the (p) poly-SiO$_x$N$_y$ layers on FZ substrates after hydrogenation. With increasing T_{SPC}, iV_{oc} slightly decreased and J_c was constant within the uncertainties leading to the conclusion that at least for the rather thick interfacial oxide with a thickness of 2.5 nm used throughout this thesis the influence of the temperature up to 1000°C can be considered as not degrading the passivation quality.

In contrast, the variation of the duration t_{SPC} strongly decreased iV_{oc} by ~ 60 mV and increased J_c by ~ 60 fA/cm^2 which can be explained by detrimental strong in-diffusion of boron. Boron penetration induced defects at the SiO$_x$/c-Si interface can be excluded as an explanation since these should be saturated during hydrogenation (Sec. 5.2.5). A similar passivation degradation in the range of $t_{SPC} = 30-60$ min was observed for low pressure CVD deposited in-situ phosphorus doped (n) poly-SiO/SiO$_x$ contacts [195]. Hence, the duration of the SPC seems to be a critical parameter for dopant in-diffusion and thus has to be adjusted carefully. In a strict sense, this conclusion is only valid for the constant temperature of $T_{SPC} = 920°C$ during t_{SPC} variation. Likewise, the slight degradation of the passivation quality under variation of the temperature only holds true for the constant duration of $t_{SPC} = 180$ min. This corresponds to the already degraded passivation quality in Fig. 5.25 b). Altogether it is sensible to increase T_{SPC} rather than t_{SPC} in order to avoid a degradation

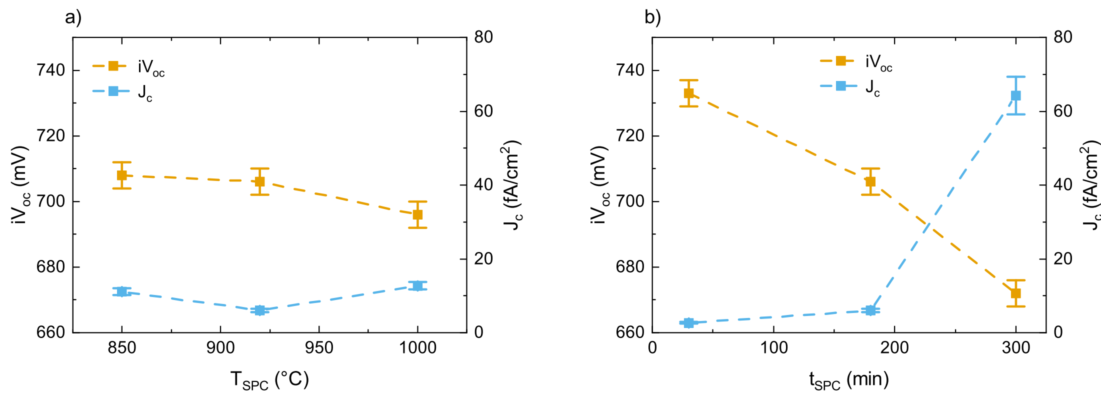

FIGURE 5.25. PCD determined passivation quality in terms of implied open circuit voltage iV_{oc} and contact recombination current density J_c for PECVD deposited (p) poly-SiO$_x$N$_y$ layers on FZ substrates as function of a) the SPC temperature T_{SPC} at a constant duration of $t_{SPC} = 180$ min and of b) the SPC duration t_{SPC} at a constant temperature of $T_{SPC} = 920°C$. Dashed lines are a guide for the eye.

of the passivation quality. Interestingly, the same conclusion was drawn in the previous section in order to achieve lower resistivities.

It should be emphasized that the standard SPC parameters of $T_{SPC} = 920°C$ and $t_{SPC} = 30$ min led to the highest passivation quality presented in this thesis with $iV_{oc} = 734$ mV and $J_c = 2.3$ fA/cm^2 after hydrogenation. This values constitute a significant improvement compared to the MSD deposited (n) poly-Si layers without incorporated light elements and a maximal achieved passivation quality of $iV_{oc} = 719$ mV and $J_c = 7.9$ fA/cm^2 (Sec. 5.2.5). Typically, n-type poly-Si is reported to yield higher passivation qualities compared to p-type poly-Si and yet the passivation quality of the (p) poly-SiO_xN_y layer is higher. One reason for this could be the larger band gap as discussed in Sec. 5.2.3 which might enhance the field-effect passivation (Sec. 2.4.3). Another explanation could simply be that the whole (p) poly-SiO_xN_y process was adjusted carefully as described throughout this chapter while for the (n) poly-Si layers no optimization of the $POCl_3$-diffusion parameters and as such of the dopant concentration was executed. Independent of the exact reason the incorporation of light elements might not only offer a strategy for a decreased parasitic absorption but also for a high passivation quality with p-type poly-Si/SiO_x contacts.

5.4.5. Section Summary

A larger crystallinity and in turn a lower parasitic absorption J_{PA} and a lower resistivity were achieved rather by higher temperatures T_{SPC} than by longer durations t_{SPC}. Likewise, the degradation of the passivation quality by detrimental strong dopant in-diffusion was significantly stronger for the t_{SPC} variation supporting T_{SPC} as being more suitable for reaching larger crystallinities.

CHAPTER 6

Classification in Context of Solar Cell Performance

In the introduction of Chapter 5 an overview was given regarding influences of process parameters during poly-Si/SiO_x fabrication on the solar cell efficiency (Fig. 5.1). These relations should hold regardless of the specific poly-Si layer composition wherefore in Sec. 6.1 each relation is discussed based on the in Chapter 5 presented data for all layer types simultaneously. For each dependency all available data is shown but for a specific layer not all quantities were determined, in particular not if the layer was only deposited on silicon but not on FS substrates. Hence, the number of data points per layer type may differ from one plot to another. For the purpose of consistency, the legend and symbols corresponding to a layer type are the same throughout this chapter even if no data point of a specific layer type might be shown. Sec. 6.2 provides a detailed analysis on a future application of the best performing layers for each layer type in an actual solar cell by means of the selectivity S_{10} and an ideal solar cell efficiency η_{ideal}.

All fits performed and shown in this chapter are intended to underline the observed trends and do not claim an underlying strict relation to the chosen fit function. Furthermore, throughout this chapter no uncertainties are plotted as each data point belongs to one single sample and thus no statistics are available. Details regarding systematical uncertainties can be found in the corresponding sections in Chapter 3.

6.1. Dependencies Between Process Parameters and Solar Cell Performance

In this section the data presented previously in Chapter 5 for all layer types, namely for MSD deposited (p) / (n) poly-Si and PECVD deposited (p) poly-Si / (p) poly-SiO_x / (p) poly-SiO_xN_y / (p) poly-SiC_x, are summarized and simultaneously discussed in light of the dependencies between the process parameter variations and the solar cell efficiency as summarized in Fig. 5.1. Starting from the dependencies which arise from a variation of the dopant concentration expressed as $\xi_{B/P}$, the dependencies regarding the incorporation of light elements and regarding the SPC parameter variations are simultaneously discussed as functions of the crystallinity χ_c since it was identified to be a key parameter for both variations. The remaining dependencies that are subsequently outlined are connected to a widening of the optical band gap E_{04}.

Besides these dependencies arising from a variation of the process parameters, the solar cell efficiency is mainly influenced by the contact recombination current density J_c, the contact resistance ρ_c represented by $\rho_{PCD/HE}$ according to eq. 1.7 and the parasitic absorption current density J_{PA}. Therefore, dependencies between those quantities are also examined in the following.

6.1.1. Dependencies Regarding the Dopant Concentration $\xi_{B/P}$

All dependencies shown in Fig. 6.1 are functions of $\xi_{B/P}$ which should be interpreted carefully for two reasons. First, the GD-OES measured intensity for either boron or phosphorus depends on the corresponding spectral emission line as well as on the detector type. As $\xi_{B/P}$ is determined by the integral over these intensities, the absolute values of ξ_B for boron and ξ_P for phosphorus are not comparable. Second, at some point during the experimental phase of this thesis the boron detector was replaced by a different model reducing the measured intensities roughly by a factor of two and thus comparability is not necessarily guaranteed even though the affected measurements were corrected by this factor.

The first dependency regarding the dopant concentration deals with J_c after hydrogenation as function of $\xi_{B/P}$. An optimal dopant concentration should exist due to a decrease from the larger band offset for low $\xi_{B/P}$ and an increase due to detrimental strong dopant in-diffusion for large $\xi_{B/P}$. Except for the MSD deposited (p) poly-Si layers, all layer types showed an excellent passivation quality with $J_c < 10$ fA/cm^2 at least for one layer. The only significant trend in Fig. 6.1 a) is a continuous decrease of J_c for the MSD deposited (n) poly-Si layers. Yet, it is not clear if this trend could be extended to values close to $J_c \approx 1$ fA/cm^2 as were reported before for (n) poly-Si/SiO$_x$ contacts [23]. Since large phosphorus concentrations close to the solubility limit were found for these layers (Sec. 5.2.1), it is assumed that J_c cannot be significantly reduced by adjusting the dopant

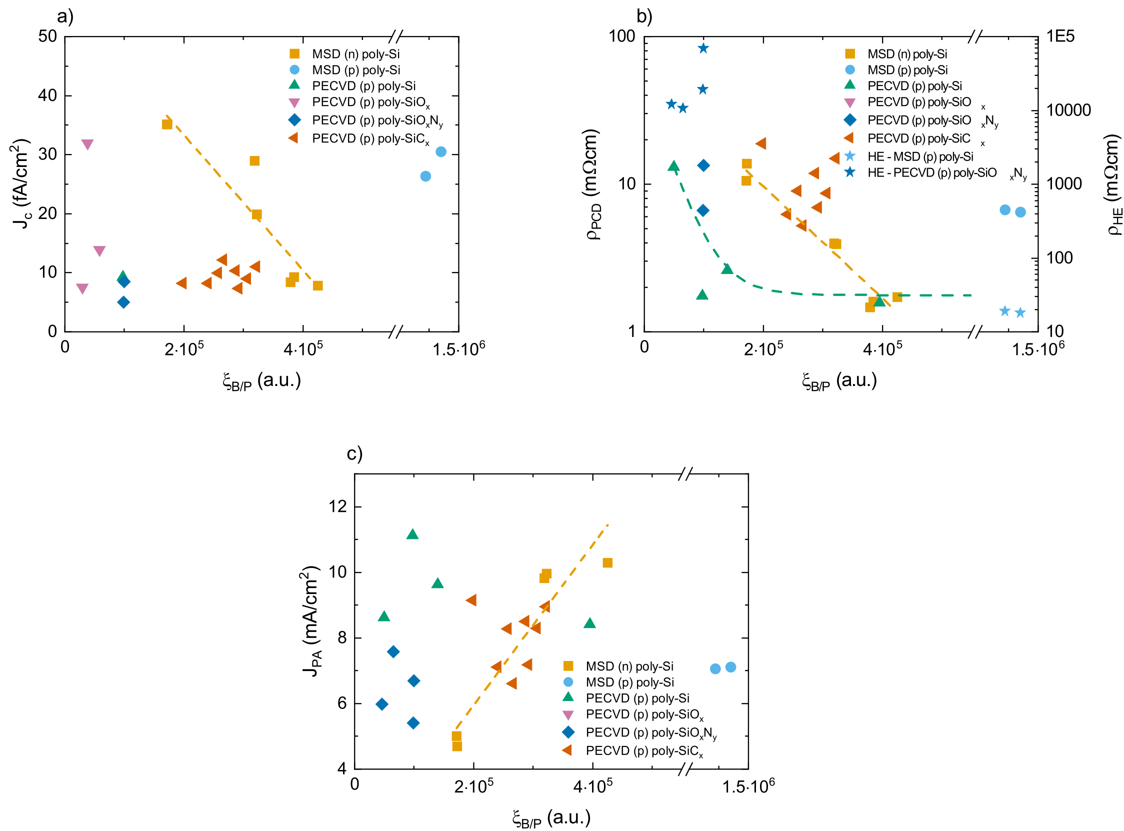

FIGURE 6.1. Dependencies for all layer types between the dopant concentration expressed as $\xi_{B/P}$ and a) the contact recombination current density J_c, b) the resistivity $\rho_{PCD/HE}$ and c) the parasitic absorption current density J_{PA}. Dashed lines are fits to the data of the corresponding color.

concentration. A reason for the difference to lower values reported in the literature could be the observed sputter damage (Sec. 5.2.5) if the hydrogenation does not completely compensate the induced damage to the interfacial oxide.

For all other layer types no clear trend was observed as no explicit variation of the dopant concentration was performed. Solely for the PECVD deposited (p) poly-SiC_x layers a slight increase in J_c for higher ξ_B can be supposed, which is supported by the similar dependency on the carbon concentration for both $J_c(c_C)$ and $\xi_B(c_C)$ (Sec. 5.3.5). Another conclusion can be drawn from the rather large values for the MSD deposited (p) poly-Si layers with $J_c > 25$ fA/cm^2. As the corresponding ξ_B values are one order of magnitude larger, the rather high J_c values are most likely caused by detrimental strong in-diffusion of dopants into the substrate. A reason why this detrimental strong in-diffusion was not observed for the MSD deposited (n) poly-Si layers could be that the interfacial oxide is a stronger diffusion barrier for phosphorus compared to boron (Sec. 1.3).

In Fig. 6.1 b) the relation between $\xi_{B/P}$ and the resistivity $\rho_{PCD/HE}$ is shown and a clear decrease is expected for higher dopant concentrations. Such decreasing trends were found for the PECVD deposited (p) poly-Si layers and the MSD deposited (n) poly-Si layers with a saturation at similar values of roughly $\rho_{PCD} \approx 1.6$ mΩcm. In both cases $\xi_{B/P}$ was varied intentionally while for all other layer types without explicit variation of $\xi_{B/P}$ the vertically distributed values with differences in resistivities of up to a factor of five are attributed to the incorporation of light elements rather than to a difference in dopant concentration (Sec. 5.3.4).

The remaining dependency concerning the dopant concentrations, as summarized in Fig. 5.1, is an increased parasitic absorption current density J_{PA} due to FCA. In the corresponding Fig. 6.1 c) the previously discussed FCA of the MSD deposited (n) poly-Si layers (Sec. 5.2.3) can be seen as clear increase of J_{PA} by more than a factor of two for larger ξ_P. In contrast, all layer types with incorporated light elements are vertically distributed, as it is also the case in Fig. 6.1 b) regarding ρ_{PCD}. This similarity arises from the dependency of both ρ_{PCD} and J_{PA} on the light elements concentrations (Sec. 5.3.3). In contrast, the data belonging to the PECVD deposited (p) poly-Si layers are distributed horizontally, meaning that J_{PA} of these layers is completely ignorant to ξ_B in the investigated range. In particular, no significant FCA occurs in these cases. Interestingly, also the MSD deposited (p) poly-Si layers with a significantly larger boron concentration showed an intermediate parasitic absorption of $J_{PA} \approx 7$ mA/cm^2 and were thus also not dominated by FCA. This observation is in line with an expected weaker FCA for holes compared to electrons due to the larger effective masses and is also evident from the parametrization in [196].

In summary, all dependencies regarding the dopant concentration as expected from the overview in Fig. 5.1 were observed under explicit variation of the dopant concentration while the unintended variation of the dopant concentration due to incorporation of light elements under constant diborane flow ratio as observed in Sec. 5.3.1 seems to play a minor role.

6.1.2. Dependencies Regarding the Crystallinity χ_c

The crystallinity χ_c was found to be a key parameter as it increased both the resistivity $\rho_{PCD/HE}$ and the parasitic absorption J_{PA} of the poly-Si layer, which at least for the (p) poly-SiO_xN_y was observed to overcompensate the beneficial reduction of J_{PA} by the band gap widening (Sec. 5.3.3). Besides the (p) poly-SiO_xN_y and (p) poly-SiC_xlayers with incorporated light elements, only crystallinity data for

the MSD deposited (p) poly-Si layers are available and shown in Fig. 6.2. For all other layer types the crystallinities presented in Table 5.1 were determined from different experiment series and thus comparability is not necessarily ensured. Nevertheless, as the crystallinities therein were found to be larger than $\chi_c \gtrsim 80\%$, the crystallinity does rather not seem to be a limiting factor for these pure poly-Si layers without incorporated light elements.

In Fig. 6.2 a) J_{PA} is presented as function of χ_c for all available data. As expected, a clear decrease in J_{PA} was observed with higher χ_c whilst the relation for the (p) poly-SiC_x layers showed less scattering from the trend compared to the (p) poly-SiO_xN_y layers. As discussed in Sec. 5.3.3, this decreasing relation could be extended to even lower J_{PA} values by decreasing the carbon concentration and hence increasing χ_c. In contrast, for the (p) poly-SiO_xN_y layers an optimum of J_{PA} under variation of the oxygen and nitrogen concentration was already discussed (Sec. 5.3.3). The lowest parasitic absorption in Fig. 6.2 a) corresponds to these optimal concentrations. Altogether, the incorporation of light elements was able to reduce J_{PA} below the reference values of the MSD deposited (p) poly-Si layers (Fig. 6.2 a).

In Fig. 6.2 b) the resistivity $\rho_{PCD/HE}$ is shown as function of χ_c. Similar to J_{PA}, the decrease of ρ_{PCD} for higher χ_c showed less scattering for the (p) poly-SiC_x layers whereas the HE measured resistivities ρ_{HE} of the (p) poly-SiO_xN_y layers appeared similar. It thus seems that for the layers with incorporated light elements a crystallinity of roughly $\chi_c \approx 55\%$ cannot be exceeded with the standard SPC parameters (marked by the vertical dashed black line in Fig. 6.2 b). In line with the discussion of J_{PA} (Fig. 6.2 a) it seems to be possible for the (p) poly-SiC_x layers to further reduce ρ_{PCD} with lower carbon concentrations $c_C < 5$ at% and thus larger χ_c. This similarity underlines the character of χ_c as a key parameter for poly-Si/SiO_x contacts with incorporated light elements.

In summary, both dependencies regarding the crystallinity as summarized in Fig. 5.1, namely larger J_{PA} and $\rho_{PCD/HE}$ values for higher crystallinities, were observed for the layers with incorporated light elements. For the standard SPC parameters a maximum crystallinity of $\chi_c \approx 55\%$ was found. This crystallinity could be further increased and thus J_{PA} and ρ_{PCD} decreased by an adjustment of

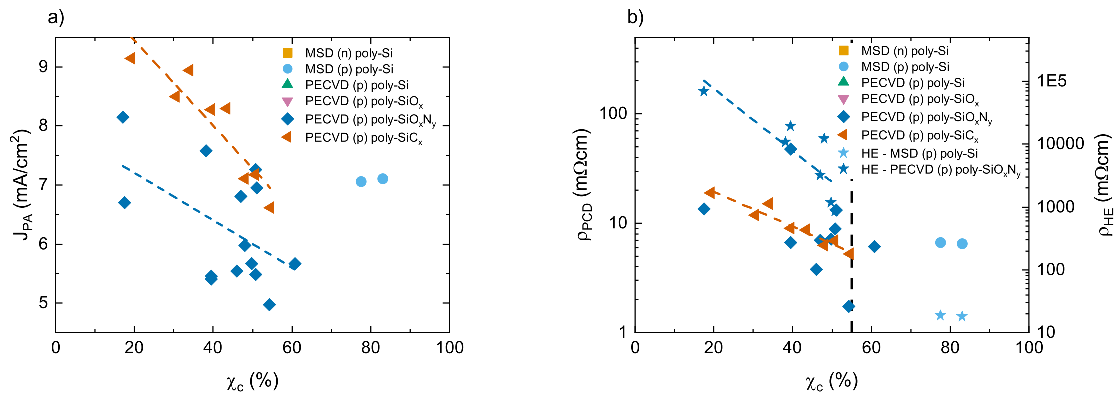

FIGURE 6.2. Dependencies for all layer types between the crystallinity χ_c and a) the parasitic absorption current density J_{PA} and b) the resistivity $\rho_{PCD/HE}$. Vertical dashed black line marks the maximum achievable crystallinity for the standard SPC parameter of $\chi_c \approx 55\%$ and the other dashed lines are fits to the data of the corresponding color.

the SPC parameters but at the expense of a higher J_c (Sec. 5.4). Regarding the (p) poly-SiC$_x$ layers the crystallinity could also be increased by a reduction of the carbon concentration (Sec. 5.3.2).

6.1.3. Dependencies Regarding the Optical Band Gap E_{04}

The remaining two dependencies of the summary in Fig. 5.1 are related to the widening of the optical band gap E_{04}, which should decrease the parasitic absorption current density J_{PA} as well as the contact recombination current density J_c. Fig. 6.3 a) shows J_{PA} as function of E_{04} and two distinct linear relations evolved for both dopant polarities separately. In general, both relations clearly represent the decreased parasitic absorption by widening the optical band gap. For the boron doped layers, the layers with incorporated light elements showed larger E_{04} maximum values compared to the pure (p) poly-Si layers. Also regarding the (p) poly-Si layers, a difference between both deposition methods PECVD and MSD was observed likely caused by the absence of hydrogen during growth and SPC of the MSD deposited layers as discussed before in the context of significantly different internal stresses (Sec. 5.2.2).

In the case of phosphorus doping, the large difference in J_{PA} may be attributed to FCA in the samples with $J_{PA} \approx 10$ mA/cm^2. Even if the lowest parasitic absorption was found for (n) poly-Si without incorporated light elements, this layer showed a too high resistivity and a too low passivation quality for being appropriate for an actual poly-Si/SiO$_x$ contact.

It should be noted that on the one hand both J_{PA} and E_{04} were determined by the same SE measurement and hence the observed clear linear relations could also be reduced to this fact. On the other hand, as all poly-Si layers were modeled by two oscillators with ten fit parameters (Sec. 3.4.1) there should be enough degrees of freedom for J_{PA} and E_{04} to vary independently.

The influence of E_{04} on the passivation quality in terms of J_c is shown in Fig. 6.3 b). In contrast to all other dependencies discussed in this section, no clear dependency is observed if each layer type is evaluated separately. However, if all data points are considered together regardless of their layer type it can be stated that most of the lowest J_c values were found for larger E_{04} which reflects the lager band offset.

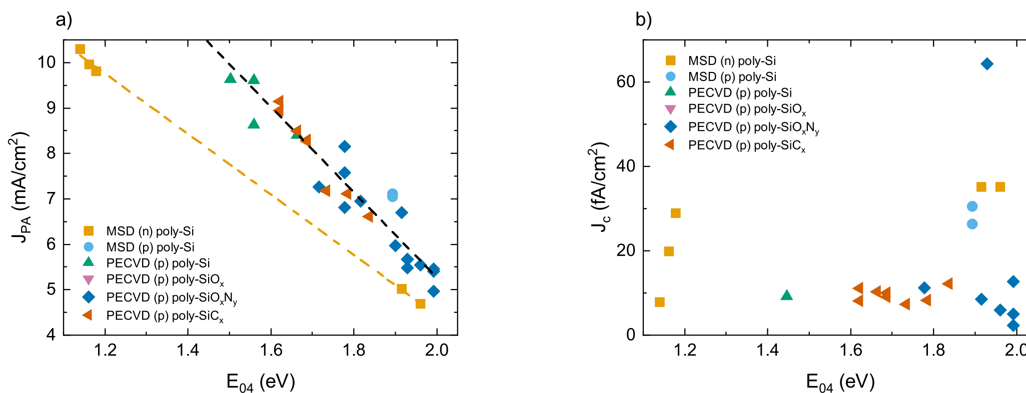

FIGURE 6.3. Dependencies for all layer types between the optical band gap E_{04} and a) the parasitic absorption current density J_{PA} and b) the contact recombination current density J_c. Dashed lines are linear fits of all data points for (n) doped (yellow) and (p) doped (black) layers separately.

In summary, both dependencies regarding a decrease in J_{PA} and J_c for higher E_{04} were observed for all layer types. However, these relations have to be interpreted cautiously as the band gap of a mixed-phase material is not well-defined.

6.1.4. Dependencies Between J_c, ρ_{PCD} and J_{PA}

Apart from the dependencies between the process parameters and the solar cell efficiency as summarized in Fig. 5.1 and discussed so far, the efficiency of a solar cell based on poly-Si/SiO$_x$ contacts is mainly determined by its selectivity $S_{10}(J_c, \rho_c)$ (eq. 1.9). Additionally, if applied on the front side of a solar cell, also parasitic absorption J_{PA} plays an important role. In order to gain information about limitations and trade-offs regarding the efficiency, dependencies between these parameters J_{PA}, J_c and ρ_{PCD} as a measure for ρ_c are plotted in Fig. 6.4 in all combinations. It was found to be practical to divide the layer types into two groups, namely the pure poly-Si layers without incorporated light elements and the layers with incorporated light elements.

Fig. 6.4 a) shows an overall increase in J_c with lower J_{PA} for all pure poly-Si layers without incorporated light elements, depicted by the linear fit through all data points corresponding to these layers. This relation reflects the opposing effects of higher doping concentrations on J_c and J_{PA} where the J_c is reduced by a larger band offset and J_{PA} is increased by FCA absorption. Interestingly, FCA was

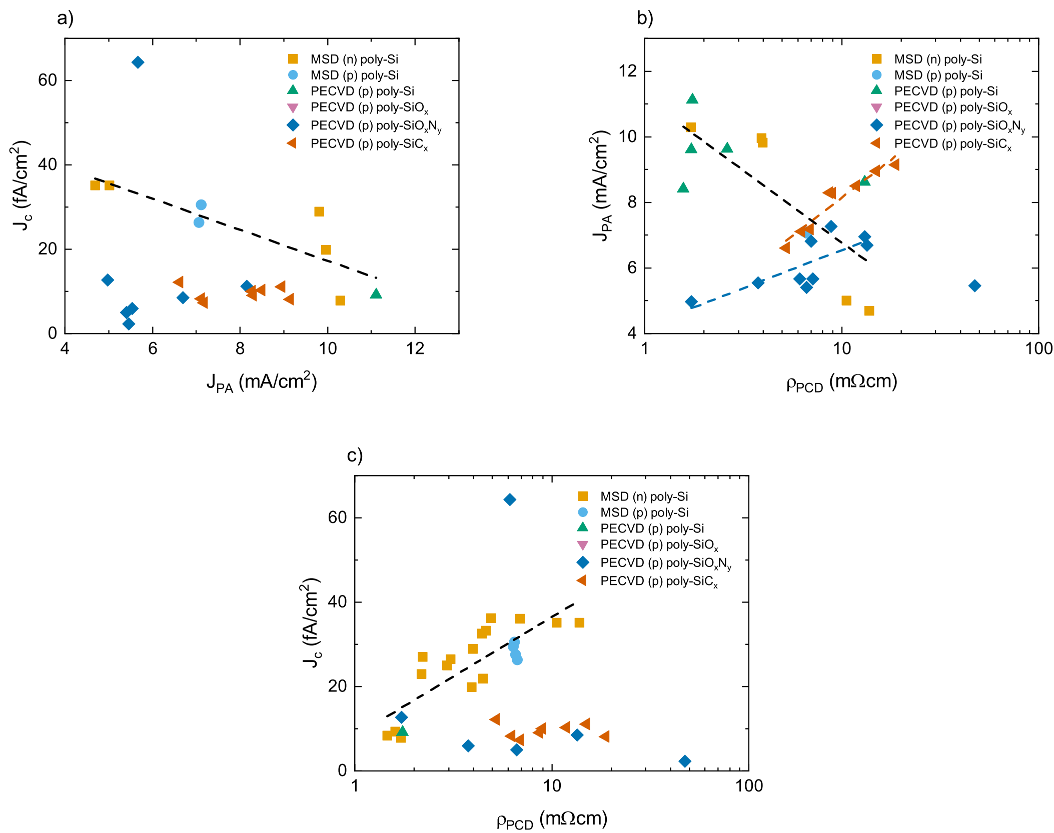

FIGURE 6.4. Dependencies for all layer types between J_c, ρ_{PCD} and J_{PA} in all combinations. Dashed lines are fits to the data of the corresponding color. Black dashed lines are fits for all pure poly-Si layers without incorporated light elements. In b) the outlier at $\rho_{PCD} = 47.5$ mΩcm was not included in the fit.

observed explicitly only for the MSD deposited (n) poly-Si layers but seems to be relevant for all layer types without incorporated light elements according to this relation.

Regarding the layers with incorporated light elements the J_c values were lower compared to almost all values of the layers without incorporated light elements. As was discussed above in Sec. 6.2, J_{PA} was found to be dominated by the crystallinity of the poly-Si layers, whereas this crystallinity should not affect J_c. The basically horizontal distribution of the layers with incorporated light elements in Fig. 6.4 a) directly reflects this relation. Thus, for these layers it is possible to tune the parasitic absorption without influencing the passivation quality.

Considering the resistivity instead of the passivation quality, continuous relations between decreasing ρ_{PCD} and decreasing J_{PA} values were observed for the layers with incorporated light elements as shown in Fig. 6.4 b). Since both the resistivity and the parasitic absorption were found to be dominated by the crystallinity (Fig. 6.2), these relations are a result of the crystallinity differences which were found to be $\chi_c \lesssim 60\%$. Therefore, a significant improvement towards lower J_{PA} and ρ_{PCD} should be expected for even larger crystallinities.

The relations for lower J_{PA} with lower ρ_{PCD} were fitted by a linear function of the $\log(\rho_{PCD})$ data in the semi-logarithmic plot in Fig. 6.4 b), which corresponds to a logarithmic function in a linear x-axis scale. The intercepts of these linear fits with the y-axis could be interpreted as a minimum achievable parasitic absorption a value of $J_{PA} \approx 4.2$ mA/cm^2 for the (p) poly-SiO_xN_y layers and a slightly lower value of $J_{PA} \approx 3.5$ mA/cm^2 for the (p) poly-SiC_x layers. As the slope of the fit for the (p) poly-SiC_x layers is twice as large, the improvement for higher crystallinities is expected to be significantly stronger for this layer type.

Also in Fig. 6.4 b) an inverted trend can be seen for all pure poly-Si layers without incorporated light elements whereas two data point groups around $\rho_{PCD} \approx 2$ mΩcm and $\rho_{PCD} \approx 9$ mΩcm evolved. As the corresponding crystallinities for these layers are assumed to be sufficiently large with $\chi_c \gtrsim 80\%$ (Table 5.1), this trend is rather attributed to FCA as was also concluded for the trend in Fig. 6.4 a). Based on this finding an adjustment of the dopant concentration could yield data points in between both groups on the line of the fit corresponding to a trade-off between parasitic absorption and resistivity. Admittedly, the choice of a linear connection between both groups is based solely on simplicity. A relation with a curvature towards lower J_{PA} and ρ_{PCD} would be equally justified. This curved relation would also imply that a finer adjustment of the dopant concentration could yield an improved performance if applied in an actual solar cell.

In Fig. 6.4 c) J_c is shown as function of ρ_{PCD} with a similar horizontal distribution of the layers with incorporated light elements as was also found in Fig. 6.4 a). This similarity arises from the strong dependency of both J_{PA} and ρ_{PCD} on the crystallinity (Sec. 6.1.2) and basically means that also the resistivity of the poly-Si layer can be tuned without significantly influencing the passivation quality.

Furthermore, in Fig. 6.4 c) the significantly larger number of data points of the MSD deposited (n) poly-Si layers compared to all previous figures presented in this chapter exists due to a larger number of layers on FZ substrate than on FS substrates during the $POCl_3$-diffusion parameter variation (Sec. 5.2). FS substrates are necessary for SE and RS measurements and thus for the determination of J_{PA}, E_{04} and χ_c while one of each is shown in all previous figures of this chapter. In contrast, both quantities in Fig. 6.4 c) were determined by PCD on FZ substrates only.

Regarding the pure poly-Si layers without incorporated light elements a clear relation for lower J_c with lower ρ_{PCD} is visible in Fig. 6.4 c) as is evident from the fit through all data points of these layers. According to the dependency overview in Fig. 5.1, such a proportional relation between J_c and ρ_{PCD} should only exist for a variation of the dopant concentration which reduces J_c by a larger band offset and ρ_{PCD} by additional charge carriers. As only two different $POCl_3$-diffusion parameter sets were tested, also two separated data point groups would be expected for the MSD deposited (n) poly-Si layers similar to the groups in Fig. 6.4 b). The rather continuous relation is consequently a hint for a large scattering of phosphorus concentrations in the resulting layers even if placed in the same $POCl_3$-diffusion. Such inhomogeneous phosphorus concentrations could be related to the relative thickness inhomogeneity of $\sim 9\%$ for MSD deposited layers (Sec. 2.3.2) as the resulting phosphorus concentration depends on this thickness (Sec. 2.4.1). Nevertheless, the relation between high passivation quality and low resistivity seems to hold for all pure poly-Si layers without incorporated light elements regardless of the deposition type and dopant polarity.

Similar to the fits in Fig. 6.4 b), the intercept of the fit for the pure poly-Si layers can be interpreted as a minimum achievable J_c for this layer type. The corresponding fit intercept value of ~ 8.3 fA/cm^2 is comparable to the lowest observed value of $J_c = 7.9$ fA/cm^2 for a MSD deposited (n) poly-Si layer (Sec. 5.2.5). However, this lower limit is significantly larger than previously reported values for (n) poly-Si/SiO_x contacts in the range of 1 fA/cm^2 [23] and could therefore be related to the sputter damage during a-Si deposition as already mentioned above.

6.2. Applicability in a Solar Cell

As already stated in the previous section, the measured quantities J_c, ρ_{PCD} and J_{PA} mainly determine the performance of a poly-Si/SiO_x contact. In this section they are related to an application in a solar cell via the selectivity $S_{10}\left(J_c, \rho_{PCD}\right)$ and an ideal solar cell efficiency $\eta_{ideal}\left(J_c, J_{PA}\right)$, each as function of two out of these three parameters. Based on these quantities the applicability of the investigated layers in an actual solar cell is assessed by a comparison of the best performing layer for each layer type under consideration of the poly-Si layer thickness d_{poly}.

6.2.1. Selectivity S_{10} and Ideal Solar Cell Efficiency η_{ideal} as Indicators for Solar Cell Performance

In Sec. 1.3.3 the selectivity S_{10} was described as figure of merit for passivating contacts. According to eq. 1.9, it is a function of the contact recombination current density J_c and the contact resistance ρ_c. ρ_c is in turn a linear function of the resistivity of the poly-Si layer ρ_{PCD} if charge carrier transport is assumed to be dominated by transport via pinholes in the interfacial oxide and thus limited by the spreading resistance (eq. 1.7). In [7] this assumption was made for a 2.1 nm thick interfacial oxide being too thick for tunneling transport and hence this assumption should also hold for the even thicker interfacial oxide of 2.5 nm used throughout this thesis.

Combining eq. 1.9 and 1.7 the selectivity S_{10} can be written as function of the two measured quantities J_c and ρ_{PCD} as

$$S_{10}\left(J_c, \rho_{PCD}\right) = \log\left(\frac{\pi\, r_{pin}\, n_{pin}\, V_{th}}{J_c\, \rho_{PCD}}\right) \tag{6.1}$$

with the radius of a pinhole r_{pin} and the areal pinhole density n_{pin}. In order to estimate these pinhole related parameters, the detection of local current paths by conductive atomic force microscopy (cAFM) was reported, whereas it is not clear if each current path corresponds to an actual pinhole [197, 198]. A more reliable method was introduced in [199] which determines n_{pin} by TMAH based wet-chemical selective etching of the silicon substrate below these nanometer sized pinholes. The resulting etch pit dimensions are in the µm range and detected by optical microscopy. Pinhole densities determined by this method are in agreement with the corresponding charge carrier transport model [18] and reached lowest values in the order of $\sim 10^6$ cm^{-2}. As the thermally grown interfacial oxide used throughout this thesis was thicker and the standard temperature during junction formation was colder compared to the ones used in [199], an upper limit for the pinhole density of $n_{pin} = 1 \cdot 10^6$ cm^{-2} was applied in eq. 6.1.

The same authors also investigated the pinhole diameter and found a lower limit value of $r_{pin} =$ 2.5 nm for wet-chemically grown interfacial oxides from TEM images [200]. For thermally grown oxides no pinholes were found which can be explained either by too small pinhole diameters r_{pin} or by too low pinhole densities n_{pin} so that it is very unlikely to encounter a pinhole in a TEM image. However, in [30] the authors used the same value of $r_{pin} = 2.5$ nm as input for their model explicitly describing charge carrier transport via pinholes for rather thick interfacial oxides > 2 nm. Therefore, $r_{pin} = 2.5$ nm was also used in eq. 6.1. As neither the pinhole density nor the diameter were measured within this thesis but only roughly estimated from literature, the selectivities determined by eq. 6.1 should rather be seen as a rough orientation enabling a comparison between the investigated layer types.

Though the selectivity S_{10} is connected to a maximum achievable solar cell efficiency via eq. 1.11 and is as such useful for comparing the different layer types, it does not consider the parasitic absorption within the poly-Si layer. In order to also include the measured parasitic absorption current density J_{PA} in the comparison, a hypothetical ideal solar cell efficiency was determined based on the one-diode model (Sec. 1.1). Therein, the current-voltage characteristics are completely characterized by the saturation current density J_0 and the short circuit current density J_{sc} (eq. 1.1). The following simplifications were made:

- I) Recombination takes place only at the contacts leading to $J_0 = 2\,J$ assuming equal J_c for both sides of the solar cell and thus for both polarities. In particular, $J_{0,bulk} = 0$ fA/cm^2.
- II) Parasitic absorption in the poly-Si layer described by J_{PA} is the only optical loss mechanism and hence $J_{sc} = J_{ph,ideal} - J_{PA}$ with an ideal photogenerated current of $J_{ph,ideal} =$ 43.6 mA/cm^2 according to [7].
- III) No metal contacts are applied and thus the series resistance is $R_s = 0$ Ωcm^2. In particular, the lateral resistivity of the poly-Si layer is neglected and thus not a limiting factor.
- IV) No shunt related losses are considered, hence $R_{sh} = \infty$.

Based on these assumptions and eq. 1.1−1.4, the hypothetical ideal solar cell efficiency $\eta_{ideal}(J_c, J_{PA})$ can be determined as function of the measured contact recombination and parasitic absorption current densities. It should be noted that the absolute values of η_{ideal} are rather large due to the simplifications I)−IV) and can easily approach the theoretical limit of silicon solar

cells of 29.43% [201]. An actual solar cell would yield efficiencies reduced by roughly estimated $\sim 4\%_{abs}$ and hence the absolute values of η_{ideal} should be interpreted carefully. Nevertheless, trends and changes in absolute values are indeed relevant for an actual solar cell implementation.

The selectivity $S_{10}(J_c, \rho_{PCD})$ according to eq. 6.1 is not affected by the parasitic absorption J_{PA} whereas the ideal solar cell efficiency $\eta_{ideal}(J_c, J_{PA})$ does consider the parasitic absorption J_{PA} but not the resistivity of the poly-Si layer ρ_{PCD}. In order to discuss both the parasitic absorption J_{PA} as well as the resistivity of the poly-Si layer ρ_{PCD} with respect to an application on the front side of a solar cell, both quantities are plotted against each other in Fig. 6.5.

A continuous increase of η_{ideal} for higher S_{10} is observable for both the (p) poly-SiO_xN_y and (p) poly-SiC_x layers. This trend is attributed to a higher crystallinity which increases η_{ideal} by a lower parasitic absorption and S_{10} by a lower resistivity. It could be expected that these trends can be extended towards even larger efficiencies and selectivities if the crystallinity is further increased, again underlining the key role of the crystallinity.

In contrast, for the pure poly-Si layers without incorporated light elements an exponential trend is observed which is related to the dopant concentrations. High dopant concentrations increase S_{10} due to a lower resistivity and a larger band offset but at the same time decrease η_{ideal} due to FCA and vice versa for low concentrations. In Sec. 6.1.4 the hypothesis was raised that an optimal dopant concentration might exist between the two data point groups in Fig. 6.4. This hypothesis is not supported by the data in Fig. 6.5 as is evident from the exponential fit. This exponential relation basically means that either large η_{ideal} values with low parasitic absorption or large S_{10} values with low resistivity can be achieved but not large values for both at the same time. Based on the continuous increase towards large η_{ideal} and S_{10} for the layers with incorporated light elements and based on the exponential relation for the layers without light elements it is concluded that only the former layers are candidates for an application on the front side of a solar cell.

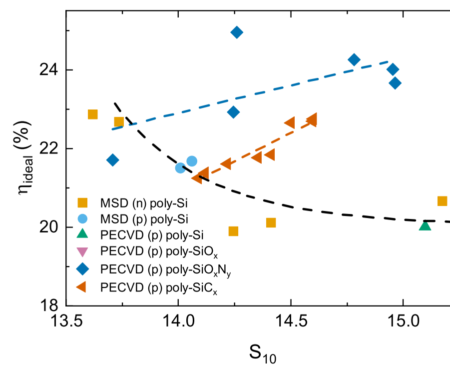

FIGURE 6.5. Ideal solar cell efficiency $\eta_{ideal}(J_c, J_{PA})$ according to the idealized one-diode model as function of the selectivity $S_{10}(J_c, \rho_{PCD})$ according to eq. 6.1 for all layer types. Dashed lines are fits to the data of the corresponding color. The black dashed line is an exponential fit for all pure poly-Si layers without incorporated light elements.

6.2.2. Applicability of Best Performing Layers

For each layer type the best performing layer was chosen based on the largest η_{ideal}. The corresponding parameters relevant for the solar cell performance are depicted in Table 6.1, namely the measured parasitic absorption current density J_{PA}, contact recombination current density J_c, the contact resistance $\rho_c\,(\rho_{PCD})$ according to eq. 1.7, the selectivity $S_{10}\,(J_c, \rho_{PCD})$ according to eq. 6.1 and the ideal solar cell efficiency $\eta_{ideal}\,(J_c, J_{PA})$ according to the idealized one-diode model introduced in the previous section. Solely for the (p) poly-SiO_x layers only the J_c value was accessible as the simultaneous resistivity measurement failed due to a too large resistivity. Therefore, the (p) poly-SiO_x layers can directly be excluded for an application in an actual solar cell. It should also be noted that all values were measured on FZ substrates except for the (p) poly-SiC_x layers which were measured on Cz substrate.

The PECVD deposited (p) poly-Si layer and the MSD deposited (n) poly-Si layer show a clear similarity in all parameters and no difference between both dopant polarities was observed, which does not fit to the literature [23]. Indeed, based on Table 1.1 a selectivity larger than $S_{10} \approx 16$ could be expected for electron selective contacts whereas a lower selectivity of $S_{10} \approx 14$ would be expected for hole selective contacts. Therefore, it should be assumed that the selectivities in Table 6.1 are overestimated. This could easily be explained by the just roughly estimated values of the pinhole density and diameter in eq. 6.1 based on the literature. In this context it should be emphasized that the selectivity is defined on a logarithmic scale and thus rather small differences in S_{10} could be a result of significant differences in J_c or ρ_c (eq. 1.9).

However, the selectivities of the (p) poly-SiO_xN_y and (p) poly-SiC_x layers are in line with literature values for hole selective contacts. The lower selectivities of these layers are compensated by a low parasitic absorption J_{PA} leading to significantly larger η_{ideal} values compared to the pure (p) poly-Si layers without incorporated light elements. Thus, there seems to be a fundamental trade-off between the selectivity and the parasitic absorption. Based on this observation it could be useful to define a figure of merit for passivating contacts on the front side of a solar cell not only considering the passivation quality J_c and contact resistance ρ_c but also the parasitic absorption J_{PA}.

TABLE 6.1. Parameters relevant for solar cell performance for the best performing layer for each layer type, namely the measured parasitic absorption current density J_{PA}, the contact recombination current density J_c, the contact resistance $\rho_c\,(\rho_{PCD})$ according to eq. 1.7, the selectivity $S_{10}\,(J_c, \rho_{PCD})$ according to eq. 6.1 and the ideal solar cell efficiency $\eta_{ideal}\,(J_c, J_{PA})$ according to the idealized one-diode model introduced in Sec. 6.2.1.

Layer type	J_c (fA/cm^2)	ρ_c (mΩcm^2)	J_{PA} (mA/cm^2)	S_{10}	η_{ideal} (%)
PECVD (p) poly-Si	9.2	**2.2**	11.1	15.1	20.0
MSD (p) poly-Si	26.3	8.5	7.1	14.1	21.7
MSD (n) poly-Si	7.9	**2.2**	10.3	**15.2**	20.7
PECVD (p) poly-SiO_x	7.5	-	-	-	-
PECVD (p) poly-SiO_xN_y	**2.3**	60.5	**5.5**	14.3	**25.0**
PECVD (p) poly-SiC_x	7.3	8.8	7.2	14.6	22.8

Another trade-off is identified between the lowest contact recombination current density J_c and the largest contact resistance ρ_c in Table 6.1. Both quantities belong to the (p) poly-SiO_xN_y layer and result in a selectivity which is comparable to the one of the (p) poly-SiC_xlayer with intermediate J_c and ρ_c. Considering that this similar selectivity was achieved on Cz substrates one could expect a significantly reduced J_c on FZ substrates with a similar ρ_c. Thereby, the (p) poly-SiC_x could close the gap to the (p) poly-SiO_xN_y layer or yield even larger S_{10} or η_{ideal}. Furthermore, this best performing (p) poly-SiC_x layer showed the second largest crystallinity of all (p) poly-SiC_x layers with $\chi_c = 50.6\%$ and a carbon concentration of $c_C = 8.2$ at% which could be further increased by even lower c_C. The larger crystallinity would in turn decrease both the contact resistance ρ_c and the parasitic absorption current density J_{PA} leaving J_c unchanged and consequently further increasing both S_{10} and η_{ideal}.

As stated above, both S_{10} and η_{ideal} cannot be transferred into a real solar cell since S_{10} only characterizes a single poly-Si/SiO_x contact and η_{ideal} assumes similar J_c values on both sides and as such a contact recombination current density regardless of the dopant polarity. In practice, both polarities have to be present in an actual solar cell. Regarding the parameters in Table 6.1 it is suggested to combine the hole selective PECVD deposited (p) poly-SiO_xN_y layer on the front side with the electron selective MSD deposited (n) poly-Si layer on the rear side of an actual solar cell. According to the idealized one-diode model of a solar cell introduced in the previous section, this would result in an ideal solar cell efficiency of $\eta_{ideal,max} = 24.2\%$ if the J_c values of both layers are summed up and the J_{PA} value of the (p) poly-SiO_xN_y layer is utilized. This more realistic value constitutes an upper limit for the solar cell efficiency if the layers investigated within this thesis are applied in a solar cell. For a real solar cell it should be kept in mind that the lateral conductivity of the (p) poly-SiO_xN_y might even be larger by two orders of magnitude as hypothesized from the HE measurements (Sec. 5.2.4). In case of a local metal grid as is necessary for application on the front side the selectivity and thus the efficiency would be significantly reduced. A similar argument is valid for the (p) poly-SiC_x layers as the corresponding HE measurement completely failed.

6.2.3. Influence of poly-Si Layer Thickness on Solar Cell Performance

The upper limit for the solar cell efficiency determined in the previous section holds for a poly-Si layer thickness of $d_{poly} = 100$ nm on the front side, since this assumption was made for the determination of J_{PA} along with a 75 nm SiN_x:H ARC on top of the poly-Si/SiO_x contact (Sec. 3.4.3). This poly-Si thickness was chosen as an appropriate thickness for standard screen printing metallization without harming the interfacial oxide. Current research activities aim at an optimization of the screen-printing process in order to contact significantly thinner poly-Si layers (Sec. 1.3.4). In order to investigate the effect of the poly-Si layer thickness on the solar cell performance if applied on the front side, J_{PA} was recalculated in the range of $d_{poly} = 0 - 100$ nm in 5 nm steps for the best performing (p) poly-Si and (p) poly-SiO_xN_y layer with the highest and lowest J_{PA} value in Table 6.1. A thickness of $d_{poly} = 0$ nm corresponds to the case of a direct contact between the SiN_x:H ARC and the interfacial oxide which does not represent a useful application in an actual solar cell.

In Fig. 6.6 a) J_{PA} is plotted as function of d_{poly} with a clear decrease of the parasitic absorption for thinner layers down to $J_{PA} = 0$ mA/cm^2 at $d_{poly} = 0$ nm for both layer types. The gap between the (p) poly-Si and (p) poly-SiO_xN_y layer decreases simultaneously and reduces also to zero towards

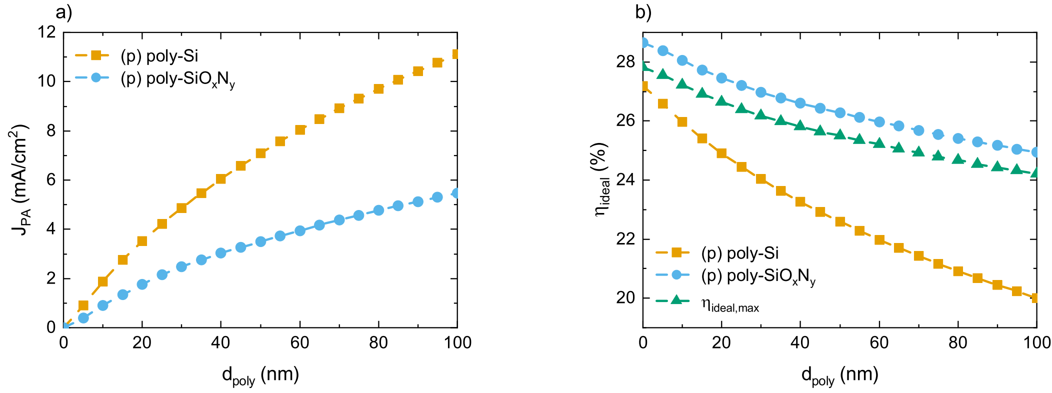

FIGURE 6.6. a) Parasitic absorption current density J_{PA} and b) ideal solar cell efficiency η_{ideal} according to the idealized one-diode model as described in Sec. 6.2.1 as functions of the (p) poly-Si or (p) poly-SiO_xN_y layer thickness d_{poly}. Also in b) the solar cell efficiency limit $\eta_{ideal,max}$ for the layers investigated within this thesis as function of d_{poly}.

$d_{poly} = 0$ nm. Hence, the benefit from a thinner poly-Si layer in terms of a reduced parasitic absorption is larger for layers with larger absorption coefficients. Furthermore, the slope of the curves increases for $d_{poly} < 30$ nm. Thus, in this region the gain in efficiency per reduced thickness is expected to be larger.

In Fig. 6.6 b) the ideal solar cell efficiency η_{ideal} according to the idealized one-diode model shows a similar increase of the slope of η_{ideal} towards $d_{poly} = 0$ nm. The corresponding curves show similar features compared to Fig. 6.6 a) apart from the gap in η_{ideal} for $d_{poly} = 0$ nm. This gap is attributed to the difference in J_c between both layer types. If an improved screen-printing technology would allow a thickness reduction from $d_{poly} = 100$ nm down to $d_{poly} = 30$ nm, this would translate into an efficiency gain of $\sim 4\%_{abs}$ for the (p) poly-Si and of $\sim 2\%_{abs}$ for the (p) poly-SiO_xN_y layer whilst the latter would still be $\sim 3\%_{abs}$ more efficient. Therefore, even though the efficiency gain for pure poly-Si layers without incorporated light elements is stronger, the incorporation of light elements will yield significantly higher efficiencies if applied on the front side of a solar cell. This holds also for very thin layers with $d_{poly} < 30$ nm.

The upper limit for the solar cell efficiency $\eta_{ideal,max}$, as introduced in the previous section, with the (n) poly-Si on the rear side and the (p) poly-SiO_xN_y on the front side is also shown in Fig. 6.6 b) as function of d_{poly}. The corresponding curve follows the curve of the (p) poly-SiO_xN_y with a constant gap which originates from the larger J_c value of the MSD deposited (n) poly-Si layer on the rear side. In contrast, the gap to the (p) poly-Si layer with strong parasitic absorption if applied on the front side of a solar cell is with $\sim 4.2\%_{abs}$ comparably large at $d_{poly} = 100$ nm and decreases for thinner poly-Si layers. Thus, the suggested combination of the MSD deposited (n) poly-Si layer as electron selective contact on the rear side and the PECVD deposited (p) poly-SiO_xN_y layer on the front side significantly benefits from the reduced parasitic absorption on the front side and would further benefit from a reduction of the poly-SiO_xN_y layer thickness to $d_{poly} = 30$ nm,. This thickness reduction would in turn increase the ideal efficiency limit by $\sim 2\%_{abs}$ to $\eta_{ideal,max} = 26.2\%$.

Conclusions

Several dependencies between the composition of poly-Si layers and the performance of solar cells if applied as poly-Si/SiO_x contacts have been identified. First of all, strategies for the avoidance of blistering during solid phase crystallization (SPC) of plasma enhanced chemical vapor deposited (PECVD) in-situ doped (p) a-Si:H layers were developed. These mostly aim at an increase of the microstructure factor R^* of the as-deposited layers before SPC which was identified to correlate with less blistering. This was achieved by low boron concentrations, incorporation of light elements and low deposition temperatures. Additionally, high deposition temperatures also reduced blistering by a lower hydrogen concentration. The optical band gap of the as-deposited layers was successfully tuned but not preserved during SPC to poly-Si.

In order to quantify the elemental composition, GD-OES calibrations were developed as well as a correction for measurement artifacts from atmospheric contaminations. For all crystallized poly-Si layer compositions a difference between total and electrically active dopant concentration was found as well as a concentration pile-up close to or within the interfacial oxide for both dopant polarities, while the phosphorus pile-up was more pronounced.

Another asymmetry between both dopant polarities for the pure poly-Si layers without incorporated light elements was identified as an efficiency limitation due to free carrier absorption (FCA) for phosphorus doping and due to detrimental strong in-diffusion for boron doping. Additionally, magnetron sputtering deposited (MSD) in-situ doped (p) poly-Si layers were limited by bulk defects which were only partly saturated during hydrogenation. A further asymmetry was found between both deposition techniques with significantly lower internal stress σ for MSD compared to PECVD deposited poly-Si.

In the context of light element incorporation most importantly the crystallinity χ_c was identified as a key parameter determining all properties of the layers relevant for an application in a solar cell. For larger concentrations of light elements the crystallinity decreased and thus raised the parasitic absorption current density J_{PA} as well as the contact resistance ρ_c. Larger crystallinities were achieved rather by higher temperatures T_{SPC} than longer durations t_{SPC} of the SPC for the (p) poly-SiO_xN_y layers and by lower carbon concentrations c_C for the (p) poly-SiC_x layers which could be further enlarged by even lower concentrations $c_C < 5$ at%.

The incorporation of light elements showed several differences between the (p) poly-SiO_xN_y and (p) poly-SiC_x layers. For the former optimal oxygen and nitrogen concentrations $c_{O/N}$ were found regarding the parasitic absorption and passivation quality while for the latter these properties could be further optimized by decreasing the carbon concentrations c_C and thus increasing the crystallinity χ_c. An exception to this is the passivation quality in terms of contact recombination current density J_c of the (p) poly-SiC_x layers which was found to be determined by the unintentionally varied boron

concentration ξ_B and as such independent of the carbon concentration c_C in the investigated range. Regarding the contact resistance ρ_c both layer types showed a continuous increase for larger concentrations of light elements, while an internal stress σ relaxation was observed for the (p) poly-SiO_xN_y layers and a stress enlargement for the (p) poly-SiC_x layers. Altogether the desired band gap widening was observed for the incorporation of light elements but only a reduced parasitic absorption current density J_{PA} was verified while an increased passivation quality was not clearly identified.

A simultaneous examination of all layer types revealed two basic trade-offs. The first trade-off is between the passivation quality J_c and the contact resistance ρ_c and was explicitly present for (n) poly-Si and (p) poly-SiO_xN_y layers. As both properties determine the selectivity S_{10}, this trade-off is interpreted as a principle limitation of this selectivity. The second trade-off exists between the selectivity S_{10} and the parasitic absorption J_{PA} for all pure poly-Si layers without incorporated light elements. Therefore, these layers are not suitable for an application on the front side of a solar cell even if the parasitic absorption would be sufficiently low this would still imply a low selectivity according to this trade-off.

Taking into account the best performing layer for each layer type an excellent passivation quality with contact recombination current densities of $J_c < 10$ fA/cm^2 and selectivities in the range of $S_{10} = 14.1 - 15.2$ were achieved with a potential for further optimization. It has to be emphasized that the lowest contact recombination current density measured in this thesis of $J_c = 2.3$ fA/cm^2 was found for the boron doped (p) poly-SiO_xN_y layers. Such low values close to 1 fA/cm^2 are rather typical for phosphorus doped poly-Si layers and thus the incorporation of light elements might enable equally high passivation qualities also for boron doping. In this context it should also be noted that a high passivation quality of $J_c = 7.3$ fA/cm^2 was found for the best performing (p) poly-SiC_x layer on a silicon Cz substrate while the contact recombination current densities of all other layer types were determined on silicon FZ substrates. This qualifies carbon incorporation as the most promising strategy for future optimizations regarding reduced parasitic absorption by incorporation of light elements for an application on the front side of a solar cell.

The most promising combination of these best performing layers for an application in an actual solar cell is the MSD deposited (n) poly-Si layer on the rear side and the PECVD deposited (p) poly-SiO_xN_y layer on the front side. This combination leads to an idealized solar cell efficiency limit of $\eta_{ideal,max} = 24.2\%$ which would be further increased by $\sim 2\%_{\mathrm{abs}}$ when the poly-Si layer thickness d_{poly} is reduced from 100 nm to 30 nm. Considering a future optimization of the (p) poly-SiC_x layer as a replacement for the (p) poly-SiO_xN_y layer on the front side, this thesis proves the suitability of an application of poly-Si/SiO_x contacts with incorporated light elements on the front side of a solar cell.

List of Publications

J. Steffens, H.-W. Becker, S. Gerke, S. Joos, G. Hahn and B. Terheiden, "Replacing NRA by fast GD-OES measurements as input to a model based prediction of hydrogen diffusion in a-Si", Energy Procedia **124**, 180–187 (2017) `10.1016/j.egypro.2017.09.315`.

J. Steffens, M. A. Fazio, D. Cavalcoli and B. Terheiden, "Multi-characterization study of interface passivation quality of amorphous sub-stoichiometric silicon oxide and silicon oxynitride layers for photovoltaic applications", Sol. Energy Mater. Sol. Cells **187**, 104–112 (2018) `10.1016/j.solmat.2018.07.024`.

J. Steffens, G. Hahn and B. Terheiden, "Towards a fast determination of the hydrogen concentration in thin passivating a-Si:H layers using GD-OES", AIP Conf. Proc. **1999**, 020021 (2018) `10.1063/1.5049260`.

A. Merkle, S. Seren, H. Knauss, B. Min, J. Steffens, B. Terheiden, R. Brendel and R. Peibst, "Atmospheric pressure chemical vapor deposition of in-situ doped amorphous silicon layers for passivating contacts", Proc. 35th EUPVSEC, 785–791 (2018) `10.4229/35thEUPVSEC20182018-2DV.3.49`.

F. Geml, J. Engelhardt, J. Steffens, L.-F. Reinalter, G. Micard and G. Hahn, "GD-OES depth profiling and calibration of B doped dielectric layers", AIP Conf. Proc. **2147**, 020003 (2019) `10.1063/1.5123808`.

J. Steffens, J. Rinder, G. Hahn and B. Terheiden, "Compensation of the sputter damage during a-Si deposition for poly-Si/SiO_x passivating contacts by ex-situ P-doping", AIP Conf. Proc. **2147**, 040018 (2019) `10.1063/1.5123845`.

J. Steffens, J. Rinder, G. Hahn and B. Terheiden, "Correlation between the optical bandgap and the monohydride bond density of hydrogenated amorphous silicon", J. Non-Cryst. Solids: X **5**, 100044 (2020) `10.1016/j.nocx.2020.100044`.

S. Jafari, J. Steffens, M. Wendt, B. Terheiden, S. Meyer and D. Lausch, "Occurrence of Sharp Hydrogen Effusion Peaks of Hydrogenated Amorphous Silicon Film and Its Connection to Void Structures", Phys. Status Solidi B, 2000097 (2020) `10.1002/pssb.202000097`.

J. Steffens, S. Weit, J. Rinder, R. Glatthaar, S. Möller, G. Hahn and B. Terheiden, "Influence of the Carbon Concentration on (p) Poly-SiC_x Layer Properties With Focus on Parasitic Absorption in Front Side Poly-SiC_x/SiO_x Passivating Contacts of Solar Cells", IEEE J. Photovolt. **10**, 1624–1631 (2020) `10.1109/JPHOTOV.2020.3023506`.

Bibliography

[1] S. Philipps and W. Warmuth, “Fraunhofer ISE: Photovoltaics report”, updated: 14 November (2019).

[2] K. Yamamoto, D. Adachi, K. Yoshikawa, W. Yoshida, T. Irie, K. Konishi, T. Fujimoto, H. Kawasaki, M. Kanematsu, H. Ishibashi, T. Uto, Y. Takahashi, T. Terashita, G. Koizumi, N. Nakanishi, and M. Yoshimi, “Record-breaking efficiency back-contact heterojunction crystalline Si solar cell and module”, Proc. 33rd EUPVSEC, 201–204 (2017) 10.4229/EUPVSEC20172017-2BP.1.1.

[3] U. Würfel, A. Cuevas, and P. Würfel, “Charge carrier separation in solar cells”, IEEE J. Photovolt. **5**, 461–469 (2015) 10.1109/JPHOTOV.2014.2363550.

[4] M. Green, *Solar cells: operating principles, technology and system applications* (The University of New South Wales, Kensington, 1998).

[5] R. Hall, “Electron-hole recombination in germanium”, Phys. Rev. **87**, 387 (1952) 10.1103/PhysRev.87.387.

[6] W. Shockley and W. Read Jr., “Statistics of the recombinations of holes and electrons”, Phys. Rev. **87**, 835 (1952) 10.1103/PhysRev.87.835.

[7] R. Brendel and R. Peibst, “Contact selectivity and efficiency in crystalline silicon photovoltaics”, IEEE J. Photovolt. **6**, 1413–1420 (2016) 10.1109/JPHOTOV.2016.2598267.

[8] K. R. McIntosh and L. E. Black, “On effective surface recombination parameters”, J. Appl. Phys. **116**, 014503 (2014) 10.1063/1.4886595.

[9] T. Dullweber and J. Schmidt, “Industrial silicon solar cells applying the passivated emitter and rear cell (PERC) concept - A review”, IEEE J. Photovolt. **6**, 1366–1381 (2016) 10.1109/JPHOTOV.2016.2571627.

[10] A. Blakers, A. Wang, A. Milne, J. Zhao, and M. Green, “22.8% efficient silicon solar cell”, Appl. Phys. Lett. **55**, 1363–1365 (1989) 10.1063/1.101596.

[11] J. Melskens, B. W. H. van de Loo, B. Macco, L. E. Black, S. Smit, and W. M. M. E. Kessels, “Passivating contacts for crystalline silicon solar cells: From concepts and materials to prospects”, IEEE J. Photovolt. **8**, 373–388 (2018) 10.1109/JPHOTOV.2018.2797106.

[12] S. W. Glunz, F. Feldmann, A. Richter, M. Bivour, C. Reichel, H. Steinkemper, J. Benick, and M. Hermle, “The irresistible charm of a simple current flow pattern - 25% with a solar cell featuring a full-area back contact”, Proc. 31st EUPVSEC, 259–263 (2015) 10.4229/EUPVSEC20152015-2BP.1.1.

[13] S. De Wolf, A. Descoeudres, Z. C. Holman, and C. Ballif, “High-efficiency silicon heterojunction solar cells: A review”, Green **2**, 7–24 (2012) 10.1515/green-2011-0018.

[14] T. G. Allen, J. Bullock, X. Yang, A. Javey, and S. D. Wolf, “Passivating contacts for crystalline silicon solar cells”, Nature Energy **4**, 914–928 (2019) 10.1038/s41560-019-0463-6.

[15] T. Matsushita, T. Aoki, T. Otsu, H. Yamoto, H. Hayashi, M. Okayama, and Y. Kawana, “Semi-insulating polycrystalline-silicon (SIPOS) passivation technology”, Jpn. J. Appl. Phys. **15**, 35–40 (1976) 10.7567/JJAPS.15S1.35.

[16] M. Rienäcker, A. Merkle, U. Römer, H. Kohlenberg, J. Krügener, R. Brendel, and R. Peibst, “Recombination behavior of photolithography-free back junction back contact solar cells with carrier-selective polysilicon on oxide junctions for both polarities”, Energy Procedia **92**, 412–418 (2016) 10.1016/j.egypro.2016.07.121.

[17] F. Feldmann, M. Bivour, C. Reichel, M. Hermle, and S. W. Glunz, “Passivated rear contacts for high-efficiency n-type Si solar cells providing high interface passivation quality and excellent transport characteristics”, Sol. Energy Mater. Sol. Cells **120**, 270–274 (2014) 10.1016/j.solmat.2013.09.017.

[18] R. Peibst, U. Römer, Y. Larionova, M. Rienäcker, A. Merkle, N. Folchert, S. Reiter, M. Turcu, B. Min, J. Krügener, D. Tetzlaff, E. Bugiel, T. Wietler, and R. Brendel, “Working principle of carrier selective poly-Si/c-Si junctions: Is tunnelling the whole story?”, Sol. Energy Mater. Sol. Cells **158**, 60–67 (2016) 10.1016/j.solmat.2016.05.045.

[19] U. Römer, R. Peibst, T. Ohrdes, B. Lim, J. Krügener, T. Wietler, and R. Brendel, “Ion implantation for poly-Si passivated back-junction back-contacted solar cells”, IEEE J. Photovolt. **5**, 507–514 (2015) 10.1109/JPHOTOV.2014.2382975.

[20] F. Feldmann, J. Schön, J. Niess, W. Lerch, and M. Hermle, “Studying dopant diffusion from poly-Si passivating contacts”, Sol. Energy Mater. Sol. Cells **200**, 109978 (2019) 10.1016/j.solmat.2019.109978.

[21] F. Feldmann, C. Reichel, R. Müller, and M. Hermle, “The application of poly-Si/SiO_x contacts as passivated top/rear contacts in Si solar cells”, Sol. Energy Mater. Sol. Cells **159**, 265–271 (2017) 10.1016/j.solmat.2016.09.015.

[22] R. Peibst, C. Kruse, S. Schäfer, V. Mertens, S. Bordihn, T. Dullweber, F. Haase, C. Hollemann, B. Lim, B. Min, R. Niepelt, H. Schulte-Huxel, and R. Brendel, “For none, one, or two polarities - How do POLO junctions fit best into industrial Si solar cells?”, Prog. Photovolt. Res. Appl., 1–14 (2019) 10.1002/pip.3201.

[23] S. W. Glunz and F. Feldmann, “SiO_2 surface passivation layers - a key technology for silicon solar cells”, Sol. Energy Mater. Sol. Cells **185**, 260–269 (2018) 10.1016/j.solmat.2018.04.029.

[24] F. Feldmann, R. Müller, C. Reichel, and M. Hermle, “Ion implantation into amorphous Si layers to form carrier-selective contacts for Si solar cells”, Phys. Status Solidi RRL **8**, 767–770 (2014) 10.1002/pssr.201409312.

[25] T. Yamamoto, K. Uwasawa, and T. Mogami, "Bias temperature instability in scaled p^+ polysilicon gate p-MOSFET's", IEEE T. Electron. Dev. **46**, 921–926 (1999) 10.1109/16.760398.

[26] U. Römer, "Polycrystalline silicon / monocrystalline silicon junctions and their application as passivated contacts for Si solar cells", Dissertation (Gottfried Wilhelm Leibniz Universität Hannover, 2015).

[27] H. De Graaff and J. De Groot, "The SIS tunnel emitter: A theory for emitters with thin interface layers", IEEE T. Electron. Dev. **26**, 1771–1776 (1979) 10.1109/T-ED.1979.19684.

[28] J. Gan and R. Swanson, "Polysilicon emitters for silicon concentrator solar cells", Proc. 21st IEEE PVSC, 245–250 (1990) 10.1109/PVSC.1990.111625.

[29] H. Steinkemper, F. Feldmann, M. Bivour, and M. Hermle, "Numerical simulation of carrier-selective electron contacts featuring tunnel oxides", IEEE J. Photovolt. **5**, 1348–1356 (2015) 10.1109/JPHOTOV.2015.2455346.

[30] R. Peibst, R. Udo, K. R. Hofmann, B. Lim, T. F. Wietler, J. Krügener, N.-P. Harder, and R. Brendel, "A simple model describing the symmetric I-V characteristics of p polycrystalline Si/n monocrystalline Si, and n polycrystalline Si/p monocrystalline Si junctions", IEEE J. Photovolt. **4**, 841–850 (2014) 10.1109/JPHOTOV.2014.2310740.

[31] D. K. Schroder, *Semiconductor material and device characterization* (John Wiley & Sons, Inc., Hoboken, NJ, 2006).

[32] J. Schmidt, R. Peibst, and R. Brendel, "Surface passivation of crystalline silicon solar cells: Present and future", Sol. Energy Mater. Sol. Cells **187**, 39–54 (2018) 10.1016/j.solmat.2018.06.047.

[33] T. Gao, Q. Yang, X. Guo, Y. Huang, Z. Zhang, Z. Wang, M. Liao, C. Shou, Y. Zeng, B. Yan, G. Hou, X. Zhang, Y. Zhao, and J. Ye, "An industrially viable TOPCon structure with both ultra-thin SiO_x and n^+-poly-Si processed by PECVD for p-type c-Si solar cells", Sol. Energy Mater. Sol. Cells **200**, 10.1016/j.solmat.2019.109926 (2019) 10.1016/j.solmat.2019.109926.

[34] A. Morisset, R. Cabal, B. Grange, C. Marchat, J. Alvarez, M.-E. Gueunier-Farret, S. Dubois, and J.-P. Kleider, "Conductivity and surface passivation properties of boron-doped poly-silicon passivated contacts for c-Si solar cells", Phys. Status Solidi A **216**, 1800603 (2019) 10.1002/pssa.201800603.

[35] D. Yan, A. Cuevas, S. P. Phang, Y. Wan, and D. Macdonald, "23% efficient p-type crystalline silicon solar cells with hole-selective passivating contacts based on physical vapor deposition of doped silicon films", Appl. Phys. Lett. **113**, 061603 (2018) 10.1063/1.5037610.

[36] J. Lossen, J. Hoß, S. Eisert, D. Amkreutz, M. Muske, J. Plentz, and G. Andrä, "Electron beam evaporation of silicon for poly-silicon/SiO_x passivated contacts", Proc. 35th EUPVSEC, 418–421 (2018) 10.4229/35thEUPVSEC20182018-2CO.10.5.

[37] F. Haase, C. Hollemann, S. Schäfer, A. Merkle, M. Rienäcker, J. Krügener, R. Brendel, and R. Peibst, "Laser contact openings for local poly-Si-metal contacts enabling 26.1%-efficient POLO-IBC solar cells", Sol. Energy Mater. Sol. Cells **186**, 184–193 (2018) 10.1016/j.solmat.2018.06.020.

[38] N. Nandakumar, J. Rodriguez, T. Kluge, T. Große, L. Fondop, P. Padhamnath, N. Balaji, M. König, and S. Duttagupta, "Approaching 23% with large-area monoPoly cells using screen-printed and fired rear passivating contacts fabricated by inline PECVD", Prog. Photovolt. Res. Appl. **27**, 107–112 (2019) 10.1002/pip.3097.

[39] A. Ingenito, G. Nogay, Q. Jeangros, E. Rucavado, C. Allebé, S. Eswara, N. Valle, T. Wirtz, J. Horzel, T. Koida, M. Morales-Masis, M. Despeisse, F.-J. Haug, P. Löper, and C. Ballif, "A passivating contact for silicon solar cells formed during a single firing thermal annealing", Nature Energy **3**, 800–808 (2018) 10.1038/s41560-018-0239-4.

[40] A. Merkle, S. Seren, H. Knauss, B. Min, J. Steffens, B. Terheiden, R. Brendel, and R. Peibst, "Atmospheric pressure chemical vapor deposition of in-situ doped amorphous silicon layers for passivating contacts", Proc. 35th EUPVSEC, 785–791 (2018) 10.4229/35thEUPVSEC20182018-2DV.3.49.

[41] S. Mack, J. Schube, T. Fellmeth, F. Feldmann, M. Lenes, and J.-M. Luchies, "Metallisation of boron-doped polysilicon layers by screen printed silver pastes", Phys. Status Solidi RRL **11**, 1700334 (2017) 10.1002/pssr.201700334.

[42] F. Feldmann, "Carrier-selective contacts for high-efficiency Si solar cells", Dissertation (Albert-Ludwigs-Universität Freiburg, 2015).

[43] B. Nemeth, D. L. Young, M. R. Page, V. LaSalvia, S. Johnston, R. Reedy, and P. Stradins, "Polycrystalline silicon passivated tunneling contacts for high efficiency silicon solar cells", J. Mater. Res. **31**, 671–681 (2016) 10.1557/jmr.2016.77.

[44] G. Yang, P. Guo, P. Procel, A. Weeber, O. Isabella, and M. Zeman, "Poly-crystalline silicon-oxide films as carrier-selective passivating contacts for c-Si solar cells", Appl. Phys. Lett. **112**, 193904 (2018) 10.1063/1.5027547.

[45] A. Ingenito, G. Nogay, J. Stuckelberger, P. Wyss, L. Gnocchi, C. Allebe, J. Horzel, M. Despeisse, F.-J. Haug, L. Philipp, and C. Ballif, "Phosphorous-doped silicon carbide as front-side full-area passivating contact for double-side contacted c-Si solar cells", IEEE J. Photovolt. **9**, 346–354 (2019) 10.1109/JPHOTOV.2018.2886234.

[46] C. Messmer, A. Fell, F. Feldmann, N. Wöhrle, J. Schön, and M. Hermle, "Efficiency roadmap for evolutionary upgrades of PERC solar cells by TOPCon: Impact of parasitic absorption", IEEE J. Photovolt. **10**, 335–342 (2020) 10.1109/JPHOTOV.2019.2957642.

[47] D. Chen, Y. Chen, Z. Wang, J. Gong, C. Liu, Y. Zou, Y. He, Y. Wang, L. Yuan, W. Lin, R. Xia, L. Yin, X. Zhang, G. Xu, Y. Yang, H. Shen, Z. Feng, P. P. Altermatt, and P. J. Verlinden, "24.58% total area efficiency of screen-printed, large area industrial silicon solar cells with the tunnel oxide passivated contacts (i-TOPCon) design", Sol. Energy Mater. Sol. Cells **206**, 110258 (2020) 10.1016/j.solmat.2019.110258.

[48] W. Pfann, "Principles of zone-melting", Journal of Metals, 747–753 (1952) 10.1007/BF03398137.

[49] J. Czochralski, "Ein neues Verfahren zur Messung der Kristallisationsgeschwindigkeit der Metalle", Zeitschrift für Physikalische Chemie **92**, 219–221 (1918) 10.1515/zpch-1918-9212.

[50] H. Z. Massoud and J. D. Plummer, "Analytical relationship for the oxidation of silicon in dry oxygen in the thin-film regime", J. Appl. Phys. **62**, 3416–3423 (1987) 10.1063/1.339305.

[51] Z. Massoud, Hisham, J. D. Plummer, and E. A. Irene, "Thermal oxidation of silicon in dry oxygen - accurate determination of the kinetic rate constants", J. Electrochem. Soc. **132**, 1745–1753 (1985) 10.1149/1.2114204.

[52] H. Z. Massoud, "Thermal oxidation of silicon in the ultrathin regime", Solid-State Eletronics **41**, 929–934 (1997) 10.1016/S0038-1101(97)00001-4.

[53] C. Krzeminski, G. Larrieu, J. Penaud, E. Lampin, and E. Dubois, "Silicon dry oxidation kinetics at low temperature in the nanometric range: Modeling and experiment", J. Apl. Phys. **101**, 064908 (2007) 10.1063/1.2711764.

[54] J. Rinder, "SiO_x/SiN_x-basierte Oberflächenpassivierung für kristalline Si-Solarzellen mit rekombinationsarmem Emitter", Master's Thesis (University of Konstanz, 2016).

[55] B. Nemeth, S. P. Harvey, D. L. Young, M. R. Page, V. LaSalvia, D. Findley, A. Kale, S. Theingi, and P. Stradins, "Critical interface: Poly-silicon to tunneling SiO_2 for passivated contact performance", AIP Conf. Proc. **2147**, 050008 (2019) 10.1063/1.5123857.

[56] A. Gallacher and J. Scott, "Gas and surface processes leading to hydrogenated amorphous silicon films", Solar Cells **21**, 147–152 (1987).

[57] R. Street, *Hydrogenated amorphous silicon*, edited by R. Cahn, E. Davis, and I. Ward (Cambridge University Press, Cambridge, 1991).

[58] D. M. Mattox, *Handbook of physial vapor deposition (PVD) processing*, 2. Edition (Elsevier Inc., Oxford, 2010), pp. 246–253, 10.1016/C2009-0-18800-1.

[59] L. Tutsch, M. Bivour, W. Wolke, M. Hermle, and J. Rentsch, "Influence of the transparent electrode sputtering process on the interface passivation quality of silicon heterojunction solar cells", Proc. 33rd EUPVSEC, 720–724 (2017) 10.4229/EUPVSEC20172017-2AV.3.8.

[60] B.-M. Meiners, D. Borchert, S. Hohage, S. Holinksi, and P. Schäfer, "Degradation of hydrogenated amorphous silicon passivation films caused by sputtering deposition", Phys. Status Solidi A **212**, 1817–1822 (2015) 10.1002/pssa.201431923.

[61] J. Steffens, J. Rinder, G. Hahn, and B. Terheiden, "Compensation of the sputter damage during a-Si deposition for poly-Si/SiO_x passivating contacts by ex-situ P-doping", AIP Conf. Proc. **2147**, 040018 (2019) 10.1063/1.5123845.

[62] M. Moreno, R. Ambrosio, A. Torres, A. Torres, P. Rosales, A. Itzmoyotl, and M. Domínguez, "Amorphous, polymorphous, and microcrystalline silicon thin films deposited by plasma at

low temperatures", in *Crystalline and non-crystalline solids*, edited by P. Mandracci (IntechOpen, 2016) Chap. 8, pp. 147–171, 10.5772/61501.

[63] T. DiStefano and D. Eastman, "The band edge of amorphous SiO_2 by photoinjection and photoconductivity measurements", Solid State Commun. **9**, 2259–2261 (1971) 10.1016/0038-1098(71)90643-0.

[64] T. Hayashi, S. Miyazaki, and M. Hirose, "Determination of band discontinuity in amorphous silicon heterojunctions", Jpn. J. Appl. Phys. **27**, L314–L316 (1988).

[65] J. Steffens, M. A. Fazio, D. Cavalcoli, and B. Terheiden, "Multi-characterization study of interface passivation quality of amorphous sub-stoichiometric silicon oxide and silicon oxynitride layers for photovoltaic applications", Sol. Energy Mater. Sol. Cells **187**, 104–112 (2018) 10.1016/j.solmat.2018.07.024.

[66] T. M. Brown, C. Bittencourt, M. Sebastiani, and F. Evangelisti, "Electronic states and band lineups in c -Si(100)/a-$Si_{1-x}C_x$:H heterojunctions", Phys. Rev. B **55**, 9904–9909 (1997) 10.1103/PhysRevB.55.9904.

[67] H.-K. Tsai, W.-L. Lin, W. J. Sah, and S.-C. Lee, "The characteristics of amorphous silicon carbide hydrogen alloy", J. Appl. Phys. **64**, 1910–1915 (1988) 10.1063/1.342501.

[68] T. Kinoshita, M. Isomura, Y. Hishikawa, and S. Tsuda, "Influence of oxygen and nitrogen in the intrinsic layer of a-Si:H solar cells", Jpn. J. Appl. Phys. **35**, 3819–3824 (1996) 10.1143/JJAP.35.3819.

[69] J. C. Bravman, G. L. Patton, and J. D. Plummer, "Structure and morphology of polycrystalline silicon-single crystal silicon interfaces", J. Appl. Phys. **57**, 2779–2782 (1985) 10.1063/1.335421.

[70] N. Fanfoni and M. Tomellini, "The Johnson-Mehl-Avrami-Kolmogorov model: A brief review", Il Nuovo Cimento **20**, 1171–1182 (1998) 10.1007/BF03185527.

[71] H.-J. Kim and C. Thompson, "Kinetic modeling of grain growth in polycrystalline silicon films doped with phosphorus or boron", J. Electrochem. Soc. **135**, 2312–2319 (1988) 10.1149/1.2096261.

[72] J. Ocenasek, P. Novak, and S. Agbo, "Finite-thickness effect on crystallization kinetics in thin films and its adaptation in the Johnson-Mehl-Avrami-Kolmogorov model", J. Appl. Phys. **115**, 043505 (2014) 10.1063/1.4862858.

[73] G. Olson and J. Roth, "Kinetics of solid phase crystallization in amorphous silicon", Materials Science Reports **3**, 1–78 (1988) 10.1016/S0920-2307(88)80005-7.

[74] J. M. Westra, R. A. C. M. M. van Swaaij, P. Sutta, K. Sharma, M. Creatore, and M. Zeman, "Study of the effect of boron doping on the solid phase crystallisation of hydrogenated amorphous silicon films", Thin Solid Films **568**, 38–43 (2014) 10.1016/j.tsf.2014.07.040.

[75] H. Li, K. Kim, B. Hallam, B. Hoex, S. Wenham, and M. Abbott, "$POCl_3$ diffusion for industrial Si solar cell emitter formation", Front. Energy **11**, 42–51 (2017) 10.1007/s11708-016-0433-7.

[76] A. Liu, D. Yan, S. P. Phang, A. Cuevas, and D. Macdonald, "Effective impurity gettering by phosphorus- and boron-diffused polysilicon passivating contacts for silicon solar cells", Sol. Energy Mater. Sol. Cells **179**, 136–141 (2018) 10.1016/j.solmat.2017.11.004.

[77] B. Vermang, H. Goverde, A. Uruena, A. Lorenz, E. Cornagliotti, A. Rothschild, J. John, J. Poormans, and R. Mertens, "Blistering in ALD Al_2O_3 passivation layers as rear contacting for local Al BSF Si solar cells", Sol. Energy Mater. Sol. Cells **101**, 204–209 (2012) 10.1016/j.solmat.2012.01.032.

[78] A. Richter, S. Henneck, J. Benick, M. Hörteis, M. Hermle, and S. Glunz, "Firing stable Al_2O_3/SiN_x layer stack passivation for the front side boron emitter of n-type silicon solar cells", Proc. 25th EUPVSEC, 10.4229/25thEUPVSEC2010-2DO.2.4 (2010) 10.4229/25thEUPVSEC2010-2DO.2.4.

[79] S. Jafari, J. Steffens, M. Wendt, B. Terheiden, S. Meyer, and D. Lausch, "Occurrence of Sharp Hydrogen Effusion Peaks of Hydrogenated Amorphous Silicon Film and Its Connection to Void Structures", Phys. Status Solidi B, 2000097 (2020) 10.1002/pssb.202000097.

[80] B. Terreault, "Hydrogen blistering of silicon: Progress in fundamental understanding", Phys. Status Solidi A **204**, 2129–2184 (2007) 10.1002/pssa.200622520.

[81] B. Aspar, H. Moriceau, E. Jalaguier, C. Lagahe, A. Soubie, B. Biasse, A. Papon, A. Claverie, J. Grisolia, G. Benassayag, F. Letertre, O. Rayssac, T. Barge, C. Maleville, and B. Ghyselen, "The generic nature of the Smart-Cut® process for thin film transfer", J. Electron. Mater. **30**, 834–840 (2001) 10.1007/s11664-001-0067-2.

[82] J. A. Aguiar, D. Young, B. Lee, W. Nemeth, S. Harvey, T. Aoki, M. Al-Jassim, and P. Stradins, "Atomic scale understanding of poly-Si/SiO_2/c-Si passivated contacts: Passivation degradation due to metallization", Proc. 43rd IEEE PVSC, 3667–3670 (2016) 10.1109/PVSC.2016.7750359.

[83] H. Kim, S. Bae, K.-s. Ji, S. Min, J. Woong, C. Hyun, K. Dong, S. Kim, Y. Kang, H.-s. Lee, and D. Kim, "Passivation properties of tunnel oxide layer in passivated contact silicon solar cells", Appl. Surf. Sci. **409**, 140–148 (2017) 10.1016/j.apsusc.2017.02.195.

[84] K. Tao, Q. Li, C. Hou, S. Jiang, J. Wang, R. Jia, Y. Sun, Y. Li, Z. Jin, and X. Liu, "Application of a-Si/mc-Si hybrid layer in tunnel oxide passivated contact n-type silicon solar cells", Solar Energy **144**, 735–739 (2017) 10.1016/j.solener.2017.01.061.

[85] H. R. Shanks and L. Ley, "Formation of pin holes in hydrogenated amorphous silicon at high temperatures and the yield strength of a-Si:H", J. Appl. Phys. **52**, 811–813 (1981) 10.1063/1.328767.

[86] M. M. Mandurah, K. C. Saraswat, and T. I. Kamins, "A model for conduction in polycrystalline silicon - Part I: Theory", IEEE T. Electron. Dev. **28**, 1163–1171 (1981) 10.1109/T-ED.1981.20504.

[87] J. Y. W. Seto, "The electrical properties of polycrystalline silicon films", J. Appl. Phys. **46**, 5247–5254 (1975) 10.1063/1.321593.

[88] M. E. Cowher and T. O. Sedgwick, "Chemical vapor deposited polycrystalline silicon", J. Electrochem. Soc. **119**, 1565–1570 (1972) 10.1149/1.2404043.

[89] N. Lu, L. Gerzberg, and J. Meindl, "A quantitative model of the effect of grain size on the resistivity of polycrystalline silicon resistors", IEEE Electr. Device L. **1**, 38–41 (1980) 10.1109/EDL.1980.25222.

[90] M. Pomaska, J. Mock, F. Köhler, U. Zastrow, M. Perani, O. Astakhov, D. Cavalcoli, R. Carius, F. Finger, and K. Ding, "Role of oxygen and nitrogen in n-type microcrystalline silicon carbide grown by hot wire chemical vapor deposition", J. Appl. Phys. **120**, 225105 (2016) 10.1063/1.4971402.

[91] M. Perani, N. Brinkmann, A. Hammud, D. Cavalcoli, and B. Terheiden, "Nanocrystal formation in silicon oxy-nitride films for photovoltaic applications: Optical and electrical properties", J. Phys. Chem. C **119**, 13907–13914 (2015) 10.1021/acs.jpcc.5b02286.

[92] T. Kilper, W. Beyer, G. Bräuer, T. Bronger, R. Carius, M. N. van den Donker, D. Hrunski, A. Lambertz, T. Merdzhanova, A. Mück, B. Rech, W. Reetz, R. Schmitz, U. Zastrow, and A. Gordijn, "Oxygen and nitrogen impurities in microcrystalline silicon deposited under optimized conditions: Influence on material properties and solar cell performance", J. Appl. Phys. **105**, 074509 (2009) 10.1063/1.3104781.

[93] S. Miyajima, A. Yamada, and M. Konagai, "Characterization of undoped, n- and p-type hydrogenated nanocrystalline silicon carbide films deposited by hot-wire chemical vapor deposition at low temperatures", Jpn. J. Appl. Phys. **46**, 1415–1426 (2007) 10.1143/JJAP.46.1415.

[94] M. Schnabel, B. W. H. van de Loo, W. Nemeth, B. Macco, P. Stradins, W. M. M. Kessels, and D. L. Young, "Hydrogen passivation of poly-Si/SiO_x contacts for Si solar cells using Al_2O_3 studied with deuterium", Appl. Phys. Lett. **112**, 203901 (2018) 10.1063/1.5031118.

[95] M. Lehmann, N. Valle, J. Horzel, A. Pshenova, P. Wyss, M. Döbeli, M. Despeisse, S. Eswara, T. Wirtz, Q. Jeangros, A. Hessler-Wyser, F.-J. Haug, A. Ingenito, and C. Ballif, "Analysis of hydrogen distribution and migration in fired passivating contacts", Sol. Energy Mater. Sol. Cells **200**, 110018 (2019) 10.1016/j.solmat.2019.110018.

[96] J. Steffens, G. Hahn, and B. Terheiden, "Towards a fast determination of the hydrogen concentration in thin passivating a-Si:H layers using GD-OES", AIP Conf. Proc. **1999**, 020021 (2018) 10.1063/1.5049260.

[97] J. Steffens, H.-W. Becker, S. Gerke, S. Joos, G. Hahn, and B. Terheiden, "Replacing NRA by fast GD-OES measurements as input to a model based prediction of hydrogen diffusion in a-Si", Energy Procedia **124**, 180–187 (2017) 10.1016/j.egypro.2017.09.315.

[98] T. Nelis and R. Payling, *Glow discharge optical emission spectroscopy: A practical guide* (The Royal Society of Chemistry, Cambridge, 2003), 10.1039/9781847550989.

[99] J. Steffens, "Investigations of preferential sputtering of Fe/W samples in the linear plasma device PSI-2 using glow discharge optical emission spectroscopy", Master's Thesis (Heinrich-Heine University Düsseldorf, 2015).

[100] V.-D. Hodoroaba, D. Klemm, U. Reinholz, E. Strub, J. Röhrich, W. Bohne, V. Hoffmann, and K. Wetzig, "Potential candidates of certified reference material for determination of hydrogen concentration with glow discharge optical emission spectrometry (GD-OES) - A feasibility study", J. Anal. Atom. Spectrom. **23**, 460–462 (2008) 10.1039/b717924c.

[101] H.-W. Becker and D. Rogalla, "Nuclear reaction analysis", in *Neutron scattering and other nuclear techniques for hydrogen in materials*, edited by H. Fritzsche, J. Huot, and D. Fruchart (Springer International Publishing Switzerland, 2016) Chap. 11, pp. 315–336, 10.1007/978-3-319-22792-4.

[102] J. S. Custer, M. O. Thompson, D. C. Jacobson, J. M. Poate, S. Roorda, W. C. Sinke, and F. Spaepen, "Density of amorphous Si", Appl. Phys. Lett. **64**, 437–439 (1994) 10.1063/1.111121.

[103] S. Gerke, H.-W. Becker, D. Rogalla, R. Job, and B. Terheiden, "Model based prediction of the trap limited diffusion of hydrogen in post-hydrogenated amorphous silicon", Phys. Status Solidi RRL **10**, 828–832 (2016) 10.1002/pssr.201600303.

[104] F. Geml, J. Engelhardt, J. Steffens, L.-F. Reinalter, G. Micard, and G. Hahn, "GD-OES depth profiling and calibration of B doped dielectric layers", AIP Conf. Proc. **2147**, 020003 (2019) 10.1063/1.5123808.

[105] F. Geml, "Entwicklung von Methodiken und Standards zur Charakterisierung von dotierten Silizium-basierten Gläsern mittels GD-OES-Analyse", Master's Thesis (University of Konstanz, 2018).

[106] C. Gonzalez-Gago, P. Smid, T. Hofmann, C. Venzago, V. Hoffmann, and W. Gruner, "The use of matrix-specific calibrations for oxygen in analytical glow discharge spectrometry", Anal. Bioanal. Chem. **406**, 7473–7482 (2014) 10.1007/s00216-014-8186-9.

[107] P. Sanchez, B. Fernandez, A. Menendez, D. Gomez, R. Pereiro, and A. Sanz-Medel, "A path towards a better characterisation of silicon thin-film solar cells: Depth profile analysis by pulsed radiofrequency glow discharge optical emission spectrometry", Prog. Photovolt. Res. Appl. **22**, 1246–1255 (2014) 10.1002/pip.2387.

[108] P. R. Griffiths and J. A. de Haseth, *Fourier transform infrared spectrometry*, 2. Edition (John Wiley & Sons, Inc., Hoboken, NJ, 2007).

[109] M. Cardona, "Vibrational spectra of hydrogen in silicon and germanium", Phys. Status Solidi B **118**, 463–481 (1983) 10.1002/pssb.2221180202.

[110] A. H. M. Smets, W. M. M. Kessels, and M. C. M. van de Sanden, "Vacancies and voids in hydrogenated amorphous silicon", Appl. Phys. Lett. **82**, 1547–1549 (2003) 10.1063/1.1559657.

[111] G. Lucovsky, R. J. Nemanich, and J. C. Knights, "Structural interpretation of the vibrational spectra of a-Si:H alloys", Phys. Rev. B **19**, 2064–2073 (1979) 10.1103/PhysRevB.19.2064.

[112] G. Lucovsky, J. Yang, S. S. Chao, J. E. Tyler, and W. Czubatyj, "Oxygen-bonding environments in glow-discharge-deposited amorphous silicon-hydrogen alloy films", Phys. Rev. B **28**, 3225–3233 (1983) 10.1103/PhysRevB.28.3225.

[113] R. Stoudek and J. Humlicek, "Infrared spectroscopy of oxygen interstitials and precipitates in nitrogen-doped silicon", Physica B **376-377**, 150–153 (2006) 10.1016/j.physb.2005.12.040.

[114] E. Bustarret, M. Bensouda, M. Habrard, J. C. Bruyère, S. Poulin, and S. Gujrathi, "Configurational statistics in a-$Si_xN_yH_z$ alloys: A quantitative bonding analysis", Phys. Rev. B **38**, 8171–8184 (1988) 10.1103/PhysRevB.38.8171.

[115] J. Mouro, A. Gualdino, V. Chu, and J. P. Conde, "Microstructure factor and mechanical and electronic properties of hydrogenated amorphous and nanocrystalline silicon thin-films for microelectromechanical systems applications", J. Appl. Phys. **114**, 184905 (2013) 10.1063/1.4829020.

[116] C. Manfredotti, F. Fizzotti, M. Boero, P. Pastorino, P. Polesello, and E. Vittone, "Influence of hydrogen-bonding configurations on the physical properties of hydrogenated amorphous silicon", Phys. Rev. B **50**, 18046–18053 (1994) 10.1103/PhysRevB.50.18046.

[117] H. Shanks, J. Fang, L. Ley, M. Cardona, F. J. Demond, and S. Kalbitzer, "Infrared spectrum and structure of hydrogenated amorphous silicon", Phys. Status Solidi B **100**, 43–56 (1980) 10.1002/pssb.2221000103.

[118] J. Steffens, J. Rinder, G. Hahn, and B. Terheiden, "Correlation between the optical bandgap and the monohydride bond density of hydrogenated amorphous silicon", J. Non-Cryst. Solids: X **5**, 100044 (2020) 10.1016/j.nocx.2020.100044.

[119] P. Vandenabeele, *Practical Raman spectroscopy: An introduction* (John Wiley & Sons, Ltd., 2013).

[120] C. Smit, R. A. C. M. M. van Swaaij, H. Donker, A. M. H. N. Petit, W. M. M. Kessels, and M. C. M. van de Sanden, "Determining the material structure of microcrystalline silicon from Raman spectra", J. Appl. Phys. **94**, 3582–3588 (2003) 10.1063/1.1596364.

[121] A. Zwick and R. Carles, "Multiple-order scattering in crystalline and amorphous silicon", Phys. Rev. B **48**, 6024–6032 (1993) 10.1103/PhysRevB.48.6024.

[122] B. D. Beier and A. J. Berger, "Method for automated background subtraction from Raman spectra containing known contaminants", Analyst **134**, 1198–1202 (2009) 10.1039/b821856k.

[123] L. Houben, M. Luysberg, P. Hapke, R. Carius, F. Finger, and H. Wagner, "Structural properties of microcrystalline silicon in the transition from highly crystalline to amorphous growth", Philos. Mag. A **77**, 1447–1460 (1998) 10.1080/01418619808214262.

[124] Z. Iqbal, A. P. Webb, and P. Capezzuto, "Raman scattering from small particle size polycrystalline silicon", Solid State Commun. **37**, 993–996 (1981) 10.1016/0038-1098(81)91202-3.

[125] M. Ledinsky, A. Vetushka, J. Stuchlik, T. Mates, A. Fejfar, J. Kocka, and J. Stepanek, "Crystallinity of the mixed phase silicon thin films by Raman spectroscopy", J. Non-Cryst. Solids **354**, 2253–2257 (2008) 10.1016/j.jnoncrysol.2007.09.073.

[126] G. Faraci, S. Gibilisco, P. Russo, and A. R. Pennisi, "Modified Raman confinement model for Si nanocrystals", Phys. Rev. B **73**, 033307 (2006) 10.1103/PhysRevB.73.033307.

[127] E. Edelberg, S. Bergh, R. Naone, M. Hall, and E. S. Aydil, "Luminescence from plasma deposited silicon films", J. Appl. Phys. **81**, 2410–2417 (1997) 10.1063/1.364247.

[128] A. Gajović, D. Gracin, K. Juraić, J. Sancho-Parramon, and M. Čeh, "Correlating Raman-spectroscopy and high-resolution transmission-electron-microscopy studies of amorphous / nanocrystalline multilayered silicon thin films", Thin Solid Films **517**, 5453–5458 (2009) 10.1016/j.tsf.2009.01.086.

[129] C. Ossadnik, S. Veprek, and I. Gregora, "Applicability of Raman scattering for the characterization of nanocrystalline silicon", Thin Solid Films **337**, 148–151 (1999) 10.1016/S0040-6090(98)01175-4.

[130] H. Miura, H. Ohta, N. Okamoto, and T. Kaga, "Crystallization-induced stress in silicon thin films", Appl. Phys. Lett. **60**, 2746–2748 (1992) 10.1063/1.106864.

[131] I. De Wolf, "Stress measurements in Si microelectronics devices using Raman spectroscopy", J. Raman Spectrosc. **30**, 877–883 (1999) 10.1002/(SICI)1097-4555(199910)30:10<877::AID-JRS464>3.0.CO;2-5.

[132] G. A. Myers, S. S. Hazra, M. P. de Boer, C. A. Michaels, S. J. Stranick, R. P. Koseski, R. F. Cook, and F. W. DelRio, "Stress mapping of micromachined polycrystalline silicon devices via confocal Raman microscopy", Appl. Phys. Lett. **104**, 191908 (2014) 10.1063/1.4878616.

[133] H. Fujiwara, *Spectroscopic ellipsometry - Principles and applications* (Maruzen Co. Ltd, Tokyo, Japan, 2007).

[134] H. Fujiwara and R. W. Collins, *Spectroscopic ellipsometry for photovoltaics volume 1: Fundamental principles and solar cell characterization*, edited by W. T. Rhodes (Springer International Publishing AG, 2018), 10.1007/978-3-319-75377-5.

[135] D. V. Likhachev, "Model selection in spectroscopic ellipsometry data analysis: Combining an information criteria approach with screening sensitivity analysis", Appl. Surf. Sci. **421**, 617–623 (2017) 10.1016/j.apsusc.2016.09.139.

[136] C. M. Herzinger, B. Johs, W. A. Mcgahan, J. A. Woollam, W. Paulson, and I. Introduction, "Ellipsometric determination of optical constants for silicon and thermally grown silicon dioxide via a multi-sample, multi- wavelength, multi-angle investigation", Journal of Applied Physics **83**, 3323–3336 (1998).

[137] G. E. Jellison and F. A. Modine, "Parameterization of the optical functions of amorphous materials in the interband region", Appl. Phys. Lett. **69**, 371–373 (1996) 10.1063/1.118064.

[138] G. E. Jellison and F. A. Modine, “Erratum: "Parameterization of the optical functions of amorphous materials in the interband region"[Appl. Phys. Lett. 69, 371 (1996)]”, Appl. Phys. Lett. **69**, 2137 (1996) 10.1063/1.118155.

[139] G. E. Jellison, F. A. Modine, P. Doshi, and A. Rohatgi, “Spectroscopic ellipsometry characterization of thin-film silicon nitride”, Thin Solid Films **313-314**, 193–197 (1998) 10.1016/S0040-6090(97)00816-X.

[140] D. Aspnes, J. Theeten, and F. Hottier, “Investigation of effective-medium models of microscopic surface roughness by spectroscopic ellipsometry”, Phys. Rev. B **20**, 3292–3302 (1979) 10.1103/PhysRevB.20.3292.

[141] J. Tauc, R. Grigorovici, and A. Vancu, “Optical properties and electronic structure of amorphous germanium”, Phys. Status Solidi **15**, 627–637 (1966) 10.1002/pssb.19660150224.

[142] A. Dolgonos, T. O. Mason, and K. R. Poeppelmeier, “Direct optical band gap measurement in polycrystalline semiconductors: A critical look at the Tauc method”, J. Solid State Chem. **240**, 43–48 (2016) 10.1016/j.jssc.2016.05.010.

[143] A. R. Zanatta, “Revisiting the optical bandgap of semiconductors and the proposal of a unified methodology to its determination”, Scientific Reports **9**, 11225 (2019) 10.1038/s41598-019-47670-y.

[144] E. C. Freeman and W. Paul, “Optical constants of rf sputtered hydrogenated amorphous Si”, Phys. Rev. B **20**, 716–728 (1979) 10.1103/PhysRevB.20.716.

[145] L. A. A. Pettersson, L. S. Roman, and O. Inganas, “Modeling photocurrent action spectra of photovoltaic devices based on organic thin films”, J. Appl. Phys. **86**, 487–496 (1999) 10.1063/1.370757.

[146] G. F. Burkhard, E. T. Hoke, and M. D. Mcgehee, “Accounting for interference, scattering, and electrode absorption to make accurate internal quantum efficiency measurements in organic and other thin solar cells”, Adv. Mater. **22**, 3293–3297 (2010) 10.1002/adma.201000883.

[147] L. J. van der Pauw, “A method of measuring specific resistivity and Hall effect of discs of arbitrary shape”, Philips Res. Repts **13**, 1–9 (1958).

[148] M. A. Green and M. W. Gunn, “Four point probe Hall effect and resistivity measurements upon semiconductors”, Solid State Electron. **15**, 577–585 (1972) 10.1016/0038-1101(72)90159-1.

[149] A. A. Ramadan, R. D. Gould, and A. Ashour, “On the van der Pauw method of resistivity measurements”, Thin Solid Films **239**, 272–275 (1994) 10.1016/0040-6090(94)90863-X.

[150] R. A. Sinton and A. Cuevas, “Contactless determination of current-voltage characteristics and minority-carrier lifetimes in semiconductors from quasi-steady-state photoconductance data”, Appl. Phys. Lett. **69**, 2510–2512 (1996) 10.1063/1.117723.

[151] A. Herguth, “On the meaning(fullness) of the intensity unit ’suns’ in light induced degradation experiments”, Energy Procedia **124**, 53–59 (2017) 10.1016/j.egypro.2017.09.339.

[152] A. L. Blum, J. S. Swirhun, R. A. Sinton, F. Yan, S. Herasimenka, T. Roth, K. Lauer, J. Haunschild, B. Lim, K. Bothe, Z. Hameiri, B. Seipel, R. Xiong, M. Dhamrin, and J. D. Murphy, “Interlaboratory study of eddy-current measurement of excess-carrier recombination lifetime”, IEEE J. Photovolt. **4**, 525–531 (2014) 10.1109/JPHOTOV.2013.2284375.

[153] K. R. McIntosh and R. A. Sinton, “Uncertainty in photoconductance lifetime measurements that use an inductive-coil detector”, Proc. 23rd EUPVSEC, 77–82 (2008) 10.4229/23rdEUPVSEC2008-1AO.6.2.

[154] D. E. Kane and R. M. Swanson, “Measurement of the emitter saturation current by a contactless photoconductivity decay method”, Proc. 18th IEEE PVSC, 578–583 (1985).

[155] A. Kimmerle, J. Greulich, and A. Wolf, “Carrier-diffusion corrected J_0-analysis of charge carrier lifetime measurements for increased consistency”, Sol. Energy Mater. Sol. Cells **142**, 116–122 (2015) 10.1016/j.solmat.2015.06.043.

[156] A. Richter, S. W. Glunz, F. Werner, J. Schmidt, and A. Cuevas, “Improved quantitative description of Auger recombination in crystalline silicon”, Phys. Rev. **86**, 165202 (2012) 10.1103/PhysRevB.86.165202.

[157] G. Micard, “Seminar on PCD measurement and its connected physical quantities”, Personal communication, University of Konstanz (2019).

[158] R. Saleh and N. H. Nickel, “The influence of boron concentrations on structural properties in disorder silicon films”, Appl. Surf. Sci. **254**, 580–585 (2007) 10.1016/j.apsusc.2007.06.024.

[159] E. Bertran, J. L. Andujar, A. Canillas, C. Roth, J. Serra, and G. Sardin, “Effects of deposition temperature on properties of r.f. glow discharge amorphous silicon thin films”, Thin Solid Films **205**, 140–145 (1991) 10.1016/0040-6090(91)90295-9.

[160] J. Müllerova, M. Fischer, M. Netrvalova, M. Zeman, and P. Sutta, “Influence of deposition temperature on amorphous structure of PECVD deposited a-Si:H thin films”, Cent. Eur. J. Phys. **9**, 1301–1308 (2011) 10.2478/s11534-011-0041-4.

[161] S. Li, M. Pomaska, J. Hoß, J. Lossen, F. Pennartz, M. Nuys, R. Hong, A. Schmalen, J. Wolff, F. Finger, U. Rau, and K. Ding, “Poly-Si / SiO_x / c-Si passivating contact with 738 mV implied open circuit voltage fabricated by hot-wire chemical vapor deposition”, Appl. Phys. Lett. **114**, 153901 (2019) 10.1063/1.5089650.

[162] W. Liu, L. Zhang, F. Meng, W. Guo, J. Bao, J. Liu, D. Wang, and Z. Liu, “Characterization of microvoids in thin hydrogenated amorphous silicon layers by spectroscopic ellipsometry and Fourier transform infrared spectroscopy”, Scripta Materialia **107**, 50–53 (2015) 10.1016/j.scriptamat.2015.05.018.

[163] Z. Remes, M. Vanecek, P. Torres, U. Kroll, A. Mahan, and R. Crandall, “Optical determination of the mass density of amorphous and microcrystalline silicon layers with different hydrogen contents”, J. Non-Cryst. Solids **227-230**, 876–879 (1998) 10.1016/S0022-3093(98)00207-5.

[164] G. D. Cody, T. Tiedje, B. Abeles, B. Brooks, and Y. Goldstein, “Disorder and the optical-absorption edge of hydrogenated amorphous silicon”, Phys. Rev. Lett. **47**, 1480–1483 (1981) 10.1103/PhysRevLett.47.1480.

[165] A. P. Sokolov, A. P. Shebanin, O. A. Golikova, and M. M. Mezdrogina, “Structural disorder and optical gap fluctuations in amorphous silicon”, J. Phys.: Condens. Matter **3**, 9887–9894 (1991) 10.1088/0953-8984/3/49/005.

[166] S. Yamasaki, “Optical absorption edge of hydrogenated amorphous silicon studied by photoacoustic spectroscopy”, Philos. Mag. B **56**, 79–97 (1987) 10.1080/13642818708211226.

[167] M. Daouahi, A. Ben Othmane, K. Zellama, A. Zeinert, M. Essamet, and H. Bouchriha, “Effect of the hydrogen bonding and content on the opto-electronic properties of radiofrequency magnetron sputtered hydrogenated amorphous silicon films”, Solid State Commun. **120**, 243–248 (2001) 10.1016/S0038-1098(01)00350-7.

[168] S. Gupta, R. S. Katiyar, G. Morell, and S. Z. Weisz, “The effect of hydrogen on the network disorder in hydrogenated amorphous silicon”, Appl. Phys. Lett. **75**, 2803–2805 (1999) https://doi.org/10.1063/1.125155.

[169] N. Maley and J. Lannin, “Influence of hydrogen on vibrational and optical properties of a-$Si_{1\text{-}x}H_x$ alloys”, Phys. Rev. B **36**, 1146–1152 (1987) 10.1103/PhysRevB.36.1146.

[170] M. Yamaguchi and K. Morigaki, “Effect of hydrogen dilution on the optical properties of hydrogenated amorphous silicon prepared by plasma deposition”, Philos. Mag. B **79**, 387–405 (1999) 10.1080/13642819908206415.

[171] M. Legesse, M. Nolan, and G. Fagas, “Revisiting the dependence of the optical and mobility gaps of hydrogenated amorphous silicon on hydrogen concentration”, J. Phys. Chem. C **117**, 23956–23963 (2013) 10.1021/jp408414f.

[172] K. Zellama, L. Chahed, P. Sladek, M. Theye, J. von Bardeleben, and P. Roca i Cabarrocas, “Hydrogen-effusion-induced structural changes and defects in a-Si:H films: Dependence upon the film microstructure”, Phys. Rev. B **53**, 3804–3812 (1996) 10.1103/PhysRevB.53.3804.

[173] K. Inoue, F. Yano, A. Nishida, H. Takamizawa, T. Tsunomura, Y. Nagai, and M. Hasegawa, “Dopant distribution in gate electrode of n- and p-type metal-oxide-semiconductor field effect transistor by laser-assisted atom probe”, Appl. Phys. Lett. **95**, 043502 (2009) 10.1063/1.3186788.

[174] P. G. Snyder, Y.-M. Xiong, and J. Woollam, “Graded refractive index silicon oxynitride thin film characterized by spectroscopic ellipsometry”, J. Vac. Sci. Technol. A **10**, 1462–1466 (1992) 10.1116/1.578266.

[175] N. Khelifati, S. Tata, A. Rahal, R. Cherfi, A. Fedala, M. Kechouane, and T. Mohammed-Brahim, “The annealing temperature effect on the electrical properties of boron-doped hydrogenated amorphous silicon a-Si:H(B)”, Phys. Status Solidi C **7**, 679–682 (2010) 10.1002/pssc.200982718.

[176] S. Yamasaki, A. Matsuda, and K. Tanaka, "Anomalous optical and structural properties of B-doped a-Si: H", Jpn. J. Appl. Phys. **21**, L789–L791 (1982) 10.1143/JJAP.21.L789.

[177] T. Mueller, S. Schwertheim, and W. R. Fahrner, "Crystalline silicon surface passivation by high-frequency plasma-enhanced chemical-vapor-deposited nanocomposite silicon suboxides for solar cell applications", J. Appl. Phys. **107**, 014504 (2010) 10.1063/1.3264626.

[178] T. Baak, "Silicon oxynitride; a material for GRIN optics", Applied Optics **21**, 1069–1072 (1982) 10.1364/AO.21.001069.

[179] Z. Jun-chao, X. Li-min, F. Ming, and H. Hong-Bo, "Wide-angle and broadband graded-refractive-index antireflection coatings", Chinese Phys. B **22**, 044201 (2013) 10.1088/1674-1056/22/4/044201.

[180] R. Glatthaar, "Fabrication and characterisation of polycrystalline Si layers with reduced parasitic absorption for passivating contacts of solar cells", Master's Thesis (University of Konstanz, 2019).

[181] J. Steffens, S. Weit, J. Rinder, R. Glatthaar, S. Möller, G. Hahn, and B. Terheiden, "Influence of the Carbon Concentration on (p) Poly-SiC_x Layer Properties With Focus on Parasitic Absorption in Front Side Poly-SiC_x/SiO_x Passivating Contacts of Solar Cells", IEEE J. Photovolt. **10**, 1624–1631 (2020) 10.1109/JPHOTOV.2020.3023506.

[182] B. deB. Darwent, "Bond dissociation energies in simple molecules", in *National standard reference data series*, 31 (National Bureaau of Standards, Washington, 1970).

[183] S. Solmi, A. Parisini, R. Angelucci, A. Armigliato, D. Nobili, and L. Moro, "Dopant and carrier concentration in Si in equilibrium with monoclinic SiP precipitates", Phys. Rev. B **53**, 7836–7841 (1996) 10.1103/PhysRevB.53.7836.

[184] F. Lau, L. Mader, C. Mazure, C. Werner, and M. Orlowski, "A model for phosphorus segregation at the silicon-silicon dioxide interface", Appl. Phys. A **49**, 671–675 (1989) 10.1007/BF00616992.

[185] A. Carabelas, D. Nobili, and S. Solmi, "Grain boundary segregation in silicon heavily doped with phosphorus and arsenic", J. Phys. Colloques **43**, C1 187–192 (1982) 10.1051/jphyscol:1982125.

[186] M. K. Stodolny, J. Anker, B. L. Geerligs, G. J. Janssen, B. W. Van De Loo, J. Melskens, R. Santbergen, O. Isabella, J. Schmitz, M. Lenes, J. M. Luchies, W. M. Kessels, and I. Romijn, "Material properties of LPCVD processed n-type polysilicon passivating contacts and its application in PERPoly industrial bifacial solar cells", Energy Procedia **124**, 635–642 (2017) 10.1016/j.egypro.2017.09.250.

[187] A. Liu, D. Yan, J. Wong-Leung, L. Li, S. P. Phang, A. Cuevas, and D. Macdonald, "Direct observation of the impurity gettering layers in polysilicon-based passivating contacts for silicon solar cells", ACS Appl. Energy Mater. **1**, 2275–2282 (2018) 10.1021/acsaem.8b00367.

[188] D. A. Clugston and P. A. Basore, “Modelling free-carrier absorption in solar cells”, Prog. Photovolt. Res. Appl. **5**, 229–236 (1997) 10.1002/(SICI)1099-159X(199707/08)5:4<229::AID-PIP164>3.0.CO;2-6.

[189] T. Makino and H. Nakamura, “Resistivity changes of heavily-boron-doped CVD-prepared polycrystalline silicon caused by thermal annealing”, Solid State Eletron. **24**, 49–55 (1980) 10.1016/0038-1101(81)90211-2.

[190] L. Palmetshofer, “Rutherford backscattering spectroscopy (RBS)”, in *Surface and thin film analysis: a compendium of principles, instrumentation, and applications*, edited by G. Friedbacher and H. Bubert, 2. Edition (Wiley-VCH Verlag, 2011) Chap. 11, pp. 191–202, 10.1002/9783527636921.ch11.

[191] W. A. P. Claassen, H. A. J. T. v. d. Pol, and A. H. Goemans, “Characterization of silicon-oxynitride films deposited by plasma-enhanced CVD”, J. Electrochem. Soc. **133**, 1458–1464 (1986) 10.1149/1.2108934.

[192] D.-S. Wuu, R.-H. Horng, C.-C. Chan, and Y.-S. Lee, “Plasma-deposited amorphous silicon carbide films for micromachined fluidic channels”, Appl. Surf. Sci. **144-145**, 708–712 (1999) 10.1016/S0169-4332(98)00911-8.

[193] S. Habermehl and R. T. Apodaca, “Correlation of charge transport to intrinsic strain in silicon oxynitride and Si-rich silicon nitride thin films”, Appl. Phys. Lett. **84**, 215–217 (2004) 10.1063/1.1639132.

[194] G. Smolinsky and T. P. H. F. Wendling, “Measurements of temperature dependent stress of silicon oxide films prepared by a variety of CVD methods”, J. Electrochem. Soc. **132**, 950–954 (1985) 10.1149/1.2113992.

[195] H. Park, S. Bae, S. J. Park, J. Y. Hyun, C. H. Lee, D. Choi, D. Kang, H. Han, Y. Kang, H.-S. Lee, and D. Kim, “Role of polysilicon in poly-Si/SiO_x passivating contacts for high-efficiency silicon solar cells”, RSC Adv. **9**, 23261–23266 (2019) 10.1039/c9ra03560e.

[196] S. C. Baker-Finch, K. R. McIntosh, D. Yan, K. C. Fong, and T. C. Kho, “Near-infrared free carrier absorption in heavily doped silicon”, J. Appl. Phys. **116**, 063106 (2014) 10.1063/1.4893176.

[197] K. Lancaster, S. Großer, F. Feldmann, V. Naumann, and C. Hagendorf, “Study of pinhole conductivity at passivated carrier-selected contacts of silicon solar cells”, Energy Procedia **92**, 116–121 (2016) 10.1016/j.egypro.2016.07.040.

[198] S. Richter, Y. Larionova, S. Großer, M. Menzel, H. Schulte-Huxel, R. Peibst, R. Brendel, and C. Hagendorf, “Evaluation of localized vertical current formation in carrier selective passivation layers of silicon solar cells by conductive AFM”, AIP Conf. Proc. **2147**, 040017 (2019) 10.1063/1.5123844.

[199] D. Tetzlaff, J. Krügener, Y. Larionova, S. Reiter, M. Turcu, F. Haase, R. Brendel, R. Peibst, U. Höhne, J. Kähler, and T. F. Wietler, “A simple method for pinhole detection in carrier selective POLO-junctions for high efficiency silicon solar cells”, Sol. Energy Mater. Sol. Cells **173**, 106–110 (2017) 10.1016/j.solmat.2017.05.041.

[200] D. Tetzlaff, J. Krügener, Y. Larionova, S. Reiter, M. Turcu, R. Peibst, U. Höhne, J.-D. Kähler, and T. Wietler, "Evolution of oxide disruptions: The (w)hole story about poly-Si/c-Si passivating contacts", Proc. 43rd IEEE PVSC, 221–224 (2016) 10.1109/PVSC.2016.7749582.

[201] A. Richter, M. Hermle, and S. W. Glunz, "Reassessment of the limiting efficiency for crystalline silicon solar cells", IEEE J. Photovolt. **3**, 1184–1191 (2013) 10.1109/JPHOTOV.2013.2270351.

Zusammenfassung

Im Rahmen von Solarzellen basierend auf poly-Si/SiO_x Kontakten wurden verschiedene Abhängigkeiten zwischen der poly-Si Schichtzusammensetzung und der Solarzelleneffizienz identifiziert. Zunächst wurden Strategien zur Vermeidung von Blasenbildung während der Festphasenkristallisation (englisch: solid phase crystallization, SPC) von durch plasma-unterstützte Gasphasenabscheidung (englisch: plasma enhanced chemical vapor deposition, PECVD) aufgewachsenen und in-situ dotierten (p) a-Si:H Schichten entwickelt. Diese Strategien zielen im Wesentlichen auf eine Erhöhung des Mikrostrukturfaktors R^* der im abgeschiedenen Zustand belassenen Schichten vor der SPC ab, welche mit reduzierter Blasenbildung korreliert. Diese Erhöhung wurde durch geringe Bor-Konzentrationen, Beimischung von leichten Elementen und niedrigen Abscheidetemperaturen erreicht, während hohe Abscheidetemperaturen die Blasenbildung ebenfalls durch eine geringere Wasserstoffkonzentration verringerten. Die Anpassung der optischen Bandlücke der im abgeschiedenen Zustand belassenen Schichten konnte leider nicht auf die poly-Si Schichten nach der SPC übertragen werden.

Um die Elementzusammensetzungen zu bestimmen wurden Kalibrationen für die Glimmlampenspektroskopie (englisch: glow discharge optical emission spectroscopy, GD-OES) entwickelt, ebenso wie eine Korrektur für Messartefakte von atmosphärischen Verunreinigungen. Für alle poly-Si Schichten wurde eine Differenz zwischen gesamter und elektrisch aktiver Dotierkonzentration für alle Schichttypen und beide Dotierpolaritäten gefunden. Ebenso wurde eine erhöhte Dotierkonzentration nahe dem Grenzflächenoxid identifiziert, während die Anreicherung von Phosphor jedoch höher ausfiel.

Eine weitere Asymmetrie zwischen beiden Dotierpolaritäten wurde in den reinen poly-Si Schichten ohne Beimischung leichter Elemente gefunden, wo die Effizienz im Falle einer Phosphor-Dotierung durch Absorption durch freie Ladungsträger und im Falle von einer Bor-Dotierung durch zu starke Eindiffusion limitiert ist. Zusätzlich sind Magnetron-gesputterte (englisch: magnetron sputter deposition, MSD) in-situ dotierte (p) poly-Si Schichten durch Volumendefekte limitiert, welche nur teilweise durch die Hydrogenierung abgesättigt wurden. Eine weitere Asymmetrie wurde zwischen beiden Schichtaufwachsmethoden gefunden in Form von deutlich verringerten internen Spannungen σ für die MSD aufgewachsenen poly-Si Schichten im Vergleich zu den PECVD aufgewachsenen Schichten.

Im Kontext der Beimischung leichter Elemente wurde der Kristallinität χ_c eine Schlüsselrolle zugeschrieben, da sie alle Parameter beeinflusst, welche für eine Anwendung in einer Solarzelle relevant sind. Höhere Konzentrationen von leichten Elementen verringerten die Kristallinität und folglich erhöhten sich die Stromdichte der parasitären Absorption J_{PA} und der Kontaktwiderstand ρ_c. Höhere Kristallinitäten wurden für (p) poly-SiO_xN_y Schichten eher durch erhöhte Temperaturen T_{SPC} als

durch längere Dauern t_{SPC} der SPC und für (p) poly-SiC_x Schichten durch eine geringere Kohlenstoffkonzentration c_C erreicht, welche zukünftig durch noch geringere Konzentrationen $c_C < 5$ at% weiter erhöht werden könnte.

Die Beimischung von leichten Elementen zeigte einige Unterschiede zwischen den (p) poly-SiO_xN_y und (p) poly-SiC_x Schichten. Für die ersteren wurden optimale Sauerstoff- und Stickstoffkonzentrationen $c_{O/N}$ im Hinblick auf parasitäre Absorption und Passivierqualität gefunden, während für die letzteren diese Eigenschaften durch eine weiter reduzierte Kohlenstoffkonzentration und damit erhöhte Kristallinität in Zukunft verbessert werden können. Eine Ausnahme bildet die Passivierqualität ausgedrückt als Kontaktrekombinationsstromdichte J_c der (p) poly-SiC_x Schichten, welche von der unbeabsichtigt variierten Bor-Konzentration ξ_B bestimmt wurde und daher in dem untersuchten Bereich unabhängig von der Kohlenstoffkonzentration c_C ist. Bezüglich des Kontaktwiderstandes ρ_c zeigten beide Schichttypen einen Anstieg mit höherer Konzentration leichter Elemente, wohingegen innere Spannungen σ in den (p) poly-SiO_xN_y Schichten gelöst und in den (p) poly-SiC_x Schichten verstärkt wurden. Insgesamt wurde die erwünschte Bandlückenvergrößerung unter Beimischung von leichten Elementen beobachtet, welche allerdings lediglich zu einer verringerten parasitären Absorption J_{PA}, aber nicht eindeutig zu einer erhöhten Passivierqualität führte.

Eine simultane Betrachtung aller Schichttypen offenbarte zwei Zielkonflikte. Der erste Zielkonflikt besteht demnach zwischen der Passivierqualität J_c und dem Kontaktwiderstand ρ_c und wurde explizit für die (n) poly-Si und (p) poly-SiO_xN_y Schichten gefunden. Da beide Größen in die Selektivität S_{10} einfließen, wird dieser Zielkonflikt als prinzipielle Limitierung dieser Selektivität interpretiert. Der zweite Zielkonflikt besteht zwischen der Selektivität S_{10} und der parasitären Absorption J_{PA} für alle reinen poly-Si Schichten ohne Beimischung von leichten Elementen. Daher sind diese Schichten für eine Anwendung auf der Vorderseite einer Solarzelle ungeeignet, selbst wenn die parasitäre Absorption prinzipiell gering genug wäre, da eben dieser Zielkonflikt eine entsprechend zu geringe Selektivität impliziert.

Unter Betrachtung der vielversprechendsten Schichten pro Schichttyp wurde eine exzellente Passivierqualität mit Kontaktrekombinationsstromdichten $J_c < 10$ fA/cm^2 und Selektivitäten im Bereich von $S_{10} = 14.1 - 15.2$ erreicht, mit Potential für weitere Optimierungen. Dabei sei besonders die niedrigste in dieser Arbeit gemessene Kontaktrekombinationsstromdichte von $J_c = 2.3$ fA/cm^2 hervorgehoben, welche mit einer Bor-dotierten (p) poly-SiO_xN_y Schicht erzielt wurde. Vergleichbar niedrige Werte nahe 1 fA/cm^2 sind eher typisch für Phosphor-dotierte poly-Si Schichten und daher scheint die Beimischung von leichten Elementen geeignet zu sein um ähnlich hohe Passivierqualitäten auch für Bor-dotierte Schichten zu erzielen. In diesem Zusammenhang sollte ebenfalls erwähnt werden, dass eine hohe Passivierqualität von $J_c = 7.3$ fA/cm^2 auch mit der vielversprechendsten (p) poly-SiC_x Schicht auf Cz Substrat erzielt wurde, während die Kontaktrekombinationsstromdichten aller anderen Schichttypen auf Silizium FZ Substraten gemessen wurden. Daraus folgernd ist Kohlenstoffbeimischung die vielversprechendste Strategie für zukünftige Optimierungen im Hinblick auf eine reduzierte parasitäre Absorption durch Beimischung von leichten Elementen als Anwendung auf der Vorderseite einer Solarzelle.

Die aussichtsreichste Kombination dieser vielversprechendsten Schichten im Hinblick auf eine Anwendung in einer Solarzelle ist die MSD aufgewachsene (n) poly-Si Schicht auf der Rückseite und die PECVD abgeschiedene (p) poly-SiO_xN_y Schicht auf der Vorderseite. Diese Kombination führt

zu einer maximal erreichbaren idealisierten Solarzelleneffizienz von $\eta_{ideal,max} = 24.2\%$, welche um weitere $\sim 2\%_{\mathrm{abs}}$ erhöht werden kann, wenn die poly-Si Schichtdicke d_{poly} von 100 nm auf 30 nm reduziert wird. Unter Berücksichtigung einer zukünftigen weiteren Optimierung der (p) poly-SiC_x Schicht als Alternative für die (p) poly-SiO_xN_y Schicht auf der Vorderseite belegt diese Arbeit die Anwendbarkeit von poly-Si/SiO_x Kontakten auf der Vorderseite einer Solarzelle durch Beimischung von leichten Elementen in die poly-Si Schicht.

APPENDIX A

Appendix

A.1. List of tools

TABLE A.1. List of all tools used for sample processing in alphabetical order.

		Processing tools		
Tool	**Functionality**	**Specifics**	**Model**	**Manufacturer**
Fast firing furnace (FF)	Fast infrared heating under atmospheric pressure on a belt for hydrogenation	Samples placed on silicon dummies	DO 9.700-300-FF-CANtrol	Centrotherm International AG
Magnetron sputtering tool (MSD)	Argon plasma based magnetron sputtering system with confocal target arrangement in vacuum for hydrogen-free a-Si deposition	Tool located in clean room environment. Samples placed on silicon dummies Base pressure $\sim 10^{-8}$ mTorr. RF power supply.	AJA ATC 2200	AJA International Inc.
Direct plasma enhanced chemical vapor deposition tool (PECVD)	Parallel plate direct plasma reactor in vacuum with two chambers for either intrinsic a-Si:H / SiN_x:H / a-SiO_x:H or boron doped a-Si:H / a-SiO_x:H / a-SiO_xN_y:H / a-SiC_x:H deposition	Samples placed on silicon dummies. Base pressure $\sim 10^{-4}$ mTorr. 13.56 MHz RF power supply. Electrode distance $\sim$ 24 mm.	Plasmalab System 100	Oxford Instruments
Microwave-based plasma enhanced chemical vapor deposition in-line tool (PECVD)	Microwave-excited plasma in-line reactor for SiN_x:H deposition	2.45 GHz RF power supply.	SiNA	Meyer Burger Technology AG
Quartz tube furnace (SPC)	High temperature treatment under atmospheric pressure with two tubes for SPC either N_2 ambient or $POCl_3$-diffusion for ex-situ doping	-	E 1200 HAT 300-4	Centrotherm International AG
Wet Benches	Basin-based wet bench system for substrate cleaning, native oxide removal and Cz substrate saw damage etch and chemical polishing	-	-	Ramgraber GmbH

TABLE A.2. List of all tools used for characterization in alphabetical order.

Characterization tools				
Method	**Target parameter**	**Technical Details**	**Model**	**Manufacturer**
Electrochemical capacitance-voltage profiling (ECV)	Charge carrier concentration depth profiles $n_{e/h}(z)$	-	Wafer Profiler CVP21	DAGE / WEP
Fourier-transform infrared spectroscopy (FT-IR)	Absorption strength I_x Bond density N_x Hydrogen concentration c_H	Light source 500-4000 cm^{-1}. Measurement chamber N_2 flooded.	Vertex 80	Bruker Optics
Glow discharge optical emission spectroscopy (GD-OES)	Raw intensity I_i Qualitative concentration ξ_i Concentration c_i Raw depth profile $I_i(s)$ Calibrated depth profile $c_i(z)$	PMT detectors with 2 kHz data acquisition rate. Base pressure measurement chamber and optics chamber $\sim 10^{-2}$ mbar. 13.56 MHz power supply. Water cooling system at 17°C. Argon 5.0 purity.	GDA 750 HR	Spectruma Analytik GmbH
Hall-effect measurement (HE)	Resistivity ρ_{HE} Charge carrier mobility $\mu_{e/h}$ and concentration $n_{e/h}$	Measurement in the dark.	HMS5000	Ecopia Corporation
Nuclear resonant reaction analysis (NRA)	Hydrogen concentration c_H	Measurements performed by Hans-Werner Becker at RUBION, Ruhr University of Bochum	-	-
Optical Microscopy (OM)	Surface structures	-	Axio Imager M1m	Carl Zeiss
Photoconductance decay measurement (PCD)	Resistivity ρ_{PCD} Contact recombination current density J_c Implied open circuit voltage iV_{oc}	Table heater set temperature 30°C.	Sinton lifetime tester WCT120	Sinton Instruments Inc.
Raman spectroscopy (RS)	Crystallinity χ_c Crystallite size d_c Internal stress σ	Laser wavelength 488 nm at 1 mW power to avoid laser induced crystallization. Combined resolution of EMCCD detector and optical grating $\sim$ 1 cm^{-1}.	WITec alpha300 R	WITec GmbH
Rutherford backscattering spectrometry (RBS)	Carbon concentration c_C	Measurements performed by Sören Möller at the Institute of Energy and Climate Research - Plasma Physics IEK-4, Forschungszentrum Jülich.	-	-
Scanning electron microscopy (SEM)	Surface structures	-	Neon 40 EsB	Carl Zeiss
Spectroscopic ellipsometry (SE)	Layer thickness d Refractive index profile $n(z)$ Optical band gaps E_{gap}, E_{04} Parasitic absorption current density J_{PA}	Rotating detector and analyzer. Spectral range $240-2000$ nm with $\sim$ 1 nm resolution. Xenon lamp light source.	Vertical VASE Rotating analyzer ellipsometer	J.A. Woollam Co., Inc.

A.2. GD-OES Calibration Standards

TABLE A.3. Standards used for GD-OES calibration and corresponding certified concentration c_i and relative sputter rate q according to eq. 3.4 sorted by element. Last row contains the pure iron reference for the determination of the relative sputter rate q with a fixed value of $q = 1$ per definition.

Name	Manufacturer	c_x (at%)	q
	Hydrogen calibration c_H		
a-Si:H laboratory standard 100	[97]	19.22 ± 0.08	0.209 ± 0.027
a-Si:H laboratory standard 150	[97]	17.67 ± 0.08	0.199 ± 0.025
a-Si:H laboratory standard 200	[97]	15.61 ± 0.07	0.187 ± 0.024
a-Si:H laboratory standard 250	[97]	13.77 ± 0.07	0.190 ± 0.024
a-Si:H laboratory standard 300	[97]	12.27 ± 0.07	0.190 ± 0.024
a-Si:H laboratory standard 400	[97]	10.10 ± 0.06	0.178 ± 0.022
IARM 178D	LGC Standards	0.074 ± 0.009	0.326 ± 0.006
IARM 271A	LGC Standards	0.596 ± 0.183	0.316 ± 0.010
	Phosphorus calibration c_P		
11X 8C U	MBH Analytical Ltd.	1.346 ± 0.012	1.416 ± 0.125
JK SUS NiP-1	Swerea Kimab	10.467 ± 0.361	1.37 ± 0.01
	Boron calibration c_B		
BSG laboratory standard E	[104, 105]	7.20 ± 0.30	0.204 ± 0.010
BSG laboratory standard Z	[104, 105]	15.40 ± 0.41	0.190 ± 0.010
	Oxygen calibration c_O		
CE 650 A	Swerea Kimab	45.562 ± 0.100	0.19 ± 0.01
	Nitrogen calibration c_N		
JK 49	Corrosion and Metals Research Institute Stockholm	7.044 ± 0.224	1.026 ± 0.053
TiN	Volker Hoffmann, IFW Dresden e.V.	50 ± 1	0.29 ± 0.01
	Pure iron reference for determination of q		
EZRM 089-1	ECISS	-	1

A.3. a-SiC$_x$ PECVD Deposition Parameters

TABLE A.4. PECVD deposition parameters plasma power P, chamber pressure p, deposition temperature T_{set}, methane gas flow ratio R_{CH4} and duration t of all investigated a-SiC$_x$:H layers for constant $R_{B2H6} = 1.4\%$ and corresponding RBS measured carbon concentrations c_C.

P (W)	p (mTorr)	T_{set} (°C)	R_{CH4} (%)	t (s)	c_C (at%)
20	800	400	33	300	6.9 ± 0.3
40	800	300	33	240	8.2 ± 0.4
40	800	400	33	180	8.8 ± 0.4
20	800	400	50	420	10.3 ± 0.5
40	350	400	50	420	12.2 ± 0.6
20	800	400	66	510	14.6 ± 0.7
40	800	300	50	300	17.8 ± 0.9
100	800	400	50	270	21.5 ± 1.1

Acknowledgements

One could misunderstand the term monograph as describing a work being prepared by a single person. In fact, this is hardly true and therefore I appreciate each contribution made to this work. In particular I would like to thank

Prof. Giso Hahn for supervision, reviewing the final version and providing the infrastructure

Prof. Johannes Boneberg for reviewing the final version

Barbara Terheiden for being at the right time either patient, supportive or corrective and for providing the necessary flexibility

Johannes Rinder for highly valuable input, endless discussions and continuous support in the lab

Raphael Glatthaar for being a hard-working and self-reliant master student which resulted in essential contributions to this thesis

Swetlana Weit for a large frustration tolerance during acquisition of a huge data set and for providing the same for analysis in this thesis

Frank Huster because sometimes quality beats quantity

Manuela Linke for tireless and unconditional support, managing my everyday life during the writing phase and simply being around

Hannah Tendyck for encouragement to start the dissertation in the first place

Bernd Ottengraf for being the root cause of my dedication to physics

My family for continuous encouragement and accepting the distance between us

Josh Engelhardt, Barbara Rettenmaier, Lisa Mahlstaedt and all technicians for keeping the devices running

Vincent Bezold and Moritz Fuchsloch for support in sample processing and characterization

All colleagues for a pleasant working environment and support in all imaginable situations

Without an adequate presentation of the results there is no value in such a work regardless of its scientific relevance. In this sense I would further like to thank Manuela Linke, Raphael Glatthaar, Johannes Rinder, Barbara Terheiden, David Sperber and Hannah Tendyck for proof reading at different stages.